University of Liverpool

Department of Chemistry

UNIVERSITY OF LIVERPOOL

Synthesis and Characterisation of porous Organic/ Inorganic Hybrid Materials

Thesis submitted in accordance with the requirements of the University of Liverpool for the degree of Doctor of Philosophy

By

James Thomas Anthony Jones

2009

“ Copyright © and Moral Rights for this thesis and any accompanying data (where applicable) are retained by the author and/or other copyright owners. A copy can be downloaded for personal non-commercial research or study, without prior permission or charge. This thesis and the accompanying data cannot be reproduced or quoted extensively from without first obtaining permission in writing from the copyright holder/s. The content of the thesis and accompanying research data (where applicable) must not be changed in any way or sold commercially in any format or medium without the formal permission of the copyright holder/s. When referring to this thesis and any accompanying data, full bibliographic details must be given, e.g. Thesis: Author (Year of Submission) "Full thesis title", University of Liverpool, name of the University Faculty or School or Department, PhD Thesis, pagination.”

Dedication

Dedicated to my family and friends

Most notably my daughter Elizabeth Charlotte Jones

Acknowledgements

Throughout my PhD I have received guidance and suggestions off many people both internally within the chemistry department and externally from other academic institutions however, there are some people who deserve a specific mention.

Firstly my most profound thanks to my academic supervisor Dr. Yaroslav Khimyak for allowing me to undertake my PhD studies and providing me with the support and guidance during the highs and lows of the past three and half years. Secondly, the assistance of Dr. Jean-Baptiste Guilbaud with the solid-state NMR experiments at the beginning of my PhD and for the many Fridays evening entertainment. Further acknowledgements go to Drs. Andrew Fogg and John Claridge for their useful input and advice. I would also like to thank Drs. Colin Wood and Calum Dickinson for assistance with the gas sorption and Transmission Electron Microscopy measurements and useful discussions. The input and advice from Dr Craig bridges regarding low angle powder diffraction is also acknowledged. Finally I thank Paul Wiper for being a dedicated MSc student and conducting many additional laboratory experiments as well as the remaining Khimyak group.

A special mention is given to my family in particular my parents, brothers and sisters for putting up with the endless complaining when things were going wrong and the boring chemistry conversations. I also thank Jamie, Helan, Joanne, and Tom just some of the many friends I have made during my PhD and all those I have forgotten to mention for the many social events which have made some workdays very difficult. Finally, I thank my daughter Libby for providing me both the incentive to achieve and nice distractions from the world of chemistry.

"If the greatest writer of the written word would have written that story no one would have believed it - that really was something"

Cliff Morgan, 1973.

Synthesis and Characterization of porous Organic/ Inorganic Hybrid Materials

The synthesis of multi-functional periodic mesoporous organosilicas (PMOs), which are PMOs containing two or more organic bridges/ metal centres covalently bound within the framework, has been developed over the past ten years. The mesoscopic structure of PMOs is already relatively well known and has been determined from powder XRD and gas sorption measurements. PMOs are non-soluble amorphous frameworks and therefore, solid-state NMR is ideally suited to determining their molecular level composition and structure. Here we present the synthesis of mono/ multi-functional PMOs consisting of $-CH_2CH_2-$/-CH=CH- and $-CH_2CH_2-$/$-C_6H_4-$ functionalities, with the aim of demonstrating the adaptability of a novel pre-hydrolysis protocol under both acid and basic conditions. The development of multi-functional porous composites is of particular importance in both catalytic and chromatographic applications.

The synthesis of a highly ordered -CH=CH-PMO using a block co-polymer template under acid conditions and its post synthetic modification *via* exposure to bromine vapour or thermal treatment is presented. ^{1}H-^{13}C CP/MAS kinetics and wide-line separation (WISE) NMR experiments confirmed the presence of strong interactions between the hydrophilic components of the template with the PMO framework. The understanding of such interactions could enable their optimisation in order to form highly ordered mesoporous solids. The location of the -CH=CH- bridges was probed using ^{13}C CP/MAS kinetics and confirmed the presence of both bulk wall and surface functionalities, confirming their availability for bromination.

The synthesis of multi-functional PMOs using a selection of $-CH_2CH_2-$, -CH=CH-, and $-C_6H_4-$ bridges under acidic and basic conditions raised questions about their phase purity. That is do the organic bridges co-condense to form one homogenous framework or phase separate to form a physical mixture of two frameworks, an oversight by previous researchers in this topic. Such an oversight is most likely due to the difficulty in determining homogeneity of such essentially amorphous solids which requires the application of advanced 2D NMR experiments.

Silica precursor pre-hydrolysis prior to their addition to the organic template solution was used to influence the homogeneity of the framework. The effects of such protocols were investigated using ^{1}H-^{29}Si CP kinetics and heteronuclear correlation (HETCOR)

experiments. The application of separate pre-hydrolysis in the synthesis of -CH_2CH_2-/-CH=CH-PMOs under acidic conditions resulted in structural heterogeneities consisting of domains of the same functionality within the same framework. On the other hand, in the same system joint pre-hydrolysis resulted in a highly structurally homogeneous system. Similar pre-hydrolysis protocols were applied to -CH_2CH-/-C_6H_4-PMO's prepared under both acidic and basic conditions. Under acidic conditions a -CH_2CH-/-C_6H_4-PMO synthesised without pre-hydrolysis resulted in a random distribution of the bridges within the same framework. However, under both joint and separate pre-hydrolysis conditions resulted in domain structures. The analogous base catalysed syntheses always resulted in a domain structure with or without of pre-hydrolysis.

The introduction aluminium into the synthesis of -CH_2CH_2-/-CH=CH-PMOs prepared using pre-hydrolysis provided an additional probe to how the pre-hydrolysis solutions affected the resulting mesoporous solid. In this case ^{1}H-^{27}Al HETCOR experiments enabled, for the first time, the confirmation of a homogenous distribution of Al within the porous network.

Finally, conjugated microporous polymer networks which have shown potential as hydrogen storage materials were characterised on a molecular level using solid-state NMR. Assignments of the ^{13}C CP/MAS spectra are presented. The analysis of ^{13}C CP/MAS kinetics is correlated with molecular simulations and porosity in order to explain changes in molecular motions as a function of monomer length used in the synthesis of the polymers.

List of Publications originating from individual and collaborative projects on inorganic and organic solids published during the PhD.

1) Jones, J. T. A., Wood, C. D., Dickinson, C., Khimyak, Y. Z. Periodic mesoporous organosilicas with domain functionality: Synthesis and advanced characterisation. *Chem. Mat.* **2008**, 20, 3385-3397.
2) Vercaemst, C., Jones, J. T. A., Khimyak, Y. Z., Martins, J. C., Verpoort, F., Van der Voort, P. Spectroscopic evidence of thermally induced metamorphosis in ethenylene-bridged periodic mesoporous organosilicas. *Phys. Chem. Chem. Phys.* **2008**, 10, 5349-5352.
3) Vercaemst, C., Ide, M., Wiper, P. V., Jones, J. T. A., Khimyak, Y. Z., Verpoort, F., Van der Voort, P. Ethylene-bridged periodic mesoporous organosilicas: From *E* to *Z*. *Chem. Mat.* **2009**. DOI:10.1021/cm902164t.
4) Jiang, J. X., Su, F. B., Trewin, A., Wood, C. D., Niu, H., Jones, J. T. A., Khimyak, Y. Z., Cooper, A. I. Synthetic control of the pore dimension and surface area in conjugated microporous polymer and copolymer networks. *J. Am. Chem. Soc.* **2008**, 130, 7710-7720.
5) Jiang, J. X., Trewin, A., Su, F. B., Wood, C. D., Niu, H. J., Jones, J. T. A., Khimyak, Y. Z., Cooper, A. I. Microporous poly(tri(4-ethynylphenyl)amine) networks: Synthesis, properties, and atomistic simulation. *Macromol.* **2009**, 42, 2658-2666.
6) Stockel, E., Wu, X. F., Trewin, A., Wood, C. D., Clowes, R., Campbell, N. L., Jones, J. T. A. Khimyak, Y. Z., Adams, D. J., Cooper, A. I. High surface area amorphous microporous poly(aryleneethynylene) networks using tetrahedral carbon- and silicon-centred monomers. *Chem. Commun.* **2009**, 212-214.
7) Wang, W. X., Carter, B. O., Bray, C. L., Steiner, A., Bacsa, J., Jones, J. T. A., Cropper, C., Khimyak, Y. Z., Adams, D. J., Cooper, A. I. Reversible methane storage in a polymer-supported semi-clathrate hydrate at ambient temperature and pressure. *Chem. Mat.* **2009**, 21, 3810-3815.
8) Hetterley, R. D., Mackey, R., Jones, J. T. A., Khimyak, Y. Z., Fogg, A., M., Kozhevnikov, I.,V., One-step conversion of acetone to methyl isobutyl ketone over Pd-mixed oxide catalysts prepared from novel layered double hydroxides. *J. Catal.* **2008**, 258, 250–255
9) Michael J. Ingleson, J. Perez Barrio, J. Bacsa, A. Steiner, G. R. Darling, J. T. A. Jones, Y. Z. Khimyak, and M. J. Rosseinsky., $Mg(BH_4)_2$ confined in Metal Organic Frameworks, a system with a significantly reduced dehydriding temperature. *Angew. Chem. Int. Ed.* **2009**, 48, 2012-2016.
10) Dawson, R.; Su, F. B.; Niu, H. J.; Wood, C. D.; Jones, J. T. A.; Khimyak, Y. Z.; Cooper, A. I., Mesoporous Poly(phenylenevinylene) Networks. *Macromolecules* **2008**, 41, 1591-1593.

Presentations at conferences

1) Royal Society of Chemistry Nuclear Magnetic Resonances Discussion group, 19th June 2008, Oral and Poster presentation titled 'Periodic mesoporous organosilicas with domain functionality: synthesis and solid-state NMR characterization'.
2) British Zeolite Association, 31st March - 2nd April 2008, Oral presentation titled 'Periodic mesoporous organosilicas with domain functionality: synthesis and advanced characterization'.

3) Catalysis: Fundamentals and Practise summer school, 3rd - 7th September 2007, Poster presentation titled 'Periodic Mesoporous Organosilica with hierarchical functionality characterised by Solid-state NMR'.
4) MC8: Advancing Materials by Chemical Design, 2nd - 5th July 2007, Poster presentation titled 'Periodic Mesoporous Organosilica with hierarchical functionality characterised by Solid-state NMR'

List of Abbreviations

BET	Brunauer, Emmet and Teller
BJH	Barrett, Joyner and Halenda
CMP	Conjugated Microporous Polymer
COF	Covalent-Organic Framework
CP/MAS	Cross Polarisation Magic Angle Spinning
CPN	Co-Polymer Network
CRAMPS	Combined Rotations and Multi-Pulse Sequence
CSA	Chemical Shift Anisotropy
CTAB	Cetyltrimethylammonium Bromide
DAS	Dynamic Angle Spinning
DOR	Double Rotation
DUMBO	Decoupling Using Mind Boggling Optimization
EISA	Evaporation Induced Self-Assembly
EOF	Element-Organic Framework
FID	Free Induced Decay
FS-LG	Frequency Switched Lee Goldburg
GPC	Gel Permeation Chromatography
HETCOR	Heteronuclear Correlation
IUPAC	International Union for Pure and Applied Chemistry
LCT	Liquid-Crystal Templating
LG-CP/MAS	Lee-Goldburg Cross Polaraisation Magic Angle Spinning
MAS	Magic Angle Spinning
MCM	Mobil Corporation Material
MOF	Metal-Organic Framework
MQMAS	Multiple Quantum Magic Angle Spinning
NCMP	Nitrogen containing Conjugated Microporous Polymers
NL-DFT	Non-Local Density Functional Theory
NMR	Nuclear Magnetic Resonance
NOESY	Nuclear Overhauser Spectroscopy
ODTABr	Octadecyltrimethylammonium Bromide
PAF	Principle Axis Frame

PMO	Periodic Mesoporous Organosilica
PSD	Pore Size Distribution
PPM	Parts Per Million
PXRD	Powder X-Ray Diffraction
r. f.	Radio Frequency
SBA	Santa Barbara Acid
SBU	Secondary Building Unit
SEM	Scanning Electron Microscopy
STMAS	Satellite Transition Magic Angle Spinning
TEM	Transmission Electron Microscopy
TEOS	Tetraethyl Orthosilicate
TMS	Tetramethylsilane
TPPM	Two Pulse Phase Modulation
$T_{1\rho}$	Spin-lattice relaxation time in the rotating frame
VCT	Variable Contact Time
WISE	Wideline Separation

Table of contents:

Introduction

Chapter 1

1. Introduction

Porous materials possessing high surface areas and large pore diameters are of great importance due to their applications as heterogeneous catalysts. All porous molecular sieves are classified into three groups (Fig. 1.1) by the International Union for Pure and Applied Chemistry (IUPAC)[1] according to their pore diameters:

1. Macroporous: 50 to 100 nm *e.g.* alumina[2] and titania materials.[3]
2. Mesoporous: 2 to 50 nm *e.g.* Silica[4-8] and alumina.[9,10]
3. Microporous: less than 2 nm *e.g.* zeolites[11,12] and metal-organic frameworks (MOFs).[13,14]

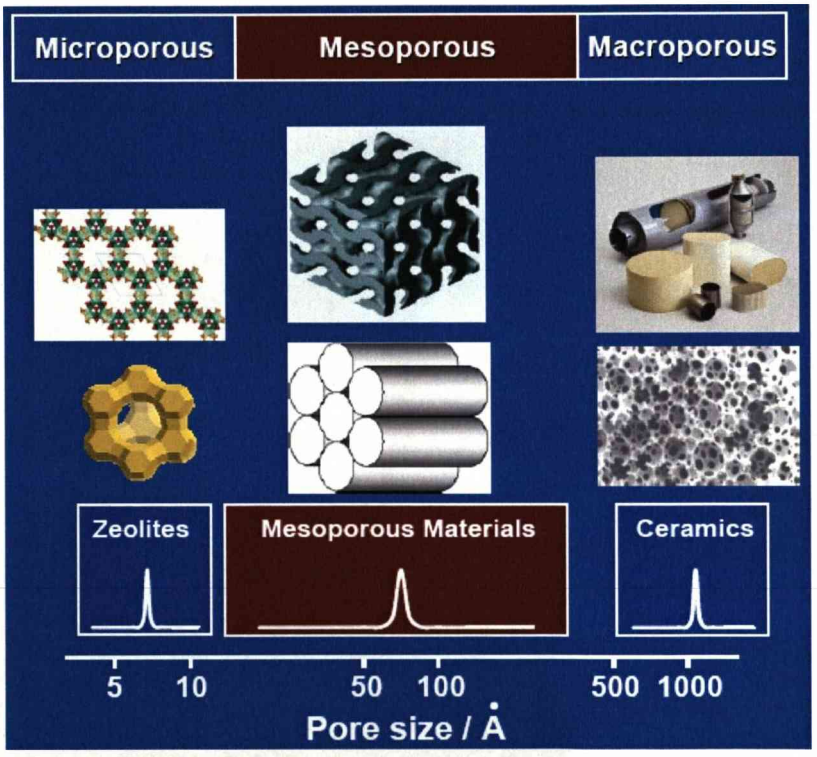

Figure 1.1. Classification of porous solids according to IUPAC.

Microporous zeolites are the most widely used molecular sieves in industrial processes such as mercaptane oxidation in petroleum refining, commonly known as 'sweetening' of petrol and diesel fuel.[15] This is due to their high thermal stability and crystallinity. A more recent class of crystalline microporous materials, MOFs enabled the introduction of organic components within the framework. Early MOFs such as MOF-5 is composed of octahedral Zn-O-C clusters and benzene struts (Zn_4O(1,4-

benzenedicarbonate)$_3$).[16] The ability to increase the strut length by using more conjugated aromatics such as pyrenedicarbonate and tri-phenyldicarbonate enables controlled optimisation of pore dimensions with free pore diameters of 12.6 to 19.1 Å.[17] However, poor thermal stability at temperatures above 300°C has limited their application.[16,18,19] Work by Wood *et al.* on amorphous microporous polymers composed solely of Carbon and Hydrogen have also shown promise in gas storage applications.[20] However, one of the main drawbacks of microporous zeolites and MOFs is the small pore/cage channels and in some cases even smaller pore windows. For example, one of the largest pore windows and subsequent pore volume for a high silica zeolite UTD-1 composed of a 14-tetrahedral-atom pore opening was reported by Davis *et al.*[21] More recently the synthesis of ITQ-21, a zeolite with a 3-D porous network containing cavities of 1.18 nm and pore windows of 0.74 nm has been demonstrated.[22] Despite the increased pore dimensions of zeolites and MOFs their cavities are still too small and make the diffusion of large or bulky molecules in the framework difficult.

This problem aided the development of porous solids with larger pore dimensions with a major breakthrough by Mobil researchers in 1992 with the preparation of Mobil Corporation Material 41 (MCM-41).[4,8] MCM-41 is a mesoporous silicate with high thermal stability and larger pore diameters (20 - 40 Å), than its microporous zeolite analogues. The increased pore dimensions of MCM-41 enable host-guest chemistry with larger molecules *i.e.* metal clusters[23] and proteins possible.[24] Mesoporous silicas, unlike zeolites which have molecularly ordered repeating units and a well defined unit cell, do not contain any crystalline regions. The amorphous nature of the mesoporous silica walls also makes detailed molecular properties more difficult to be assessed using X-ray diffraction techniques. Since the discovery of MCM-41 a significant number of researchers have investigated the formation of various other mesoporous silicate phases which are discussed in the following sections.

1.1 Mesoporous silicates

The synthesis of MCM-41[4,8] relies on supramolecular templating. The process of templating is dependent on the interactions (discussed in the following sections) between a structure directing agent and a reactive species which assembles around the template to form a framework material. The use of supramolecular templates is in contrast to microporous zeolites which use either molecular templates such as tetrapropylammonium salts for ZSM-5[25] or large alkaline metal cations such as Sodium for Zeolite A.[26,27] The supramolecular templates used for MCM synthesis are usually quaternary alkylammonium salt cationic surfactants such as C_{18} or C_{16}-trimethylammonium bromide which form micelles when dispersed in basic/aqueous solutions at ambient temperature. The symmetry of the surfactant mesophase for example, hexagonal or cubic is subsequently replicated on the structure of the resulting porous solid. A silica source such as tetraethylorthosilicate (TEOS) undergoes hydrolysis and co-operative assembly around the template micelles. Heating the resulting gel to high temperature under static conditions facilitates the condensation process of the silica precursor. The surfactant is then removed by either calcination or an ion exchange process. The result is the MCM-41 material which possesses a 2-dimensional hexagonal porous network (Fig. 1.2). The discovery of MCM-41 also lead to the synthesis of other mesoporous silicate phases with different structural properties such as MCM-48 which consists of a 3-dimensional cubic network of pores.[28]

There are several proposed mechanisms explaining the formation of MCM-41 *via* cationic templating. The initial "liquid crystal templating" (LCT) mechanism was proposed by Mobil.[4,8] In this mechanism surfactant molecules form micellar rods which organise into a hexagonal lyotropic liquid crystal (LC) phase prior to addition of the silicate precursor (Fig. 1.2). The silicate precursor occupies the space between the LC phase and condenses to form an hexagonal array. These initial assumptions resulted from the dependence of structure of the resulting product on the surfactant chain length and the effect of variation of surfactant/SiO_2 molar ratios. Where the variation of CTMAOH/TEOS molar ratios from 0.6 to 2 resulted in phase transitions from hexagonal at 0.6 (MCM-41), cubic at 1.0 (MCM-48), lamellar at 1.3 (MCM-50) and cubic octamer at 1.9 ($[(CTMA)SiO_{2.5}]_8$) as monitored by PXRD.[28,29] Davis *et al.*[30] used *in-situ* ^{14}N NMR experiments to conclude that the initial liquid crystal phase proposed by Mobil did not develop during the synthesis of MCM-41.

Instead it was proposed that initial silicate monolayers formed on isolated surfactant micellar rods which were randomly ordered and eventually packed into a hexagonal mesostructure.

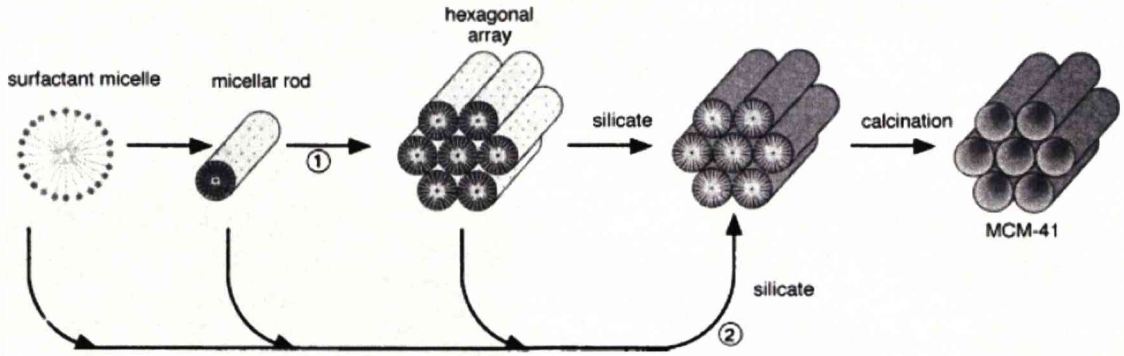

Figure 1.2. Liquid crystal templating pathway proposed by Mobil, 1) formation of hexagonal array and 2) addition of silicate precursor.[4]

Further work by Steel *et al.*[31] with the aid of ^{14}N NMR, suggested that a hexagonal LC phase formed upon the addition of the silicate species. In this mechanism silicate layers formed with cylindrical template rods intercalated between layers which upon heating caused the layers to collapse forming a hexagonal mesophase. A slight variation of the afore mentioned model was proposed by Stucky *et al.*[32] in which powder X-ray diffraction indicated the presence of a lamellar phase prior to the formation of the hexagonal mesostructure. In this system electrostatic attraction between the silicate anions and the cationic surfactant head groups formed an initial lamellar phase. However, as the silicate species condensed the charge density is reduced, thus curvature is introduced to maintain the charge density balance with the surfactant head groups (Fig. 1.3).

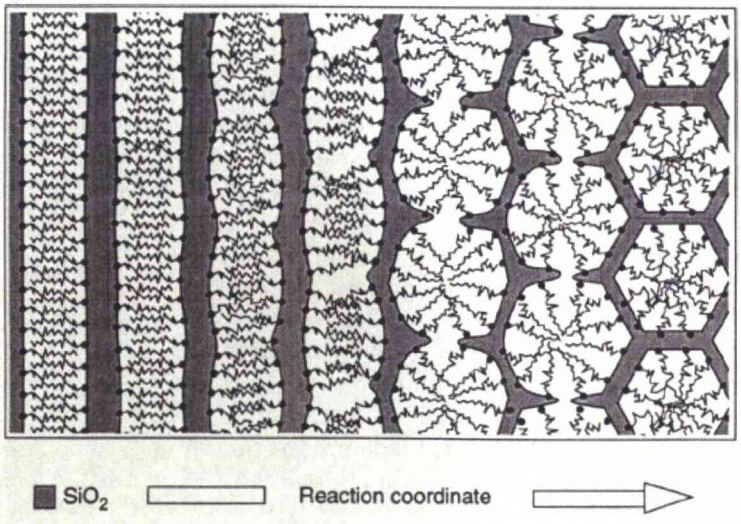

Figure 1.3. Schematic representation of the phase transformation from a lamellar to hexagonal mesostructure during the synthesis of MCM-41.[32]

Although the proposed mechanisms of formation differ, they all rely on the electrostatic attraction between the silicate precursors (I) and the cationic surfactant head group (S) initially proposed by Huo and co-workers.[5,33]

Another family of mesoporous silicas was developed by Zhao *et al*[7]. The synthesis of SBA-15 (Santa Barbara Acid 15) uses a tri-block copolymer templating agent which consists of poly(ethylene oxide)-poly(propylene oxide)-poly(ethylene oxide) blocks. The most common templates are P123 ($PEO_{20}PPO_{70}PEO_{20}$) and F127 ($EO_{106}PO_{70}EO_{106}$). The co-polymer is dispersed in an aqueous/acidic solution to which a silica source (TEOS) is added and the reaction proceeds via self assembly (Fig. 1.4). SBA-15 can be considered as a 2-dimensional hexagonal network with pore diameters ranging from 50 – 100 Å and surface areas of *ca.* 1000 m^2g^{-1}. The increase in wall thickness compared to MCM-type materials gives SBA-15 an enhanced hydrothermal stability.[7] The increased wall thickness may be related to the changes at the inorganic/ template interface. With cationic templating the inorganic walls do not entangle with the template and a well defined interface is formed. However, with block co-polymers the PEO blocks are integrated with the inorganic phase which has been confirmed *via* solid-state NMR spin diffusion experiments.[34,35]

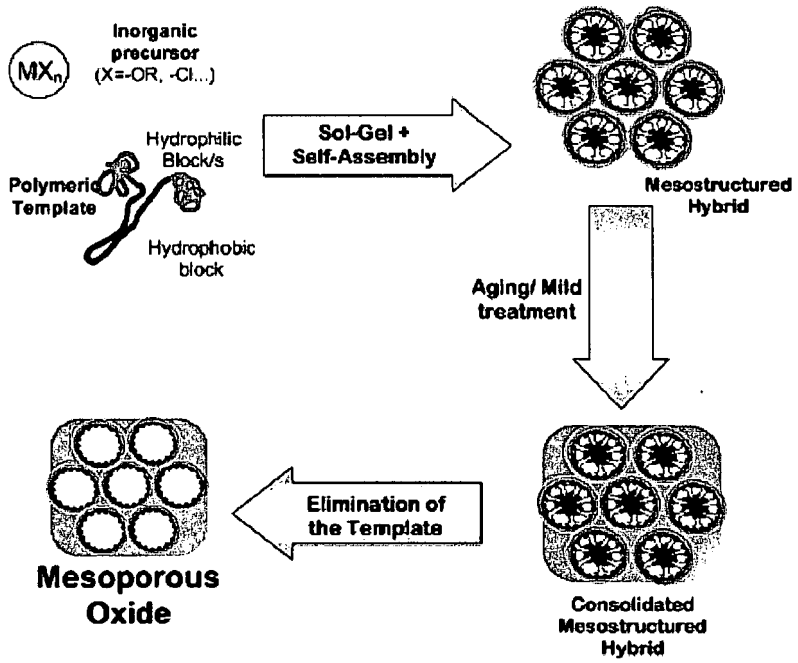

Figure 1.4. Schematic representation of the steps leading to the formation of mesoporous silicas prepared via block co-polymer templating.[34]

Integration of the PEO template components with the inorganic phase also results in the presence of microporosity in the final product. Indeed the extent of microporosity may

be further controlled by adjusting the temperature (80 - 100 °C) and time (0 - 48 hrs) of aging with longer aging times leading to reduced microporosity.[36] Therefore, improved segregation of the PEO and inorganic phases must occur with increasing aging times (Fig. 1.5). Temperature and aging time therefore affect the wall thickness and degree of pore wall condensation.[37]

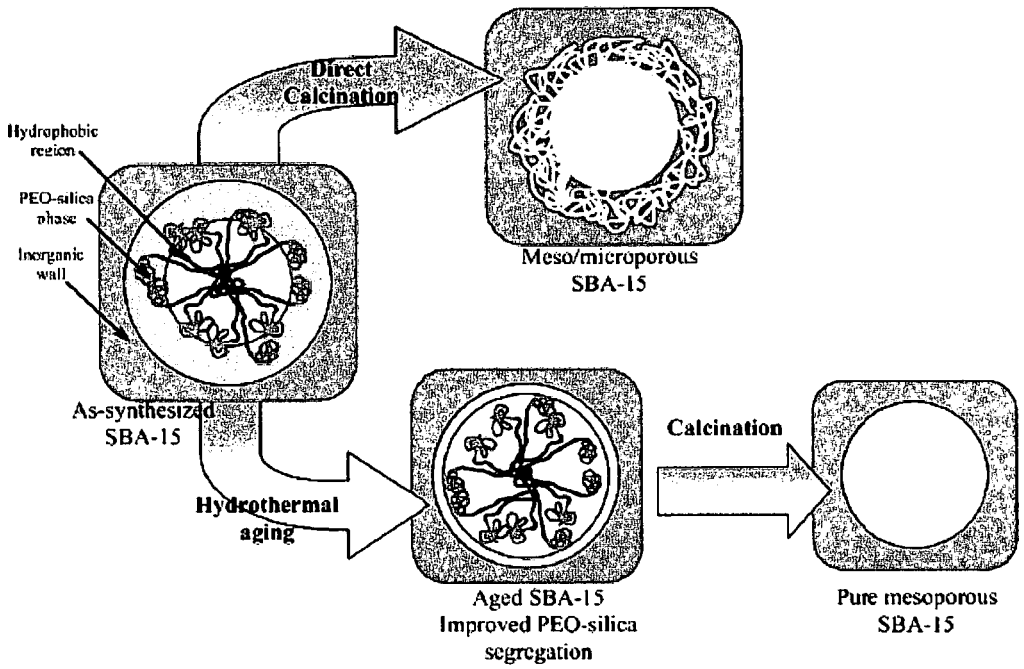

Figure 1.5. Representation of changing inorganic and PEO phase segregation as a function of aging.[34]

Since SBA-15 was synthesised, many other types have been reported in the literature including SBA-16 and SBA-11 which both form a 3-dimensional cubic mesophase synthesised using non-ionic tri-block ($EO_{106}PO_{70}EO_{106}$) F127 and di-block co-polymer ($C_{16}H_{33}(OCH_2CH_2)_{10}OH$, Brij56) respectivly.[6]

The main advantages of mesoporous silicates over microporous materials are that they have much higher surface areas, larger pore diameters and volumes which allow larger more bulky molecules to enter the porous network. Further advantages of mesoporous silicas include the possibility of introducing organic functionalities into the framework leading to organic/ inorganic hybrid materials which can further expand their range of catalytic applications.

1.2 Organic-Inorganic Hybrid materials

Silica based mesoporous organic-inorganic hybrids are a modification of mesoporous silicates and to date have been synthesised *via* three different methodologies.

1.2.1 Post synthetic functionalisation

This technique relies on placing organic groups in the pores of mesoporous silicas such as MCM or SBA-types by grafting them onto the pore walls.[38] This pathway involves the reaction of the surface silanol groups in mesoporous silicate with an organosilane in an appropriate organic solvent such as Ethanol (fig. 1.6).[39]

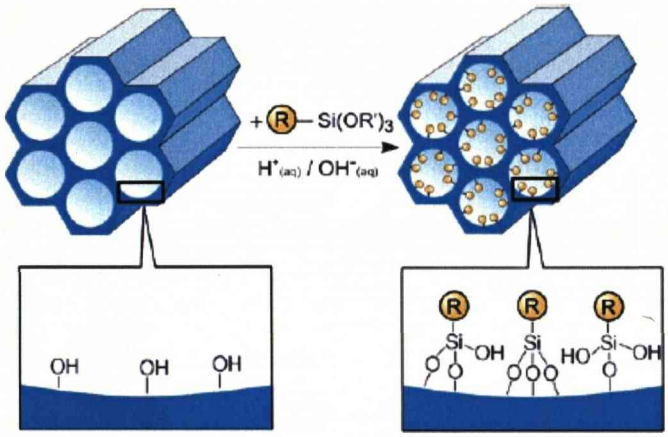

Figure 1.6. Post synthetic grafting of mesoporous silica using terminal organosilanes.[39]

The main advantage of this technique is that the mesoporous framework remains thermally stable after grafting of the organic groups and retains its mesoporous structure. The main limitation of post synthetic grafting is that it is difficult to ensure homogeneous distribution of the organic moieties in the mesopores as the pore openings are more reactive to the organosilane due to restricted transport within the framework. Limited diffusion of the organosilane in the mesopores might eventually result in pore blocking leading to a significant decrease in surface area. The introduction of the terminal organic functionalities reduces the pore diameters/volume which makes their applications as hosts for large molecules (*i.e.* proteins) less favourable (Figure 1.7).[40]

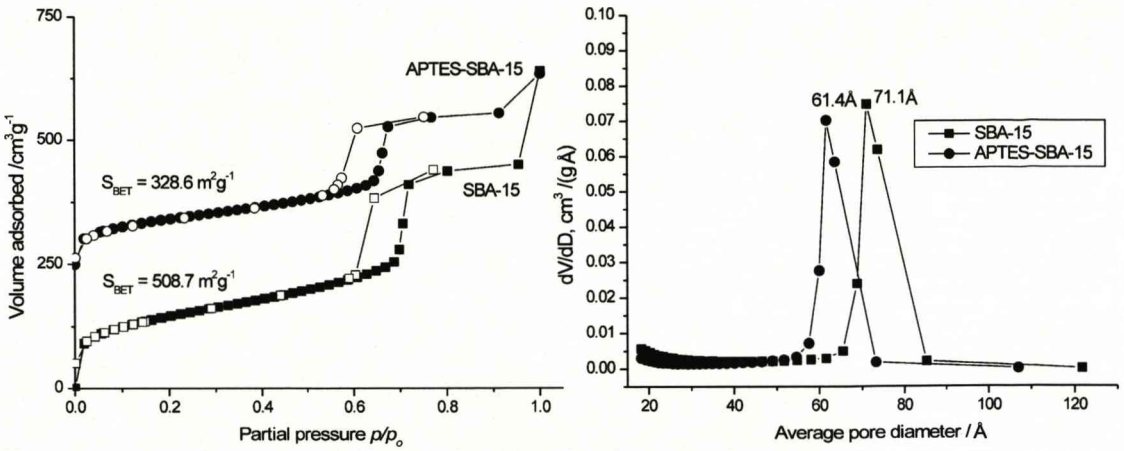

Figure 1.7. N_2 adsorption-desorption isotherms and pore size distribution plots of SBA-15 before and after the grafting of 3-aminopropyltriethoxysilane. Note a decrease the resulting surface area and pore diameter.

1.2.2 Co-condensation pathway

The co-condensation pathway involves the use of two silica precursors, a tetraalkoxysilane ($Si(OR)_4$) and a terminal alkyl trialkoxysilane ($R\text{-}Si(OR)_3$). The synthesis is carried out using a '*one pot*' method where both precursors are added to a surfactant solution using cationic[41,42] or block co-polymer templating[43] pathways (Fig. 1.8). The main advantage of this technique over grafting is a more homogeneous distribution of the organic groups in the pores. Furthermore, the organic groups are embedded into the pore walls thus pore blocking no longer occurs. Disadvantages of co-condensation is that as the organosilane content increases mesoporous ordering is decreased and exceeding 40 % loading leads to disordered products.[39]

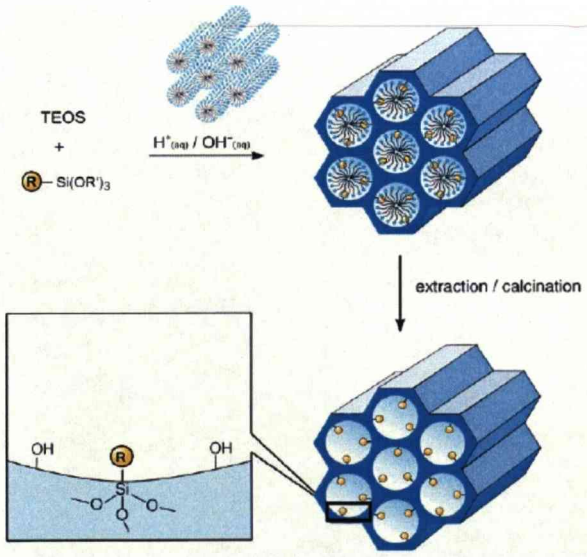

Figure 1.8. Co-condensation method for the synthesis of silica based hybrid materials.[39]

1.2.3 Periodic Mesoporous Organosilicas

The first syntheses of ordered periodic mesoporous organosilicas (PMO) with organic groups embedded into the pore walls by the research groups of Stein, Ozin and Inagaki[44-46] set a new direction in the research of mesoporous molecular sieves. PMO are synthesized using bridged organosilica precursors ($(EtO)_3Si\text{-}R\text{-}Si(OEt)_3$) in conditions analogous to those for the preparation of mesoporous silicas. The use of organo-bridged silica precursors allows the homogeneous distribution of organic groups in the pore walls which is a major advantage over earlier post synthetic grafting[47] or co-condensation methods. To date many different bridging organic functionalities have been incorporated into the pore walls of PMOs ranging from simple $-CH_2CH_2-$ bridges[48,49] to more complex cyclic three-ring silsesquioxane $[(EtO)_2Si(CH_2)]_3$ precursors (Table 1.1).[50] The possibility of incorporating many different organic functionalities enables the properties of these materials such as hydrophobic/ hydrophilic behaviour to be adjusted more easily compared to mesoporous silicas.

Table 1.1. Periodic mesoporous Organosilicas synthesized using various organic bridges and templating pathways.

Year	Author	Organic bridge	Template	S_{BET} /m^2g^{-1}	Reference
1999	Inagaki	$-CH_2CH_2-$	ODTABr	750	46
	Melde	$-CH_2CH_2-$	CTABr	1234	44
		$-CH{=}CH-$		1210	
	Asefa	$-CH_2CH_2-$/TEOS	CTABr	637	45
2000	Sayari	$-CH_2CH_2-$	CTACl	850	48
	Asefa	$-CH_2-$	CTAB	NR	51
	Guan	$-CH_2CH_2-$	CTACl	770	49
2001	Zhu	$-CH_2CH_2-$	P123	957	52
	Lee	$-CH_2CH_2-$	ODTABr	799	53
	Burleigh	$-CH_2CH_2-$	P123	928	54
		$-CH_2CH_2-$/ $\equiv Si\text{-}(CH_2)_3NH(CH_2)_2NH_2$	CTACl	910	55
	Temtsin	$-C_6H_3(CH_3)-$	cetylpyridinium chloride	794	56
		$-C_6H_3(CH_3)_2-$		1108	

Year	Author	Organic bridge	Template	S_{BET} /m^2g^{-1}	Reference
2002	Inagaki	-C_6H_4-	CTACl	818	57
	Kapoor	-C_6H_4-C_6H_4-	CTACl	869	58
	Yang	-C_6H_4-/ -C_3H_6SH	CTACl	643	59
	Kuroki	1,3,5-(trisilyl)benzene	cetylpyridinium chloride	880	60
	Sayari	-CH_2CH_2-	Brij 76	1024	61
	Goto	-C_6H_4-	P123	1029	62
2003	Wang	-C_6H_4-	Brij 76	840	63
		-C_6H_4-	Brij 56	899	
	Yokoi	TEOS/-$C_3H_6NH_2$	Sodium dodecyl sulfate	760	64
	Guo	-CH_2CH_2-	P123	737	65
		-CH_2CH_2-	F127	989	66
	Burleigh	-CH_2-	Brij-56	872	67
		-C_6H_4-		901	
		-CH_2CH_2-		1080	
2004	Hunks	-C_6H_4-	Brij 56	1073	68
		-C_6H_4-CH_2-		1134	
		-CH_2-(C_6H_4)-CH_2-		743	
	Wahab	-CH_2CH_2-/ -$(CH_2)_3$-NH-$(CH_2)_3$-	CTABr	759	69
	Liu	TEOS/ Bridged cylcodextrin	P123	554	70
	Wang	-CH=CH-	Brij 56	847	71
			P123	624	
	Yang	-CH_2CH_2-/ -$(CH_2)_3SH$	Brij 76	1401	72
		-C_6H_4-/ -$(CH_2)_3SH$		1056	
2005	Cornelius	-CHCH(C_6H_4)CHCH-	ODTACl	730	73
	Zhang	-CH_2-	P123	1030	74
	Xia	-CH=CH-	CTABr	1884	75
	Landskron	Tri-methylene bridged 3 ring system	P123	967	76
	Hunks	-CH_2CH_2-	P123	704	77
		-$(CH_2)_2Si(O)_2(CH_2)_2$-		1122	

Year	Author	Organic bridge	Template	S_{BET} /m^2g^{-1}	Reference
2006	Morell	MT^3	P123	714	78
		BTET		550	
	Morell	-C_6H_4-/-C_4H_4S-	P123	640	79
			Brij 76	1120	
	Grudzien	-CH_2CH_2-/ isocyanurate	P123	773	80
2007	Treuherz	-CH_2CH_2-/-CH=CH-	ODTABr	783	81
	Whitnall	C-60/TEOS	P123	242	82
	Cho	-C_6H_4-/-CH_2CH_2-/-C_4H_4S-	PEO-PLGA-PEO	1006	83
	Li	TEOS/-$CH_2CH_2(C_6H_4)CH_2CH_2$-	P123	221	84
	Vercaemst	-CH=CH- (all trans)	P123	1018	85
2008	Morell	1,4-bis(triethoxysilyl)-2-(1-methoxyethyl) benzene	Brij 76	820	86
	Jones	-CH_2CH_2-/-CH=CH-	P123	1310	87
	Luo	-$(CH_2)_3NHCONH(CH_2)_3$-	CTABr	924	88
	Coutinho	-C_6H_4-/-$(CH_2)_3NH_2$	ODTACl	694	89
	Yang	-C_6H_4-/-C_6H_4-C_6H_4-	ODTABr	586	90

Stein *et al.*[44] demonstrated the possibility of introducing organic groups accessible for chemical modification *via* bromination reactions. The next major development was by Dutartre *et al.* introducing the block co-polymer P123 as a template for -CH_2CH_2-PMOs. The use of block co-polymers resulted in the PMOs with large pore dimensions in the range of 5.8 - 7.7 nm and increased wall thickness (*ca.* 1.6 nm). The introduction of 1,4-benzene bridges into PMOs by Inagaki *et al.* was the first example of aromatic functionalities in PMOs yet, the authors also observed remarkable structural properties as a direct result of the benzene bridges.[57] The aromatic bridges formed molecularly ordered pore walls *via* π-π stacking along the channel axis as observed by transmission electron microscopy (TEM), electron diffraction patterns (Fig. 1.9) and PXRD. The images show a well ordered hexagonal array of pores whereas the electron diffraction pattern (Insert of B) shows diffused spots due to the 7.6 Å periodicity (large arrow) perpendicular to the direction of the spots due to the channel arrangement (small arrow). Molecular simulations using COMPASS

force field[91,92] suggested a layered pore wall structure composed of $O_{1.5}Si\text{-}C_6H_4\text{-}SiO_{1.5}$ units which correlates well with the TEM images.

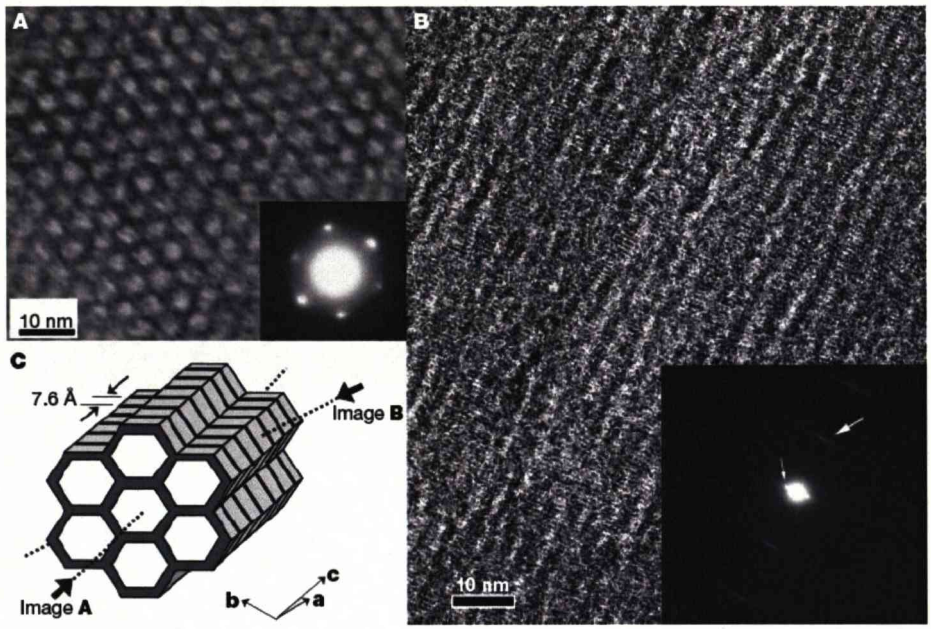

Figure 1.9. TEM images of $-C_6H_4$-PMO taken along the [001] incidence parallel to the channels (A) and the [100] incidence perpendicular to the pore channels (B) reported by Inagaki *et al.*[57]

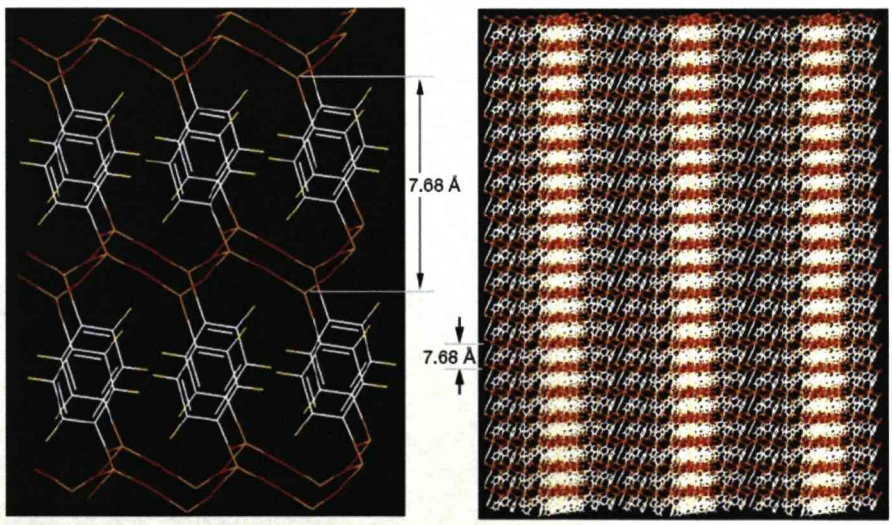

Figure 1.10. Structural models of the layered pore wall conformation of the $-C_6H_4$-PMO (left) and the layered conformation along the c-a direction of the hexagonal lattice reported by Inagaki *et al.*[57]

Further studies on PMOs have been focused on the introduction of multiple organic bridges and/or tethers into the same mesoporous framework. Early work was conducted in 2002 by Yang *et al.* with the introduction of thiol tethers into the synthesis mixtures which could be further treated with HNO_3 to form sulphuric acid functionalities.[59] However, the authors noted that even when using 67 % loading of the thiol tether only 25% was incorporated into the mesostructure. There is also no discussion on how the thiol groups are distributed within the framework. Following the research of Yang and co-workers there have been many publications on the incorporation of thiol and amine tethers within PMOs for use as surface catalysts in processes such as the liquid phase condensation of phenol with acetone to form bisphenol A and the nitroaldol condensation of benzaldehyde and nitromethane.[72,78,93-97]

Despite the increasing applications of such porous solids there are very few studies probing the location and distribution of the organic functionalities within the porous frameworks. A previous publication from our group made the first attempt to probe the locations of $-CH_2CH_2-$ and -CH=CH- functionalities within quaternary ammonium templated PMOs.[81] In this paper the application of ^1H-^{13}C and ^1H-^{29}Si CP/MAS kinetics confirmed the presence of phase pure PMOs yet the organic groups formed segregated domains. Further work by Sayari *et al.* focused on a bifunctional phenyl/ biphenyl PMO which showed high levels of molecular organisation within the pore walls (Fig. 1.11).[90]

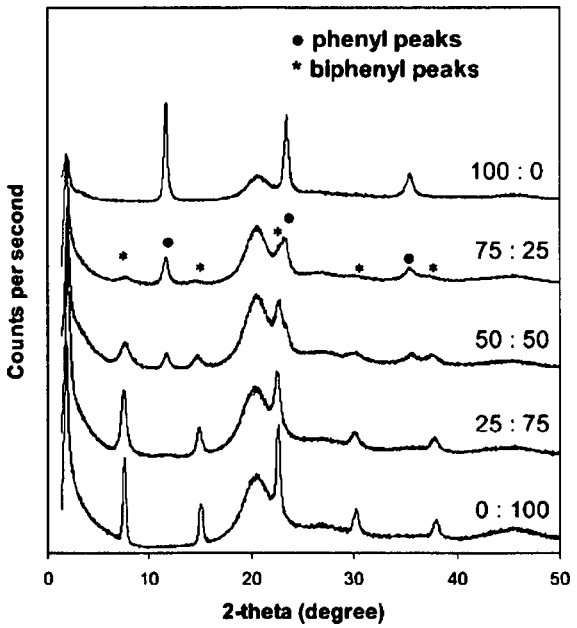

Figure 1.11. PXRD patterns of phenyl/biphenyl PMOs with the phenyl:biphenyl ratio indicated on the right reported by Sayari *et al.*[90]

From the PXRD (fig. 1.11) one can see the influence of different organic spacers on the layered pore wall structure. The 100 % biphenyl PMO results in a d_{001} spacing of 11.6 Å corresponding to the length of the O-Si-C_6H_4-C_6H_4-Si-O units being observed. The 100 % phenyl PMO results in a d_{001} spacing of 7.6 Å. The authors concluded that the presence of both sets of reflections in the 50:50 PMO confirmed that the organic groups were segregated into domains or phase separation had occurred. Clearly, the ability to direct and control the distribution of the organic functionalities is challenging both in terms of synthetic design and characterisation. Firstly, the complex behaviour of different bridging silicon alkoxides for example, saturated -CH_2CH_2- and un-saturated -CH=CH- functionalities towards each other during the hydrolysis and condensation steps and secondly, the characterisation of materials without long range ordering possessing amorphous pore walls at the molecular level is difficult using conventional PXRD and imaging techniques such as SEM and TEM.

As already seen above, PMOs can be synthesised using various combinations of organic bridges and templates. However, thus far, reported PMOs have mostly been synthesized using cationic templates (trialkylammonium[48,49,57] or pyridinium[60] surfactants) and non-ionic surfactants (oligomeric alkyl poly(ethylene oxide) *e.g.* Brij[71,98,99] and poly(alkylene oxide) block copolymers *e.g.* Pluronic).[6,7,66,100] Materials formed using cationic surfactants tend to be synthesized in basic medium *via* an S^+I^- pathway (Fig. 1.12a) where the surfactant (S) is positively charged and the silicate species are negatively charged (I) with the governing co-assembly interactions being electrostatic.[39] Cetylpyridinium chloride templates in acidic medium were used for the preparation of toluene, -$C_6H_3(CH_3)$- PMO. Yet a halide salt was required and the mesostructured materials were formed *via* a $S^+X^-I^+$ pathway (Fig. 1.12b), where X = F^-, Cl^- or Br^-, and the silicate species are positively charged.[56,101] Solids formed using cationic templates show either a 2D hexagonal or 3D cubic mesostructures analogous to those of MCM-41 and MCM-48[28] silicas with pore diameters and surface areas in the region of 20-30 Å and 500 to 1000 $m^2\ g^{-1}$ respectively.

Syntheses of PMO's using non-ionic surfactants are usually carried out in acidic medium with the co-assembly pathway of $S^0(I)^0$, where hydrogen bonding is the main driving force for co-assembly (Fig. 1.12c). However, if the synthesis is carried out in strongly acidic media (pH<2, the isoelectric point, at which point the oxygen of the Si-OH bearing inorganic species becomes protonated) a mediator anion is required. The mediator ion is usually in the form of a halide anion and a $S^0H^+X^-I^+$ co-assembly pathway occurs (Fig. 1.12d). In this system the hydrophilic groups of the surfactant carry a δ^+ charge thus

increasing H-bonding interactions and forming ion-pairs with the inorganic salt.[9,102,103] Solids synthesized using the tri-block co-polymers P123 or F127 exhibit the same symmetry and arrangement of pores SBA-15 and SBA-16[6,7] materials respectively possessing pore diameters of 50-100 Å and surface areas in excess of 800 $m^2 g^{-1}$. The advantages of using tri-block copolymers over cationic templates are the increase in wall thickness, thus improved hydrothermal stability, and increased pore diameters both in pure and organosilica materials.[7]

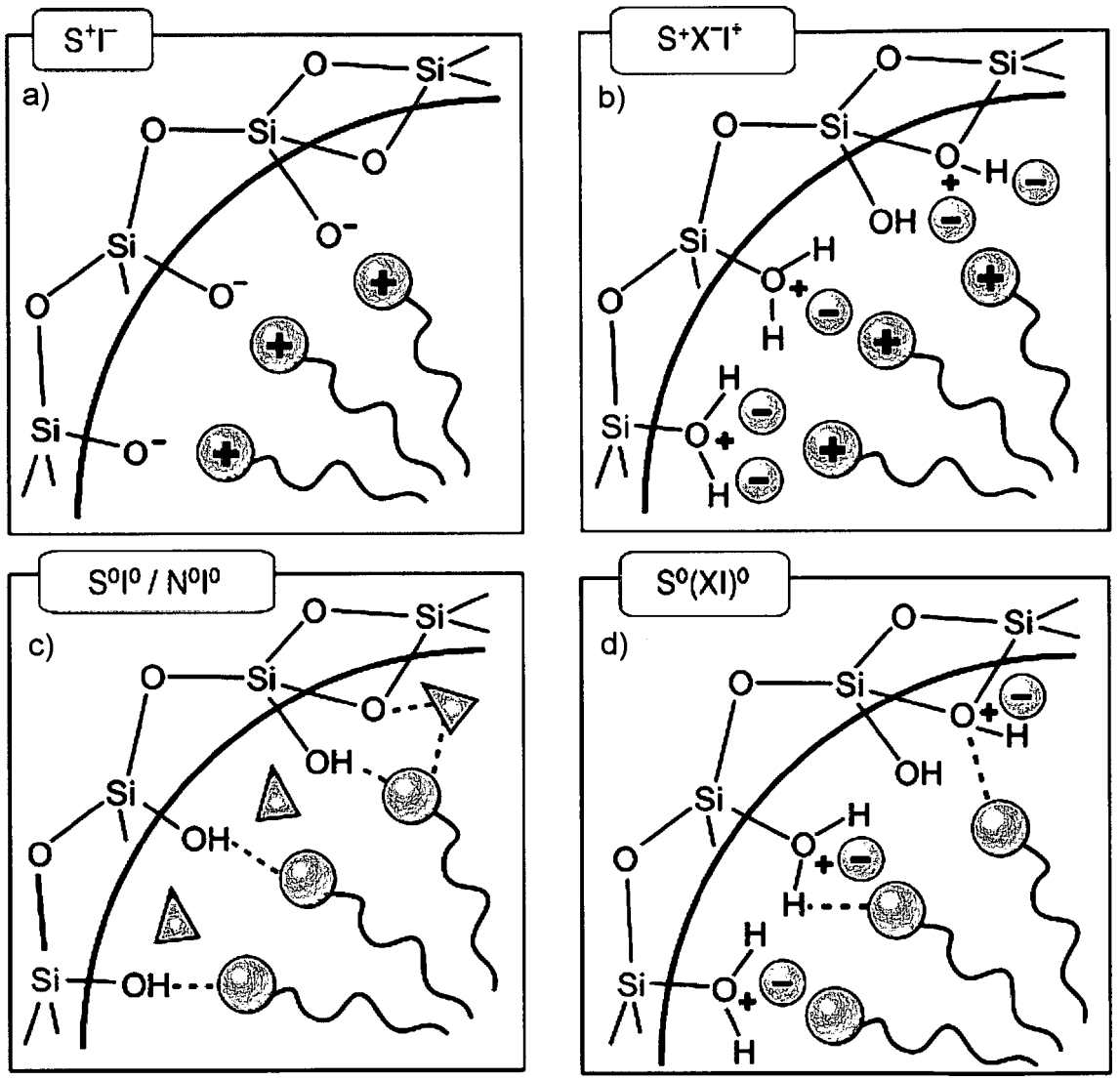

Figure 1.12. Intermolecular interactions between the inorganic precursors and the template species: a) cationic templating in basic media, b) cationic templating in acidic media, c) non-ionic templating at pH> 2 and d) non-ionic templating at pH <2. S or N = template species, I = inorganic precursor and X = halide anion such as Cl^- or F^-.[39]

1.3. Incorporation of heteroatoms into mesoporous solids

Incorporation of heteroatoms into mesoporous silica *via* isomorphous substitution widens the scope of their catalytic applications. Transition metals are widely used as heterogeneous catalysts. Thus incorporation of titanium and iron in MCM-41 enables photo catalytic reactions *i.e.* epoxidation of styrene.[104,105] The incorporation of aluminium into MCM and SBA materials generates Brønsted acidic sites.[106-109] Various transition metal containing mesoporous silicas are listed in table 1.2.

Table 1.2. A selection of heteroatom containing mesoporous silicas and their applications as heterogeneous catalysts.

Author	Mesoporous silica phase	Heteroatom	Incorporation method	Catalytic process	Reference
Chen	MCM-41	Tungsten	Direct	Oxidation of cyclopentene	110
Luo	MCM-41	Titanium	Direct	Oxidation	111
Melero	SBA-15	Titanium	Direct/ Grafting	Epoxidation of 1-octene	112
Shulz	MCM-41	Vanadium	Direct	N/A	113
Sakthivel	MCM-41	Chromium	Direct	Oxidation of alkylaromatics	114
Panpranot	MCM-41	Cobalt	Incipient wetness	CO hydrogenation	115

The synthesis of transition metal doped mesoporous silicas must take into account the relative hydrolysis rates of the silicon and transition metal alkoxides to ensure homogeneous distribution of heteroatoms in the porous network.[116] For example, the synthesis of Ti-MCM-41 uses titanium *tert*-butoxide ($Ti(^tOBu)_4$) which hydrolyses at a faster rate compared to $Si(OC_2H_5)_4$. Increasing Titanium content was shown to decrease the long range ordering of MCM-41.[117] This may be related to the different ionic radii of Ti^{4+} (0.68 Å) and Si^{4+} (0.41 Å). Thus the larger Ti^{4+} ion substituted randomly in place of Si^{4+} may distort the geometry around Ti from tetrahedral.[117] The presence of tetrahedral titanium in the porous network has been determined using ultra-violet - visible spectroscopy diffuse reflectance

(DRS UV-Vis) where the absorption band corresponding to tetrahedral titanium in SBA-15 is observed in the region of 210-230 nm.[118]

Incorporation of Aluminium is considered easier in terms of synthesis and characterisation as aluminium *iso*-propoxide ($Al(OC_3H_7)_3$) has a similar hydrolysis rate to that of $Si(OC_2H_5)_4$. Al-MCM solids tend to become more disordered as the aluminium content increases compared to their purely siliceous analogues.[119,120] Although hydrothermal synthesis has been the main method for the synthesis of transition metal containing MCM/ SBA silicas, the use of post synthetic grafting has also been demonstrated for obtaining high loading levels with retention of mesostructure.[108,120] Post synthetic grafting of aluminium onto SBA-15 is often used in preference to the hydrothermal synthesis route due to the high solubility of Al^{3+} at low pH.[121] Post synthetic grafting of aluminium has been performed using precursors such as, sodium aluminate ($NaAlO_2$),[122] aluminium *tert-* and *n-* butoxide[123,124] and less commonly ammonium hexafluoroaluminate ($(NH_4)_3AlF_6$).[125] The procedure is usually carried out by placing the calcined SBA-15 into a purely aqueous or basic /aqueous solution containing the aluminium source and stirring the suspension at ambient temperatures. The speciation of Al in an alumination solution of $AlCl_3 \cdot 6H_2O$ in tetramethylammonium hydroxide (TMAOH) was studied by Zeng *et. al.* as a function of [TMAOH]/[Al] ratio using solution phase ^{27}Al NMR.[121] The authors observed the presence of two main aluminium species present, octahedral $[Al(H_2O)_6]^{3+}$ and tetrahedral Al as a tridecamer $[AlO_4Al_{12}(OH)_{24}(H_2O)_{20}]^{7+}$ with increasing teterahedral content at higher [OH]/[Al] ratios. A linear correlation between an increase in [OH]/[Al] and aluminium incorporation into the final SBA-15 solid was also observed.

Although most literature syntheses use grafting to synthesise Al-SBA-15 some methods for a direct one pot co-condensation have been reported. The first method is to carefully control the pH of the synthesis mixture, the so called "pH adjusting method".[123,126] Whereby, a weak base such as NH_3 or TMAOH is used at set intervals in the hydrothermal process to increase the pH >5. The second approach uses an evaporation induced self-assembly (EISA) method to prepare Al-SBA-15. The synthesis is carried out in the absence of the mineral acid (HCl) using a P123/TEOS/$AlCl_3 \cdot 6H_2O$/EtOH/H_2O gel composition and the resulting mixture is placed in a Petri dish to undergo the EISA process.[127,128]

1.3.1 Incorporation of Heteroatoms into PMOs

The incorporation of aluminium[129] and titanium[130] into -CH_2CH_2-PMOs synthesised *via* S^+I^- pathway has been demonstrated. The synthesis of Al and Ti-PMOs is similar to that for Al/Ti MCM-41 but can influence the mesoscopic ordering different ways as discussed below. The template removal procedure for Al-PMOs is additionally difficult due to the potential acid leaching of aluminium from the framework in concentrated HCl/EtOH extraction solutions. A different approach was demonstrated, whereby a diluted HCl/EtOH solution (8.8 $x10^{-3}$ mol L^{-1}) was used with the extraction process being repeated thrice.[129] The repeated extraction procedure relies on an equilibrium process being present between the HCl and quaternary ammonium salt electrostatically bound to the organosilica framework (fig.1.13).

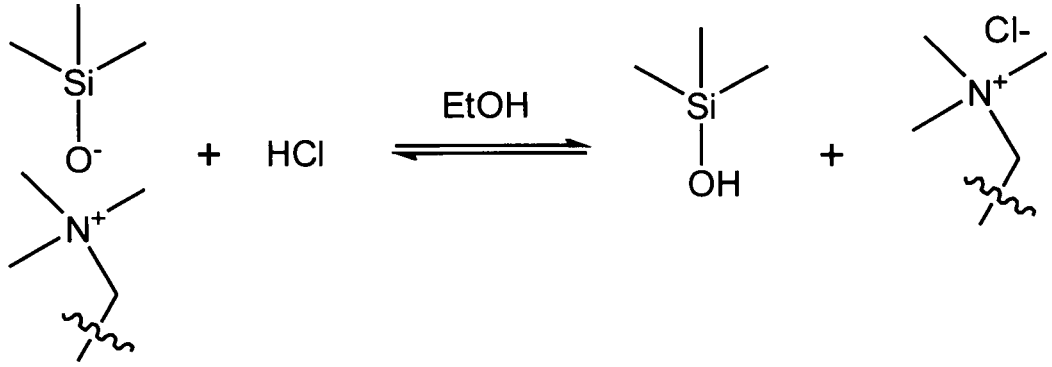

Figure 1.13. Reaction mechanism of the template extraction procedure used for the removal of cationic templates from organosilicas.

The standard concentration of an extraction solution, (1M HCl/EtOH) means the HCl is in excess thus pushes the equilibrium to the right within 4 to 6 hours to yield the mesoporous organosilica. However, at lower acid concentrations repeated cycles, where the partially extracted organosilica is isolated between each cycle, are required to push the equilibrium to the right.

The effect of heteroatoms on the degree of ordering and morphology of PMOs is highly dependent on the metal. For instance, increasing the aluminium content in Al/-CH_2CH_2-PMOs has shown to improve mesoscopic ordering confirmed both by powder XRD and nitrogen adsorption isotherms.[129] This observation is in contrast to the effect of incorporation of aluminium in MCM-41 (see above). On the other hand, Ti-CH_2CH_2-PMOs displayed a decrease in mesoscopic ordering as the titanium content increases, consistent with changes observed for Ti-MCM-41. The incorporation of transition metals into PMOs has further advantages to their mesoporous silica analogues in that the organic bridges can be

changed to alter the resulting properties for example, the use of a hydrophobic organic bridge to preferentially allow hydrophobic reactants to the active sites of the transition metals within the porous network. The introduction of bi-functionality to PMOs may further expand their range in various catalytic applications. Aluminium incorporated PMOs have displayed Brønsted acidity[129,131,132] whereas titanium[105,112], vanadium[133] and chromium[134] containing PMOs have shown promise in epoxidation reactions.

1.4 Aims of the Project

The introduction of multiple functionalities in mesoporous organosilicas using various transition metals or organic groups is driven by potential applications in chromatographic separation, drug delivery and catalysis. The use of multi-functional materials with limited long range ordering makes their characterisation more challenging. For example, the location of various components within the framework needs to be determined if they are to be used in heterogeneous catalysis. Thus, the main challenges are in both the design of a synthetic process which can incorporate multiple functionalities into a framework of uniform pore dimensions, and ability to determine their location within the structure. The synthetic methodology must also be able to direct the various components to specific locations within the structure. Secondly, confirming the functionalities incorporation into the structure and probing their location with respect to one another are difficult due to the lack of long range periodicity.

Therefore, the aims of this project are split into two main categories:

The synthetic part consists of applying both post-synthetic modifications (*via* bromination of –CH=CH- bonds) and direct co-condensation of different organosilanes to obtain multi-functional mesoporous organosilicas. The co-condensation of the organosilanes has been investigated using a pre-hydrolysis step in an attempt to control the distribution of the organic bridges within the mesoporous framework. The understanding of how pre-hydrolysis influences the final product will be challenging in terms of synthetic design when using different organic bridges. The influence of acid or base pre-hydrolysis of organosilanes and subsequent effects on non-ionic and cationic templated PMOs is investigated. Finally, inclusion of the 'heteroatom' aluminium and its influence on both the pre-hydrolysis step in $-CH_2CH_2-$/-CH=CH- containing PMOs and its resulting mesostructure synthesised *via* cationic templating will be discussed. The incorporation of aluminium into multi-functional PMOs is an important process in designing materials with Brønsted acidity.

Secondly, powder XRD and N_2 adsorption-desorption isotherms will be used to characterise the structural and textural properties of the resulting PMOs. The aim of which is to probe mesostructural changes as a function of synthetic pathway and pre-hydrolysis conditions. With the aid of solid-state NMR experiments such as CP/MAS, kinetics, heteronuclear and homonuclear correlations we aim to monitor; i) ratio of functionality incorporation into the framework; ii) surface and bulk pore wall dynamics of the organic

bridges; iii) the homogeneity of the organic functionalities in the framework as a function of synthetic conditions.

Finally an additional chapter is focused on the solid-state NMR characterisation of insoluble, amorphous conjugated microporous polymers networks. The ability to obtain high resolution ^{1}H-^{13}C CP/MAS spectra allows the complete assignment of all carbon environments within the network. The application of CP/MAS kinetics has also indicated changes in mobility as a function of polymer composition.

Characterisation Techniques

Chapter 2

2.1 Nuclear magnetic resonance (NMR)

2.1.1 Basics of NMR

Nuclear magnetic resonance deals with the interaction between a nucleus with a magnetic moment μ, and an external magnetic field, B. Nuclei with a spin quantum number, I, that is not equal to zero *i.e.* I = 1/2, 1, 3/2, 5/2 possesses a magnetic moment. Such nucleus can then be viewed as a small magnet which posses a magnetic moment, μ given by:

$$\mu = \gamma \hbar I \qquad \textbf{Eq 2.1}$$

Where γ is the magnetogyric ratio, constant for a given nucleus, $\hbar$ is Planks constant and I is the spin quantum number of the nucleus.

When a nucleus with a non-zero spin is placed in a magnetic field, B_0 the energy associated with the magnetic moment, μ will be:

$$E(m) = -\mu_z B_0 = -m_I \gamma \hbar B_0 \qquad m_I = (I, I-1, \ldots, -I) \qquad \textbf{Eq 2.2}$$

Thus a Zeeman splitting occurs and the energy levels of the nucleus split into (2I +1) non-degenerate levels (Fig. 2.1). The selection rule is, $\Delta m_I = \pm 1$ and the difference between the two levels is as follows:

$$\Delta E = \gamma \hbar B_0 \qquad \textbf{Eq 2.3}$$

The magnitude of the Zeeman splitting is dependent on the B_0 field and the magnetogyric ratio (Eq 2.3) and is therefore different for each nucleus under study.

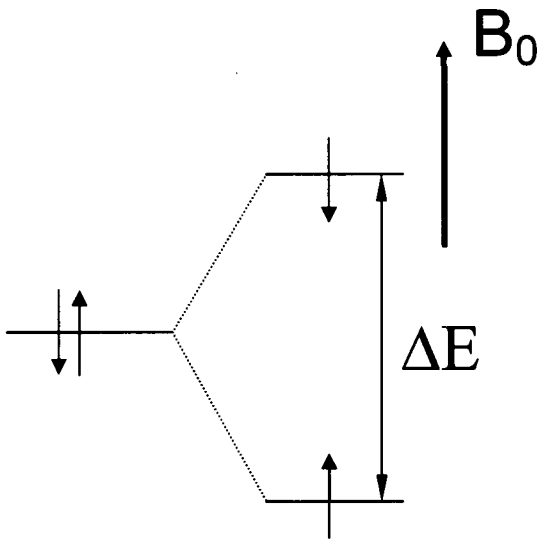

Figure 2.1. Zeeman splitting of a spin I = ½ nuclei in a magnetic field, B_0.

From figure 2.1 it can be seen that the spin of a nuclei may align parallel (spin up) or anti-parallel (spin down) with respect to the B_0 field. When multiple spins with a magnetic moment are placed in a magnetic field the nuclear magnetic moments are aligned preferentially with the applied B_0 field. However, thermal equilibrium effects cause a distribution of orientations although the net nuclear magnetization remains parallel to that of the applied B_0 field (fig. 2.2).

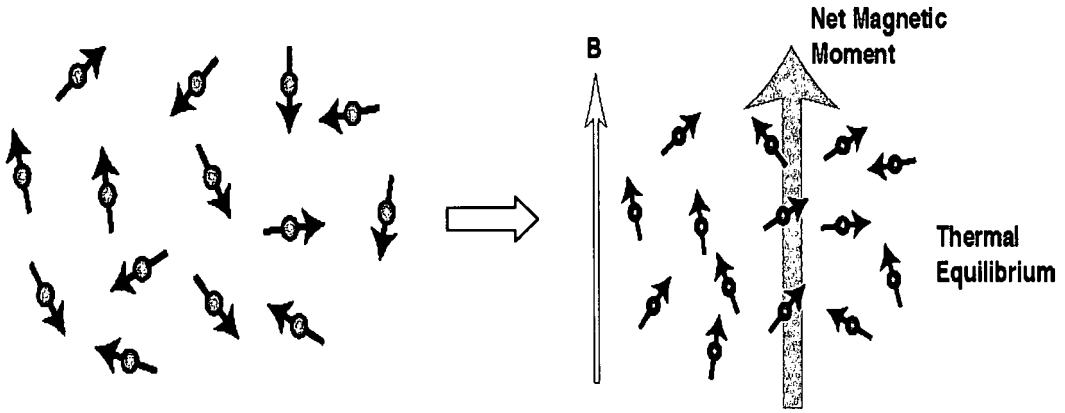

Figure 2.2. Picture representation of spin system without an external magnetic field (left) and in a static magnetic field, B (right).[135]

2.1.1.2 Larmor precession

Nuclear spins as well as possessing a magnetic moment also exhibit an angular momentum which contributes to the overall net magnetisation. If the nuclei are placed in an external magnetic field B_0 a torque, T is exerted on the magnetisation vector (Eq. 2.4)

$$T = \frac{d}{dt}\left(\frac{M}{\gamma}\right) M \times B \qquad \textbf{Eq 2.4}$$

Equation 2.4 describes the motion of the magnetization vector, M in the field B and predicts that M precesses about a fixed B at a constant rate of $\omega = -\gamma B$. In NMR the applied static magnetic field is labelled B_0 and is situated along the z-axis in the laboratory frame therefore the frequency at which the magnetization precesses is labelled ω_0 and defined as the Larmor frequency (Eq.2.5).

$$\omega_0 = -\gamma B_0 \qquad \textbf{(Eq. 2.5)}$$

2.1.1.3 Chemical shift and shielding interactions

The magnetic field experienced by a nucleus is affected by surrounding electrons. The electrons produce a secondary field which in turn adds to the total field felt by the nucleus. This secondary field interaction with the nucleus is the *shielding interaction.* This interaction changes the resonance frequency of the nucleus thus giving rise to *chemical shift.* The shielding interaction is extremely small compared to most other magnetic interactions and is therefore measured in parts per million (ppm) from a standard frequency (usually that of TMS when viewing an NMR spectrum).

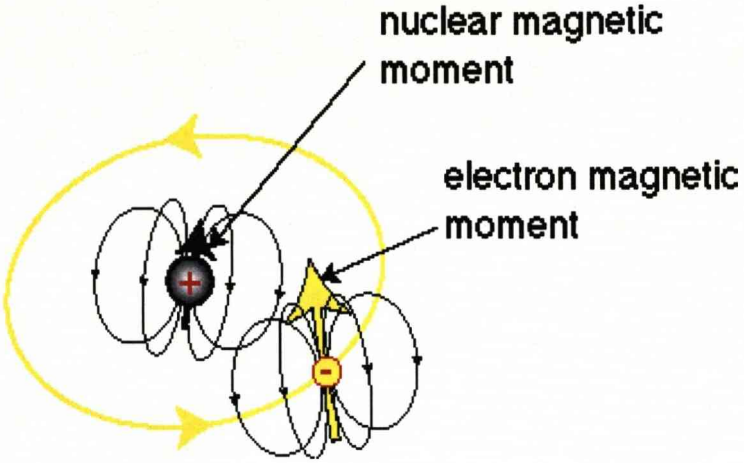

Figure 2.3. The total field felt by ^{1}H in an NMR experiment.[135]

The total effective field felt by a nucleus is therefore the external magnetic field, B_0 plus the secondary field B_i (Eq 2.6).

$$B_{eff} = B_0 + B_i \qquad \textbf{Eq 2.6}$$

The degree of shielding felt by a nucleus is described by the shielding constant, σ. The effect of the secondary field when acquiring an NMR spectrum is to induce an energy transition in the Zeeman splitting with an *rf* pulse at frequency of:

$$\upsilon = \frac{\gamma}{2\pi} B_{eff} \qquad \textbf{Eq 2.7}$$

The energy transition from high to lower energy is essentially what is observed in the Free Induced Decay (FID). The FID contains information on the frequency at which a nucleus in a particular environment resonates which decays as a function of time therefore, an NMR signal once Fourier transformed can be described as an emission spectra.

2.1.2 Solid-state NMR

Solid-state NMR is a powerful technique for observing molecular level structure when solution NMR becomes impractical *i.e.* for the study of insoluble polymers, amorphous materials and the surface of heterogeneous catalysts *i.e.* zeolites.

In solution phase NMR there is rapid molecular motion due to the high mobility of liquids. If the liquid is isotropic then all motions occurring are random and thus averaged out eliminating many nuclear spin interactions. This property is important and has enabled solution NMR to be widely used as the spectra obtained are simpler due to the limited number of magnetic interactions (2.8).

$$\hat{H}_{Total} = \hat{H}_Z + \hat{H}_{CS}^{iso} + \hat{H}_J^{iso} \qquad \textbf{Eq 2.8}$$

Where $\hat{H}_Z$ = Zeeman interaction, $\hat{H}_{CS}^{iso}$ = Chemical shift (describing chemical shielding interactions) and $\hat{H}_J^{iso}$ = spin-spin interactions (*J*-coupling).

In solids the situation becomes more complex due to reduced mobility of the molecules and atoms. As a result many of the orientation dependent nuclear spin interactions are no longer averaged out as in solutions. The extra nuclear spin interactions are given by the nuclear spin Hamiltonian for a powdered sample (Eq 2.9).

$$\hat{H}_{Total} = \hat{H}_Z + \hat{H}_{CSA} + \hat{H}_D + \hat{H}_Q + \hat{H}_J \qquad \textbf{Eq 2.9}$$

Where $\hat{H}_{CSA}$ = Chemical shift anisotropy, $\hat{H}_D$ = Dipolar coupling and $\hat{H}_Q$ = Quadrupolar coupling (observed only in spin $I > 1$). The anisotropic spin interactions have a drastic effect on a solid-state NMR spectra leading to a considerable line broadening compared to solution NMR.

2.1.3 Nuclear magnetic interactions

The Zeeman interaction is the same as that for liquids and the J-coupling Hamiltonian in solids is generally not considered as it is considerably smaller compared to other nuclear spin interactions. Therefore these terms will not be discussed in this section.

2.1.3.1 Chemical shift anisotropy (CSA)

In solid-state NMR a spectrum the chemical shift is represented by a 3-dimensional shielding tensor which is averaged out to an isotropic chemical shift in solutions. The CSA results from the fact that atoms in a molecule rarely possess a spherical electron cloud distribution and is generally considered to be an ellipsoid in shape elongated along bonds or nonbonding *p*-orbitals.[136] As the molecule has many orientations with respect to the B_0 field the chemical shielding interaction felt by the nucleus is different for every orientation and therefore so is the chemical shift (Fig. 2.4).

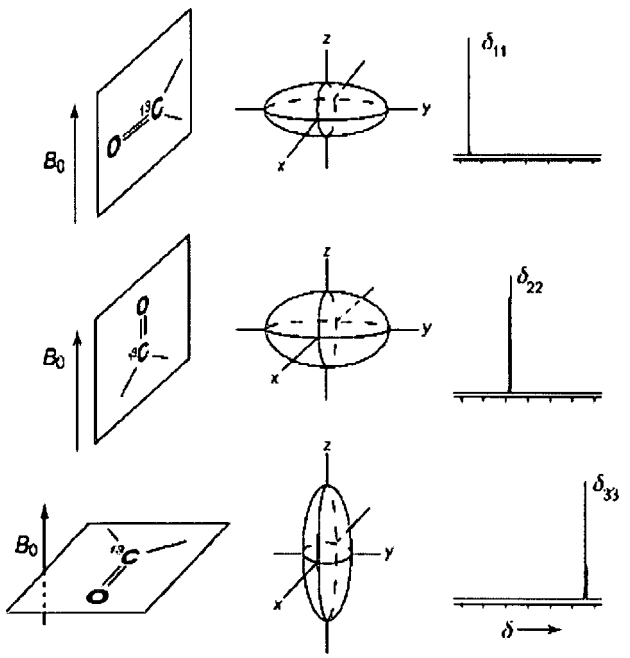

Figure 2.4. Principal values of CS tensor, the chemical shift is dependent on the orientation of the ellipsoid with respect to the B_0 field.[136]

In reality not only the three principle values are observed due to the random orientation of the molecules present within the sample thus as a result a powder pattern is obtained (Fig. 2.5).

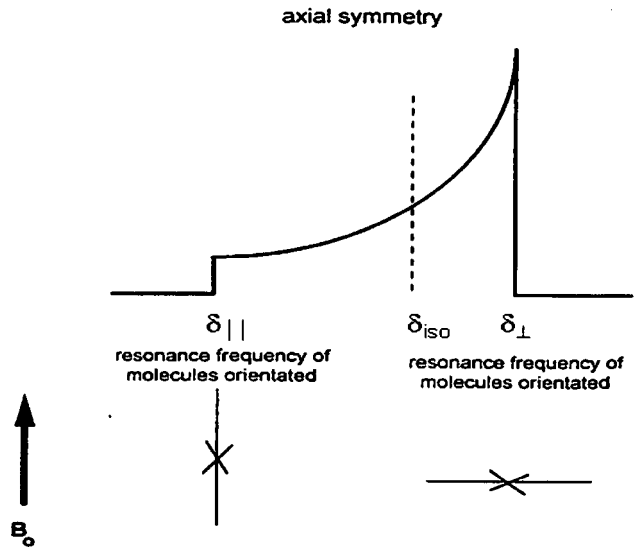

Figure 2.5. Powder pattern of molecule possessing axial symmetry with respect to the B_0 field.[137]

To understand the principal values of CSA one must first break down the chemical shift Hamiltonian.

$$\hat{H}_{CS} = \gamma B_0 I_Z \left[\delta_{iso} - \frac{1}{2}\delta_{CSA}(3\cos^2\theta - 1) \right] \quad \textbf{Eq 2.10}$$

The term θ describes the orientation of ellipsoid axis of a particular molecule with respect to the B_0 field. The Hamiltonian also describes both the isotropic chemical shift, δ_{iso}, and the magnitude of the CSA, δ_{CSA}, which are derived below:

$$\delta_{iso} = \frac{1}{3}(\delta_{11} + \delta_{22} + \delta_{33}) \quad \textbf{Eq 2.11}$$

$$\delta_{CSA} = \delta_{iso} - \delta_{33} \quad \textbf{Eq 2.12}$$

The isotropic term is simply the average of all three principal values and the CSA being equal to this average minus that of the chemical shift when the widest part of the electron cloud is aligned with the B_0 field (Eq. 2.12 and 2.13). Techniques to eliminate this effects of CSA and retain an isotropic chemical shift are discussed in section 2.1.4.

2.1.3.2 Dipolar coupling

Dipolar coupling is an interaction between magnetic fields of two spins that are relatively close in proximity to one another. The spins can be the same (homonuclear dipolar coupling) or different (heteronuclear dipolar coupling).

i) Homonuclear dipolar coupling

When two identical spins (*i.e.* ^{1}H-^{1}H spin pair) are close enough in space they are able to undergo energy conserving "flip-flop" transitions where one spin flips to a high energy state and the other spin flips to a low energy state (Fig. 2.6).

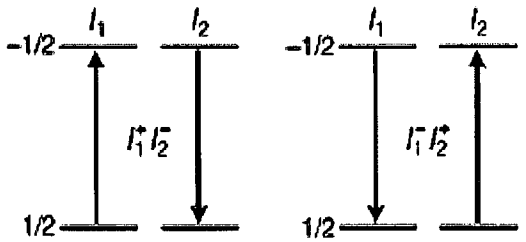

Figure 2.6. Two like spins exchanging magnetization via energy conserving "flip-flop" interactions.

The homonuclear dipolar Hamiltonian for a simple two spin system is given below:

$$H_{IS} = -d\,\tfrac{1}{2}(3\cos^2\theta - 1)(2I_{1Z}I_{2z} - \tfrac{1}{2}(I_1^+I_2^- + I_1^-I_2^+)) \quad \textbf{Eq 2.13}$$

$$\text{Where } d = (\mu_0/4\pi)(\hbar\gamma_I^2/r_{IS}^3) \quad \textbf{Eq 2.14}$$

Raising operator I^+ increases the angular momentum of a spin causing the flipping of a spin from the "down" to "up" orientation. Simultaneously the lowering operator I^- decreases the angular momentum causing a spin flip from "up" to "down". It is important to remember that this interaction only affects spins with chemical shifts that are relatively close together. From equation 2.14 one can also see that the magnetogyric ratio of a spin affects the strength of the homonuclear dipolar coupling, consequentially, spin pairs of ^{13}C or ^{29}Si will only have weak homonuclear couplings and will be rare as the chances of two ^{13}C nuclei being close together are remote (natural abundance, ^{13}C = 1.1 %). Homonuclear dipolar coupling leads to difficulties when studying ^{1}H nuclei as their interaction can be of *ca.* 100 kHz due to the large magnetogyric ratio and near 100 % natural abundance, The result of which is broad featureless spectra over a narrow chemical shift range. Despite these

problems fast Magic Angle Spinning (whereby the sample is spun at an angle of 57.54°, discussed in section 2.1.4.1) and multi-pulse homonuclear dipolar decoupling sequences such as WAHUHA (WAugh, HUber and HAeberlan),[138] FS-LG (Frequency Switched Lee Goldburg)[139] and DUMBO (Decoupling Using Mind Boggling Optimization)[140-142] have been developed to enhance spectral resolution.

ii) Heteronuclear dipolar coupling

Heteronuclear dipolar coupling arises from the interaction of the magnetic moments of two non-identical spins close in space. In general, one of the spins is usually abundant, *I* spin (^{1}H or ^{19}F) and the other is a rare, *S* spin (^{13}C or ^{29}Si). When the *I* and *S* spins are placed in a magnetic field, Zeeman splitting occurs with the *I* and *S* spin aligned either parallel or anti-parallel with respect to the B_0 field. As each spin represents a magnetic field the spins "*feel*" each others magnetic moment when they are close in space. The 'local field' of the *I* spin will therefore add or subtract to the external field felt by the *S* spin and change its resonance frequency. The strength of the heteronuclear interaction is governed by the effect the *S* spin has on the *I* spin (Eq 2.15).

$$\hat{H}_{IS} = -d(3\cos^2\theta - 1)I_Z S_Z \qquad \textbf{Eq 2.15}$$

Where *d* is the dipolar coupling constant:

$$d = (\mu_0 / 4\pi)\hbar\gamma_I\gamma_S / r_{IS}^3 \qquad \textbf{Eq 2.16}$$

Where r_{IS} = inter-nuclear distance, μ_0 = permeability of free space (= 4π x 10^7 N A^{-2}), γ_I and γ_S = magnetogyric ratios of *I* and *S* spins, I_Z and S_Z = Z component of the nuclear spin angular momentum operators *I* and *S*.

The main properties of the heteronuclear dipolar Hamiltonian are that the coupling is dependent on the magnetogyric ratios *i.e.* the higher the ratio the stronger the coupling, the coupling is inversely proportional to r^3 therefore as the distance between the spins increases the coupling rapidly decreases. Heteronuclear coupling is also orientation dependent. Thus the magnitude of coupling will change for different orientations even if the inter-nuclear distance is the same. In equation 2.15 the term θ describes the angle of the inter-nuclear vector to that of the B_0 field (fig. 2.7).

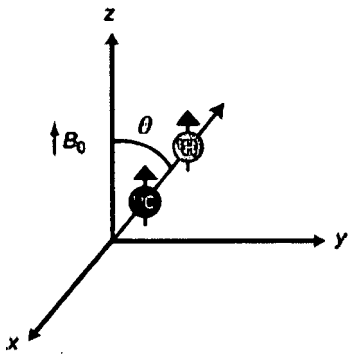

Figure 2.7. The angle between the ^{1}H-^{13}C bond vector and the static B_0 field.[136]

The effect of heteronuclear dipolar coupling on a spectrum of a crystalline material can be seen in figure 2.8 assuming that no other orientation dependent terms are present. A "Pake doublet" is observed and is a direct result of energy differences arising from H_{IS}. The relative intensities indicate the number of crystallites in a particular orientation with the most intense peaks observed when the inter-nuclear vector is perpendicular to the magnetic field. It should be noted that if the sample is placed at the "magic angle" the resonance frequency is not altered by heteronuclear dipolar coupling (fig. 2.8) at this point θ = 54.74 and $(3\cos^2\theta - 1) = 0$ in equation 2.15.

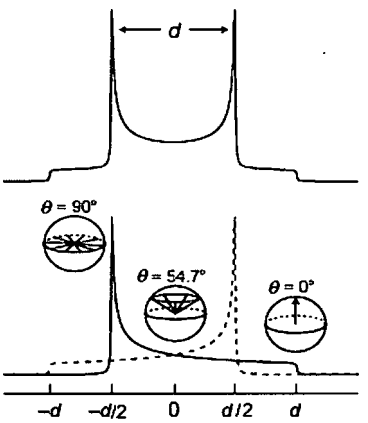

Figure 2.8. Pake pattern resulting from hetero-nuclear dipolar interaction of an *I* and *S* spin system.[136]

2.1.3.3 Quadrupolar coupling

About 74 % of all NMR active nuclei possess a spin quantum number of $I > ½$ and are classed as quadrupolar. Nuclei with a quadrupolar moment such as ^{2}H, ^{14}N $I = 1$, ^{11}B, ^{23}Na $I = 3/2$, ^{17}O, ^{27}Al $I = 5/2$, ^{59}Co $I = 7/2$ and ^{93}Nb $I = 9/2$ still possess the same interaction as spin ½ nuclei (dipolar coupling, CSA *etc.*) but also the quadrupolar Hamiltonian must be taken into account. The two main differences between spin $I = ½$ nuclei and spin $I > ½$ are summarized below:

i) For quadrupolar nuclei the allowed spin quantum number m_i values are no longer just + ½ and - ½ but become more complex depending on the nuclear spin number. For example, ^{23}Na with a spin of $I = 3/2$ there are four possible energy levels (spin states) m_i = 3/2, 1/2, - 1/2, and - 3/2 with 3 detectable transitions in the presence of an external magnetic field as shown in figure 2.9. In general there are $2I + 1$ energy levels and $2I$ detectable transitions.

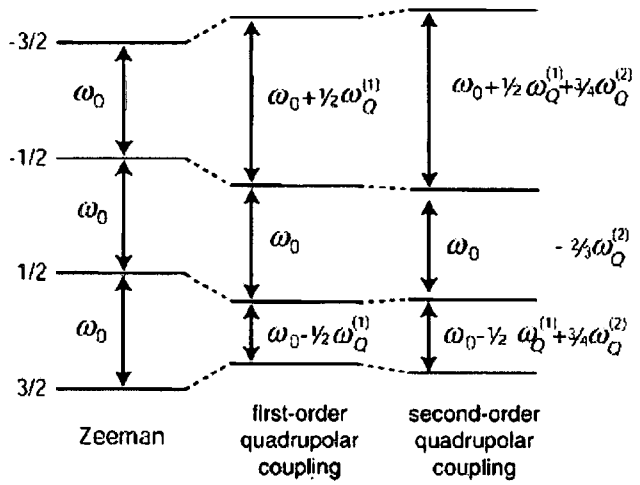

Figure 2.9. Zeeman energy levels for a 3/2 spin with the 1st and 2nd order quadrupolar interactions.[136]

ii) Quadrupolar nuclei show a non-spherical charge distribution which can couple to electric field gradients which are present in most materials. The quadrupolar coupling can be in the order of MHz causing severe line broadening in a NMR spectrum.

The quadrupolar Hamiltonian is complex and in its basic form describes the interaction between a nuclear electric quadrupole moment and an electric field gradient, V

$$\hat{H}_Q = \frac{eQ}{2I(2I-1)\hbar}\hat{\mathbf{I}} \bullet \mathbf{V} \bullet \hat{\mathbf{I}} \quad \textbf{Eq 2.17}$$

Where Q = nuclear quadrupole moment, $\hat{\mathbf{I}}$ = nuclear spin vector and $\mathbf{V}$ = electric field gradient (second-rank Cartesian tensor).

From figure 2.9 one can see that the 1st and 2nd order quadrupolar interactions change the Zeeman splitting that was defined for a spin ½ nuclei in equation 2.2. The energy corrections to the Zeeman splitting are defined below:

$$E_m^{(1)} = \frac{e^2qQ}{4I(2I-1)}(3m^2 - I(I+1))\frac{1}{2}[(3\cos^2\theta - 1) + \eta\cos 2\phi \sin^2\theta] \quad \textbf{Eq 2.18}$$

$$\begin{aligned} E_m^{(2)} = &-(e^2qQ/4I(2I-1))^2 \frac{m}{\omega_0} \times \{-\frac{1}{5}(I(I+1) - 3m^2)(3+\eta_Q^2) \\ &+ \frac{1}{28}(8I(I+1) - 12m^2 - 3)[(\eta_Q^2 - 3)(3\cos^2 - 1) + 6\eta_Q \sin^2\theta\cos 2\phi] \\ &+ \frac{1}{8}(18I(I+1) - 34m^2 - 5)[\frac{1}{140}(18+\eta^2)(35\cos^4\theta - 30\cos^2\theta + 3) \\ &+ \frac{3}{7}\eta_Q \sin^2\theta(7\cos^2\theta - 1)\cos 2\phi + \frac{1}{4}\eta_Q^2 \sin^4\theta\cos 4\phi]\} \end{aligned} \quad \textbf{Eq 2.19}$$

Where m = magnetic quantum number of the corresponding Zeeman level.

The energy splitting on the central transition (+1/2 →-1/2) is unaffected by the first order quadrupolar interaction so the transition is expected to be sharp. However, the central transition is affected by the second order quadrupolar interaction which causes line broadening if this interaction is large. Another important point of equation 2.18 is that the 1st order interaction has the same molecular orientation dependence as CSA and dipolar interactions.

Equation 2.19 describes the effect of the second order quadrupolar interaction and although complex it highlights two important points.

i) The size of $E_m^{(2)}$ is inversely proportional the external field thus the Larmor frequency of the nucleus therefore the higher the external field, B_0 the smaller $E_m^{(2)}$ becomes. This is an important point and is one of the major driving forces

behind the development of higher field strengths (at present 21 T for solid-state spectrometers (950 MHz for ^{1}H)).

ii) The orientation dependence is more complicated *c.f.* to the 1st order quadrupolar interaction. There are now three terms corresponding mathematically to the zeroth, second and fourth-order Legendre polynomials.[143]

$$\text{Zeroth-order} \qquad P_0(\cos\theta) = 1 \qquad \textbf{Eq 2.20}$$

$$\text{Second-order} \qquad P_2(\cos\theta) = -1/2(3\cos^2\theta - 1) \quad \textbf{Eq 2.21}$$

$$\text{Fourth-order} \qquad P_4(\cos\theta) = 1/8(3 - 30\cos^2\theta + 35\cos^4\theta) \quad \textbf{Eq 2.22}$$

The zeroth-order term is scalar and independent of θ therefore similar to an isotropic chemical shift. The second-order term can simply be removed by MAS as the value is zero at 54.74°. The fourth-order term is zero at different values of θ (30.56 and 70.12°), thus not averaged out by MAS (Fig. 2.10) and results in significant line broadening, this problem has limited the study of quadrupolar nuclei. Techniques such as, DOuble Rotation (DOR)[143,144] where the sample is spun at two angles simultaneously (54.74° and 30.56°) using a "rotor in rotor" design result in the second and forth order Legendre polynomials being 0 (fig. 2.10).[143] Dynamic Angle Spinning (DAS)[145] is similar to DOR, but the sample is spun sequentially at two different angles allowing faster spinning speeds. Both DOR and DAS give higher spectral resolution of quadrupolar nuclei yet require specialised probe design. More recent techniques such as Multiple Quantum Magic Angle Spinning (MQMAS)[146-148] and Satellite Transition Magic Angle Spinning (STMAS)[149-151] have enabled the correlation of a 1D spectrum with the isotropic spectrum of a particular sample at MAS speeds of up to 30 kHz. The use of MQMAS and STMAS has become more widespread as these experiments can be performed on standard solid-state MAS probeheads.

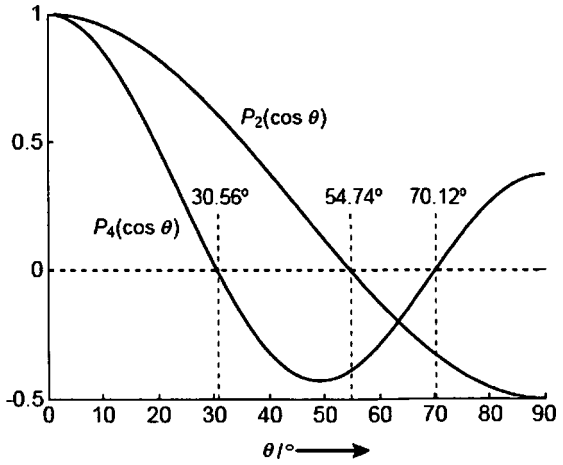

Figure 2.10. Plots of the second and forth-order Legendre polynomials as a function of θ.[136]

2.1.4 Experimental techniques in solid-state NMR

2.1.4.1 Magic angle Spinning (MAS)

Magic angle spinning is a widely used technique in the majority of solid-state NMR experiments and is used primarily to remove the effects of chemical shift anisotropy (CSA). MAS also assists in the removal of heteronuclear dipolar couplings and for narrowing lines from quadrupolar nuclei. More recently, fast MAS has been used for the removal of homonuclear dipolar interactions as spinning speeds of up to 70 kHz are now achievable on commercial probes with 30 kHz being routine for most laboratories. For strong homonuclear interactions (^{1}H and ^{19}F) spinning speeds of 30 kHz are not sufficient to remove these effects so more complex decoupling pulse sequences are generally used.

In solids the MAS technique (Fig. 2.11) is aiming to achieve the same *i.e.* "spin out" the CSA and dipolar interactions. The reason for spinning at a set angle is due to orientational dependence of the nuclear spin interactions indicated by the term $(3\cos^2\theta - 1)$. Where θ is the angle describing the orientation of the spin interaction tensors such as the shielding tensor and dipolar coupling tensor.

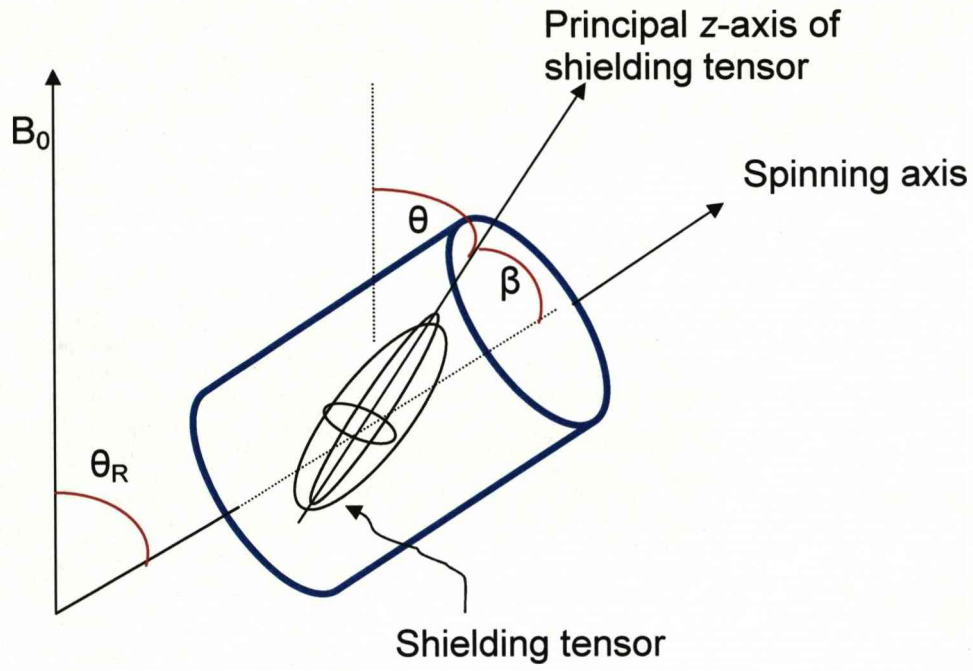

Figure 2.11. Magic angle spinning experiment to remove chemical shift anisotropy with the chemical shielding tensor represented by an ellipsoid which is fixed for every molecule within the powdered sample.

If the sample is spun at θ_R then θ varies with time as the molecules are rotated with the sample and the nuclear spin interaction becomes:

$$\left\langle 3\cos^2\theta - 1 \right\rangle = \frac{1}{2}(3\cos^2\theta_R - 1)(3\cos^2\beta - 1) \qquad \textbf{Eq 2.23}$$

Where β = the angle between the principal z-axis shielding tensor and the spinning axis which is fixed for a given nucleus within a solid sample but in a powder takes up all possible values. θ_R is the angle between the applied field and spinning axis and θ is the angle between the principle z-axis shielding tensor and the applied field, which again takes up all possible values (fig. 2.11). If however θ_R is set to an angle of 54.736° then $(3\cos^2\theta_R - 1) = 0$ thus the average $(3\cos^2\theta - 1)$ is also equal to zero. Therefore the value of θ at high spinning speeds is averaged rapidly compared with the anisotropy of the interaction.

2.1.4.2 Decoupling and r.f. pulses

As seen in section 2.1.4.1 MAS is an efficient technique for removing CSA and assists in the removal of dipolar interactions. However, if MAS is to average out an interaction it needs to be three times the frequency of the interaction. This is difficult in the

case of homonuclear (particularly ^{1}H-^{1}H) and heteronuclear interactions. Therefore more complex methods using *r.f.* pulses are used. When recording spectra of a dilute spin, such as ^{13}C or ^{29}Si, coupled with an abundant spin like ^{1}H or ^{19}F nearby significant line broadening is observed due to heteronuclear dipolar coupling. This effect cannot be removed easily by MAS alone but used in conjunction with high power *r.f.* irradiation during acquisition of the free induction decay (FID) of the dilute X spin yields high spectral resolution. This type of decoupling is commonly known as 'high-power decoupling'. The close-to-resonance *r.f.* irradiation causes the ^{1}H spins to undergo rapid and repeated transitions ($\alpha \leftrightarrow \beta$) at a rate determined by the power of the *r.f.* irradiation. The strength of the X-^{1}H coupling is determined by m_H in the heteronuclear dipolar Hamiltonian. Therefore, if the rate of the transition ($\alpha \leftrightarrow \beta$) is faster relative the X-^{1}H coupling strength then the coupling is averaged out to zero because m_H oscillates rapidly between ± ½. This method is limited as long acquisition times under high-power decoupling can cause sample heating and possibly damage the probehead. To eliminate this problem more sophisticated methods of decoupling have been developed including Two Phase Pulse Modulation (TPPM) which uses two high-power pulses of differing in phase by 10 to 70°[137,152] and X inverse X (XiX) which uses two pulses differing in phase by 180°.[153]

Homonuclear decoupling techniques were mentioned in section 2.1.3.2 and from equation 2.13 one can see the homonuclear dipolar coupling Hamiltonian contains both a geometric and spin component. The geometric component can be averaged out by simply spinning at the magic angle however the spin component is more difficult to deal with. However, if the ^{1}H spins can be rotated in 'spin space' at the magic angle then for a single rotor period the effective Hamiltonian takes the form of:

$$H_{eff} = \lambda\left(\omega_a I_{Az'} + \omega_b I_{Bz'}\right) \qquad \textbf{Eq. 2.24}$$

The dipolar and spin coupling terms are removed and the chemical shift terms in the tilted frame x' y' z' are modified by a scaling factor λ.

In general there are two main types of homonuclear decoupling methods, multi-pulse and phase modulated sequences. The multi-pulse sequences such as FSLG work by applying the LG condition. That is if an off resonance RF field with an offset $\Delta\omega=\omega 1/\tan\theta$, is applied, an effective RF field inclined at θ (with respect to z) is created in the rotating frame. Therefore if $\theta = \theta m = 54.7°$ then the LG offset is defined as $\Delta\omega=\omega 1/\sqrt{2}$ and the effective field acting on the ^{1}H spins is tilted with z' positioned at the magic angle with respect to the

laboratory frame (B_0). The use of a frequency switch whereby the LG offset is switched from positive to negative offsets is used to improve efficiency of the technique by averaging out pulse imperfections. The FSLG decoupling sequence was used within the indirect dimension of the HETeronuclear CORrelation (HETCOR) experiments in chapters 5 to 7. Phase modulated decoupling sequences such as DUMBO use a single pulse of constant amplitude yet the phase is varied at discrete intervals to form a wave where the spin component is averaged to zero. The advantage of using phase modulation over pulse modulated sequences is their applicability as windowed decoupling sequences. That is one can apply the decoupling sequence in cycles of 256 to 512 with a single point collected between cycles to record the total homonuclear decoupled FID in a 1-dimensional experiment. The difficulty in setting up 1D CRAMPS type experiments have made these experiments rare within the literature. However, development of more sophisticated spectrometer hardware has resulted in a re-emergence of 1D CRAMPS spectra being reported.

Although the previously mentioned techniques are useful in obtaining high resolution spectra they do eliminate interactions which may give structural information such as site symmetry of a nucleus and inter-nuclear distances thus techniques have been developed which reintroduce lost nuclear spin interactions.

2.1.5 Cross polarization (CP)

Cross polarization (CP) is a common technique used in solid-state NMR for the study of dilute spins such as ^{13}C (1.1%), ^{15}N (0.03%) and ^{29}Si (4.9%), although specific enrichment may be used for ^{15}N. The reasons for using CP over a direct observation method are twofold:

i) The low abundance of the nuclei to be observed means that a high number of scans will be required in order to obtain a good signal-to-noise ratio.

ii) Long relaxation times of some low abundance nuclei (^{29}Si relaxation times are in the order of minutes) mean that long recycle delays are required hence long experimental times which is time consuming.

The use of CP eliminates both of these problems as the magnetization of the dilute spin is obtained from the transfer of magnetization of close by abundant spins thus reducing the number of scans required and the recycle delay times.

2.1.5.1 Theory of Cross-Polarization

The cross-polarization technique (Fig. 2.12) relies on heteronuclear dipolar interactions between the abundant spin (^{1}H) and dilute spins (^{13}C or ^{29}Si) thus the efficiency of CP is highly dependent on the surroundings of the nuclei.

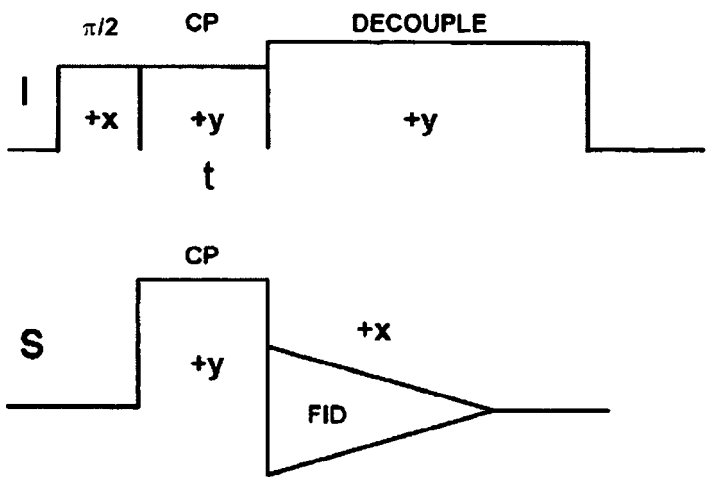

Figure 2.12. Pulse sequence used for Cross-Polarization from an abundant I to rare S spin.[154]

The principle of CP requires consideration of a doubly rotating frame. Within one frame the *I* spin rotates about B_0 (laboratory *z*-axis) at its Larmor frequency with all fields generated by the *I* spin appearing static. The S spin is in the other rotating frame rotating about B_0 at its Larmor frequency. Now a $90°_x$ pulse is applied to create *I* magnetization along $-y$ in the *I* rotating frame (Figure 2.12). A $-y$ contact pulse is then applied to create a spin-lock field labelled $B_1(I)$ which 'holds' the *I* magnetization along the –y axis of the *I* rotating frame. The field B_1 is the only field acting on the *I* spin thus the effects of the B_0 field are eliminated. Simultaneously a contact pulse is applied to the *S* spin in the same manner as to the *I* spin and creates a spin-lock field labelled $B_1(S)$, the only field acting on the *S* spin. For magnetization transfer to work the two contact pulses acting on the *I* and *S* spins must be set to a particular amplitude in order to achieve the Hartmann-Hahn matching condition shown in equation 2.25.

$$\gamma_I B_1(I) = \gamma_S B_1(S) \quad \textbf{Eq. 2.25}$$

The Hartmann/Hahn matching condition is met when the *I* and *S* nuclei presses in the rotating frame at the same rate *i.e.* the energy gaps become equal irrespective of their Zeeman splitting energies of the laboratory frame (Fig. 2.13).

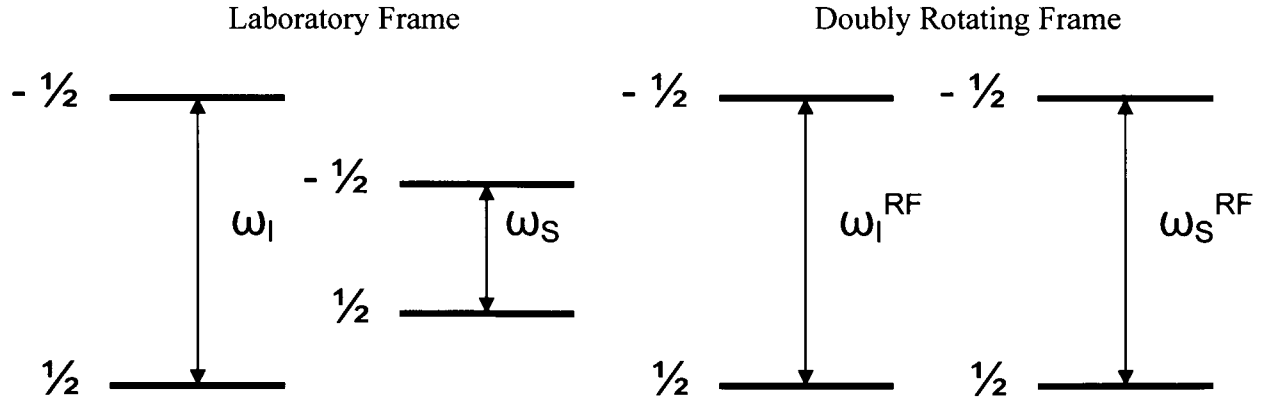

Figure 2.13. The HH matching condition in the rotating frames.

The magnetization is now transferred in the rotating frame *via* heteronuclear dipolar interactions between the *I* and *S* spins. This phenomenon can be explained by quantum mechanic considerations, discussed below.

The dipolar coupling operator (Eq. 2.26) describes the heteronuclear interaction between the *I* and *S* spins.

$$\hat{H}_{IS} = -\sum_i d_i \cdot (3\cos^2 \theta_i - 1) \cdot \hat{I}_{iz}^I \hat{S}_z^S \quad \textbf{Eq. 2.26}$$

Where d_i = dipolar coupling constant.

The equation is unaffected when transformed into the rotating frame as the two operators $\hat{I}_z$ and $\hat{S}_z$ are unaltered by rotations about the *z*-axis. As *I* and *S* magnetization are in the *x*-*y* plane they are perpendicular to *z*, the dipole-dipole operators cannot affect the total energy or the total spin polarization of the systems. The energy of the spin system is dependent on the field applied in the rotating frame (B_1) and the magnetization of the spins which are parallel to the quantization axis. When the H/H match condition is met the energy gaps for the *I* and *S* spins are equal thus the dipole-dipole operator can now act on the spin system inducing transitions on *I* which are compensated transitions by *S* or vice-versa. This also means that the net energy and polarization of the system remains constant.

2.1.5.2 Dynamics of Cross-Polarization

When conducting a CP experiment each parameter must be carefully optimised in order to obtain high quality data and to derive as much structural information as possible. Understanding the kinetics of CP is, therefore, of great importance for the interpretation of CP data. The application of CP kinetics allows one to probe the molecular motions/ dynamics of the system under study. This is carried out by recording CP spectra with different contact times (length of the spin-lock field) and monitoring the evolution of signal intensity.

The kinetics of CP can be described using different models depending on the strength of the ^{1}H-^{1}H homonuclear dipolar coupling. The classical I-S model is ideal for homogeneous solids, where the I-S heteronuclear dipolar interactions are weak and the I-I homonuclear interactions are strong enough to provide an efficient ^{1}H-^{1}H spin diffusion. The *I*-*S* model (fig. 2.14) is simplistic in its approach and takes a thermodynamic point of view, describing the system as consisting of a lattice with a huge heat capacity and two subsystems *I* and *S* with *I* having a larger heat capacity than *S*.

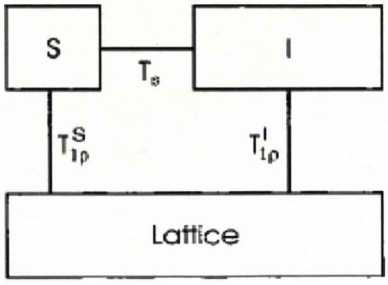

Figure 2.14. Block diagram of CP thermodynamics displaying each component and the relationship between them.[154]

For a system of an abundant (I) and a dilute (S) spin-½ nuclei, the I-S model leads to the kinetic equation:

$$I(t) = I_0\left(1 + \frac{T_{IS}}{T_{1\rho}^{S}} - \frac{T_{IS}}{T_{1\rho}^{I}}\right)^{-1}\left[\exp\left(-\frac{t}{T_{1\rho}^{I}}\right) - \exp\left(-t\left(\frac{1}{T_{IS}} + \frac{1}{T_{1\rho}^{S}}\right)\right)\right] \qquad \textbf{Eq 2.27}$$

Where I_0 is absolute amplitude, $T_{1\rho}$ is relaxation time in the rotating frame which governs the decay of the CP curve and T_{cp} is CP time constant *i.e.* the time it takes for magnetization transfer from I to S indicating the rate of CP build up thus the intensity increase at short contact times.

The equation 2.27 can be simplified because the relaxation times of some dilute spins is very long compared to the CP build-up time ($\frac{T_{IS}}{T_{1\rho}^{S}} \cong 0$):

$$I(t) = I_0\left(1 - \frac{T_{IS}}{T_{1\rho}^{I}}\right)^{-1}\left[\exp\left(-\frac{t}{T_{1\rho}^{I}}\right) - \exp\left(-\frac{t}{T_{IS}}\right)\right] \qquad \textbf{Eq 2.28}$$

The CP time constant T_{IS} is characteristic of a specific functional group because it is dependent on the number of nuclei in close enough proximity to perform CP and the mobility of the functional group. The dependence of T_{IS} on these factors is explained by the fact that CP relies on heteronuclear dipolar interactions which are dependent on inter-nuclear distances, r by a factor of $1/r^3$. The dependence of T_{IS} on mobility is because heteronuclear dipolar interactions are increasingly averaged out the more mobile a functional group Therefore a rigid system with a large number of CP 'donors' in close proximity will have a faster rate of CP than a mobile system with fewer CP 'donors'. There are some instances

where a system can have many CP 'donors' but due to high mobility the CP rate will be slower than expected. For instance, in a system containing CH, CH_2 and CH_3 groups the latter tend to be more mobile thus have a slower CP rate *c.f.* to CH_2 but similar to that of CH.

The $T_{1\rho}{}^H$ relaxation time describes the decay of signal intensity as a function of contact time. The relaxation is mostly governed by the homonuclear dipolar interactions of the *I* spin (^{1}H-^{1}H). The T_{IS} time is characteristic of particular functional groups under study whereas the $T_{1\rho}{}^H$ time is a volume property providing information on the surrounding area of the site to a distance of approximately 2 nm.[155]

Although the I-S model is applicable to the majority of systems under study, it is not sufficient to describe the CP kinetics for solids with heterogeneous proton population. Therefore an additional model that takes into account the effect of spin diffusion, I-I*-S model, has been developed.[154,156] The I-I*-S model recognises the existence of different proton populations, denoted *I** for the protons directly bound to an S spin under study and *I* for the proton network. The CP therefore proceeds in two steps: First a fast rise in signal intensity is observed due to the transfer of the magnetisation to a dilute spin, *I**-*S* by the abundant spins in close proximity. Secondly a step whereby polarisation transfer from the remote *I* spins to the *I** by spin-diffusion, allows the local *I** spins to exchange energy with the bulk *I* spins resulting in an additional increase in signal intensity at slightly longer contact time is observed. Several equations have been proposed to describe the CP kinetics, the simplest is shown below.[154]

$$I(t) = I_0 \exp\left(-\frac{t}{T_{1\rho}^I}\right)\left[1 - \lambda\exp\left(-\frac{t}{T_{df}}\right) - (1-\lambda)\exp\left(-\frac{3}{2}\frac{t}{T_{df}}\right)\exp\left(-\frac{1}{2}\frac{t^2}{T_2{}^2}\right)\right] \qquad \textbf{Eq. 2.29}$$

where $T_{1\rho}{}^I$ is the *I* spin lattice relaxation time in the rotating frame; T_{df} is the ^{1}H spin-diffusion time constant describing the strength of the homonuclear dipolar interactions and the homogeneity of the *I* spin pool; λ is defined by the number *n* of *I* spins attached to the *S* spin under study ($\lambda = 1/(n+1)$); T_2 is the spin-spin relaxation time.

2.1.6 Applications of solid-state NMR to amorphous materials

Solid-state NMR and X-ray diffraction have been widely used in the study of crystalline materials such as zeolites and molecular sieves.[157-159] The use of X-ray diffraction on amorphous systems is limited. However, solid-state NMR is sensitive to local ordering therefore ideally suited for materials lacking long-range periodicity.

The development of fast ^{1}H MAS experiments such as, ^{1}H spin diffusion experiments which allow the relative proximity of different proton environments over the medium to long range to be determined.[160] A more accurate method for ^{1}H distance determination, ^{1}H Double Quantum (DQ) MAS was applied to poly(methacrylic acid) hydrogels and showed the presence of a conformational change from an expanded to a compact contracted form as the pH was decreased.[161-163] The application of ^{1}H DQ MAS to template containing mesoporous silicate thin films has enabled the presence of H-H spin pairs between template and silonal protons that are are spatially close (<5 Å) to be determined.[164] DQ experiments have also been applied to Silicon in the form of the MAS INADEQUATE method which has enabled the assignment of unique Si sites in crystalline zeolite frameworks. However, this technique is less useful in amorphous solids due to the broadening observed in the ^{29}Si spectrum.[165,166] Heteronuclear correlation experiments between ^{1}H and ^{13}C or ^{29}Si nuclei in mesoporous organosilicas have shown the organic groups to be in close proximity to the template.[167,168]

Recently more novel ^{1}H-^{29}Si-^{1}H double CP/MAS experiments have been used to show the difference between template-framework interactions in acid and base catalysed mesoporous silicas and determine the location of the water molecules.[169]

2.2 Powder X-Ray Diffraction[170-172]

Powder x-ray diffraction is widely used in solid-state chemistry to determine the crystal structures of various compounds ranging from mixed transition metal oxides such as Iron(III) phosphates ($FePO_4$)[173,174] to organic molecules such as acetaminophen ($C_8H_9NO_2$) commonly found in paracetamol[171]. The technique itself relies on the generation of X-ray radiation (usually Cu, Co, W or Mo α radiation) in a tube using a heated filament which emits electrons. The electrons are accelerated onto a target causing the ionisation of a core electron, an outer shell electron moves into the core shell emitting white radiation along with two sharp peaks known as K_α and K_β radiation at a higher wavelength (Fig. 2.15). The K_α line appears as a doublet at high accelerating voltage consisting of $K_{\alpha1}$ and $K_{\alpha2}$ radiation. The presence of two different wavelengths is related to the splitting of the 2p orbitals in Copper which is very small (0.020 KeV) hence the two wavelengths $K_{\alpha1}$ (1.54056 Å) and $K_{\alpha2}$ (1.54439 Å) are very similar. K_β radiation is generated by the 3p to 1s electronic transition which is removed by a filter made from the element in use (Cu in the example) to create a monochromatic radiation source.

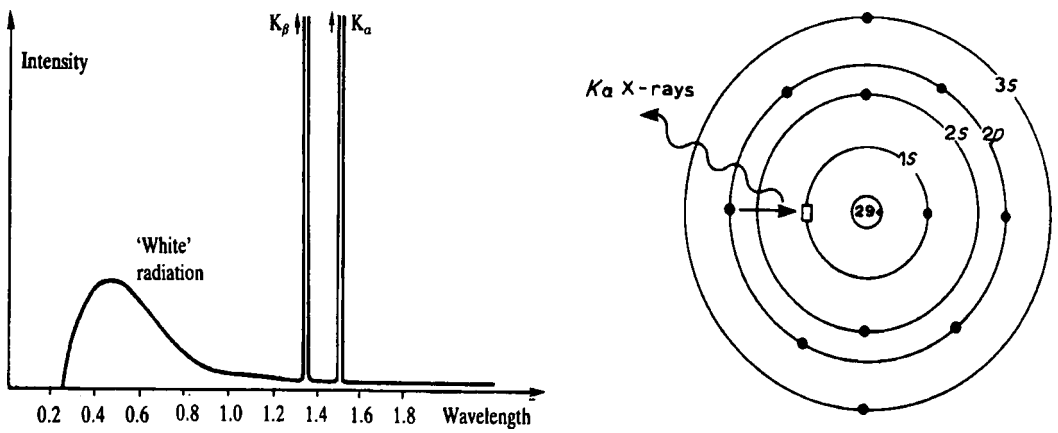

Figure 2.15. X-ray spectra produced from a Cu anode using accelerated electrons.

The X-rays generated can be classed as a sine wave that repeats periodically every 2π radians with the spatial length of each period equalling the wavelength λ. If two waves are not coincident they have a phase shift with respect to one another. The phase shift can be measured as a linear shift, Δ or equivalently as a phase shift, $\delta\varphi$ on an angular scale, such that:

$$\frac{\Delta}{\lambda} = \frac{\delta\varphi}{2\pi} \Rightarrow \delta\varphi = \frac{2\pi}{\lambda}\Delta \qquad \textbf{Eq. 2.30}$$

The detected intensity, I, of the sine wave is the square of the amplitude A. With two waves present, the amplitude is no longer the sum of the individual waves but is dependent on the phase shift $\delta\varphi$. The two extremes occur when the waves are of the same phase thus $\delta\varphi = 0$ and $\delta\varphi = \pi$, constructive and destructive interference respectively (discussed below). The intensity of the two waves can therefore be written as:

$$I = [A_1 + A_2 \exp(i\delta\varphi)]^2 \qquad \textbf{Eq. 2.31}$$

When more than two waves are present equation 2.31 becomes:

$$I = \left[\sum_j A_j \exp(i\varphi_j)\right]^2 \qquad \textbf{Eq. 2.32}$$

Where the sum is over all the sine waves and the phases φ_j are measured with respect to some origin. The acquisition of a powder diffraction pattern involves the measurement of the intensity of X-rays scattered from electrons bound to atoms. The waves scattered by the atoms at different positions are detected with a relative phase shift. It is this property that enables analysis of measured intensities to give information of relative atomic positions. The application of Bragg's law allows one to access the structural information by describing X-ray diffraction in terms of a reflection of X-rays by sets of lattice planes.

2.2.1 Bragg's Law

Bragg's law regards crystals as being built up from layers or planes acting as a semi-transparent mirror.

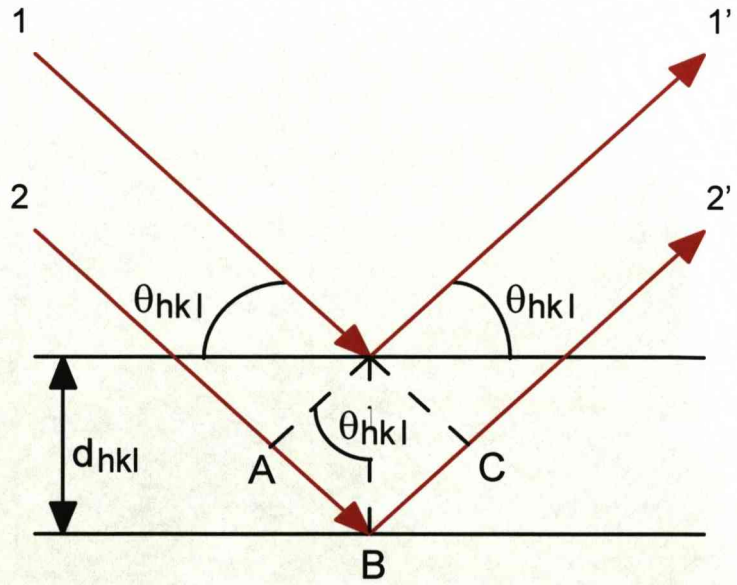

Figure 2.16. Simplified example of X-ray diffraction resulting in reflections at a particular angle, θ.

From figure 2.16 the two X-ray beams are in phase at a particular angle θ. The first beam is reflected at an angle of θ_{hkl}, the second beam with the same angle of incidence reflecting from the second plane has to travel the distance of ABC further than the first to remain in phase. For constructive interference the distance ABC must be equal to a whole number of wavelengths which is related to the distance between pairs of adjacent planes. The d_{hkl}-spacing and the angle of incidence or Bragg angle, θ_{hkl} are given by the following equations.

$$AB = BC = d_{hkl} \sin \theta_{hkl} \qquad \textbf{Eq 2.28}$$

For constructive interference the following condition must be met:

$$ABC = n\lambda \qquad \textbf{Eq 2.29}$$

Therefore:

$$2d_{hkl} \sin \theta_{hkl} = n\lambda \quad \text{Bragg's Law} \quad \textbf{Eq 2.30}$$

When Bragg's law is satisfied the reflected beams are in phase and interfere constructively and at angles other than the Bragg angle the beams are out of phase and interfere destructively thus cancel out. Bragg's angles for real crystal systems with thousands of planes are accurate to within a few tenths of a degree. The reflections observed on x-ray patterns are generally indexed according to the plane at which they diffract with the planes being labelled using Miller indices (100), (110), (111) *etc.* However, depending on the crystal structure some geometries have systematic absences of reflections and this is simply because the beams interfere destructively along the particular plane (Fig 3.17).

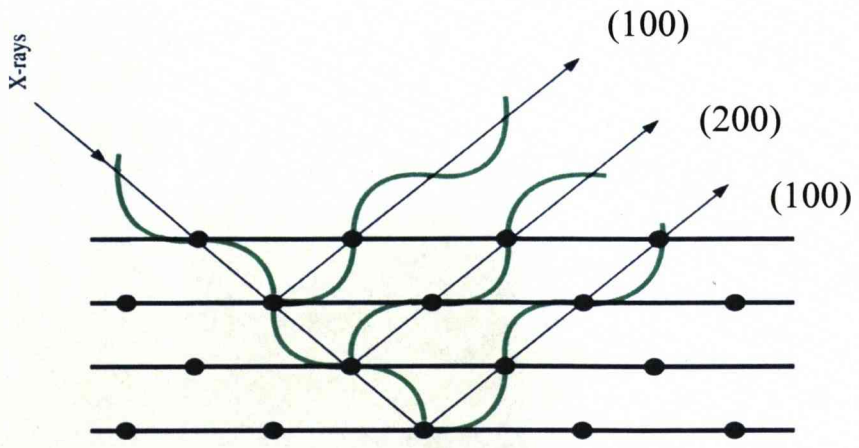

Figure 2.17. X-ray diffraction of (200) planes of a fcc structure, the (100) are out of phase with the (200) plane thus destructive interference occurs and the (100) reflection is not observed.

The presence of systematic absences due to constructive and destructive interference enabled the identification of different silica mesophases. MCM-41 is a hexagonal structure belonging to the Laue class P6mm symmetries where (100), (110) and (200) reflections interfere constructively. However, MCM-48 is a cubic phase belonging to the Laue class Im3m with (211) and (220) reflections being observed with the absence of a (100) reflection due to destructive interference (fig. 2.18).[8]

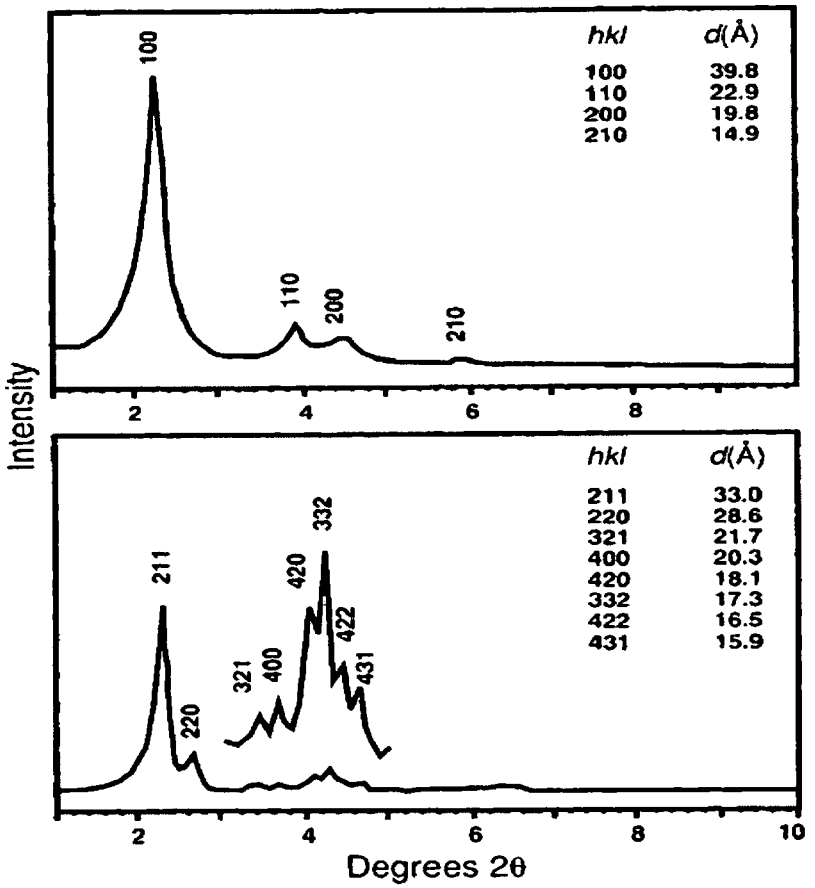

Figure 2.18. Powder XRD patterns of the hexagonal MCM-41 (top) and the cubic MCM-48 mesophase (bottom).[8]

2.3 Nitrogen adsorption isotherm analysis

Nitrogen adsorption at 77 K (boiling point of N_2) is a technique used in the characterization of catalysts because information obtainable such as surface area and porous texture is highly important for understanding the catalytic activity. Adsorption isotherms are obtained by absorbing nitrogen onto a samples surface and measuring the volume absorbed plotted against its relative pressure. The shape of an isotherm is highly dependent on the porous nature of the material under investigation. According to IUPAC, six types of isotherms are possible with only four being common in catalysis characterization.

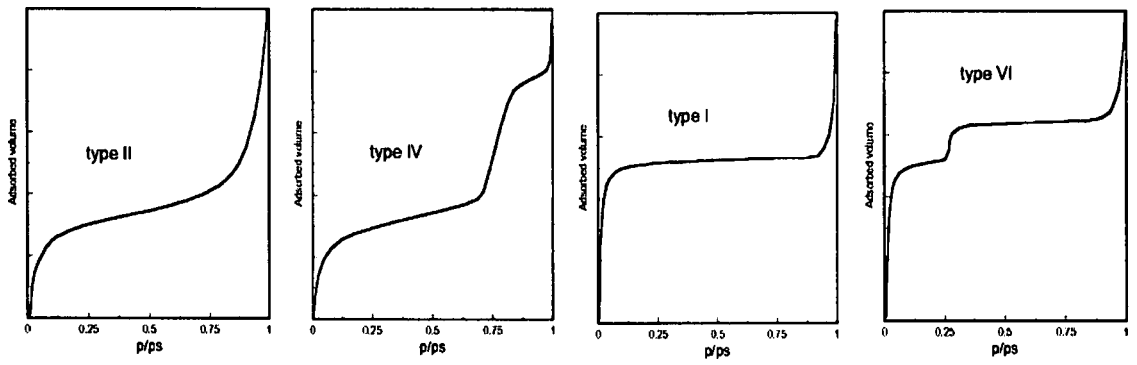

Figure 2.18. Nitrogen adsorption isotherms commonly observed in catalysts characterisation.

Type II isotherms are observed for macroporous solids. The initial increase in adsorption at low relative pressure is due to the formation of a monolayer of adsorbed molecules. The sharp increase in adsorption at high relative pressure is due to multilayer adsorption and increases until condensation pressure is reached. Although this is a general case, the mono- and multilayer processes are always overlapped but the relative pressure at which they takes place is unique to the sample depending on the strength of interactions between adsorbate and adsorbent.[175]

Type IV isotherms are associated with mesoporous solids and at low relative pressure follow the same path as for macroporous solids. The process at high relative pressure is due to multilayer adsorption in the mesopores until capillary condensation is reached at which time a sharp increase in adsorption is observed. This process occurs at lower relative pressure *c.f.* to macroporous solids because of the formation of a curved liquid-like meniscus within the pores of a particular size and shape. The relationship between the relative

pressure at which condensation occurs and the curvature of the meniscus is explained by the Kelvin equation (eq 2.31).

$$r_k = \frac{2\sigma V_l}{RT\ln(p/p_0)} \quad \textbf{Eq 2.31}$$

Where r_k = Kelvin radius (curvature radius), σ = Surface tension of the liquid condensate and V_l = Molar volume.

As the mesopores are filled, adsorption continues on the external surface of the material.

Microporous solids display type I isotherms with the adsorption taking place at very low relative pressure due to strong interactions between the adsorbate and the pore walls. The filling of the pore walls is completed at slightly higher pressure because of interactions between adsorbed molecules. After the micropores are filled adsorption continues on the external surface in a similar fashion to the mesoporous materials.

Type VI isotherms are common for uniform ultramicroporous materials with two energetically different sites with the position of the adsorption step being dependent on the material. Zeolites with high crystallinity do give isotherms of this shape. for example, Zeolite X where the step corresponds to cavity filling.

2.3.1 Desorption Hystereses in Porous materials

Once saturation of a porous material has been reached, evaporation takes place at lower pressure than that of capillary condensation resulting in a hysteresis loop. This is due to pore shape with four main types of hystereses being recognised by IUPAC classifications (fig 2.19).

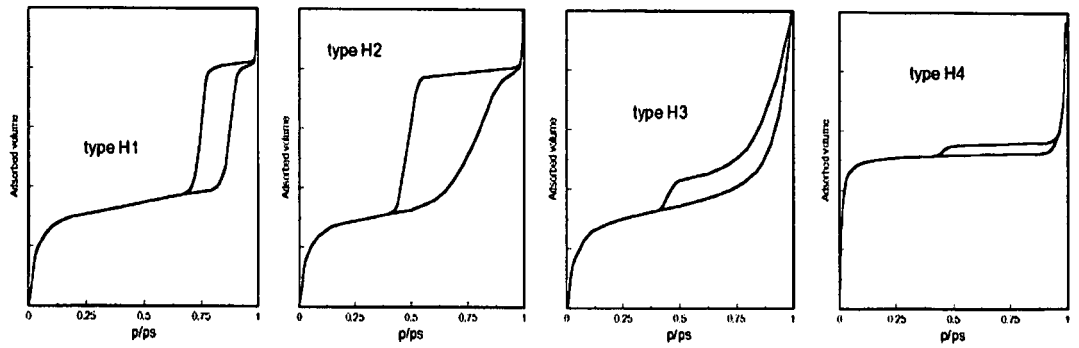

Figure 2.19. The four main types of hystereses observed for nitrogen adsorption-desorption.

Type H1 (pores of a uniform size and shape) and H2 (pores of a non-uniform size and shape) hystereses are characteristic of materials consisting of particles crossed by cylindrical channels or by aggregates or agglomerates of spheroidal particles. The hysteresis is attributed to different sizes in the pore opening and pore channels. Type H1 hysteresis is common in mesoporous molecular sieves such as MCM-41 and PMO-type materials.

Type H3 (non-uniform size or shape) and H4 (uniform size or shape) hystereses are common for aggregates of particles forming slit shaped pores such as clay type materials or zeolites. The hysteresis is observed because, during adsorption of pores formed by parallel plates, the meniscus is flat. Whereas during desorption the meniscus is cylindrical.

2.3.2 Surface Area Determination of Porous Materials

The Brunauer, Emmet and Teller (BET)[176] method for surface area determination is widely used in the characterisation of porous solids such as, zeolites, mesoporous silicas, MOFs, COFs and conjugated microporous polymers. The monolayer coverage and surface area is determined using:

$$A_s = (V_m / 22414) N_a \sigma \quad \textbf{Eq 2.32}$$

Where A_s = Surface area, V_m = Monolayer volume, N_a = Avogadro number and σ = area covered by one nitrogen molecule (accepted value is 0.162 nm^2).

The monolayer volume is estimated by three parameters of the BET equation (eq 2.33) which are:

i) The adsorbed volume, V_{ads} is dependent on the relative pressure, p/p_s.

ii) The c parameter related to heat of adsorption and liquefaction.

iii) A parameter n which relates to the mean number of layers that can be formed on the surface of a material.

$$V_{ads} = V_m \frac{cp/p_s}{1-p/p_s} \frac{1-(n+1)(p/p_s)^n + n(p/p_s)^{n+1}}{1+(c-1)(p/p_s)-c(p/p_s)^{n+1}} \quad \textbf{Eq 2.33}$$

The equation can be simplified in the assumption of $n \rightarrow \infty$ is applied thus a two parameter equation is used.

$$V_{ads} = V_m \frac{cp/p_s}{(1-p/p_s)(1+(c-1)p/p_s)} \quad \textbf{Eq 2.34}$$

Assumptions made with the BET method include: i) the heat of adsorption of the first monolayer is constant; ii) the lateral interaction of adsorbed molecules is negligible; iii) the adsorbed molecules can act as a new adsorption surface and iv) the heat of adsorption of all monolayers is the same apart from the first. Limitations of the BET model include that only reliable results are obtained in the partial pressure range of 0.05 to 0.3 due to other influences on gas adsorption at higher pressures. These include capillary condensation and saturation of the porous network.

Other methods used besides BET include the *t*-plot method which takes into account that for a variety of porous solids the adsorbed volume for unit surface (i.e. statistical thickness of the adsorbed layer) against pressure follows a single curve independent of the material. The curve is able to distinguish between non-porous, mesoporous and microporous materials (Fig 2.20). The *t*-plot method is used alongside the BET method to assist in determining the presence of a hierarchical structure possessing micro-meso porosity.

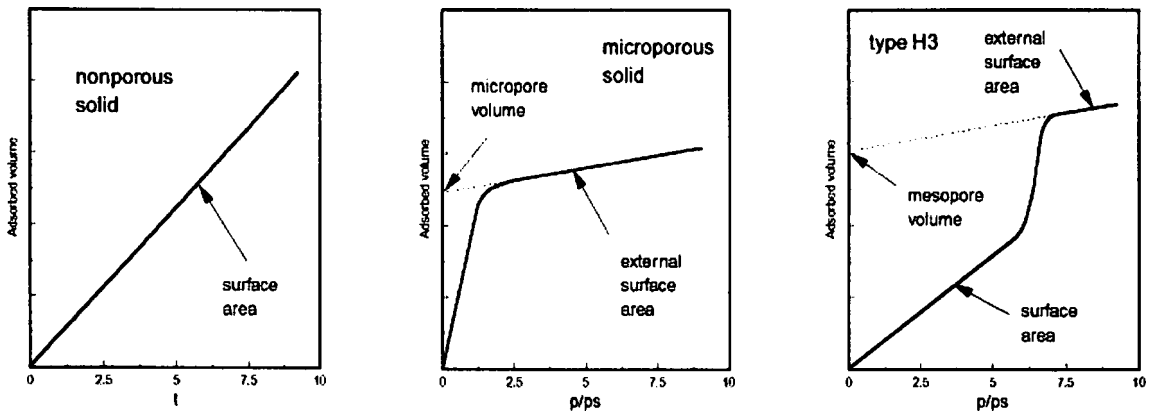

Figure 2.20. *t*-Plots of adsorption isotherms of different classes of material.

The determination of pore volumes and diameters can be performed from the N_2 adsorption-desorption isotherms of mesoporous materials and are essentially based upon the Kelvin equation (Eq. 2.31). There are several methodologies proposed within the literature such as Barrett, Joyner and Halenda (BJH method),[177,178] Pierce,[179] Cranston and Inkley,[180] Broekhof and DeBoer[181,182] *etc.* All the various models have advantages and disadvantages however, the BJH method is the most widely used for mesoporous solids and described below.

The BJH model is applied in the capillary condensation region (p/p_s>0.4). Thus each pressure increase causes an increase in the thickness of the layer adsorbed on the pore walls.

The onset of capillary condensation in the pores still results in an empty core at the centre of the pore of size r_c (fig. 2.21) defined by the Kelvin equation in the form:

$$\ln(p/p_s) = -(2\gamma w_m \cos\theta)/(RTr_c) \qquad \textbf{Eq. 2.35}$$

The assumption of either cylindrical or slit pore geometry allows the calculation of the contributions of the thickness of the adsorbed film to the total adsorption and then subsequently the core volume. From these values the core volume and size are transformed into the pore volume and size respectively. If the calculation is performed in the partial pressure range of 0.4 to 0.98 a mesopore volume and size distribution is obtained.

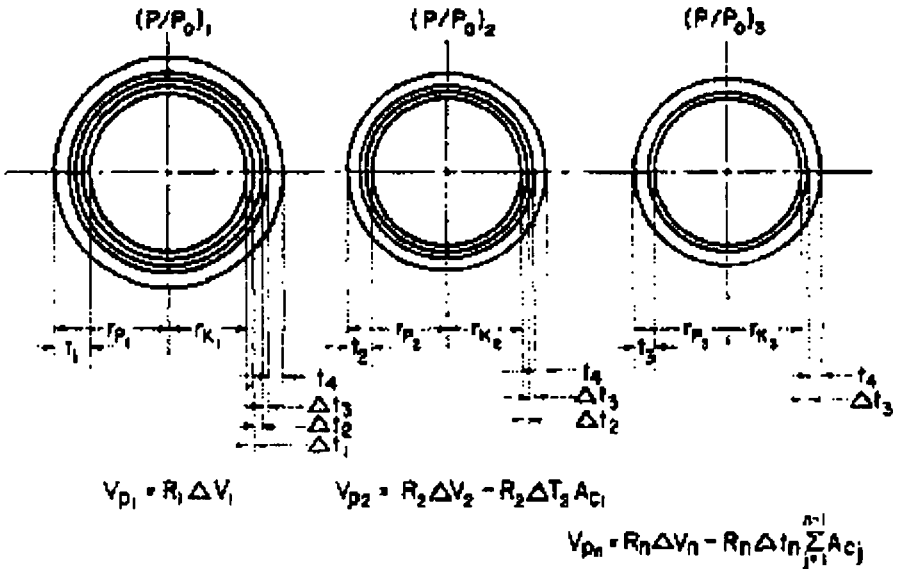

Figure 2.21. Schematic representation of assumed desorption mechanism showing three different pores and demonstrating the thinning of the physically adsorbed layer over the first three pressure increments (Figure taken from the original Barrett *et al.*[178] publication).

Experimental Section

Chapter 3

3 Experimental Part

3.1 Materials

All starting materials were used as received without further purification: organosilica precursors, 1,2-bis(triethoxysilyl)ethylene (BTSEY 80% trans isomer, 95%, Gelest), 1,2-bis(triethoxysilyl)ethane (BTSE, 99%, Aldrich), 1,4-(triethoxysilyl)benzene (BTSB, 95%, Gelest), Pluronic P123 ($M_w \approx 5800$), Octadecyltrimethylammonium Bromide (ODTABr, 98%, Aldrich), Aluminium isopropoxide ($Al^{i}(OC_3H_7)_3$, 98%, Aldrich), sodium chloride (NaCl), sodium Hydroxide (NaOH, 98%), hydrochloric acid (36 % wt.), Butanol and ethanol (98%) all from Aldrich.

3.2 Synthesis of -CH=CH-PMOs, Chapter 4

In a typical synthesis of a -CH=CH-PMO P123 (0.300 g) and NaCl (0.318 g) were dissolved in DDI water (10.53 ml), 36 % wt. $HCl_{(aq)}$ (0.57 ml) and stirred until homogenous at 40°C. The silica precursor BTSEY (0.528 ml) was added to the surfactant/acid/butanol mixture and stirred vigorously for 24 hours at 40°C. The resulting white suspension was then placed in an autoclave at 90°C for 24 hours. The products were recovered by vacuum filtration, washed sequentially with DDI water and ethanol and dried at 100°C. The final composition of the synthesis mixtures was 1 BTSEY: 0.034 P123: 3.65 HCl: 3.66 NaCl: 2.52 BuOH: 390 H_2O.

The organic template was removed by acid extraction. Typically 0.3 g of as-synthesised material was stirred in 100 ml of 1M HCl/EtOH at 50°C for 24 hours. The suspension was cooled, vacuum filtered and the resulting white solid was washed using DDI water and EtOH, and then dried at 100 °C for 24 hours.

After template removal the -CH=CH-PMO was thermally treated at 380°C for 10 h under vacuum. Bromination of the ethylene bonds was carried out using a standard literature procedure.[183] All post synthetic modifications were carried out by the research group of Prof. P. Van Der Voort (University of Gent, Belgium)

3.3 Synthesis of -CH_2CH_2-/-CH=CH-PMOs, chapter 5

In a typical synthesis of a -CH_2CH_2-/-CH=CH-PMO P123 (0.349 g) and NaCl (1.05 g) were dissolved in DDI water (3.0 ml) with a set amount of 2M $HCl_{(aq)}$ (to give a total of 9 ml after the addition of the pre-hydrolysis mixture) and stirred until homogenous at 40°C. The silica precursors BTSE (0.347 ml) and BTSEY (0.341 ml) were pre-hydrolyzed either jointly or separately in a set amount of ethanol, 2M $HCl_{(aq)}$ and time (summarised in Table 3.1) under stirring at room temperature. After the pre-hydrolysis the silica solutions were added to the acid/surfactant mixture and stirred vigorously for 24 hours at 40°C. The resulting white suspension was then placed in an autoclave at 80°C for 24 hours. The products were recovered by vacuum filtration, washed sequentially with DDI water and ethanol and dried at 100°C. The final composition of the synthesis mixtures was 0.5 BTSE: 0.5 BTSEY: 0.032 P123: 9.6 HCl: 9.6 NaCl: 344 H_2O.[87]

The organic template was removed by acid extraction. Typically 0.3 g of as-synthesized material was stirred in 100 ml of 1M HCl/EtOH at 50°C for 24 hours. The suspension was cooled, vacuum filtered with the resulting white solid was washed using DDI water and EtOH, and then dried at 100 °C for 24 hours.

In total 33 products were synthesized: 16 prepared using joint silica precursor pre-hydrolysis, 16 prepared using separate silica precursor pre-hydrolysis and one material prepared using no pre-hydrolysis to act as a reference. Other synthetic variables were ethanol content, silica/water ratio and time for the pre-hydrolysis step. The products are labelled accordingly to their pre-hydrolysis conditions, A-PMO-X-Y-Z where A = J (joint pre-hydrolysis) or S (separate pre-hydrolysis), X = 0.18, 0.24, 0.36 or 0.72 indicating Si/EtOH ratio, Y = 14 or 2.6 the Si/HCl ratio and Z = 30 or 60 minutes (pre-hydrolysis time). For example S-PMO-0.18-2.6-30 means separate pre-hydrolysis was used with Si/EtOH = 0.18, Si/HCl = 2.6 and pre-hydrolyzed for 30 minutes prior to addition to the acid/ surfactant solution.

Table 3.1. Summary of the pre-hydrolysis compositions for joint and separate pre-hydrolysis synthesis mixtures.

Sample	Si/EtOH	Si/HCl[†]	Time (min)
J/S-PMO-0.18-2.6-30	0.18	2.61	30
J/S-PMO-0.18-2.6-60	0.18	2.61	60
J/S-PMO-0.18-14-30	0.18	14.1	30
J/S-PMO-0.18-14-60	0.18	14.1	60
J/S-PMO-0.24-2.6-30	0.24	2.61	30
J/S-PMO-0.24-2.6-60	0.24	2.61	60
J/S-PMO-0.24-14-30	0.24	14.1	30
J/S-PMO-0.24-14-60	0.24	14.1	60
J/S-PMO-0.36-2.6-30	0.36	2.61	30
J/S-PMO-0.36-2.6-60	0.36	2.61	60
J/S-PMO-0.36-14-30	0.36	14.1	30
J/S-PMO-0.36-14-60	0.36	14.1	60
J/S-PMO-0.72-2.6-30	0.72	2.61	30
J/S-PMO-0.72-2.6-60	0.72	2.61	60
J/S-PMO-0.72-14-30	0.72	14.1	30
J/S-PMO-0.72-14-60	0.72	14.1	60

3.4 Synthesis of -CH_2CH_2-/-C_6H_4-PMOs, Chapter 6

3.4.1 Base Catalyzed cationic templated PMOs

The base catalysed PMO materials have been synthesised using Octadecyltrimethyl ammonium Bromide in an aqueous medium in the presence of Sodium hydroxide. The molar ratio of two silica precursors in the initial synthesis mixture is 1:1.

In a typical synthesis Octadecyltrimethylammonium Bromide (0.40 g) was dissolved in DDI water (6.75 g) and sodium hydroxide (1M aqueous solution, 4.50 ml) at 40 °C. When the solution became homogeneous, BTSE (0.347 ml) and/or BTSB (0.377 ml) in 1.2 ml of ethanol was added to the template solution and the mixture was stirred for 24 hours at 40°C. All resulting white suspensions were placed in the oven at 80°C for 4 days and then the solid products were recovered by vacuum filtration after cooling to ambient temperature. For the pre-hydrolysis materials 8 products were prepared (Table 3.2). The overall molar ratio for the synthesis mixture was as follows: 0.57 ODTABr: 0.5 BTSE: 0.5 BTSB: 2.5 NaOH: 347.5 H_2O. Three reference materials were synthesised for comparison: 1st a -CH_2CH_2-/-C_6H_4-PMO prepared without pre-hydrolysis, second a -CH_2CH_2-PMO and thirdly a -C_6H_4-PMO.

Table 3.2. Composition of pre-hydrolysis mixtures.

Sample	Si/EtOH	Si/NaOH	Time (min)
J/S-PMO-2.6-30	0.18	2.61	30
J/S-PMO-2.6-60	0.18	2.61	60
J/S-PMO-14-30	0.18	14.1	30
J/S-PMO-14-60	0.18	14.1	60

3.4.2 Acid Catalyzed block-copolymer templated PMOs

Acid catalysed PMOs have been synthesised using P123 and sodium chloride in aqueous acidic conditions (HCl). The initial ratio of the two organic bridges in the synthesis mixture is 1:1.

In a typical synthesis P123 (0.349 g) and NaCl (1.05 g) were dissolved in DDI H_2O (3 mL) and an appropriate amount of acid to give a total of 9 mL after addition of the pre-hydrolysis mixtures under stirring at 40°C. The two silica precursors BTSE (0.347 mL) and BTSB (0.377 mL) were subjected to either joint or separate pre-hydrolysis protocols as

summarized in table 2. After pre-hydrolysis the silicon/EtOH/HCl mixtures were added to the surfactant solution and stirring continued for an additional 24 hours at 40°C. The resulting white suspensions were then placed in an autoclave at 80°C for further 24 hours. The white precipitate was collected *via* vacuum filtration after cooling, washed with DDI water and then dried at 100°C. The template was extracted using 1M HCl/EtOH solution. In a typical procedure 0.3 g of as–synthesised PMO was placed in 100 mL of 1M HCl/EtOH and stirred at 50°C for 24 hours. Subsequently, the resulting suspension was cooled, filtered and washed with DDI water. In total 8 samples were prepared using pre-hydrolysis protocols, 1 bi-functional sample made without pre-hydrolysis and 2 mono-functional PMOs to act as references.

Table 3.3. Composition of pre-hydrolysis mixtures.

Sample	Si/EtOH	Si/HCl	Time (min)
J/S-PMO-2.6-30	0.12	2.61	30
J/S-PMO-2.6-60	0.12	2.61	60
J/S-PMO-14-30	0.12	14.1	30
J/S-PMO-14-60	0.12	14.1	60

All standard samples are labelled according to the organic functionalities incorporated. The pre-hydrolysed PMOs are all labelled according to their pre-hydrolysis conditions as shown in tables 1 and 2 and the templating pathway is indicated in the figure captions.

3.5 Synthesis of Al-/-CH_2CH_2-/-CH=CH-PMOs, chapter 7

In a typical synthesis Octadecyltrimethyl ammonium Bromide (0.633 g) was dissolved in DDI water (11.36 ml) and 1M NaOH (6.71 ml) at 40 °C. When the solution became homogenous a solution of BTSE (0.526 ml), BTSEY (0.524 ml), Aluminium isopropoxide (0.058 g) and ethanol (1.2 ml) was added to the template solution and stirred at 40°C for 24 hours. The resulting white suspension was placed in the oven at 95°C for 4 days and then the solid products were recovered by vacuum filtration after cooling to ambient temperature. The product was washed sequentially with deionised water and ethanol, and dried at *ca.* 70°C. The final molar composition of synthesis mixture was 0.5 BTSE: 0.5 BTSEY: 0.56 ODTABr: 347.56 H_2O: 2NaOH: $0.1Al_{ISO}$. The organic template was removed by solvent extraction. Typically, *ca.* 0.5 g of as-synthesised solid was added to 50 ml of $18.8x10^{-3}$M HCl/EtOH and stirred for 4 hours at 50°C. The resulting white product was cooled to room temperature, vacuum filtered and dried at 100 °C. The process was repeated three times to ensure near complete template removal. Bi-functional -CH_2CH_2-/-CH=CH-PMOs were synthesized using the same procedure with the omission of the Al source and the template extraction procedure used a 1M HCl/EtOH solution as described above.

The application of silicon and aluminium precursor pre-hydrolysis was also used to see if it was possible to influence the distribution of aluminium within the mesoporous framework. The Si/NaOH ratio was 14.1 along with the Si/EtOH = 0.18 with the conditions summarised in table 3.4. Joint pre-hydrolysis involved combining all 3 precursors (BTSE, BTSEY and $Al(^iOC_7H_5)_3$) in a solution of EtOH/NaOH and stirring at room temperature for 30 or 60 minutes prior to addition to the organic template solution. Whereas, the separate pre-hydrolysis conditions involved combining the aluminium precursor with either BTSE or BTSEY in one vial and the pristine silicon precursor in another. After 30 or 60 minutes both reaction mixtures are then stirred into the template solution. The final molar gel composition was kept constant irrespective of pre-hydrolysis conditions.

Two reference PMOs prepared without pre-hydrolysis are labelled as follows; Al-CH_2CH_2-/-CH=CH-PMO corresponding to a tri-functional PMO with an Si/Al = 5 and -CH_2CH_2-/-CH=CH-PMO corresponding to a bifunctional PMO synthesized in the absence of aluminium.

Table 3.4. Summary of pre-hydrolysis conditions and their corresponding sample names.

Sample	Si/Al	Time (min)
J-PMO-0-30	0	30
J-PMO-0-60	0	60
J-PMO-5-30	5	30
J-PMO-5-60	5	60
S-PMO-0-30	0	30
S-PMO-0-60	0	60
S-PMO-5-30 (-CH_2CH_2- + Al)	5	30
S-PMO-5-60 (-CH_2CH_2- + Al)	5	60
S-PMO-5-30 (-CH=CH- + Al)	5	30
S-PMO-5-60 (-CH=CH- + Al)	5	60

3.6 Characterisation conditions

3.6.1 Powder X-ray Diffraction

Powder X-ray diffraction (PXRD) patterns were measured using a Panalytical X-pert pro diffractometer with Co-$K_{\alpha 1}$ radiation with a wavelength λ = 1.789 Å. Patterns were recorded in Bragg-Brentano reflection geometry and measured in the 0.7 - 5.0, 1.2 - 8 and 10 - 40 2θ ranges, depending on the sample, using a flat bracket sample holder.

3.6.2 Nitrogen adsorption

Nitrogen adsorption-desorption isotherms were measured on a Micromeritics ASAP2420 system at -196°C. The samples were dried and evacuated for 5 hours at 120°C before analysis. The specific surface area was calculated using BET method using linear plot over a range of p/p_o = 0.06–0.20. The pore size distribution was calculated using the adsorption branch of the isotherm using Barrett-Joyner-Halenda (BJH) method. Pore volume was calculated from the amount of adsorbed nitrogen at p/p_o = 0.99. Micropore volume and surface areas were obtained from the t-plot method using Harkins-Jura reference isotherm ($t = (13.99/(0.034 - \log p/p_s))^{1/2}$).

3.6.3 Electron Microscopy

Samples for transmission electron microscopy (TEM) were prepared by grinding the powder in alcohol and a drop of the suspension was deposited onto a holey carbon film, supported by a copper grid. High-resolution electron microscopy (HREM) was performed using a JEOL 2011 microscope with a lab filament and a point resolution of 1.8 Å (acceleration voltage = 200kV).

3.6.4 Solid-State NMR

All Solid-state NMR experiments were conducted at 9.4 T using a Bruker DSX-400 spectrometer operating at 79.49, 100.61, 104.26 and 400.13 MHz for ^{29}Si, ^{13}C, ^{27}Al and ^{1}H respectively. All chemical shifts are quoted in ppm from external TMS with the exception of ^{27}Al which is quated in ppm from 1M $[Al(H_2O)_6]^{3+}$. Samples were spun in zirconia rotors driven by N_2 gas using either a 4 mm $^{1}H/X/Y$ or 2.5 mm $^{1}H/^{19}F/X$ commercial probeheads.

3.6.4.1 One dimensional magic angle spinning (MAS).

All one dimensional MAS NMR experiments were acquired using a simple pulse acquire program displayed in figure 3.1.

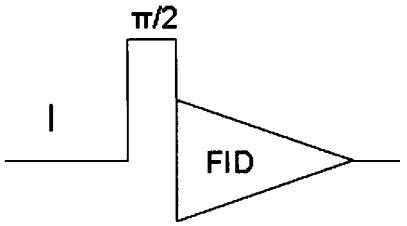

Figure 3.1. Symbolic representation of the pulse acquire MAS experiment.

- **^{1}H MAS NMR** spectra were acquired using a ^{1}H $\pi/2$ pulse length of 2.8 μs at a MAS rate of 30.0 kHz and a recycle delay of 15 s.
- **^{29}Si MAS NMR** spectra were acquired with a ^{29}Si $\pi/3$ pulse length of 2.3 μs at a MAS rate of 4.0 kHz and a recycle delay of 240 s without proton decoupling during acquisition.
- **^{27}Al MAS NMR** spectra were acquired using a ^{27}Al $\pi/10$ pulse length of 0.4 μs at a MAS rate of 10.0 kHz and a recycle delay of 1.0 s. The ^{27}Al Chemical shifts are quoted in ppm from external 1M $[Al(H_2O)_6]^{3+}$. All ^{27}Al MAS NMR spectra were acquired for 2048 scans in order to obtain quantitative information between different samples.
- **$^{13}C\{^{1}H\}$ MAS NMR** spectra were acquired using a ^{13}C $\pi/3$ pulse length of 2.6 μs at a MAS rate of 10.0 kHz and a recycle delay of 20 s with proton decoupling during acquisition.

3.6.4.2 ^{1}H-X Cross Polarisation Magic Angle Spinning (CP/MAS)

All CP/MAS NMR experiments were conducted using ramp amplitude implemented on the ^{1}H channel during the contact step (Fig. 3.2). Two pulse phase modulation (TPPM) heteronuclear dipolar decoupling with 15° phase difference between the two pulses was used during acquisition.

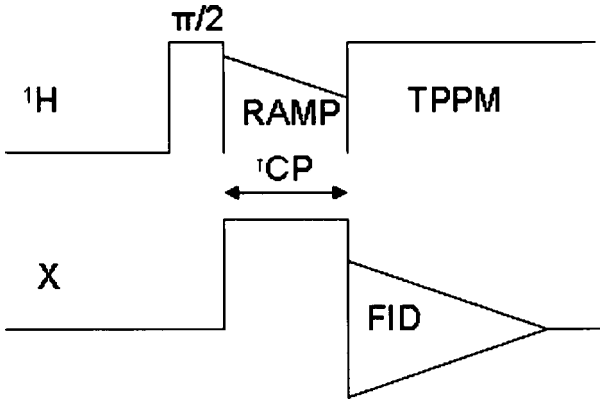

Figure 3.2. ^{1}H-X CP/MAS pulse program, where X refers to ^{13}C, ^{29}Si or ^{27}Al.

- **^{1}H-^{13}C CP/MAS NMR** spectra were acquired at a MAS rate of 8.0 kHz. A ^{1}H π/2 pulse length was 3.0 μs and the recycle delay was 8.0 s was used during acquisition. The CP contact time was 1.0 ms with the Hartman–Hahn matching condition set using Hexamethylbenzene (HMB). ^{1}H-^{13}C Variable Contact Time (VCT) CP/MAS NMR spectra were acquired using contact times in the range of 0.01 to 16.0 ms.
- **^{1}H-^{29}Si CP/MAS NMR** spectra were acquired at a MAS rate of 4.0 kHz. A ^{1}H π/2 pulse length of 3.1 μs and the recycle delay of 10 s was used during acquisition. The CP contact time was 2.0 ms with the Hartmann–Hahn matching condition set using kaolinite. The ^{1}H-^{29}Si VCT/CP MAS NMR measurements used contact times ranging from 0.05 to 16.0 ms.
- **^{1}H-^{27}Al CP/MAS NMR** spectra were acquired at a MAS rate of 10 kHz. The ^{1}H π/2 pulse length was 2.8 μs and the recycle delay was 5.0 s. The CP contact time was 2.0 ms with the Hartman-Hahn matching condition set using Gibbsite. The position of the ^{27}Al resonances is quoted in ppm with respect to $[Al(H_2O)_6]^{3+}$.

N.B. The ^{1}H-^{13}C CP/MAS NMR obtained for the microporous polymers discussed in chapter 8 were run at a MAS rate of 10 kHz and a contact time of 2 ms.

3.6.4.3 Two dimensional ^{1}H-^{13}C wideline separation (WISE)[184]

Two dimensional ^{1}H-^{13}C WISE NMR spectra were collected using a similar pulse sequence to that of CP/MAS (previous). However, between the initial ^{1}H excitation pulse and CP step a delay is implemented whereby the transverse proton magnetisation is allowed to evolve after which CP transfer and ^{13}C spectrum is obtained (Fig. 3.3). The pulse sequence results in a 2D dataset whereby a ^{1}H spectrum is obtained in the indirect t_1 dimension which is correlated to a ^{13}C spectrum in the direct t_2 dimension.

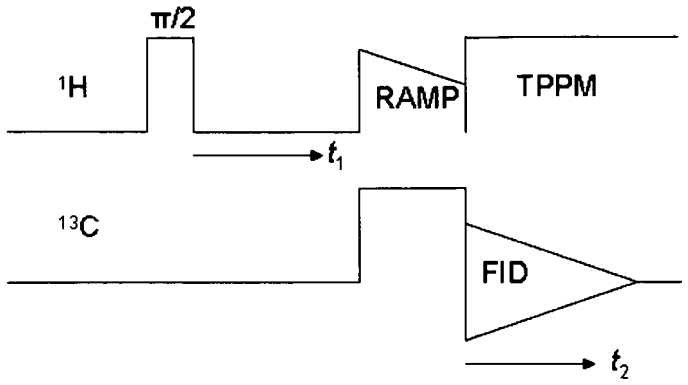

Figure 3.3. Symbolic representation of the WISE pulse program.

2D ^{1}H-^{13}C WIdeline SEparation (WISE) MAS NMR spectra were acquired at a MAS rate of 8 kHz. The ^{1}H $\pi/2$ pulse length was 3.1 μs TPPM decoupling with a rf field strength of 84.7 kHz was used during the acquisition in t_2. The Hartmann-Hahn condition was set using HMB. A fixed contact time of 80 μs was used to limit the effect of spin diffusion. Longer contact times would lead to an equilibration of the proton magnetization due to spin diffusion, and consequently to the same proton lineshape for all carbon sites.[185] States-TPPI for phase-sensitive detection in the indirect dimension was implemented to recover pure absorption lineshape. The recycle time was fixed to 2 s. 256 increments were recorded in t_1 corresponding to a dwell time of 16.7 μs at a spectral width of 59880.238 Hz. 496 transients were acquired per t_1 increment in the direct dimension.

3.6.4.4 Two dimensional ^{1}H-X Heteronuclear Correlation (HETCOR)

2D ^{1}H-X HETCOR NMR is a technique that correlates the ^{1}H chemical shifts recorded in the indirect dimension to the X nuclei chemical shifts in the direct dimension. The pulse sequence is similar to that of the WISE experiment (previous). The only difference is that during t_1, the ^{1}H's are decoupled from each other by using a homonuclear dipolar decoupling sequence (Fig. 3.4) thus ^{1}H magnetisation evolves only under the influence of their chemical shift Hamiltonian.

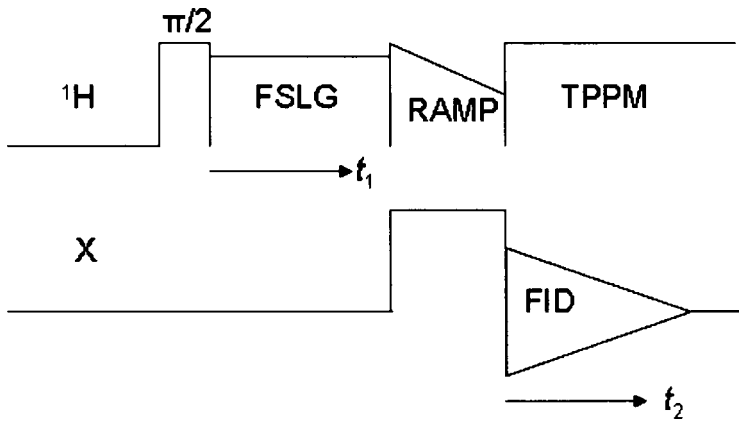

Figure 3.4. Symbolic representation of the HETCOR pulse program

2D ^{1}H-^{29}Si Heteronuclear correlation (HETCOR)[186] MAS NMR spectra were acquired at a MAS rate of 10 kHz. The 2D HETCOR experiments used Frequency-Switched Lee-Goldburg (FSLG)[136,139] homonuclear decoupling with ^{1}H *rf* field of *ca.* 80.6 kHz in t_1 and ramp-amplitude ^{1}H-^{29}Si cross-polarization with a contact time of 2.0 ms. TPPM decoupling was used during acquisition at a decoupling strength of *ca.* 80.6 kHz. The sample volume was restricted to the middle of the rotor to improve the *rf* homogeneity. States-TPPI was employed for phase sensitive detection.[135,187-189] The recycle delay was set at 2.0 s. 256 increments were recorded in t_1 to cover the full ^{1}H spectral width of 23047.920 Hz corresponding to a dwell time of 43.4 μs. 600 scans acquired in t_2 per increment.

2D ^{1}H-^{27}Al HETCOR MAS NMR spectra were acquired at a MAS rate of 10 kHz. The 2D HETCOR experiments used (FSLG) homonuclear decoupling with a ^{1}H *rf* field of approximately 80.6 kHz in t_1 and ramp amplitude ^{1}H-^{27}Al CP with a contact time of 2.0 ms. TPPM decoupling was used during acquisition at a decoupling strength of approximately 80.6 kHz. The sample volume was restricted to the middle of the rotor to improve the *rf* homogeneity. States-TPPI was employed for phase sensitive detection. The recycle delay

was set at 1.5 s. 256 increments were recorded in t_1 to cover the full ^{1}H spectral width of 23047.920 Hz corresponding to a dwell time of 43.4 μs. 800 scans acquired in t_2 per increment.

6.4.4.5 Two dimensional ^{1}H-^{1}H Spin diffusion NMR

2D ^{1}H spin diffusion NMR experiments were used to probe the relative proximity of different proton environments with the porous composites. The ^{1}H spin diffusion NMR experiment is essentially the same as the 2D nuclear Overhauser (NOESY) experiment in solution NMR whereby an initial π/2 pulse creates transverse magnetisation which evolves during t_1. Another π/2 pulse then places the magnetisation along z where it evolves for a fixed time, t_m after which the final π/2 pulse places the magnetisation along the xy plane for detection (Fig. 3.5).

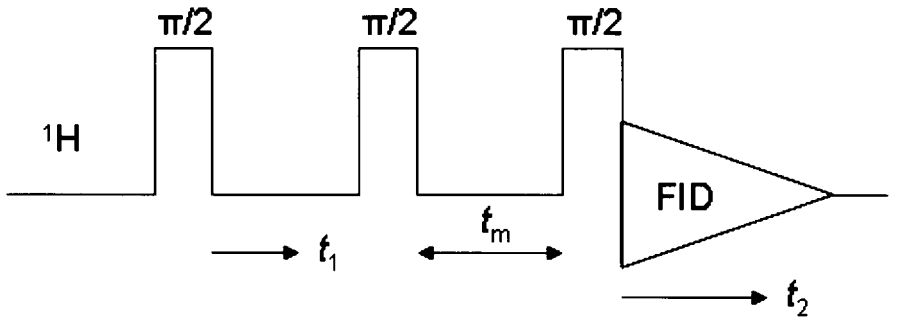

Figure 3.5. Symbolic representation of the ^{1}H spin diffusion pulse program.

2D ^{1}H spin diffusion NMR spectra were recorded at a MAS rate of 30 kHz. The ^{1}H π/2 pulse length was 2.8 μs with a recycle delay of 2 s. States-TPPI was employed for phase sensitive detection. 512 increments were recorded in t_1 to cover the full ^{1}H spectral width of 29940.12 Hz corresponding to a dwell time of 33.4 μs. 16 scans acquired in t_2 per increment. The mixing time t_m was varied between 0.5 - 80 ms.

3.6.5 Data processing

All powder XRD data were processed using PANalytical High Score plus software. Nitrogen adsorption isotherms were analysed using Micromeretics ASAP2020 software. All solid-state NMR spectra were acquired using XWINNMR 3.5 and processed using Bruker Topspin 1.3 software. The CP kinetics curves and deconvolution of spectra were fitted using Origin6.0software.

Synthesis of -CH=CH-PMO and its post synthetic modifications

Chapter 4

4.1 Introduction

The synthesis of -CH=CH- containing PMOs is of great interest due to the reactivity of the unsaturated hydrocarbon group which enables further chemical modification. Such PMOs have been synthesised from a mixture of both *cis*- and *trans*-bis(triethoxysilyl)ethene using quaternary ammonium surfactants under basic conditions[183] and block co-polymers under acidic conditions.[190,191] The synthesis of an all-*trans* -CH=CH-PMO has recently been demonstrated by Van der Voort *et al.*[85] Post synthetic modifications of ethylene PMO *via* bromination as a method for determining the reactivity of the carbon double bond has been reported by Mokaya *et al.*[183]

As the synthesis of PMOs relies on the co-assembly of template micelles and organosilica precursors which undergo hydrolysis and condensation reactions, it is important to know how the template interacts with the hybrid walls. As discussed in chapter 1, template-framework interactions are either H-bonding, ion pairing or electrostatic interactions. The magnitude of these interactions needs to be maximised in order to form a highly ordered PMO. For instance, the addition of inorganic salts *i.e.* NaCl, KCl and Na_2SO_4 into the synthesis of PMOs *via* block co-polymer templating has resulted in the improvement of mesoscopic ordering due to the introduction of ion-pairing along with H-bonding interactions. Studies on template framework interactions in mesoporous solids using solid-state NMR were reported for aluminophosphates and PMOs prepared using cationic templates such as quaternary ammonium salts.[81,192] In both instances the ^{1}H-^{13}C CP/MAS NMR kinetics was used to probe the mobility of the polar head group and aliphatic chains of the template species.

Although the morphology and porosity of -CH=CH-PMO has been studied by various groups, detailed information on their molecular level structure is scarce. Previously, our group reported the application of CP kinetics to -CH=CH-PMOs synthesized *via* cationic templating.[81] However, in non-ionically templated -CH=CH-PMOs the template framework interactions are changed to H-bonding and ion-pairing. Therefore, the molecular structure of such materials would be expected to be different from their cationic templated counterparts and needs to be studied separately.

The aim of this chapter is two-fold. Firstly, the molecular level structure of the –CH=CH-PMO synthesised using block co-polymer templating under acidic conditions was investigated. The template-framework interactions of the as-synthesised PMO were studied

using ^{1}H-^{13}C CP/MAS kinetics and 2D ^{1}H-^{13}C WIdeline SEparation (WISE) NMR. Secondly, the template extracted PMO was subjected to hydrothermal treatment and bromination to induce metamorphosis of the –CH=CH- bond to terminal –CH=CH_2 and -CH(Br)CH(Br)- functionalities respectively. Both post-synthetic modifications were used to generate multifunctional mesoporous organosilicas.

Solid-state NMR was essential is assessing molecular level changes in the composition. The ^{13}C and ^{29}Si CP/MAS kinetics were also used to probe the location of the modified functionalities in the mesoporous framework.

4.2 Results and Discussion

4.2.1 Powder X-Ray Diffraction

PXRD patterns of template extracted –CH=CH-PMO, Br/-CH=CH-PMO (-CH=CH-PMO after bromination) and T/-CH=CH-PMO (-CH=CH-PMO after thermal treatment) (Fig. 4.1) display peaks indexed to (100), (110) and (200) reflections typical of a 2D hexagonal array of pores. The high intensity reflections for the –CH=CH-PMO confirm the presence of a highly ordered mesostructure. The intensity of all reflections is reduced upon bromination and thermal treatment, whereby the –CH=CH-PMO was heated under vacuum for 10 hours at 380 °C (T/-CH=CH-PMO), suggesting a decrease in mesoscopic ordering as a consequence of post-synthetic modification. The d_{100}-spacing increases from 91.7 to 95.6 Å upon bromination. The thermal treatment of -CH=CH-PMO has resulted in a shrinking of the unit cell, commonly observed upon the calcination of the purely siliceous SBA-15 analogue.

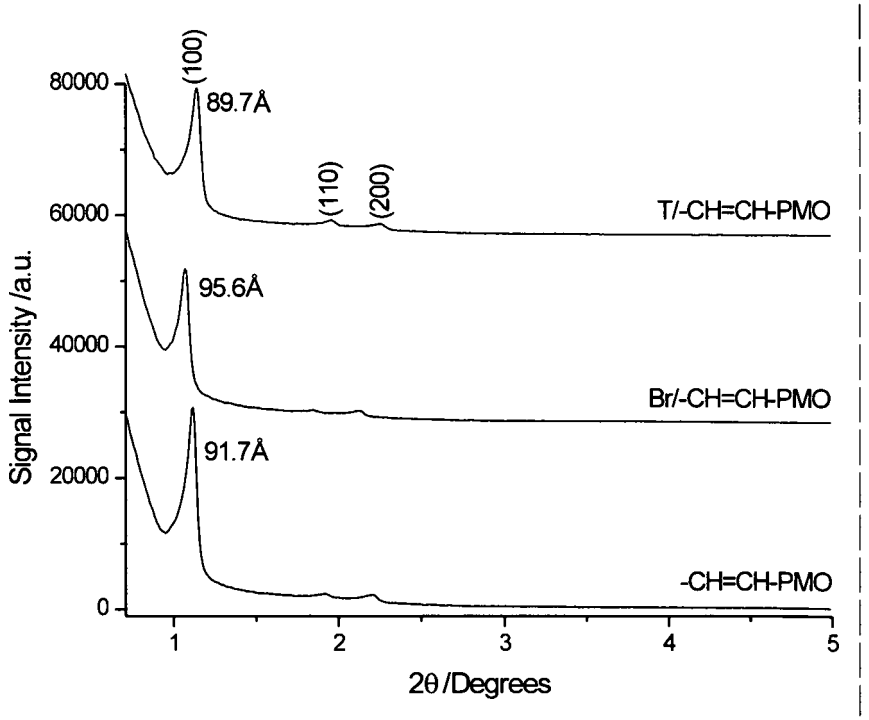

Figure 4.1. PXRD patterns for template-extracted –CH=CH-PMO, Br/-CH=CH-PMO and T/CH=CH-PMO.

4.2.2 N_2 Adsorption-Desorption Isotherms

N_2 adsorption isotherms were used to probe changes in the textural properties of the -CH=CH-PMO upon thermal treatment. The N_2 adsorption-desorption isotherms (Fig. 4.2) of the -CH=CH-, Br/-CH=CH- and T/-CH=CH-PMO display type IV isotherms according to IUPAC classification.[1] The isotherms also show a type H1 hysteresis typical of a material possessing cylindrical and uniform pore network further confirmed by the pore size distribution (PSD) plots (Fig. 4.2).

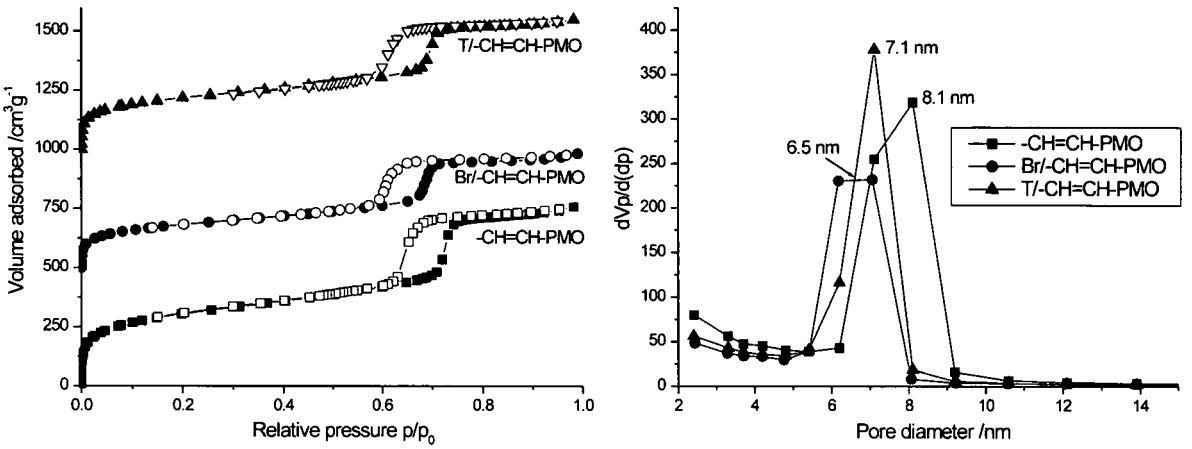

Figure 4.2. N_2 adsorption/desorption isotherms of the template extracted -CH=CH-PMO and T/-CH=CH-PMO (left) and pore size distribution plots (right). (The isotherms are offset by 500 cm^3g^{-1}) (The data were collected in the University of Ghent by the group of Prof. P. Van Der Voort).

The textural properties, summarised in table 4.1, indicate a general decrease in surface area and overall porosity upon thermal treatment. Furthermore, some shrinkage of the pores is visible from the PSD plots consistent with a decrease in pore volume. The decrease in pore diameter is consistent with an overall reduction in the unit cell parameter $\bar{a}$. The Br/-CH=CH-PMO also shows a shrinkage in pore size *c.f.* the –CH=CH-PMO yet displays the thickest pore walls. The changes are related to the addition of bromine within the pore structure which will form a layer of brominated functionalities thus reducing pore diameter and volume, the former of which is used in the calculation of wall thickness.

Both the powder XRD and N_2 adsorption isotherms confirm the presence of well ordered and highly porous PMOs even after the thermal treatment process. However, these

techniques are unable to probe the molecular level changes observed upon post synthetic modifications. Therefore solid-state NMR methodologies, sensitive to changes on the molecular level, were applied.

Table 4.1. Textural properties of -CH=CH- PMOs.

sample	S_{BET} /m^2g^{-1}	V_{ads} /cm^3g^{-1}	V_{micro}* /cm^3g^{-1}	D_{av} /nm	$\bar{a}$ † /nm	W /nm
-CH=CH-PMO	1112	1.17	0.193	8.1	10.6	2.5
Br/-CH=CH-PMO	657	0.62	0.101	6.5	11.0	4.5
T/-CH=CH-PMO	795	0.85	0.113	7.1	10.4	3.3

Pore volumes determined at $P/P_0 = 0.9$.
† Unit cell parameter $\bar{a}$ determined from d_{100} values using $\bar{a} = 2d_{100}/\sqrt{3}$.
W = wall thickness determined from $\bar{a} - D_{av}$.
* Micropore volume determined using the t-plot method.

4.3 Solid State NMR

4.3.1 Composition of PMOs

4.3.1.1 ^{1}H-^{13}C CP/MAS NMR

^{1}H-^{13}C CP/MAS NMR was used to determine the presence of the organic functionalities and template species in the PMOs. The spectrum for the as-synthesised -CH=CH-PMO (Fig. 4.3 bottom) displays a broad resonance at 146.2 ppm attributed to -CH=CH- bridges. The resonance remains unchanged upon surfactant extraction. Other resonances in the spectra of the as-synthesised PMO can be assigned to the pluronic surfactant: the peak at 16.3 ppm corresponds to the $-CH_3$ group of the PPO block; the peak at 70.9 ppm is attributed to PEO blocks; the resonances at 73.6 and 77.5 ppm correspond to CH_2 and CH sites of PPO blocks respectively.

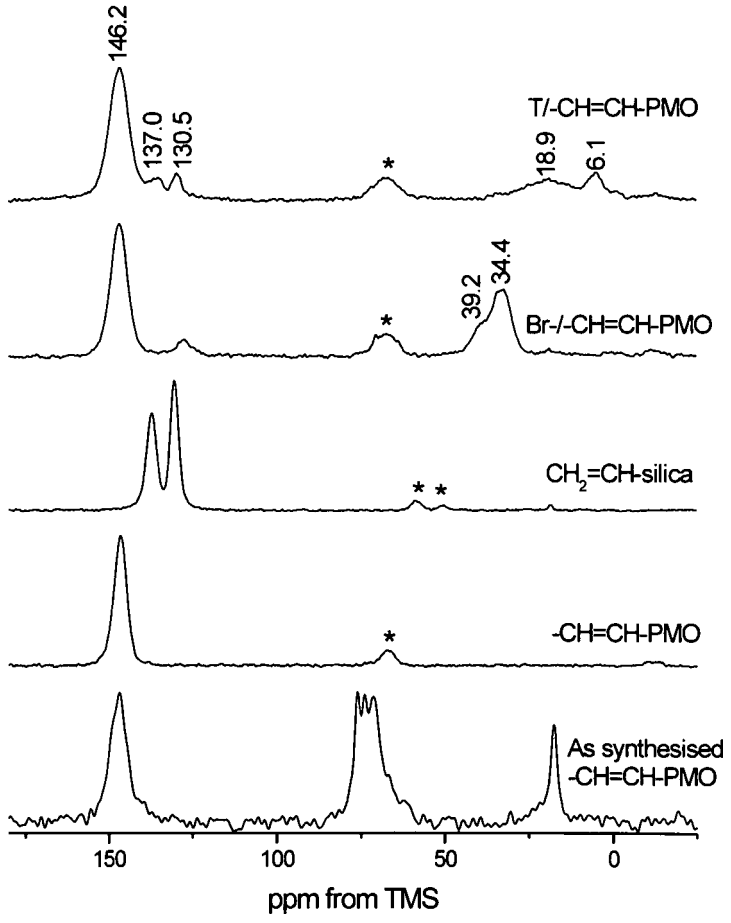

Figure 4.3. ^{1}H-^{13}C CP/MAS NMR spectra of PMOs (Asterisks denote spinning sidebands).

The CH_2=CH-silica shows two resonances at 130.5 and 137.3 ppm assigned to the CH_2 and CH sites respectively. Bromination of the –**C**H=**C**H- bridge results in the observation of three additional peaks at 34.4, 39.2 and 127.3 ppm. The peak at 34.4 ppm corresponds to ≡Si–**C**HBr-**C**HBr-Si≡ environments. The line at 39.2 ppm is due to residual ^{13}C-^{79}Br dipolar coupling affecting the ^{13}C spectrum due to the large quadrupolar moment of Bromine.[193] The addition of Bromine results in a substantial decrease in signal-to-noise ratio of the ^{1}H-^{13}C CP/MAS spectrum consistent with previous reports.[183] This effect is, most probably, a result of the ^{79}Br-^{1}H and ^{13}C-^{79}Br residual dipolar coupling interfering with the Hartmann-Hahn matching conditions for ^{1}H-^{13}C CP. As ^{79}Br and ^{13}C Larmor frequencies are very similar at 9.4 T, the ^{79}Br spins may also be excited during the transfer of magnetisation step thus spoiling the ^{1}H-^{13}C CP as a ^{1}H-^{79}Br Hartmann-Hahn condition may also be reached. The possibility of partial bromination of the double bond can be ruled out due to the absence of a -CH_2- environment which would be expected in the region of 10 to 20 ppm. The resonance at 127.3 ppm cannot be a result of pendant vinyl groups formed upon bromination as no evidence of Si-C bond cleavage was seen in the corresponding ^{1}H-^{29}Si CP/MAS spectrum. Also the resonance appears slightly up-field compared to the CH_2=CH-SiO_2 resonances at 130.5 and 137.3 ppm. Previous reports on the bromination of –CH=CH-PMOs have also observed this resonance yet it is poorly assigned to pendent vinyl groups with no ^{29}Si spectra to confirm it.[194] The use of CP kinetics to assist with this assignment was not possible due to very long acquisition times required for the Br/-CH=CH-PMO.

The thermal treatment of -CH=CH-PMO resulted in the appearance of additional resonances at 6.1, 18.9, 130.5 and 137.0 ppm (Fig. 4.3, top). The resonances at 130.5 and 137.0 ppm can be assigned to terminal vinyl-silica groups, confirmed by the ^{1}H-^{13}C CP/MAS NMR spectrum of the pure CH_2=CH-PMO. The resonances at 6.1 and 18.9 ppm are somewhat unexpected. The line at 6.1 ppm is typical of an aliphatic O_3Si-**C**H_2**C**H_2-SiO_3 bridging group. The broad resonance at 18.9 ppm suggests the formation of terminal ≡Si-CH_2CH_3 functionalities with broad line at *ca.* 19 ppm resulting from the -CH_2- groups and the resonance at 6.1 ppm a result of the terminal -CH_3.

4.3.1.2 ^{1}H-^{29}Si CP/MAS NMR

^{1}H-^{29}Si CP/MAS NMR is sensitive to changes in pore wall composition and therefore was used to determine changes in silicon environments as a result of post synthetic modifications. The –CH=CH-PMO (Fig. 4.4, bottom) displays three resonances at -64.2, -73.6 and -82.9 ppm corresponding to silicon T^n units (where n denotes the number of neighbouring tetrahedra bound to silicon *via* oxygen). The resonance at -64.2 ppm corresponds to poorly condensed R-Si(OH)$_2$(OSi) T^1 environments. The peak at -73.6 ppm is a result of partially condensed R-Si(OH)(OSi)$_2$ T^2 units, whereas the resonance at -82.9 ppm corresponds to fully condensed R-Si(OSi)$_3$ T^3 sites. The ^{1}H-^{29}Si CP/MAS NMR spectrum of the CH_2=CH-silica shows only two resonances at -70.7 and -79.3 ppm. These sites correspond to silicon T^2 and T^3 environments. The absence of any T^1 environments and the large concentration of silicon T^3 units indicate a high degree of condensation. The absence of any Q^n environments at -90 to -120 ppm indicate no Si-C bond cleavage during synthesis or template extraction of -CH=CH-PMO.

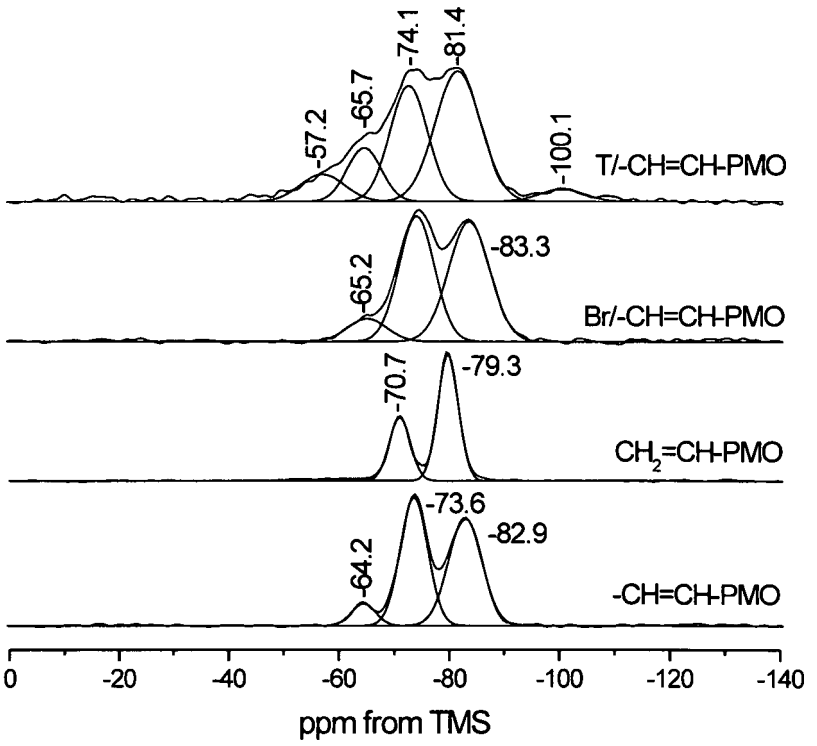

Figure 4.4. ^{1}H-^{29}Si CP/MAS NMR spectra of the template extracted PMOs.

The bromination of -CH=CH-PMO results in a broadening of the T peaks although no change in chemical shift was observed (Fig. 4.4). The broadening is a result of residual

^{29}Si-^{79}Br dipolar coupling due to Bromine incorporation. The same broadening was also seen in the ^{13}C spectrum at *ca.* 34 – 39 ppm (fig. 4.3). The presence of residual dipolar coupling in the spectra of spin ½ nuclei close in space to quadrupolar nuclei with high natural abundance has been reported in the ^{31}P spectrum of aluminophosphate $AlPO_4$-14.[195] Likewise, other reports comment on the effect of ^{14}N (which has a quadrupolar coupling constant in the order of MHz) on ^{13}C and ^{1}H spectra of peptides showing spectra acquired with and without the ^{14}N decoupling. The resulting spectra confirmed the presence of ^{1}H-^{14}N coupling as ^{1}H line narrowing was observed when ^{14}N decoupling was applied.[196,197] No change in ^{29}Si chemical shift is expected as the electron rich -CH=CH- bond is replaced by electronegative Bromine atoms. No silicon Q^n sites are observed confirming the absence of pendant vinyl groups as a result of bromination.

The ^{1}H-^{29}Si CP/MAS NMR spectrum of the thermally treated -CH=CH-PMO shows the same three major resonances, although broadening of the peaks is observed. The broadening of the two resonances at -74.1 and -81.4 ppm suggest additional -CH=CH_2 silicon $T^{2/3}$ sites to be present. This was anticipated due to the similar chemical shift of –CH=CH_2 and –CH=CH- functionalities (fig. 4.4). An increased intensity of the resonance at -65.7 ppm suggests the presence of -CH_2CH_2- and -CH_2CH_3 T^3 sites along with -CH=CH-/CH_2=CH- T^1 sites. A low-intensity resonance at -57.2 ppm is a result of aliphatic silicon T^2 resonance, consistent with ^{1}H-^{13}C CP/MAS NMR data. The low intensity line at *ca.* -100 ppm is a $Si(OSi)_3(OH)$ Q^3 site, a direct result of Si-C bond cleavage during thermal treatment. The $^{29}Si\{^{1}H\}$ MAS NMR spectrum (Fig. 4.5) confirmed the variety of chemical environments of ^{29}Si in T/-CH=CH-PMO.

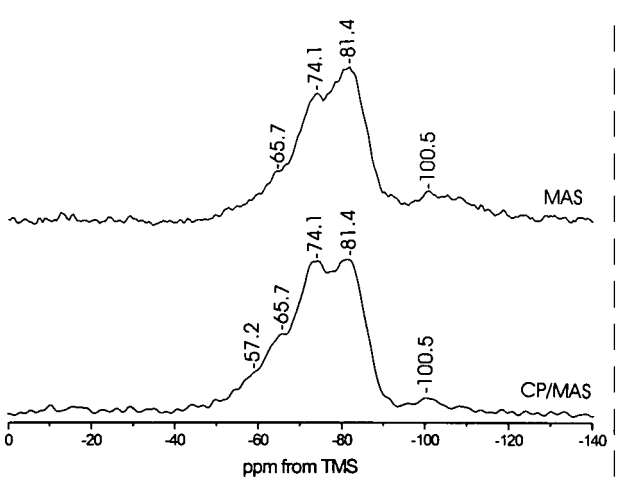

Figure 4.5. ^{1}H-^{29}Si CP/MAS (bottom) and $^{29}Si\{^{1}H\}$ MAS (top) NMR spectra of T/-CH=CH-PMO.

The degree of pore wall condensation ($(T^1 + T^2)/T^3$) (Table 4.2) remains unchanged upon bromination of -CH=CH-PMO. The $-CH=CH_2$-silica shows the most condensed network. As this material was synthesised in the absence of the template, P123, in order to form a solid network the silanol functionalities need to condense to remove hydrophilic terminal -OH functionalities. The degree of pore wall condensation of the T/-CH=CH-PMO was not determined due to the large overlap of T sites connected to sp^3 and sp^2 carbon atoms.

Table 4.2. Degree of pore wall condensation determined from the ^1H-^{29}Si CP/MAS NMR spectra by applying the formula $(T^1 + T^2)/T^3$. The lower the ratio, the more condensed the organic/inorganic framework.

Sample	Peak Area					-CH=CH- $(T^1 + T^2)/ T^3$	CH_2=CH- T^2/ T^3
	-CH=CH-			CH_2=CH-			
	T^1	T^2	T^3	T^2	T^3		
-CH=CH-PMO	0.92	6.16	6.31	//	//	1.12	//
CH_2=CH-silica	//	//	//	2.32	4.57	//	0.51
Br/-CH=CH-PMO	1.55	7.76	8.66	//	//	1.08	//

4.3.1.3 ^{1}H MAS NMR

^{1}H MAS NMR spectra (Fig. 4.6) provided further confirmation of the formation of vinyl CH_2=CH-Si≡ tethers upon thermal treatment. The -CH=CH-PMO shows three major resonances at *ca.* 2.0, 4.1 and 6.7 ppm and minor peaks between 0 and 1.8 ppm. The resonance at 2.0 ppm is due to residual acetone used in the extraction procedure. The peak at 4.1 ppm is a result of water molecules H-bonded to surface silanols whilst the resonance at 6.7 ppm is due to the -CH=CH- bridges. The CH_2=CH-silica shows a single peak at 5.9 ppm attributed to the vinyl protons. The Br/-CH=CH-PMO shows an intense peak at 5.9 ppm attributed to $(H_2O)_n$ clusters in the pore channels.[198] The peak at 3.7 ppm represents the -CH(Br)CH(Br)- proton environments whilst the resonance at 6.9 ppm is due to the un-reacted -CH=CH- bridges. The T/-CH=CH-PMO shows evidence of both double bond environments with resonances at 6.7 and 5.8 ppm. The increased intensity of the resonances between 0 and 1.8 ppm confirm the increased content of ≡Si-OH groups, consistent with the ^{1}H-^{29}Si CP/MAS NMR data.

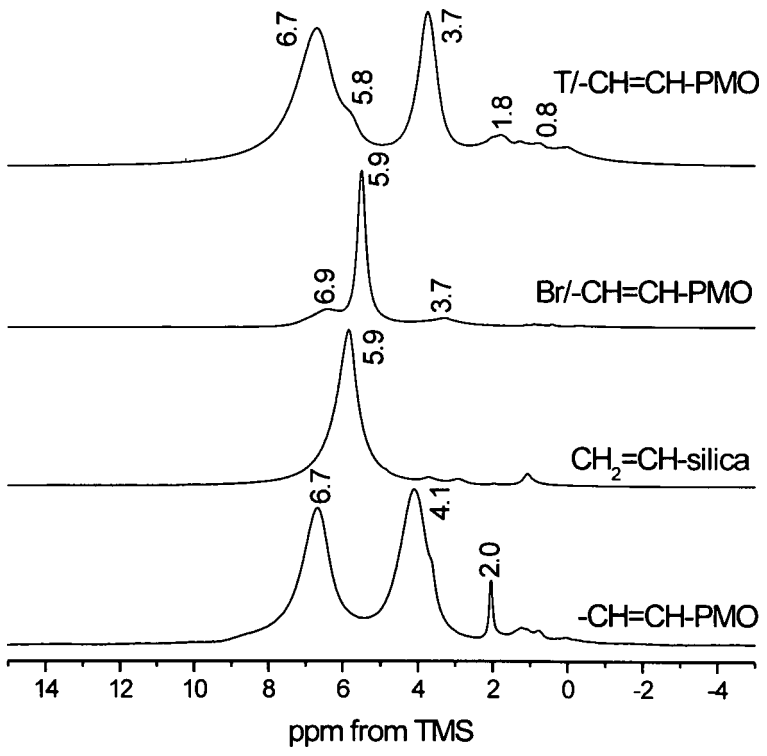

Figure 4.6. ^{1}H MAS NMR spectra of the template extracted PMO.

4.4 Template-Framework Interactions

The use of organic templates in the synthesis of both zeolites and mesoporous silicas have been shown to greatly affect the textural properties and morphology of the products.[28,199,200] The type and concentration of the template have been shown to influence the zeolite crystallinity and surface areas in ZSM-5 structures when using tetrapropyl ammonium bromide and/ or Xylitol (1,2,3,4,5-pentahydroxypentane) structure directing agents.[201,202] The use of co-templates in the synthesis of PMOs has been demonstrated to alter the morphology and cause phase changes from cubic to hexagonal structures.[203]

Therefore, to rationalise the effect of the template, it is important to understand template framework/ interactions of the as-synthesised porous solid. Also, does the entire template or only certain functional groups within the molecule interact with the pore walls? The use of single crystal X-ray diffraction has answered this question for crystalline tetra-iso-amylammonium bromide templated semi-clathrate solids where the aliphatic tail is located close to the framework and the ammonium cation located in the centre of the cage.[204] However, due to the amorphous nature of both the template and pore walls of PMOs, solid-state NMR is the only method capable of determining how the template is interacting with the framework. Previous work by Babonneau *et al.* has been conducted on characterisation of the silica-template (CTABr) interface in acid and base systems.[169] The authors concluded from ^{29}Si HETCOR and double CP experiments that in the CTAB/HCl systems the silicon Q_3 environments correlated with the Si-OH silanols and N-CH_x protons of the template. However, under basic conditions the correlation between Si-OH protons and the template is no longer observed suggesting the Q_3 sites are primarily of the Si-O^- type consistent with the pH at which the synthesis is carried out.[169] The existence of a strong correlation between the Si-O^- and $N^+(CH_3)_3$ under basic conditions confirm the so-called S^+I^- interaction mechanism and the presence of charge balancing.

4.4.1 ^{1}H-^{13}C CP/MAS Kinetics

^{1}H-^{13}C CP/MAS kinetics has been used to confirm the locations of the hydrophilic (PEO) and hydrophobic (PPO) components of the block copolymer template in mesostructured organosilicas. CP kinetics was used previously to study the template framework interactions in Cetyltrimethylammonium bromide (CTABr) templated

aluminophosphates, where the template polar head group was found to be in a more rigid environment compared to the aliphatic tail.[192]

The ^{1}H-^{13}C CP/MAS kinetics (Fig. 4.7 and Table 4.3 respectively) of the block copolymer indicate differences in mobility between the (PPO) and (PEO) components. The CP kinetics of all the template resonances follows the simplest I-S model indicating the presence of a homogeneous ^{1}H population. The hydrophilic (PEO) component (peak at 70.9 ppm) displays the fastest T_{IS} and $T_{1\rho}^{H}$ times of all template resonances. This observation confirms this block is in a highly rigid environment. The $-CH_3$ PPO resonance shows the slowest CP build up and almost no $T_{1\rho}^{H}$ relaxation. This is indicative of a highly mobile environment. The two other resonances at *ca.* 73.6 and 77.5 ppm attributed to the $-CH_2-$ and –CH- groups of the PPO block respectively, display similar CP kinetics and have T_{IS} and $T_{1\rho}^{H}$ times intermediate to those of the PEO block and the $-CH_3$.

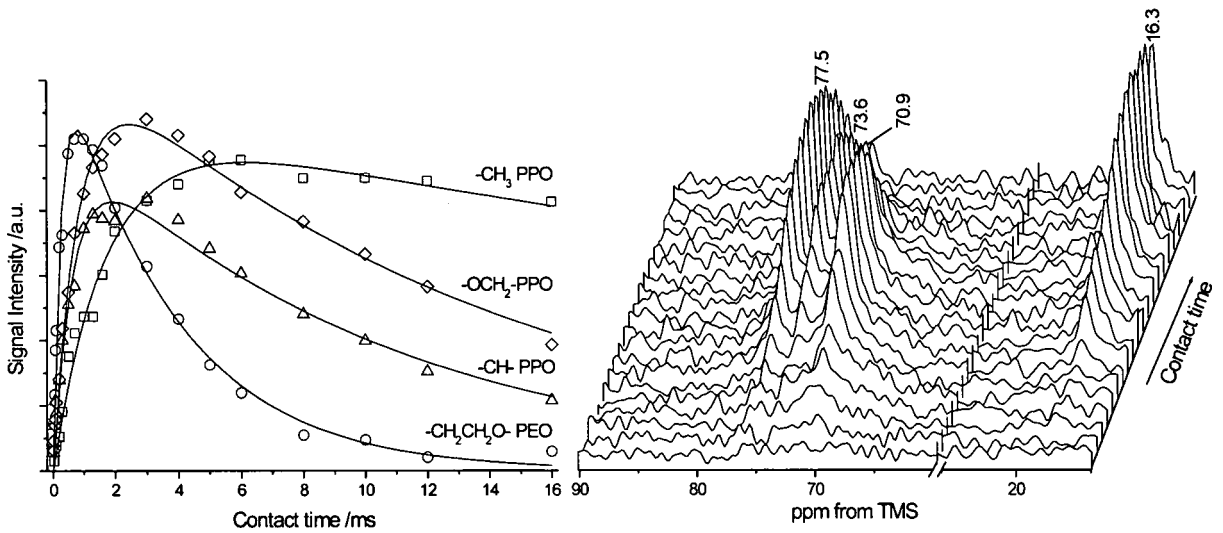

Figure 4.7. ^{1}H-^{13}C CP/MAS kinetics curves (left) and plots (right) of block-copolymer template in as-synthesised -CH=CH-PMO.

It is clear that the PEO component is interacting strongly with the pore walls of the PMO. In contrast, the PPO block shows little interaction with the framework and remains mobile in the pore channels. These observations are consistent with previous hypotheses on the template-framework interactions of tri-block co-polymers in mesoporous organosilicas.[39]

Table 4.3. ^{1}H-^{13}C CP/MAS kinetics fitting parameters for the template resonances of the as-synthesised -CH=CH-PMO.

Resonance /ppm	^{13}C Site	Signal Intensity /10^7	T_{IS}/ms	$T_{1\rho}{}^{H}$ /ms	R^2
16.3	$-CH_3$ PPO	1.06 ±0.019	1.74 ±0.094	>50	0.989
70.9	$-C_2H_4O-$ PEO	1.30 ±0.039	0.275 ±0.019	3.55 ±0.21	0.988
73.6	$-OCH_2-$ PPO	0.995 ±0.045	0.652 ±0.068	10.4 ±1.04	0.969
77.5	-CH- PPO	1.27 ±0.038	0.810 ±0.054	13.7 ±1.03	0.988

4.4.2 ^{1}H-^{13}C Wideline separation (WISE) spectroscopy

The ^{1}H-^{13}C WISE spectrum (Fig. 4.8, left) correlates the ^{13}C spectrum (structure) in the direct dimension with the ^{1}H spectrum (mobility) in the indirect dimension. That is the narrower ^{1}H lines are observed for increasingly mobile ^{1}H environments. The ^{13}C dimension shows four template resonances (Fig. 4.3 and 4.9) correlating with the broad lines in the ^{1}H dimension.

The ^{1}H wideline corresponding to the PEO block confirms the rigidity of the protons as a linewidth of 23.0 kHz is observed. However the ^{1}H lines correlating to the ^{1}H PPO environments are significantly narrower than that of the PEO species providing further confirmation that the PPO block is highly mobile within the pores of the mesoporous framework. It is also worthy to note that the ^{1}H projection of the -CH=CH- groups display a broad resonance superimposed on a narrow peak, confirming two different ^{1}H mobilities depending on the location of the functionalities in the framework, consistent with ^{1}H-^{13}C CP kinetics studies.

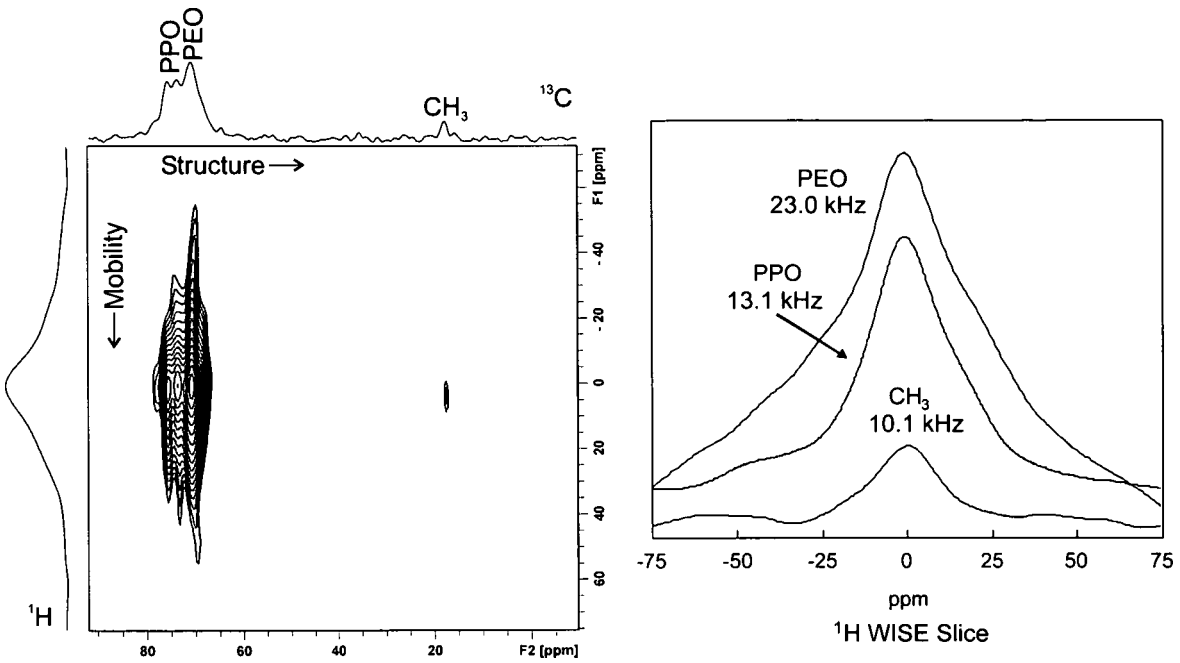

Figure 4.8. ^{1}H-^{13}C WISE NMR spectrum of the as-synthesised –CH=CH-PMO (left) and corresponding ^{1}H projections (right).

The ^{1}H-^{13}C CP/MAS kinetics curves and 2D WISE NMR spectra have both provided complementary information on the environments of the template components in as-synthesised -CH=CH-PMOs. The PEO component is strongly interacting with the hybrid pore walls whereas the PPO block is mobile in the pores (scheme 4.1). The interactions between the hybrid walls and the PEO block are H-bonding through terminal PEO -OH groups and the Si-O-Si environments as well as ion-pairing through the halide anion of the protonated ether functionality in the PEO blocks and the ≡Si-$^{+}OH_2$ functionalities as shown in the scheme.

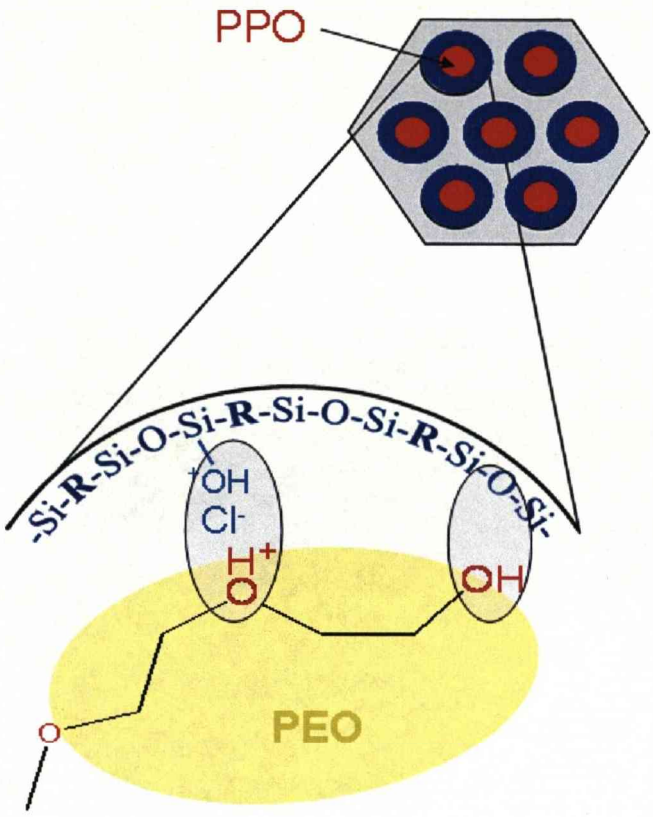

Scheme 4.1. Template-framework interactions inferred from the ^{1}H-^{13}C CP/MAS kinetics and WISE experiments.

This is the first example of the application of CP/MAS kinetics and WISE experiments to block co-polymer templated PMOs. Being able to probe the template-framework interactions could be essential when designing network with different organic functionalities. The addition of larger organic groups may alter the rigidity of the PEO components thus changing the mesoscopic ordering.

4.5 Molecular level Structure of the pore walls

4.5.1 ^{1}H-^{13}C CP/MAS kinetics

Both the ^{1}H-^{13}C and ^{1}H-^{29}Si CP/MAS kinetics curves have been fitted according to the I-S model. We note that the ^{1}H-^{13}C CP/MAS kinetics curves give unsatisfactory results when fitted using either the I-S or a more complex I-I*-S model relying on the presence of heterogeneous ^{1}H population.[154] The unusual CP-dynamics curves observed for the -CH=CH- bridges (Fig. 4.9) can only be explained using a model where two components with different T_{IS} and $T_{1\rho}^{H}$ times are identified depending on the mobility of the CP-determining ^{1}H spins. The "rigid" component displays extremely short T_{cp} and $T_{1\rho}^{H}$ times and the "mobile" component shows much longer T_{cp} and $T_{1\rho}^{H}$ times. The fast CP of the rigid components is a result of directly attached protons with reduced mobility and is indicative of a strong ^{1}H-^{13}C heteronuclear dipolar coupled network, thus representing organic bridges embedded in the bulk of hybrid pore walls. The "mobile" component can be attributed to organic bridges located at the pore wall interface where the presence of surface Si-OH groups will also influence the CP kinetics.

The ^{1}H-^{13}C CP/MAS kinetics curves (Fig. 4.9) of the as-synthesised and template extracted -CH=CH-PMO indicate the presence of both ^{1}H mobilities. This is confirmed by the increase in $T_{1\rho}^{H}$ times (Table 4.4) of the surface functionalities upon extraction of the template. Clearly, when template is in the mesopores, a more rigid proton environment is present on the pore surface with the CP kinetics being dominated by the PEO block of the template. However, upon template extraction the mobility of the interface protons is increased as the main CP source changes from the template to surface ≡SiOH which have increased mobility at the pore wall interface. Meanwhile, the $T_{1\rho}^{H}$ times of the bulk functionalities remain unchanged. The CH_2=CH-silica kinetics parameters still indicate evidence of different ^{1}H motilities despite no mesoscopic ordering being observed. This is most likely due to the formation of a condensed organosilica network where surface and bulk network environments remain.

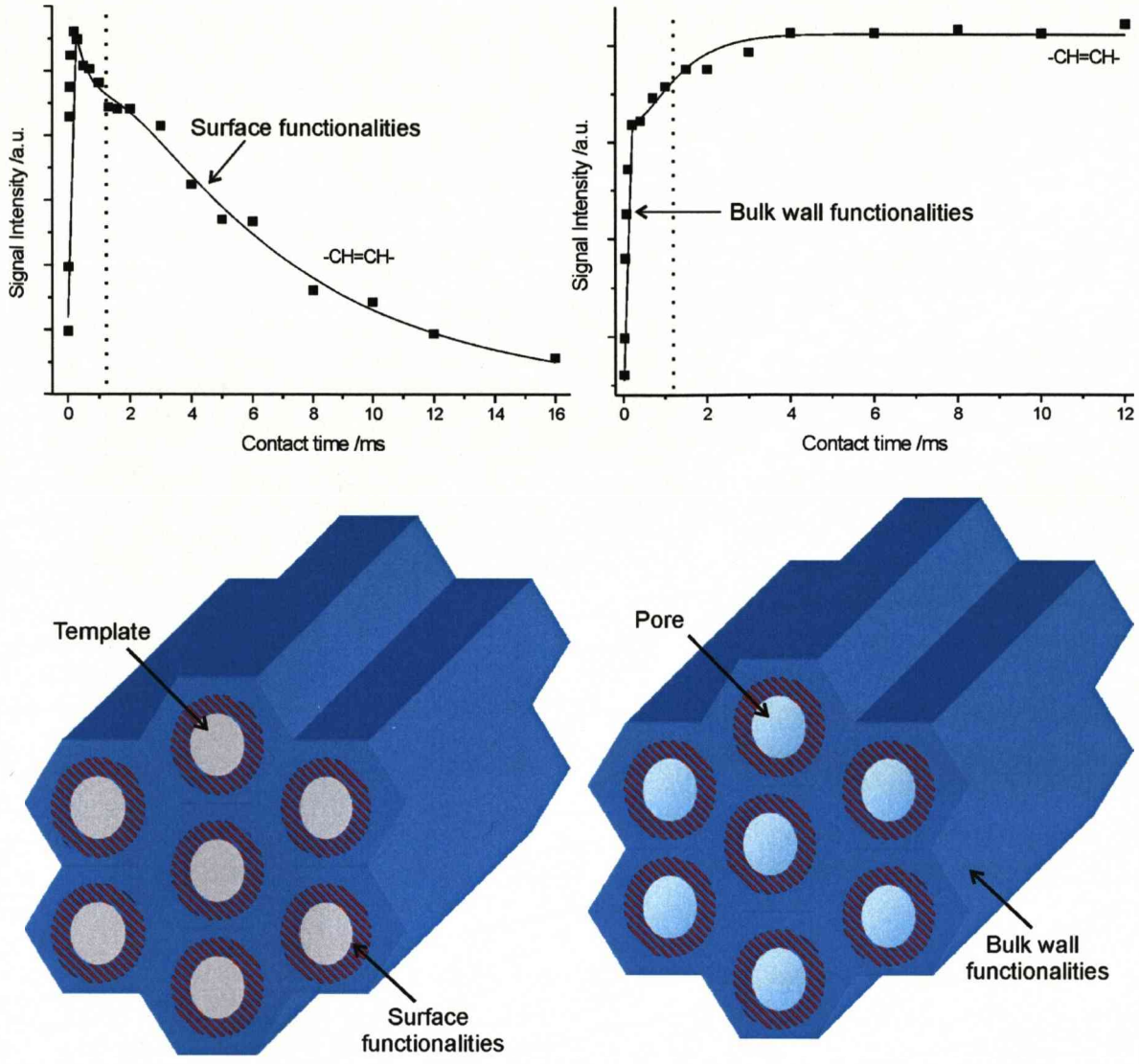

Figure 4.9. ^{1}H-^{13}C CP/MAS kinetics curves of the as-synthesised and template extracted -CH=CH-PMO (Top) and a representation of location of functionalities in the mesoporous structure (bottom). The initial intensity increase and decrease at contact times <1 ms correspond to the bulk wall functionalities. At contact times >1 ms the kinetics is dominated by the surface functionalities with their location indicated by the red shaded area around the pores.

The CP kinetics is affected by the thermal treatment of -CH=CH-PMO (Table 4.4) in that an increase in T_{IS} time is observed for the surface component. Most notably there is a decrease in the I_s/I_f ratio from 1.41 to 1.28 (Table 4.4) upon thermal treatment, thus confirming that it is mostly surface functionalities which undergo metamorphosis. The -CH_2CH_2- kinetics curve suggests the functionality is mostly located at the surface with an I_s/I_f = 1.70 which is consistent with the changes observed for the -CH=CH- functionality.

The locations of two vinyl resonances cannot be determined accurately due to their low intensity in the ^{1}H-^{13}C CP/MAS NMR spectra. The effect of bromine on the ^{1}H-^{13}C CP/MAS spectrum of Br/-CH=CH-PMO (section 4.3.1) will also influence the CP kinetics data due to the interference of bromine during the magnetisation transfer step thus making it difficult to compare with the -CH=CH-PMO.

Table 4.4. ^{1}H-^{13}C CP/MAS kinetics parameters for the PMOs.

^{13}C Site		Signal Intensity / 10^7	T_{IS} / ms	$T_{1\rho}{}^{H}$ / ms	I_s/I_f	R^2
A-CH=CH-PMO						
-CH=CH-	Fast	0.596 ±0.021	0.047 ±0.004	0.537 ±0.032	0.95	0.992
	Slow	0.566 ±0.021	0.782 ±0.057	6.26 ±0.402		
E-CH=CH-PMO						
-CH=CH-	Fast	1.47 ±0.064	0.053 ±0.005	0.534 ±0.039	1.41	0.996
	Slow	2.07 ±0.016	0.750 ±0.023	>100		
CH_2=CH-silica						
CH_2=	Fast	4.90 ± 0.703	0.030 ± 0.001	1.69 ± 0.06	1.01	0.994
	Slow	4.95 ± 0.198	1.74 ± 0.110	12.21 ± 0.95		
=CH-	Fast	5.94 ± 0.794	0.16 ± 0.005	2.58 ± 0.01	1.26	0.998
	Slow	7.50 ± 0.243	2.53 ± 0.120	13.2 ± 0.81		
T/-CH=CH-PMO‡						
-CH_2CH_2-	Fast	0.397 ±0.026	0.015 ±0.003	0.501 ±0.080	1.70	0.947
	Slow	0.676 ±0.022	0.415 ±0.041	40.1 ±9.00		
-CH=CH-	Fast	3.88 ±0.131	0.037 ±0.003	1.03 ±0.071	1.28	0.987
	Slow	4.95 ±0.071	1.74 ±0.078	>100		

† CP kinetics curves fitted using peak integrals.
‡ CP kinetics of the CH_2=CH- resonances at ca. 130.5 and 137 ppm undetermined due to poor signal to noise.

4.5.2 ^{1}H-^{29}Si CP/MAS Kinetics

The ^{1}H-^{29}Si CP/MAS kinetics (Fig. 4.9 and Table 4.4) confirm changes in the pore wall dynamics upon bromination and thermal treatment. All PMOs show that the T_{IS} times increase with Si condensation from R-Si(OH)$_2$(OSi) T^1 to R-Si(OSi)$_3$ T^3 environments. This is to be expected due to protons in the Si-OH moieties facilitating CP 'build up'.

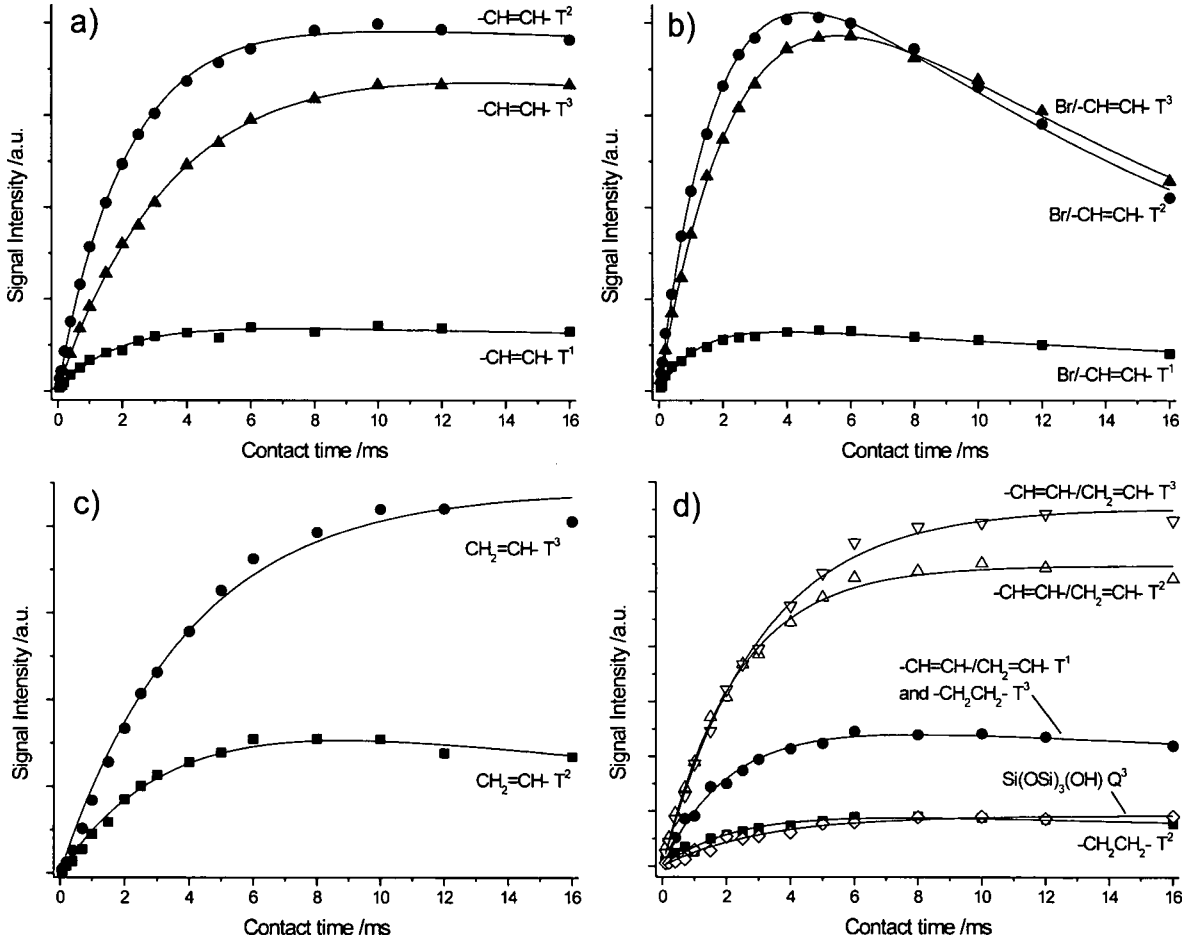

Figure 4.11. ^{1}H-^{29}Si CP/MAS kinetics curves of the template-extracted a) –CH=CH-PMO, b) Br/-CH=CH-PMO, c) CH_2=CH-silica and d) T/-CH=CH-PMO.

The –CH=CH-PMO T sites show no evidence of $T_{1\rho}{}^{H}$ relaxation suggesting the 'proton pool' is sparsely populated and only weak network of ^{1}H-^{1}H dipolar couplings is present. The CH_2=CH-silica $T^{2/3}$ environments displays the longer CP 'build-up' times compared to the bridging PMOs because of increased proton mobility. This change is associated with both the amorphous nature and lack of an extended framework in the CH_2=CH-silica.

The large decrease in $T_{1\rho}{}^{H}$ relaxation times upon bromination is a direct consequence of dipolar couplings between the proton and quadrupolar (I = 3/2) bromine nucleus, thus

confirming its incorporation into the mesostructure. These dipolar couplings occur due to a spatial orientation dependence in the rotating frame Hamiltonian of the second order quadrupolar term expressed in tensors of rank 0, 2 and 4 (see chapter 2). The rank 0 spherical term is isotropic, the second is averaged out by MAS, whilst the rank 4 component remains, thus influencing the relaxation behaviour of both ^{1}H and ^{29}Si nuclei.[137]

Table 4.4. ^{1}H-^{29}Si CP/MAS kinetics fitting parameters of the template extracted PMOs. (fitted using the I-S model and I-S model without $T_{1\rho}{}^{H}$ relaxation)[154]

Resonance /ppm	^{29}Si Site	Signal Intensity /10^7	T_{IS} /ms	$T_{1\rho}{}^{H}$ /ms	R^2
-CH=CH-PMO					
-64.1	-CH=CH- T^1	0.673 ±0.012	1.53 ±0.099	n/a	0.986
-73.5	-CH=CH- T^2	3.93 ±0.023	2.01 ±0.038	n/a	0.999
-82.6	-CH=CH- T^3	3.43 ±0.023	3.20 ±0.057	n/a	0.999
Br/-CH=CH-PMO					
-65.2	-CH=CH- T^1	0.371 ±0.016	1.20 ± 0.118	27.9 ± 4.78	0.980
-74.1	-CH=CH- T^2	2.80 ±0.052	1.95 ± 0.062	14.9 ± 0.620	0.999
-83.3	-CH=CH- T^3	2.80 ±0.060	2.66 ± 0.085	15.0 ± 0.668	0.999
CH_2=CH-silica					
-70.9	CH_2=CH- T^2	3.95 ±0.081	3.45 ±0.172	34.6 ±4.46	0.992
-79.3	CH_2=CH- T^3	8.83± 0.203	3.98 ±0.223	n/a	0.993
T/-CH=CH-PMO					
-57.2	-CH_2CH_2- T^2	0.504 ±0.016	2.31 ±0.206	n/a	0.962
-65.7	$T^{1/3}$ site	1.31 ±0.022	2.09 ±0.106	n/a	0.989
-74.1	-CH=CH- T^2	2.74 ±0.029	2.29 ±0.073	n/a	0.997
-81.4	-CH=CH- T^3	3.26 ±0.034	3.00 ±0.084	n/a	0.998
-100.1	$Si(OSi)_3(OH)$	0.465 ±0.015	3.18 ±0.270	n/a	0.981

After the thermal treatment of the -CH=CH-PMO the relative intensity of the resonance at *ca.* -65 ppm has increased compared to that for $T^{2/3}$ sites at *ca.* -74 to -81 ppm (Table 4.4). The CP build up time T_{IS} has also increased confirming that -CH_2CH_2- T^3 sites have formed, as there are fewer Si-OH compared to the -CH=CH- T^1 environments. The

presence of saturated functionalities within the framework has also resulted in a decrease in T_{1S} times for the -CH=CH- $T^{2/3}$ environments compared to the initial -CH=CH-PMO. The silicon Q^3 site shows long T_{1S} times along with no evidence of $T_{1\rho}{}^H$ relaxation typical of silicon Q^n sites.

The ^{13}C, ^{29}Si CP/MAS and VCT CP/MAS studies have all indicated the formation of vinyl and $-CH_2CH_2-$ functionalities along with silicon Q^n environments upon thermal treatment. A possible mechanism explaining their formation is depicted in scheme 4.2. Herein, by means of elevating the temperature, terminal vinyl groups and siloxane bridges are generated *via* proton transfer from silanol groups to ethenylene bridging groups.[191] The absence of any surfactant in the pores excludes the possibility that the proton transfer descends from the surfactant template.

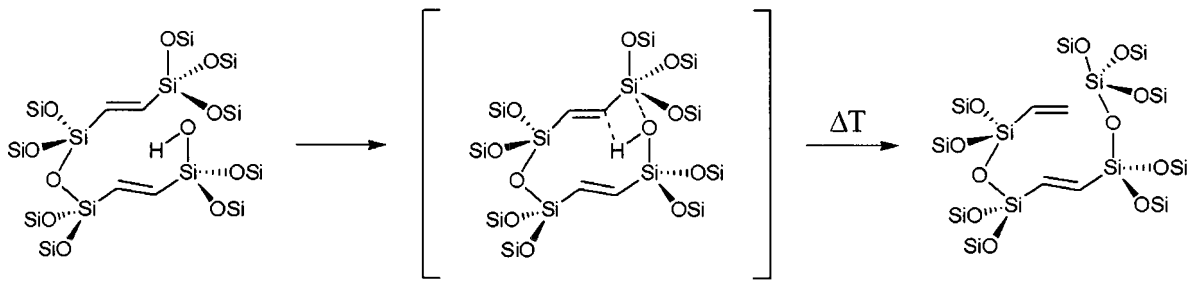

Scheme 4.2. The silanol – ethene interaction and the cleavage of the Si-C bond of the ethenylene-bridge, leading to the formation of a pendant vinyl group and a siloxane bridge.

4.6 Conclusions

The two different methods have been successful in preparation of multifunctional PMOs from a mono-functional -CH=CH-PMO. The confirmation of retention of the mesostructure along with mesoporosity upon post synthetic modification is essential if these materials are to be used for catalytic applications. The application of ^{1}H-^{13}C CP/MAS NMR was successful in confirming the variety of organic functionalities present in the mesostructure. The ^{1}H-^{29}Si CP/MAS experiments were sensitive to localised changes in silicon environments in the pore walls upon post synthetic modification. In particular, direct evidence of Si-C bond cleavage upon thermal treatment by the appearance of silicon Q^n species confirmed metamorphosis had occurred.

The application of CP kinetics experiments also enabled the location of the functionalities within the mesoporous framework to be assessed. ^{1}H-^{13}C CP/MAS kinetics confirmed the majority of modified functionalities are located at the pore wall interface (Scheme 4.3). ^{1}H-^{29}Si CP kinetics was also invaluable in confirming the bromine incorporation into the mesostructure due to the decrease in $T_{1\rho}{}^{H}$ relaxation times.

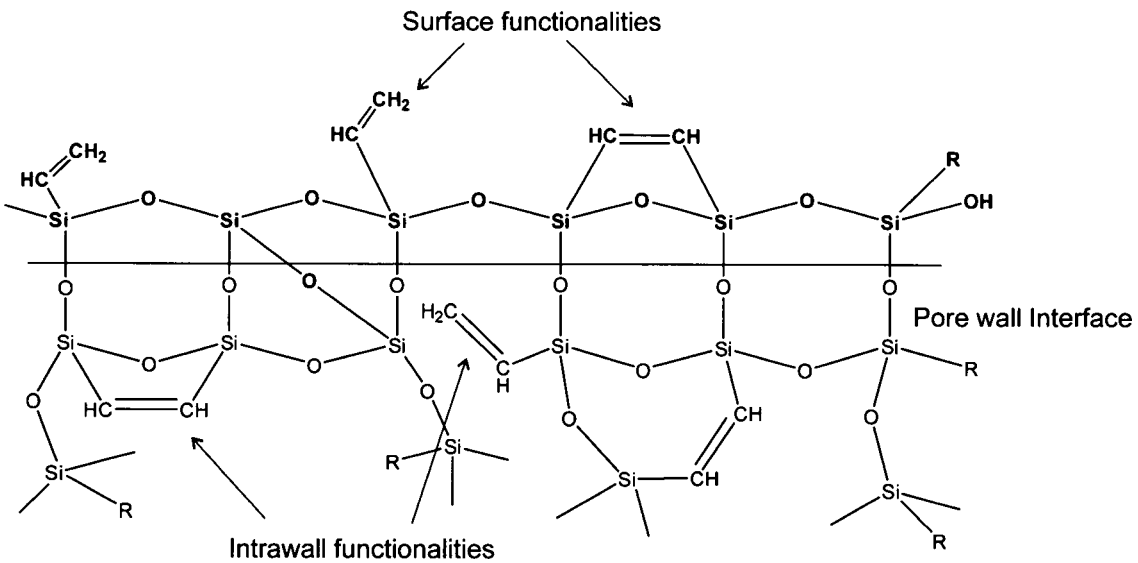

Scheme 4.3. Representation of the pore wall of T/-CH=CH-PMO. (R = -CH=CH- or -$CH=CH_2$.

Direct synthesis of bi-functional PMOs: A Solid-state NMR Study

Chapter 5

5.1 Introduction

In the previous chapter the formation of multifunctional PMOs was achieved using post synthetic treatment steps such as bromination and thermal treatments (see chapter 4). Post synthetic treatment of mesoporous silicas and PMOs can be a useful method for incorporating additional functionalities, as in amine functionalized SBA-15.[205] Drawbacks, *i.e.* the inhomogeneous distribution of the grafted functionalities and pore blocking, can limit the applicability of this method. The direct synthesis of bi-functional PMOs has focused on the incorporation of heteroatoms *via* isomorphous substitution in order to expand the range of catalytic applications in the resulting PMO. Aluminium incorporated PMOs have displayed Brønsted acidity[129,131,132] whereas titanium[105,112], vanadium[133] and chromium[134] containing PMOs have shown promise in epoxidation reactions. Other forms of bifunctionality have come in combining bridging ($(EtO)_3Si$-R-$Si(OEt)_3$) and terminal (R-$Si(OEt)_3$) organosilane precursors. The use of 1,2-bis(triethoxysilyl)ethylene (BTSEY) and triethoxyvinylsilane (TEV) *via* cationic templating in basic medium resulted in materials with a 2D hexagonal structure containing vinyl groups embedded in the pore walls and terminal vinyl groups in the pore channels. The presence of vinyl groups in the pore channels clearly reduces the surface area of the products (S_{BET} values of *ca.* 600 m^2 g^{-1} are reported).[56] The incorporation of two organic groups into the pore walls has been reported where 1,4-bis(triethoxysilyl)benzene (BTEB) and 2,5-Bis(triethoxysilyl)thiophene (BTET) were co-condensed to form a 2D hexagonal structure using non-ionic templates P123 or Brij76.[39]

The pre-hydrolysis of silica source has been applied in the preparation of transition metal functionalized PMOs with the main purpose being to equalize the hydrolysis rates of the two precursors.[131] Titania precursors such as titanium chloride or titanium *tert*-butoxide hydrolyze and condense at faster rates than their silica counterparts. Thus, pre-hydrolysis of the silica source (usually tetraethylorthosilicate, TEOS) is required to obtain a homogeneous phase pure Ti-incorporated materials.[206] Investigations into the relative hydrolysis/condensation rates of 1st row transition metals (or metalloid) alkoxides have shown that a triethanolamine ligand (2, 2', 2"-nitriletriethanol) equalizes hydrolysis/ condensation rates of various precursors due to its complexing ability.[207,208] Although the incorporation of different organic functionalities within the same mesostructure has been reported in the literature, information on the structure of such solids at a molecular level is

still scarce. Moreover, the ability to direct different functionalities and determine the location of the organic groups in the products has proven difficult in terms of both development of new synthesis strategies and advanced characterization.

In this chapter we have focused on the preparation of a bifunctional -CH_2-CH_2-/-CH=CH-PMO using salt assisted non-ionic templating in aqueous acidic medium. We aim to demonstrate that the introduction of a silica precursor pre-hydrolysis step in the synthetic procedure can alter the properties of the products. The use of joint and separate silica source pre-hydrolysis protocols can result in different distribution patterns of the organic groups within the porous framework. We also aim to probe the structure of such materials on a molecular level using advanced solid-state NMR to determine the distribution of organic functionalities. Such complex materials may offer uses as solid phases in chromatographic separation and further functionalisation leading even to controlled drug delivery systems.

5.2 Results and Discussion

5.2.1 Synthetic Observations

The synthesis of PMOs relies on the self-assembly of surfactant template and organosilicate secondary building units formed *via* the hydrolysis and condensation of initial organosilane precursors.[39,103] The joint hydrolysis mixtures consisted of both $-CH_2-CH_2-$ and -CH=CH-bridged precursors in appropriate amounts of 2M HCl and ethanol in the same container. Synthesis mixtures with identical Si/HCl and Si/C_2H_5OH ratios were used in separate pre-hydrolysis protocols when the precursors with different organic bridges were combined only at the stage of addition to the template solution. The introduction of joint and separate pre-hydrolysis of the silica precursors could facilitate the formation of homo- and hetero- organo-functionalized secondary building units (SBU) prior to self-assembly with the template. The formation of two types of organo-functionalised SBUs might affect the overall distribution of organic groups in the products (scheme 1). This has been probed using advanced characterisation methodologies sensitive to the local organisation in solids with limited long-range ordering.

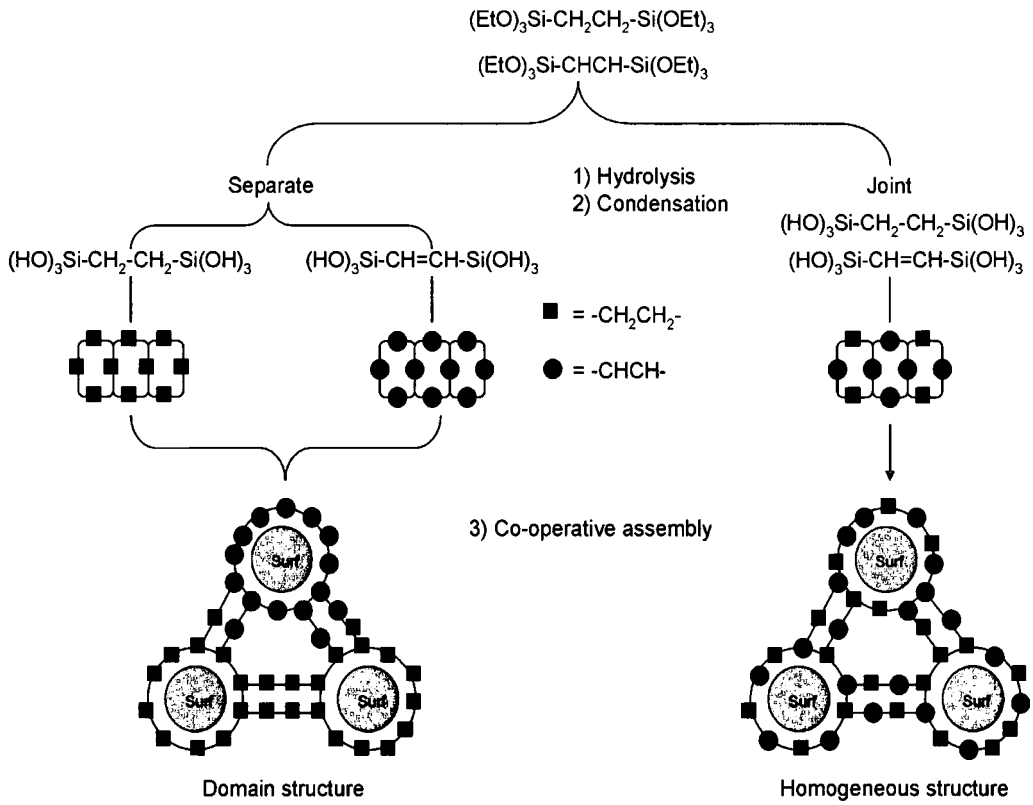

Scheme 5.1. Formation of homo- and hetero- organo-functionalised SBUs and the resulting bifunctional PMOs prepared using the joint and separate pre-hydrolysis protocols.

The pre-hydrolysis protocols were used to find an optimum balance between size of the SBUs and their ability to undergo the self-assembly with the template required to form ordered porous materials. Clearly, once traces of the bulk amorphous organosilica product are formed (*i.e.* the case of very large SBUs), their assembly with the template is restricted. Although direct measurements of the sizes of SBUs are beyond the scope of this report, indirect conclusions can be made from observations of the hydrolysis mixtures. The latter are consistent with previous studies on the hydrolysis/condensation rates and resulting particle sizes of tetraethyl orthosilicate (TEOS) in H_2O/EtOH/HCl solutions.[209]

The hydrolysis of metal (or metalloid) alkoxides can be promoted using either acidic or basic catalysts. The mechanism of hydrolysis is based on the nucleophilic attack at the electropositive metal centre. Once the water ligand is bound to the metal, proton transfer occurs to the leaving alkoxy group.[210,211] The condensation of metal alkoxides proceeds either through water or alcohol elimination reactions leading to the formation of metal-oxygen-metal bonds (equations below).

$$\text{Si-OH} + \text{HO-Si} \longrightarrow \text{Si-O-Si} + H_2O$$

$$\text{Si-OR} + \text{HO-Si} \longrightarrow \text{Si-O-Si} + \text{ROH}$$

For alkoxysilanes, the rate of hydrolysis is dependent on several factors, such as nature of organic bridging group, temperature, time and Si/acid ratio. The relative hydrolysis/condensation rates of the two organosilane precursors were found to be different and, generally, the -CH=CH-bridged precursor hydrolysed/condensed faster than the one with $-CH_2-CH_2-$groups. Viscous gels, and eventually white rigid solids encapsulating the solvent, were obtained in the separately pre-hydrolyzed mixtures with high Si/EtOH ratios containing only $(EtO)_3Si-CH=CH-Si(OEt)_3$. As the C=C double bond is more electron rich compared to C-C single bond, the silicon atoms in BTSEY are more susceptible to nucleophilic attack from water causing hydrolysis rates to increase according to the principle of "electronegativity equalisation".[212] The increase in positive charge on the silicon atoms of $(H_5C_2O)_3$-Si-CH=CH-$Si(OC_2H_5)_3$ is also evident from the ^{29}Si NMR data (discussed below) as the ^{29}Si resonances attributed to -HC=CH-SiO_3 environments appear down-field compared to chemical shifts of silicon sites in the $-CH_2-CH_2-SiO_3$ units.

The ethanol content in the pre-hydrolysis mixtures was a key factor controlling the rates of hydrolysis/condensation. The jointly and separately pre-hydrolysed synthesis mixtures with a Si/EtOH = 0.18 remained clear solutions. As the ethanol content was

reduced to Si/EtOH = 0.24 an increase in hydrolysis/condensation rates was observed. The synthesis mixture with -CH=CH- bridged precursor resulted in a cloudy viscous solution after 60 min (Si/HCl = 14.1). The analogous synthesis mixture with $-CH_2-CH_2-$bridged organosilane remained clear and colourless, though its viscosity increased after 60 min. A further reduced content of ethanol (Si/EtOH = 0.72) resulted in both the jointly and separately hydrolysed mixtures forming white solids after 5 min irrespectively of the HCl content. These observations can be explained by the molecular separation effect reported for $Si(OC_2H_5)_4/HCl/C_2H_5OH$ systems.[209,213] Diluting the hydrolysis mixtures with ethanol increases the separation of the silica precursors and water within the solution thus slowing down the rates of hydrolysis/condensation.

The effect of the Si/HCl ratio on the rates of hydrolysis/condensation is evident from the separately pre-hydrolyzed solutions with Si/EtOH = 0.24. Both BTSE and BTSEY solutions remain clear when Si/HCl = 14.1. However, when Si/HCl = 2.6 the BTSEY mixture became a cloudy viscous solution. With HCl acting as a homogeneous catalyst it is clear that increasing its content in the reaction medium increases the rates of hydrolysis/condensation.

5.2.2 Powder XRD

The -CH_2-CH_2-/-CH=CH-PMO prepared without pre-hydrolysis of silica source displayed powder XRD patterns typical of a 2-dimenstional hexagonal SBA-15 type phase with a sharp reflection (d_{100}= 92.5 Å). The value of d_{100} increased to 97.0 Å after removal of the template (fig. 5.1).

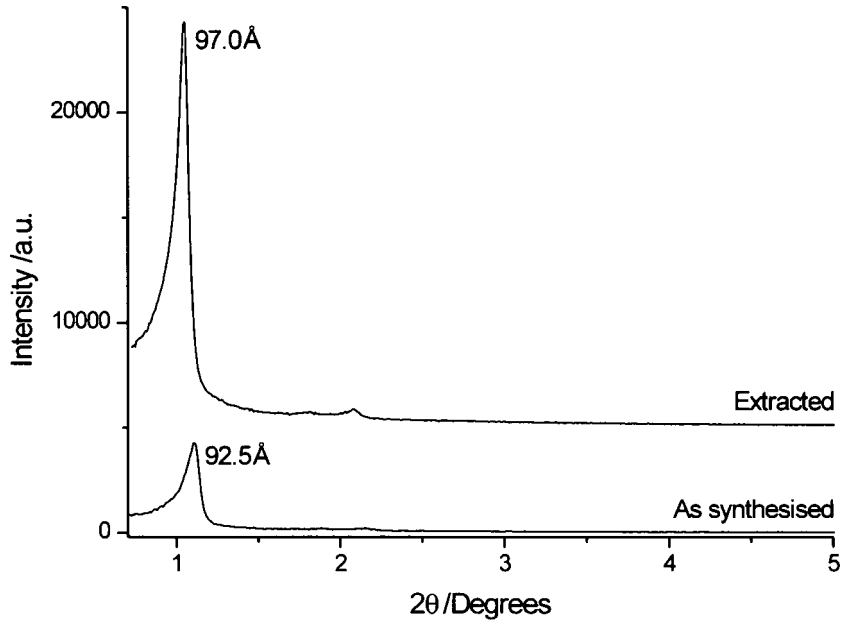

Figure 5.1. Powder XRD patterns of -CH_2CH_2-/-CH=CH-PMO.

The degree of mesoscopic ordering is reduced in all pre-hydrolyzed products (Figure 5.2 and 5.3) compared to the reference PMO indicated by the much broader low angle reflections. This is consistent with formation of larger SBU (see above) interacting with the template and assembling into surfactant-organosilica hybrids with lower degree of mesoscopic ordering. The J-PMO's show a broad reflection with d_{100} = 74.3 - 85.8 Å. The peak is shifted to lower angles (d_{100} = 87.3 - 93.9 Å) for products prepared using separate pre-hydrolysis. The broader reflections for the S-PMOs suggest a reduced mesoscopic ordering with respect to their jointly pre-hydrolysed counterparts.

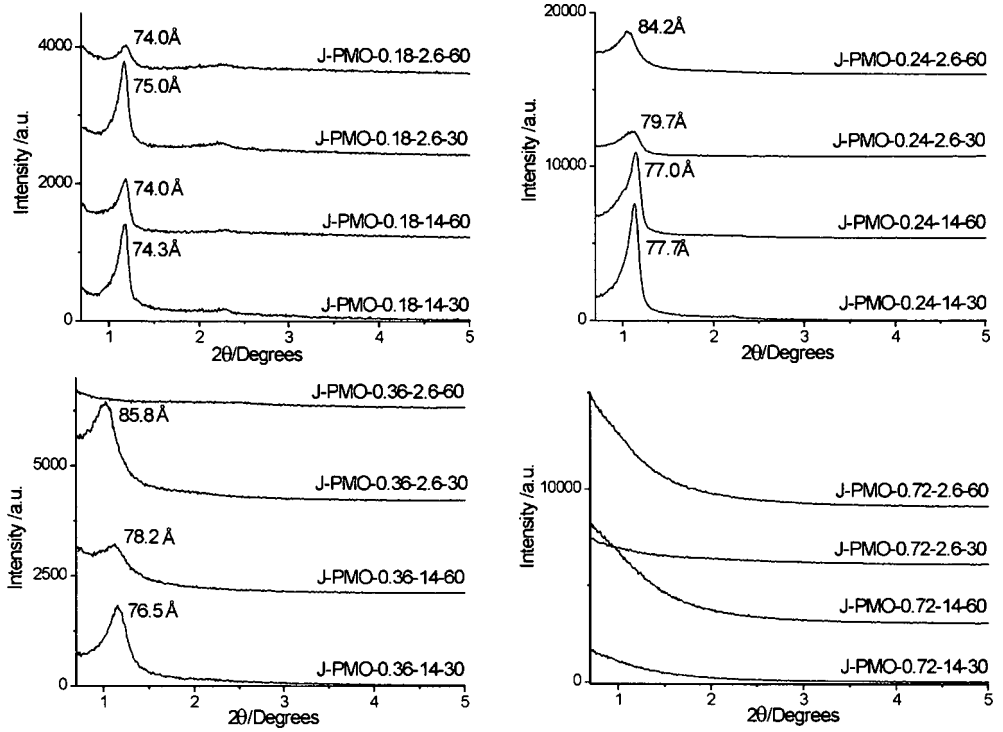

Figure 5.2. Powder XRD patterns of the as synthesized PMOs prepared using joint pre-hydrolysis of the organosilica precursors.

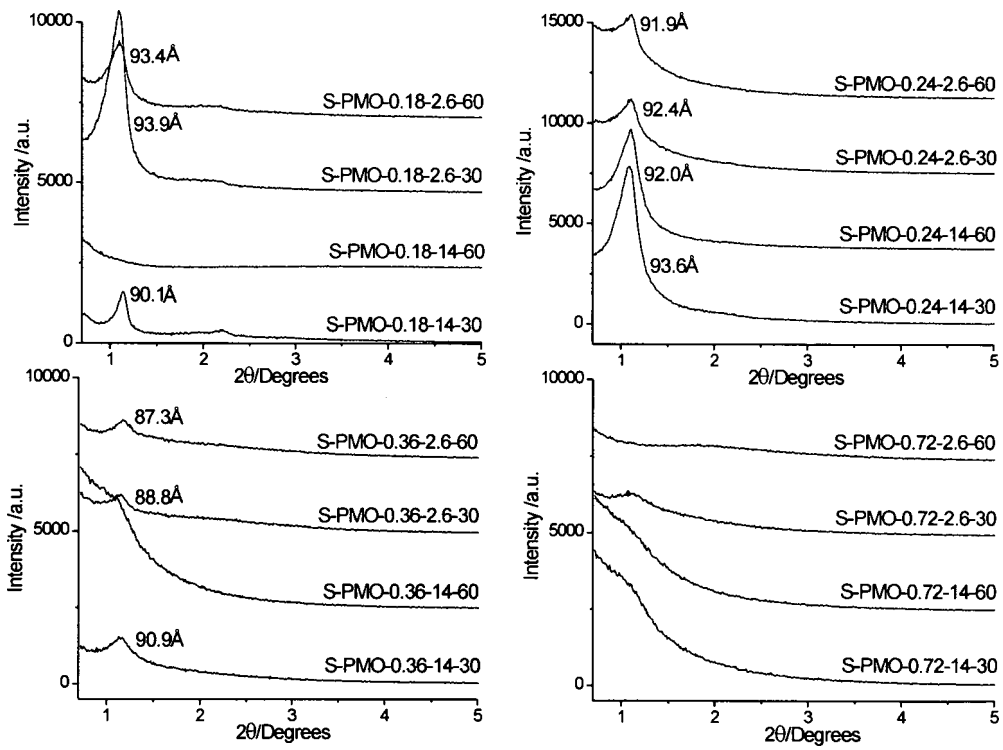

Figure 5.3. Powder XRD patterns of the as-synthesised PMOs prepared using separate pre-hydrolysis of the organosilica precursors.

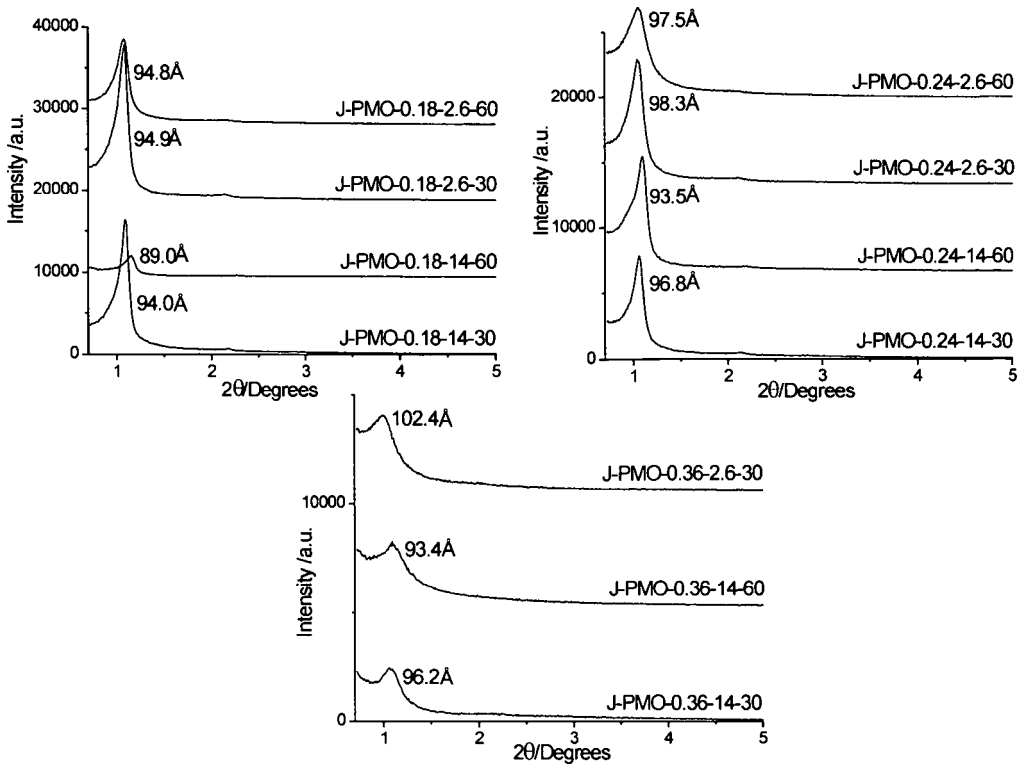

Figure 5.4. Powder XRD patterns of the surfactant extracted PMOs prepared using joint pre-hydrolysis of the organosilica precursors.

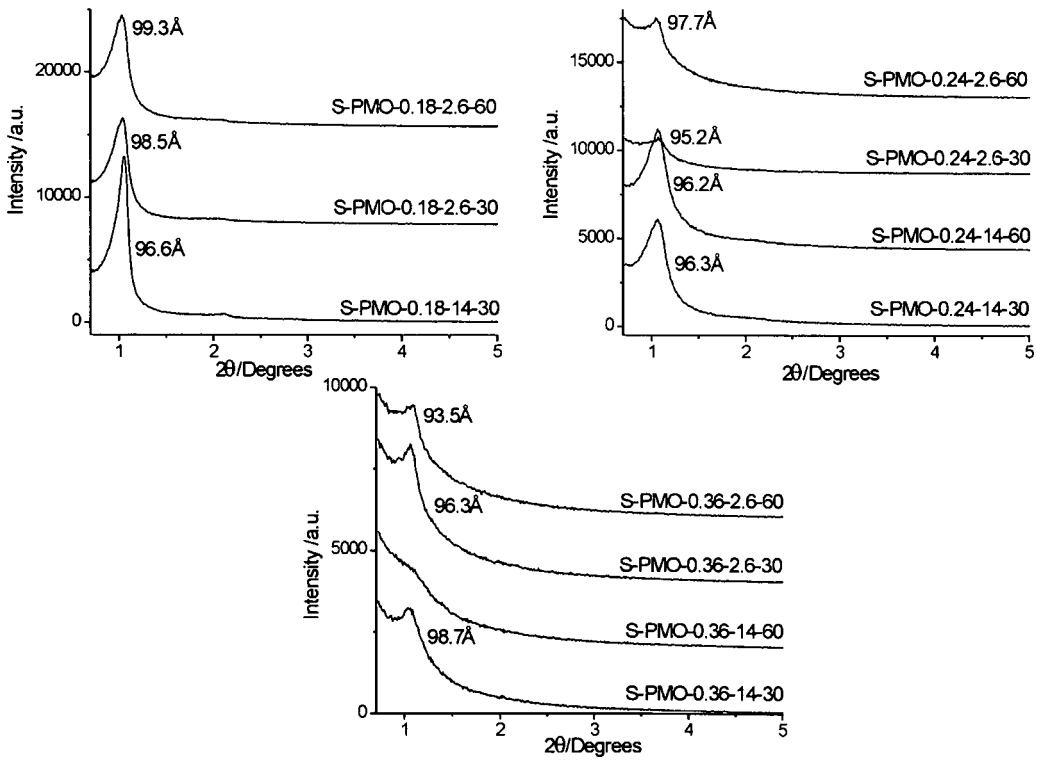

Figure 5.5. Powder XRD patterns of the surfactant extracted PMOs prepared using separate pre-hydrolysis of the organosilica precursors.

The powder XRD patterns of the template extracted products (Fig. 5.4 and 5.5) display a significant increase of the intensity, typical for mesoporous silicas.[214] The narrowing of the reflections upon the template extraction indicates a slight increase in long-range ordering. The d_{100}-spacings for the J-PMOs increased from *ca.* 85.8 to 95.5 Å upon surfactant extraction, although no change in d_{100}-spacing's was observed for the separately pre-hydrolyzed materials. Such an increase was not accompanied by a change in the degree of condensation of pore walls derived from the ^{1}H-^{29}Si CP/MAS NMR spectra (see below).

The degree of mesoscopic ordering is affected by the composition of pre-hydrolysis solution. The regions of formation of the ordered and disordered materials as a function of Si/EtOH/HCl (2M aqueous solution) are indicated in Figure 5.6. A decrease in mesoscopic ordering as the Si/EtOH ratio increases in the pre-hydrolysis mixtures is observed. Very rapid hydrolysis/condensation rates of the organosilane precursors at Si/EtOH = 0.72 prevent effective self-assembly of the pre-formed large SBU's with the template and lead to products with no mesoscopic ordering (Fig. 5.2d and 5.3d). A general decrease in mesoscopic ordering was observed as the pre-hydrolysis time increased from 30 to 60 min (Fig. 5.2a-c and 5.3a). These observations indicate that a balance between the concentration of SBU's and their size is required to form an ordered PMO.

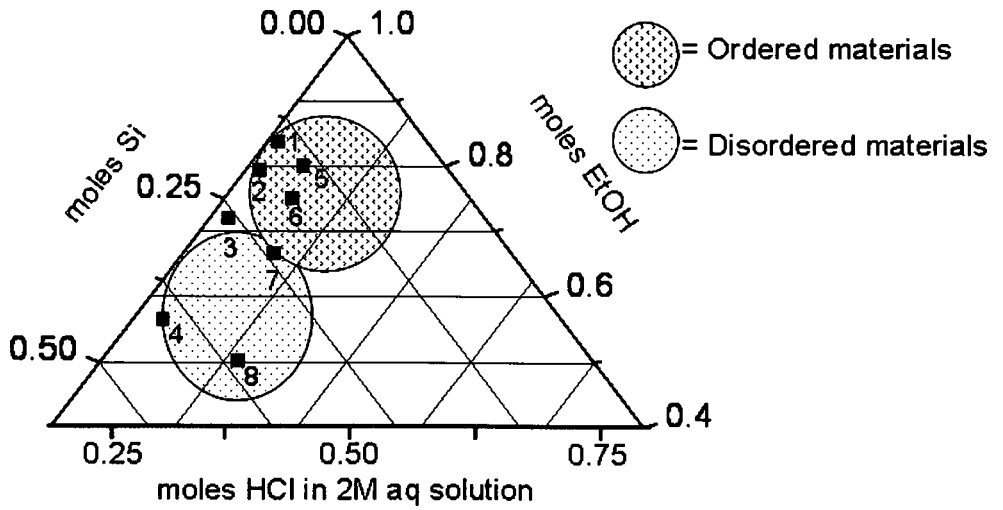

Figure 5.6. Composition of the pre-hydrolysis mixtures in terms of silica/ethanol/$HCl_{(aq)}$ ratio. 1) PMO-0.18-14, 2) PMO-0.24-14, 3) PMO-0.36-14, 4) PMO-0.72-14, 5) PMO-0.18-2.6, 6) PMO-0.24-2.6, 7) PMO-0.36-2.6 and 8) PMO-0.72-2.6.

The effect of the Si/HCl on the ordering of the materials is dependent on the Si/EtOH ratio. At high ethanol concentrations, an increase in HCl content in the hydrolysis mixture

has little effect on the ordering of the resulting products (Figure 1a). However, as the ethanol content is decreased, an increase in HCl concentration causes a reduction in the overall ordering of the products (Figure 1b). This observation is again closely linked to the molecular separation effect discussed above.

The salt assisted templating using nonionic surfactants in strong acidic media can be classified as a $S^0H^+X^-I^+$ pathway where the Cl^- ions form ion pairs with $\equiv Si(OH_2)^+$ species as well as the protonated PEO group of the surfactant with the driving force for co-operative assembly being H-bonding and ion pairing. This pathway remains valid for the selected range of pre-hydrolysis conditions, although in the system under study it appears less effective as the concentration of reactive $\equiv Si(OH_2)^+$ species is reduced due to the formation of large SBU's and hence leading to the less ordered materials (Figures S1d and S2d).

5.2.3 Transmission electron microscopy

The hexagonal symmetry of the -CH_2-CH_2-/-CH=CH-PMOs prepared without and with joint or separate pre-hydrolysis was confirmed by TEM images (Fig. 5.7). The parallel view to the pores of the -CH_2-CH_2-/-CH=CH-PMO (Fig. 5.7a) shows a honeycomb like structure while the perpendicular view (Fig. 5.7b) shows a well ordered material with well defined pore channels. The TEM image for jointly pre-hydrolyzed product J-PMO-0.18-2.6-30 (Fig. 5.7c) indicates a similar structure to that of the reference material (Fig. 5.7a) yet the honeycomb like arrangement is distorted. The TEM image of the separately pre-hydrolyzed material S-PMO-0.18-2.6-30 shows two distinct pore domains in the mesoporous framework, suggesting preferential distribution of -CH_2-CH_2- and -CH=CH- functional groups. The presence of such domains results in distorted hexagonal arrangement of pores leading to broadening of powder XRD reflections for products obtained using both separate and joint pre-hydrolysis protocols (Figure 5.7). All images for the bifunctional PMO's indicate that the materials are phase pure with no separation into two frameworks being observed. The unit cell parameter *a* of the mesostructure, estimated from the TEM images (*ca.* 87.6 Å), is in good agreement with the XRD results.

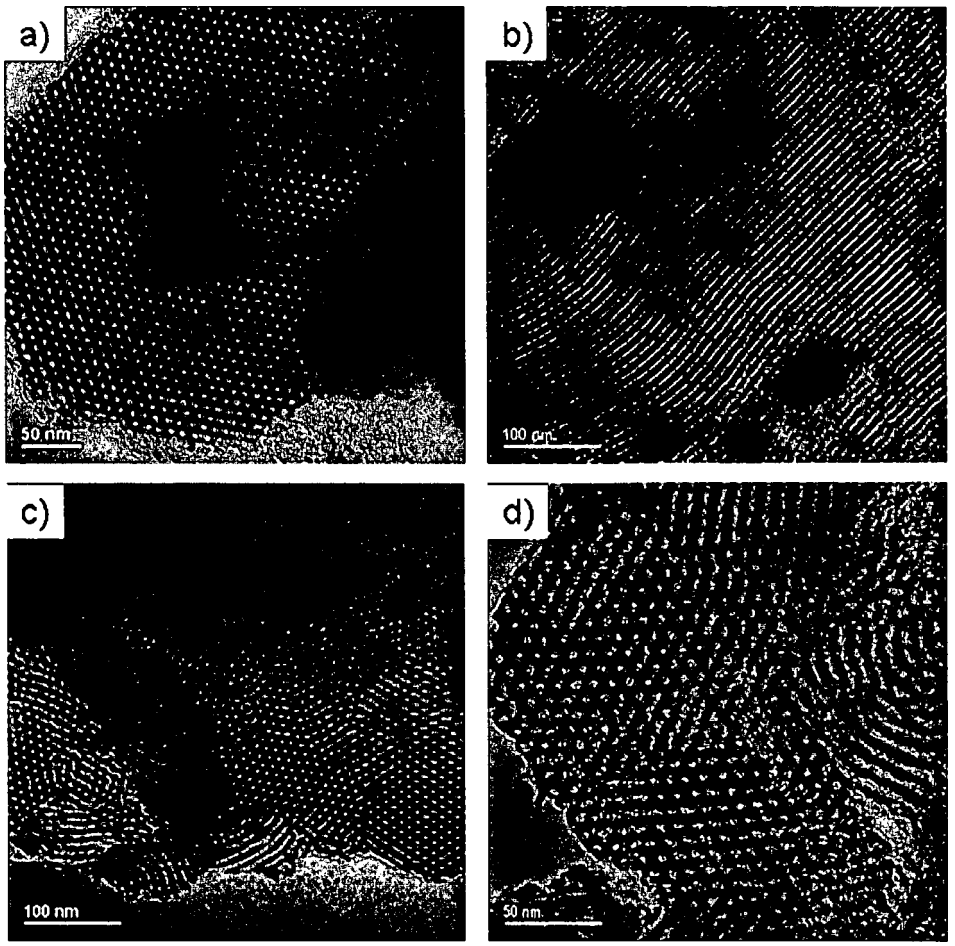

Figure 5.7. TEM images of the template extracted PMO's: a) -CH_2CH_2-/-CHCH-PMO view parallel to the pores b) -CH_2CH_2-/-CHCH-PMO view perpendicular to the pores c) J-PMO-0.18-2.6-30 d) S-PMO-0.18-2.6-30.

5.2.4 Nitrogen adsorption-desorption isotherms

The bifunctional -CH_2-CH_2-/-CH=CH-PMOs display high surface areas and large pore volumes (Table 5.1). Consistently with the results of powder XRD, the reference -CH_2-CH_2-/-CH=CH-PMO (Fig. 5.8) shows the highest degree of mesoscopic ordering with the sharpest capillary condensation step on the adsorption branch ($p/p_o \approx 0.65$). The adsorption/desorption isotherm can be ascribed as a type IV isotherm with a type H1 hysteresis. Type H1 hystereses indicate the material possess cylindrical pores of uniform size and shape.

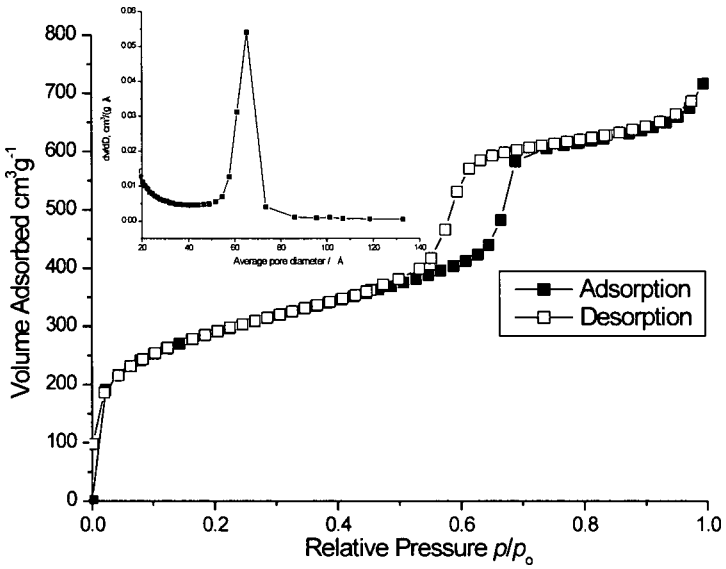

Figure 5.8. N_2 adsorption/ desorption isotherm of surfactant extracted -CH_2CH_2-/-CH=CH-PMO with the pore size distribution calculated from the adsorption branch (insert).

The majority of products prepared using the pre-hydrolysis step showed isotherms similar to that for the reference solid. However, in agreement with results of powder XRD, the overall degree of ordering is reduced. The BET surface areas, total pore volumes, micropore volumes and micropore areas for the jointly pre-hydrolysed materials are higher than for their separately pre-hydrolysed analogues. The nitrogen adsorption-desorption isotherms and pore size distribution curves of the jointly pre-hydrolyzed materials show a narrow pore size distribution with average pore diameters of *ca.* 57 Å determined from the adsorption branch of the isotherm (fig. 5.9). The material J-PMO-0.24-14-60 shows a type H2 hysteresis suggesting cylindrical pores of a non-uniform shape and size (*i.e.* ink-bottle type pores).

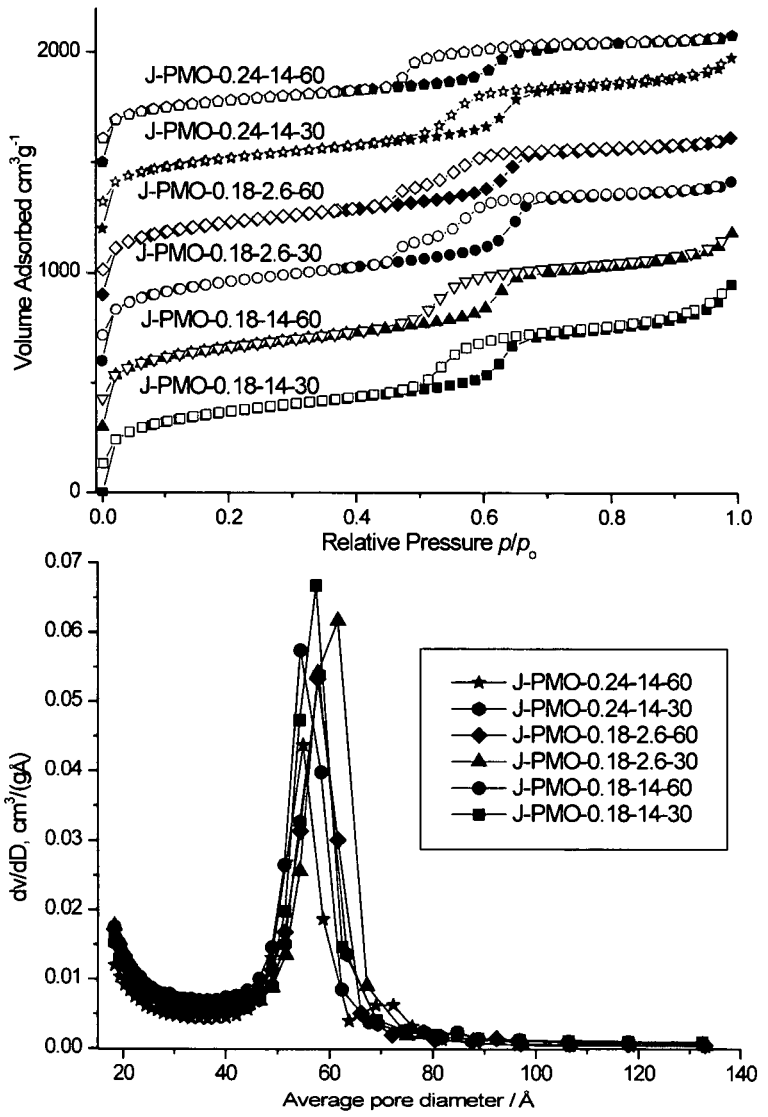

Figure 5.9. Nitrogen adsorption-desorption isotherms of surfactant extracted PMOs (top) and pore size distribution plots calculated from the adsorption branch of the N_2 isotherms (bottom), prepared using joint pre-hydrolysis.

The adsorption-desorption isotherms for the separately pre-hydrolysed materials confirmed a decrease in mesoscopic ordering upon the decrease in ethanol content during the pre-hydrolysis (fig. 5.10). The desorption branch on the isotherms of S-PMO-0.18-2.6-30/ -60 show a second step at $p/p_0 = 0.45$, such a step is also present on the isotherms of J-PMO-0.18-2.6-30/ -60. This implies the presence of two different pore openings consistent with previous studies of mesoporous silicas.[215] For example, large pore cubic (*Fm3m*) mesoporous silicas with different pore openings displayed either H1 or H2-type hystereses. Van Der Voort *et al.* also observed a second desorption step at $p/p_0 = 0.45$ and explained it as

a direct result of pore blocking.[216] The interpretation that blocked pores remain filled until the vapour pressure is lowered (p/p_0 = 0.45), after which a cavitation of the condensed N_2 occurs, and closed sections spontaneously empty is supported by non-local density functional theory (NLDFT) of adsorption and hysteresis in cylindrical pores.[217] The separately pre-hydrolyzed materials (Figure 5.10) show a narrow pore size distribution with a maximum at *ca.* 62 Å which becomes increasingly broader as the ethanol content is reduced and the pre-hydrolysis time is increased.

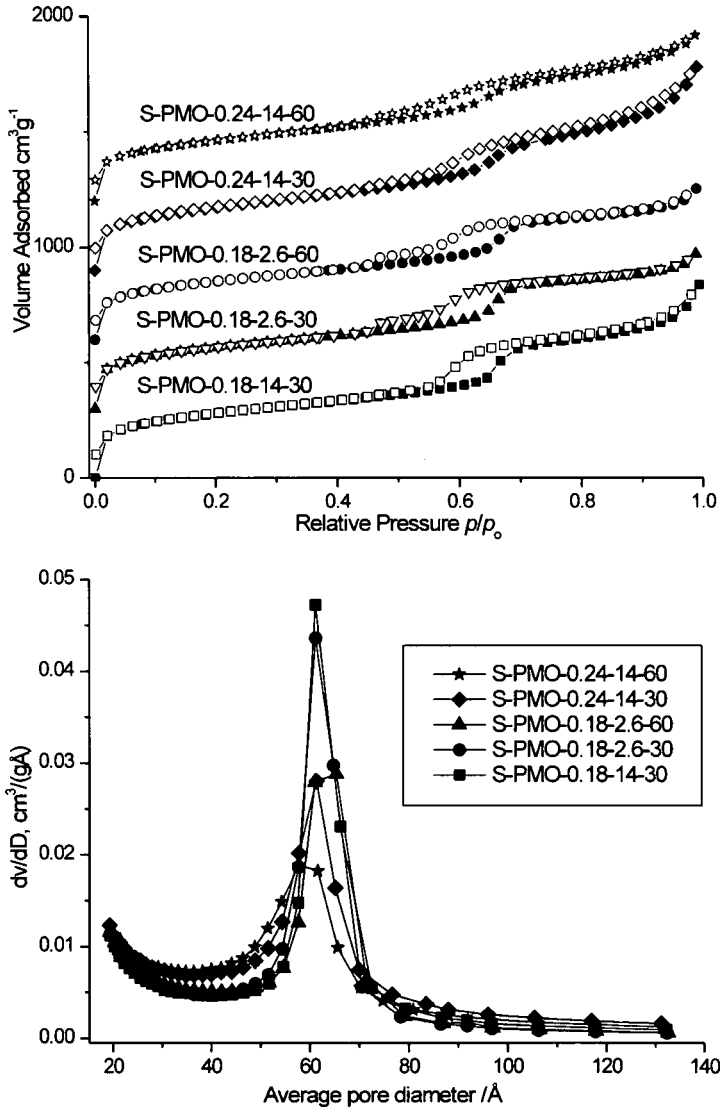

Figure 5.10. Nitrogen adsorption-desorption isotherms of surfactant extracted PMOs (TOP) and PSD plots (bottom), prepared separate joint pre-hydrolysis.

Table 5.2. Textural properties of surfactant extracted bifunctional PMOs

Sample	S_{BET} /m^2g^{-1}	V_{ads} /cm^3g^{-1}	D_{AV}^{ads} /Å	d_{100} /Å	$a^{\dagger}$ /Å	W /Å	mV_{ads}^{*} /cm^3g^{-1}	mS^{*} /m^2g^{-1}
CH_2CH_2/CHCH-PMO	1040	1.04	65.3	97.0	112	46.7	0.101	248
J-PMO-0.18-14-30	1310	1.34	57.4	94.0	109	51.1	0.139	336
J-PMO-0.18-14-60	1290	1.27	54.4	89.0	103	48.4	0.125	307
J-PMO-0.18-2.6-30	1290	1.23	61.6	94.9	110	48.0	0.125	308
J-PMO-0.18-2.6-60	1170	1.08	57.7	94.8	109	51.7	0.105	263
J-PMO-0.24-14-30	1130	1.13	58.0	96.8	112	53.8	0.113	276
J-PMO-0.24-14-60	994	0.88	54.9	93.5	108	53.1	0.137	319
S-PMO-0.18-14-30	997	1.14	61.1	96.9	112	50.8	0.097	236
S-PMO-0.18-2.6-30	946	0.97	61.1	98.5	114	52.6	0.092	224
S-PMO-0.18-2.6-60	904	0.93	65.4	99.3	115	49.3	0.077	192
S-PMO-0.24-14-30	978	1.24	61.5	96.3	111	49.7	0.057	154
S-PMO-0.24-14-60	943	1.05	57.8	96.2	111	53.3	0.067	173

Pore volumes determined at $P/P_0 = 0.9$.
† Unit cell parameter $\bar{a}$ determined from d_{100} values using $\bar{a} = 2d_{100}/\sqrt{3}$.
W = wall thickness determined from $\bar{a} - D_{av}$.
* Micropore volume and surface area determined using the t-plot method.

The results of N_2 adsorption are in good agreement with conclusions about mesoscopic ordering of the products derived from the powder XRD. Although powder XRD and nitrogen adsorption are capable of determining the overall mesoscopic ordering and textural properties of bifunctional PMOs, these methods are limited in probing the molecular level structure of such materials. Obtaining such information, in order to determine the composition, location and mobility of organic functionalities within the pore walls of PMOs, is particularly challenging due to their amorphous frameworks.

5.3 Solid-state NMR

5.3.1 ^{1}H-^{13}C CP/MAS NMR

^{1}H-^{13}C CP/MAS NMR was used to determine the presence of organic functionalities in the framework and assess the efficiency of template extraction. The NMR spectrum of the as-synthesised -CH_2-CH_2-/-CH=CH-PMO (Fig. 5.11) displays two broad resonances attributed to -CH_2-CH_2- (5.2 ppm) and -CH=CH- (147.1 ppm) bridges in the framework. These resonances remain unchanged upon surfactant extraction (Fig. 5.12). Other resonances in the spectra of the as-synthesized PMO are attributed to the pluronic surfactant: the peak at 16.7 ppm corresponds to the -CH_3 group of the PPO block; the peak at 70.7 ppm is attributed to PEO blocks; the resonances at 73.1 and 77.3 ppm correspond to CH_2 and CH sites of PPO blocks respectively.[218] In general, the surfactant peaks are narrower than those of the organic bridges, indicating a higher mobility of the surfactant PEO-PPO-PEO blocks typical of surfactant-organosilica materials.[81]

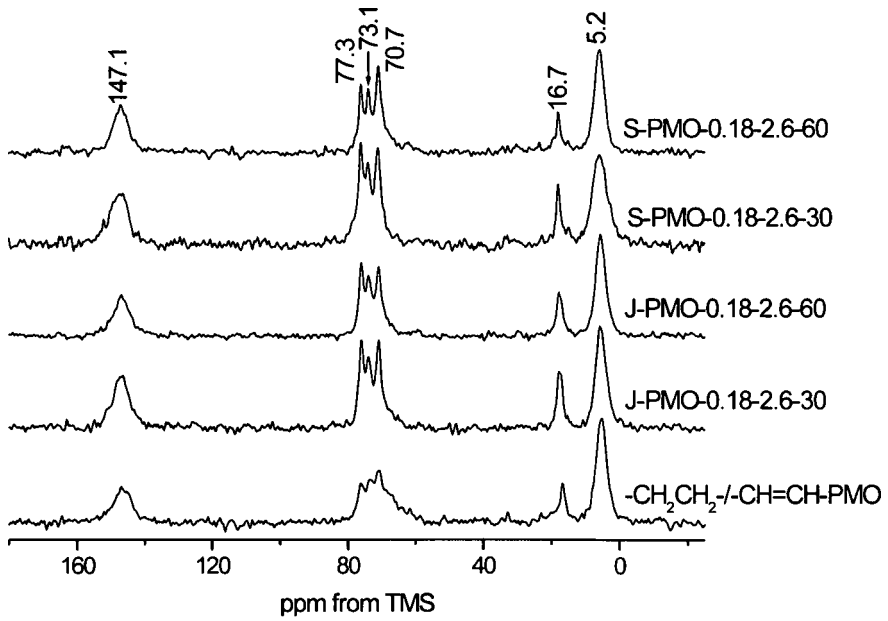

Figure 5.11. ^{1}H-^{13}C CP/MAS NMR spectra of the as-synthesised PMOs

The acid extraction was sufficient to remove the majority of template (fig. 5.12 and 5.13). However, the process becomes less efficient as the ethanol content in synthesis mixtures decreases. The two resonances at 16.4 and 59.1 ppm in the spectra of the template extracted products result from the residual ethoxy groups located on the pore surface due to the extraction process.

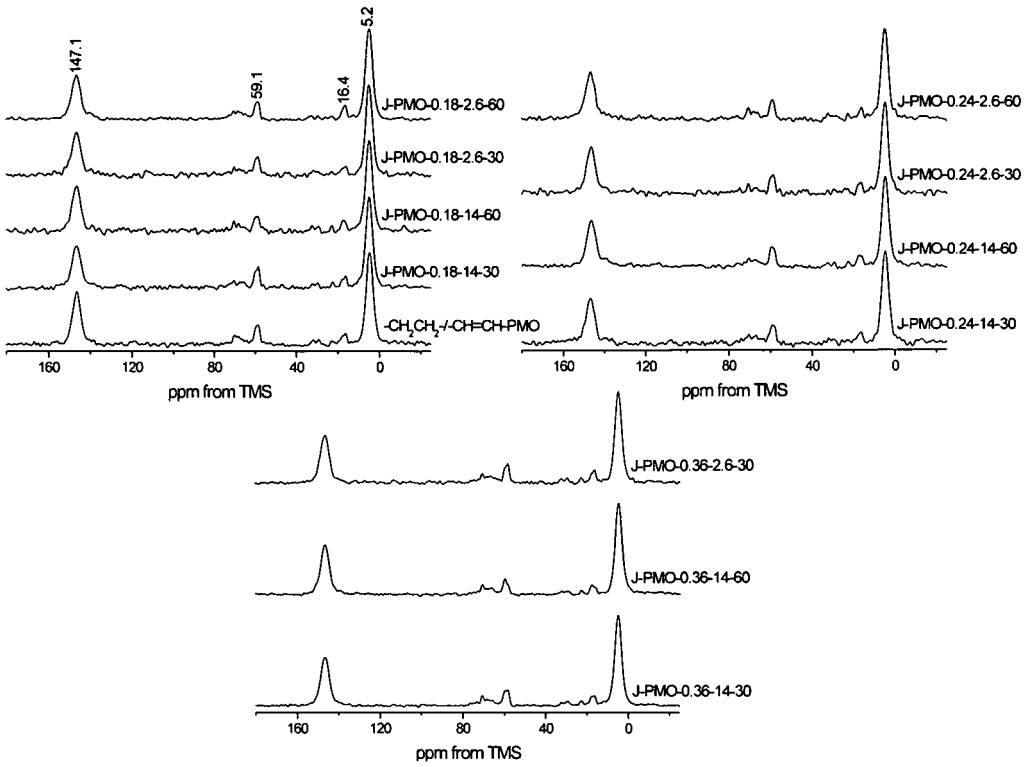

Figure 5.12. ^{1}H-^{13}C CP/MAS NMR spectra of the template extracted PMOs prepared using joint pre-hydrolysis.

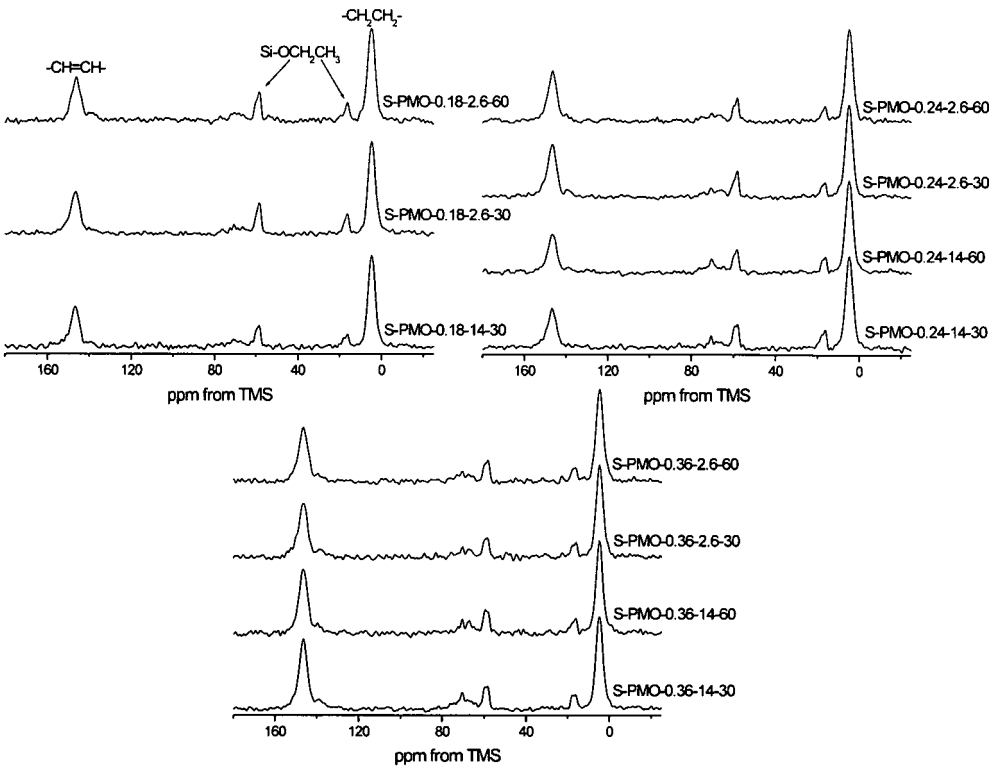

Figure 5.13. ^{1}H-^{13}C CP/MAS NMR spectra of the template extracted PMOs prepared using separate pre-hydrolysis.

5.3.2 ^{1}H-^{29}Si CP/MAS NMR

^{1}H-^{29}Si CP/MAS NMR spectra of PMOs indicate the degree of condensation of the hybrid organosilica framework and confirm the types of silicon environments present. The ^{1}H-^{29}Si CP/MAS NMR spectra (Figures 7 and ESI S9, S10) exhibit a weak resonance at –48.5 ppm corresponding to the poorly condensed T^1 sites (R-**Si**(OSi)$(OH)_2$, R = -CH_2CH_2-). The four strong resonances are assigned as follows: the lines at -56.6 and -73.4 ppm correspond to the partially condensed T^2 sites (R-**Si**$(OSi)_2(OH)$) while the resonances at −64.3 and −81.9 ppm are assigned to fully condensed T^3 sites (R-**Si**$(OSi)_3$) (R = -CH_2CH_2- and -CH=CH- respectively). The T^2 sites are typically located at the pore wall interface whereas the T^3 sites constitute the bulk of hybrid pore walls. There was no evidence of any Si-C bonds cleavage upon acid extraction as no Q^n species were observed in the region from –90 to –120 ppm both for the as-synthesized and extracted solids. The degree of condensation and relative intensity of the silicon sites remained unchanged upon surfactant extraction confirming no major changes in local structure occurred.

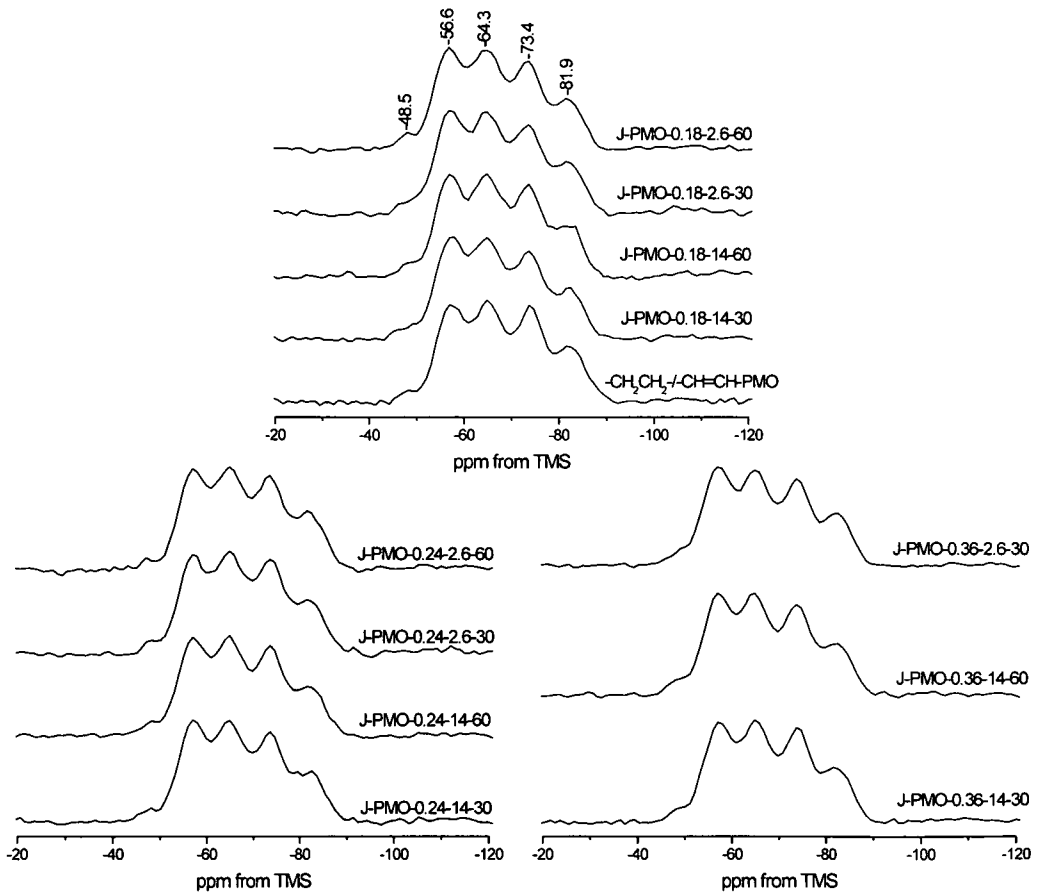

Figure 5.14. ^{1}H-^{29}Si CP/MAS NMR spectra of the template extracted PMO prepared using joint pre-hydrolysis.

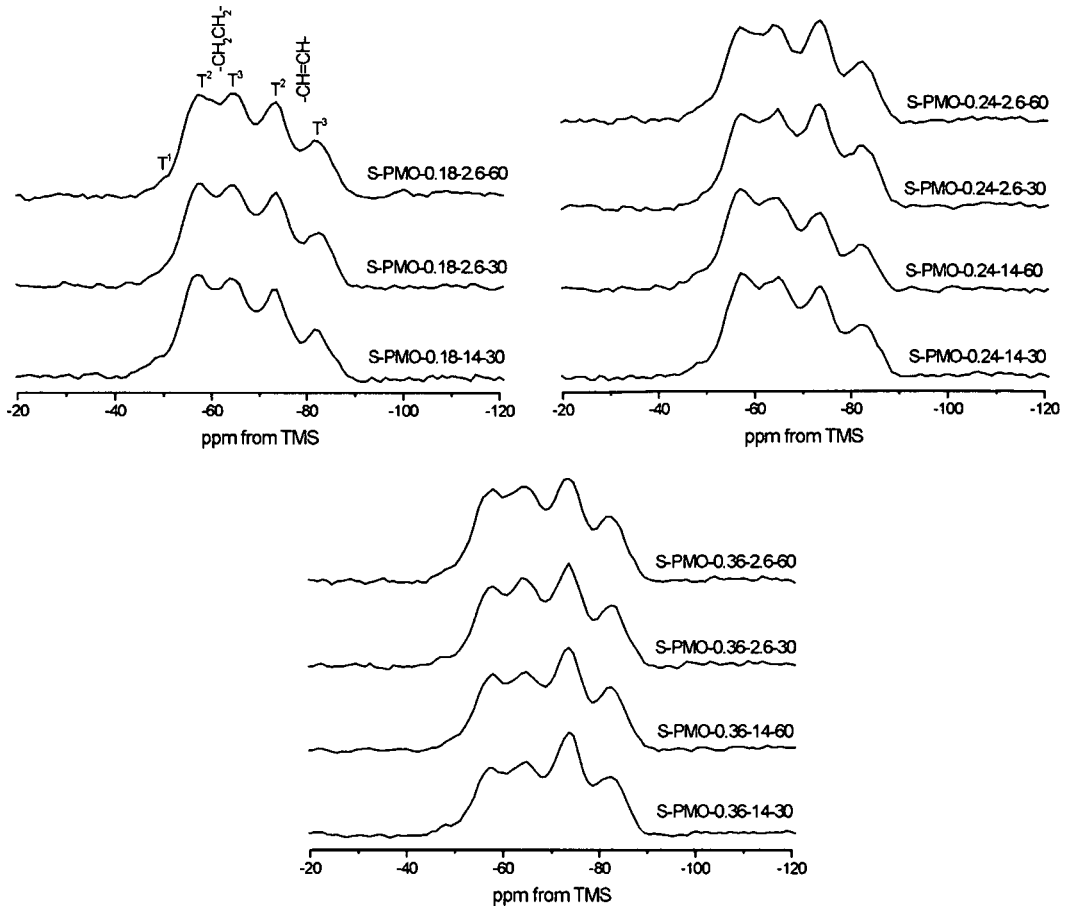

Figure 5.15. ^{1}H-^{29}Si CP/MAS NMR spectra of the template extracted PMOs prepared using separate pre-hydrolysis.

^{29}Si MAS NMR spectra (Fig. 5.16) provided quantitative information on the composition of the PMO walls. The degree of condensation $((T^1+ T^2)/T^3)$ was determined using deconvolution of the spectra (Table 5.2). In general, the silicon sites connected to -CH=CH- groups are less condensed than the ones with attached $-CH_2-CH_2-$ bridges. This observation confirms the tendency of -CH=CH- bridges to be located at the pore wall interface. The $-CH_2-CH_2-$/-CH=CH- ratio of *ca.* 1, determined from the ^{29}Si MAS NMR spectra, is in good agreement with the original synthesis composition.

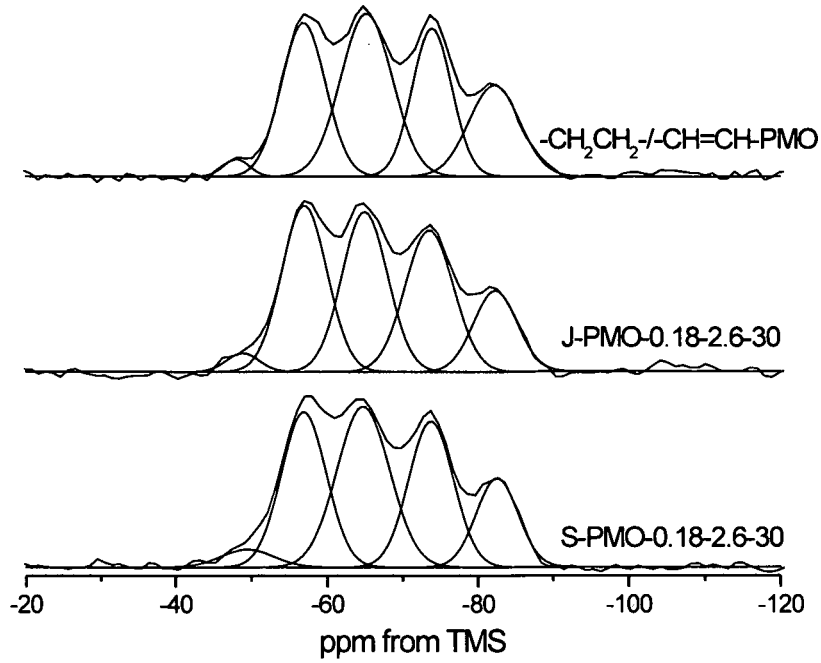

Figure 5.16. ^{29}Si MAS NMR spectra of the template extracted PMOs deconvoluted using a Gaussian function.

Table 5.2. Gaussian Deconvolution parameters of ^{29}Si MAS NMR spectra of template extracted PMOs.

Sample	Peak Area						
	-CH_2CH_2-			-CHCH-		-CH_2CH_2-	-CHCH-
	T^1	T^2	T^3	T^2	T^3	$(T^1+T^2)/T^3$	$(T^1+T^2)/T^3$
CH_2CH_2/CHCH-PMO	0.645	6.45	8.89	7.05	9.05	0.798	0.850
J-PMO-0.18-2.6-30	2.16	5.96	9.26	7.35	7.41	0.876	1.28
S-PMO-0.18-2.6-30	1.20	6.18	8.81	6.62	8.33	0.837	0.939

5.3.3 ^{1}H MAS NMR

Fast ^{1}H MAS NMR (25-30 kHz) provides sufficient resolution to assess the proton environments in the PMO's. Main ^{1}H resonances at 1.2 and 6.9 ppm are attributable to organic bridges -CH_2CH_2- and -CH=CH- respectively (Fig. 5.17). The resonance at 4.2 ppm is due to the H-bonded water and free water molecules trapped within the porous framework.

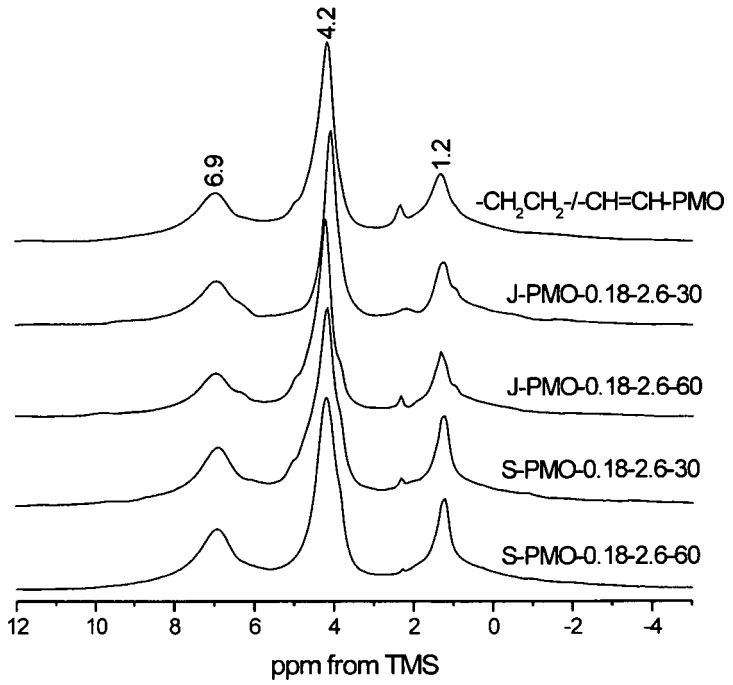

Figure 5.17. ^{1}H MAS NMR spectra of the template extracted PMOs.

The results of solid-state NMR described so far, along with powder XRD, nitrogen adsorption isotherms and TEM results suggests that well ordered mesoporous materials have been obtained. However, these results cannot confirm unambiguously that the PMOs formed are phase pure *i.e.* both organic functionalities are incorporated into the same framework. Determination of phase purity of a bifunctional PMO with amorphous frameworks is only possible *via* the application of more advanced NMR methods. Variable Contact Time (VCT) CP/MAS and HETero nuclear CORrelation (HETCOR) NMR were used to probe the dynamics of the pore walls and the distribution of the organic functionalities within the framework. The detailed analysis of structure and dynamics was performed for selected solids obtained using different pre-hydrolysis protocols: -CH_2CH_2-/-CH=CH-PMO, J-PMO-0.18-2.6-30, J-PMO-0.18-2.6-60, S-PMO-0.18-2.6-30 and S-PMO-0.18-2.6-60. These materials will be referred to as X-PMO-Y where X = J or S (joint or separate pre-hydrolysis) and Y = 30 or 60 minutes (pre-hydrolysis time) for simplification.

5.3.4 ^{1}H-^{13}C Variable Contact time CP/MAS NMR

VCT measurements are invaluable for studying structure and dynamics of complex materials and have been widely used to study polymer composites,[219] aluminophosphates[192] and mesoporous silicas[23] including PMO.[81] For the latter, such measurements were used to probe locations of the organic functionalities in the hybrid network.[81]

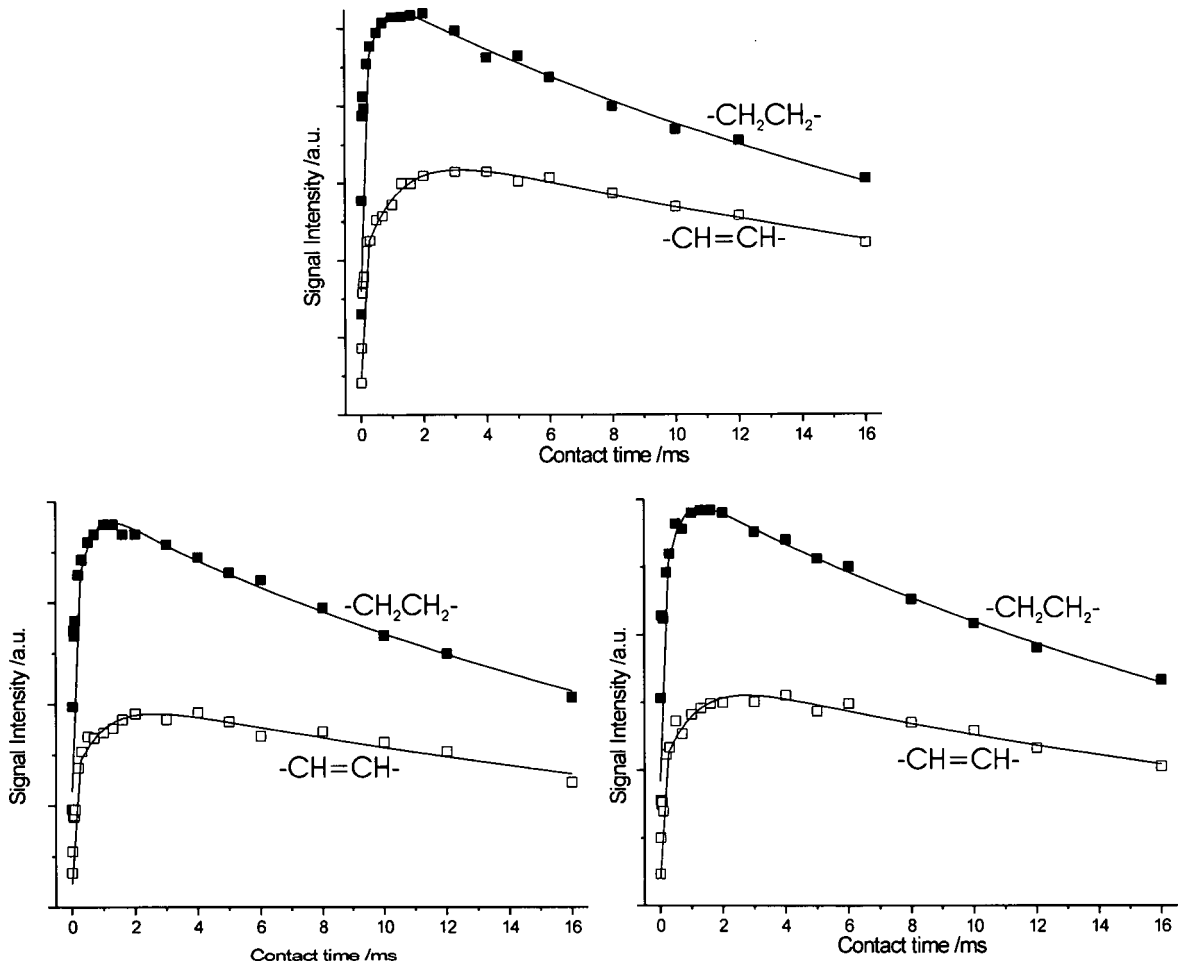

Figure 5.18. ^{1}H-^{13}C VCT CP/MAS kinetics curves of the template extracted PMOs. -CH_2CH_2-/-CHCH-PMO (top) J-PMO-30 (bottom left) and J-PMO-60 (bottom right).

Both the ^{1}H-^{13}C and ^{1}H-^{29}Si VCT CP/MAS kinetics curves have been fitted according to the I-S model. The unusual CP-dynamics curves observed for the -CH_2CH_2- and -CH=CH- bridges (Fig. 5.18 and 5.19) can only be explained using a model where two components with different T_{IS} and $T_{1\rho}{}^{H}$ times are identified depending on the mobility of the CP-determining ^{1}H source spins as seen in chapter 4. In all five products analyzed, the rigid/fast component of the -CH_2CH_2- and -CH=CH- bridges showed similar T_{cp} and $T_{1\rho}{}^{H}$ times irrespective of pre-hydrolysis conditions. This indicates that CP transfer from ^{1}H to

^{13}C is dominated by the directly attached protons and does not rely on the through space heteronuclear coupling to hydroxyl groups or adjacent organic bridges. The $T_{1\rho}{}^{H}$ times for the "mobile" component of the $-CH_2CH_2-$ bridges are shorter for S-PMOs compared to the J-PMOs (Table 5.3). This observation relates to a decrease in mobility of the protons on the organic bridges acting as a CP source. Thus the $-CH_2CH_2-$bridges at the pore wall interface of S-PMOs are in a more rigid environment.

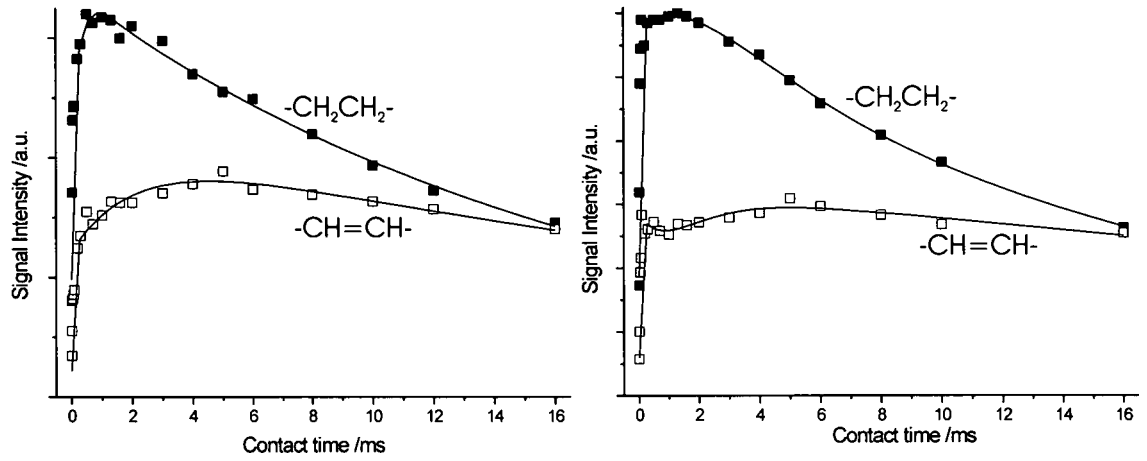

Figure 5.19. ^{1}H-^{13}C VCT CP/MAS kinetics curves of the template extracted PMOs. S-PMO-30 (left) and S-PMO-60 (right).

The longer T_{cp} times observed for both the fast and slow components of the -CH=CH-bridges compared to those for the $-CH_2CH_2-$ bridges, is a result of fewer protons acting as CP-sources. The increase in T_{CP} times of the "mobile" component compared to the "rigid" component results from a decrease in magnitude of ^{1}H-^{13}C heteronuclear dipolar coupling as a function of site mobility.

Table 5.3. ^{1}H-^{13}C VCT CP/MAS parameters obtained from the fitting of a two populations I-S model to the template extracted PMOs.

^{13}C Site		Signal Intensity / 10^7	T_{IS} / ms	$T_{1\rho}{}^{H}$ / ms	I_s/I_f	R^2
-CH_2CH_2-/-CHCH-PMO						
-CH_2CH_2-	Fast	1.52 ±0.035	0.020 ±0.002	0.592 ±0.033	1.42	0.986
	Slow	2.16 ±0.035	0.531 ±0.031	26.5 ±1.79		
-CHCH-	Fast	0.74 ±0.016	0.037 ±0.003	0.974 ±0.055	1.87	0.994
	Slow	1.39 ±0.024	1.06 ±0.048	34.7 ±2.84		
J-PMO-30						
-CH_2CH_2-	Fast	1.05 ±0.026	0.019 ±0.002	0.725 ±0.041	1.48	0.985
	Slow	1.56 ±0.026	0.593 ±0.026	25.5 ± 1.71		
-CHCH-	Fast	0.47 ±0.017	0.052 ±0.006	1.03 ±0.083	1.74	0.970
	Slow	0.82 ±0.012	0.994 ±0.047	33.4 ±2.68		
J-PMO-60						
-CH_2CH_2-	Fast	1.00 ±0.023	0.018 ±0.001	0.649 ±0.035	1.30	0.988
	Slow	1.30 ±0.022	0.562 ±0.022	24.9 ± 1.46		
-CHCH-	Fast	0.470 ±0.029	0.046 ±0.008	1.66 ±0.226	1.75	0.960
	Slow	0.823 ±0.043	1.31 ±0.138	32.2 ±7.25		
S-PMO-30						
-CH_2CH_2-	Fast	0.874 ±0.017	0.018 ±0.001	0.500 ±0.023	1.52	0.986
	Slow	1.32 ±0.011	0.412 ±0.013	18.6 ±0.602		
-CHCH-	Fast	0.486 ±0.015	0.052 ±0.005	1.96 ±0.150	1.71	0.964
	Slow	0.824 ±0.014	2.03 ±0.095	36.0 ±3.45		
S-PMO-60						
-CH_2CH_2-	Fast	0.846 ±0.016	0.027 ±0.001	0.504 ±0.018	1.07	0.994
	Slow	0.905 ±0.015	0.583 ±0.024	12.7 ±0.532		
-CHCH-	Fast	0.421 ±0.008	0.040 ±0.002	1.12 ±0.045	1.07	0.987
	Slow	0.450 ±0.012	1.49 ±0.077	33.7 ±3.98		

5.3.5 ^{1}H-^{29}Si CP/MAS kinetics

^{1}H-^{29}Si CP-kinetics curves for the -CH_2CH_2-/-CH=CH-PMO, J-PMO-30 and J-PMO-60 (Figure 5.20, Table 5.4) show much shorter T_{CP} for the -CH_2-CH_2- $T^{2,3}$ silica sites compared to those of the -CH=CH- $T^{2,3}$ sites. Shorter T_{CP} times for the T^2 sites compared with those for the T^3 sites can be explained by the presence of directly bound OH group on the T^2 sites facilitating CP build up. The difference in T_{cp} times of $T^{2,3}$ sites bound to their respective organic bridges is more pronounced for the products of separate pre-hydrolysis protocols (Figure 5.21, Table 5.4). For example, in S-PMO-60 the T_{cp} times for T^3 sites connected to -CH=CH- and -CH_2-CH_2- bridges are 3.26 and 1.58 ms respectively. Analogous J-PMO-60 prepared using joint pre-hydrolysis protocol shows T_{cp} times 3.14 ms for -CH=CH- and 1.76 ms for -CH_2CH_2- T^3 sites. The difference in T_{cp} times is less pronounced for the reference solid prepared with no pre-hydrolysis. This small change indicates a difference in the local environment of the silicon sites when separate pre-hydrolysis is used in comparison to joint pre-hydrolysis.

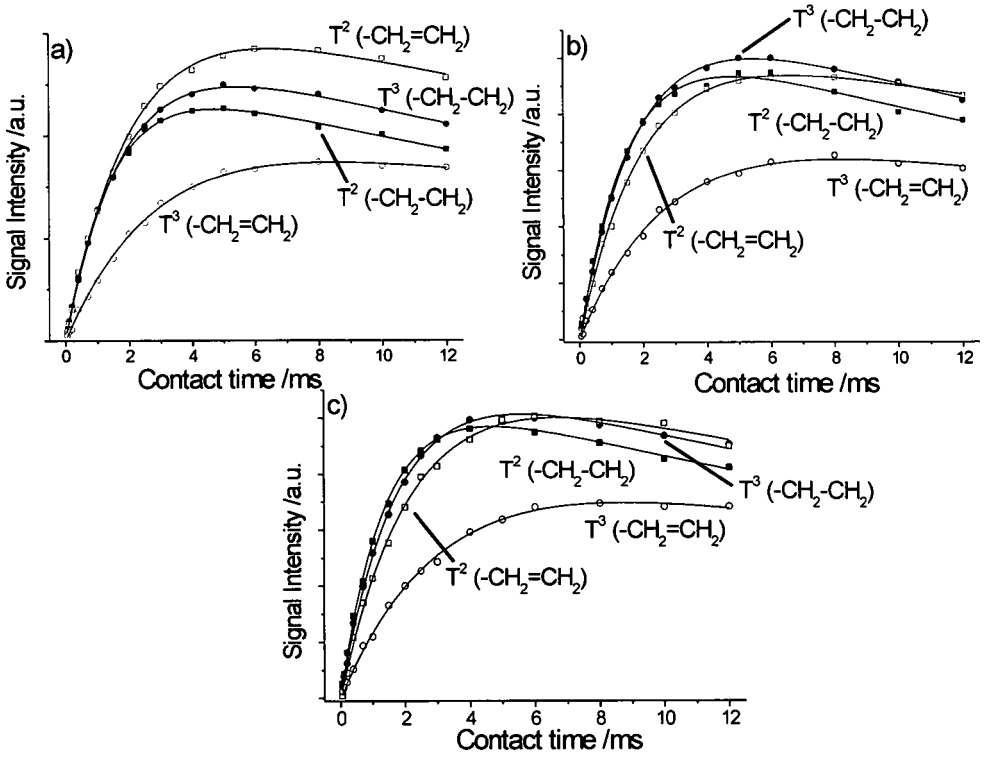

Figure 5.20. ^{1}H-^{29}Si CP/MAS NMR kinetics curves of the template extracted PMOs. a) -CH_2CH_2-/-CH=CH-PMO b) J-PMO-30 c) J-PMO-60.

The $T_{1\rho}^{H}$ times are faster for the -CH_2CH_2- $T^{2,3}$ sites *c.f.* to the -CH=CH- $T^{2,3}$ sites (figures 5.20 and 5.21). The difference in $T_{1\rho}^{H}$ relaxation times between -CH_2-CH_2- and -CH=CH- T sites is reduced as pre-hydrolysis time increases in the jointly pre-hydrolyzed materials (Table 5.5). This may indicate an increase in homogeneity of distribution of the organic functionalities within the framework. As the time of joint pre-hydrolysis increases from 30 to 60 min, the hetero co-condensation of organosilica precursors becomes significant. This is reversed for the separately pre-hydrolysed PMOs in which the difference in $T_{1\rho}^{H}$ times between the T sites of the two organic groups increases with the pre-hydrolysis time (Table 3), thus indicating an increased segregation of the organic groups within the mesostructure. Such domain structure results from the formation of monofunctional organosilica SBUs. Comparing the $T_{1\rho}^{H}$ values of pre-hydrolyzed PMOs to the reference material (-CH_2CH_2-/-CH=CH-PMO) it is clear that the two materials prepared using separate pre-hydrolysis are less homogeneous in structure compared to the reference material.

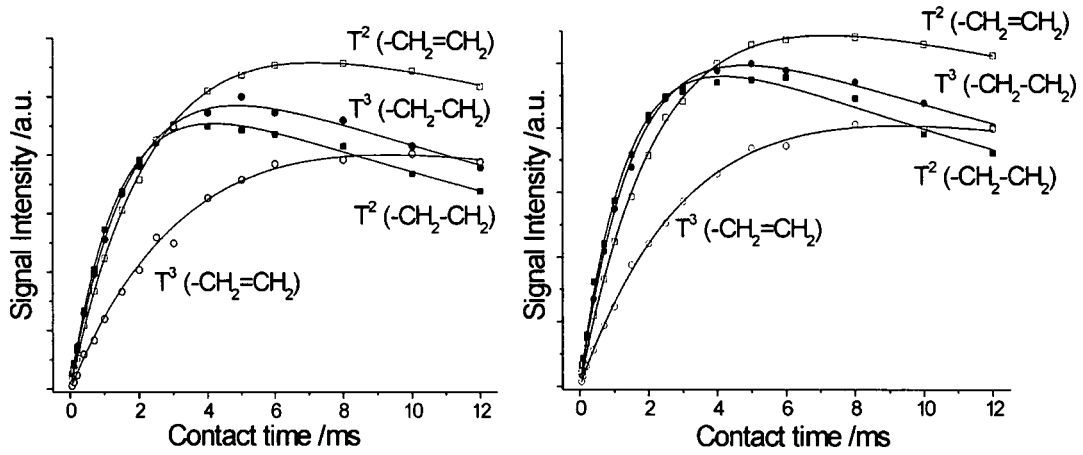

Figure 5.21. ^{1}H-^{29}Si CP/MAS NMR kinetics curves of the template extracted PMO's a) S-PMO-30 b) S-PMO-60.

Table 5.4. ^{1}H-^{29}Si CP/MAS NMR kinetics parameters for the template extracted PMOs.

Resonance /ppm	^{29}Si Site	Signal Intensity†	T_{IS} /ms	$T_{1\rho}^{H}$ /ms	R^2
-CH_2CH_2-/-CH=CH-PMO					
-56.6	-CH_2CH_2- T^2	1.06 ± 0.01	1.49 ± 0.04	30.1 ± 1.8	0.999
-64.3	-CH_2CH_2- T^3	1.18 ± 0.02	1.80 ± 0.05	30.7 ± 2.4	0.999
-73.4	-CH=CH- T^2	1.34 ± 0.01	2.07 ± 0.04	38.9 ± 2.4	0.998
-81.9	-CH=CH- T^3	0.839 ± 0.01	2.86 ± 0.06	45.1 ± 4.0	0.998
J-PMO-30					
-57.6	-CH_2CH_2- T^2	1.09 ± 0.03	1.51 ± 0.07	30.3 ± 3.4	0.998
-64.3	-CH_2CH_2- T^3	1.19 ± 0.02	1.78 ± 0.05	31.1± 2.1	0.999
-73.2	-CH=CH- T^2	1.07 ± 0.02	1.96 ± 0.07	47.9 ± 6.9	0.999
-81.4	-CH=CH- T^3	0.77 ± 0.01	2.73 ± 0.07	44.7 ± 2.3	0.999
J-PMO-60					
-56.5	-CH_2CH_2- T^2	1.11 ± 0.02	1.41 ± 0.04	33.9 ± 3.0	0.999
-64.1	-CH_2CH_2- T^3	1.19 ± 0.01	1.76 ± 0.02	35.6 ± 2.1	0.998
-72.9	-CH=CH- T^2	1.19 ± 0.01	2.22 ± 0.05	38.4 ± 1.6	0.998
-81.1	-CH=CH- T^3	0.865 ± 0.009	3.14 ± 0.08	40.1 ± 1.9	0.998
S-PMO-30					
-57.6	-CH_2CH_2- T^2	1.10 ± 0.02	1.44 ± 0.05	21.7 ± 1.4	0.998
-64.3	-CH_2CH_2- T^3	1.20 ± 0.03	1.76 ± 0.07	22.5 ± 1.9	0.998
-73.2	-CH=CH- T^2	1.35 ± 0.03	2.43 ± 0.08	38.1 ± 4.2	0.999
-81.4	-CH=CH- T^3	1.02 ± 0.01	3.56 ± 0.09	38.3 ± 1.7	0.998
S-PMO-60					
-57.0	-CH_2CH_2- T^2	1.14 ± 0.03	1.38 ± 0.07	23.7 ± 2.4	0.996
-64.0	-CH_2CH_2- T^3	1.18 ± 0.04	1.58 ± 0.04	27.7 ± 1.8	0.999
-72.9	-CH=CH- T^2	1.27 ± 0.01	2.28 ± 0.04	45.5 ± 1.6	0.999
-81.3	-CH=CH- T^3	0.99 ± 0.01	3.27 ± 0.06	45.1 ± 1.8	0.999

† All resonance intensities are normalized to that of -CH_2CH_2- T^3 site at its maximum is 1.

5.4 ^{1}H-^{29}Si Heteronuclear correlation (HETCOR) NMR

2D ^{1}H-^{29}Si HETCOR experiments provide detailed information on the spatial proximity of the two organic functionalities. The HETCOR spectrum correlates ^{29}Si resonances to ^{1}H sites in their close proximity. The spectra for the -CH_2-CH_2-/-CH=CH-PMO, J-PMO-30 and J-PMO-60 (Fig. 5.22) show the same silicon $T^{2,3}$ sites as those in the 1D ^{1}H-^{29}Si CP/MAS (discussed above) in f_2 correlated to the FSLG decoupled ^{1}H MAS spectrum in the f_1 dimension. The ^{1}H dimension shows four resonances. The resonance at 0.8 ppm is attributed to surface hydroxyl groups, a common observation in ^{1}H MAS NMR spectra of zeolitic materials.[158,159] The ^{1}H resonance at 1.8 ppm from the -CH_2-CH_2- organic bridge correlates to the silicon peaks at -56.6 and -64.3 ppm confirming the assignment of ^{1}H MAS NMR spectra. The peak at 6.8 ppm attributable to the -CH=CH- bridges correlates with the silicon T sites at -73.4 and -81.9 ppm. These auto-peaks are expected. In addition, cross-peaks correlating the -CH_2-CH_2-bridges ^{1}H resonance to the -CH=CH- silicon $T^{2/3}$ sites and *vice versa* are seen. This is indicative of a homogeneous random distribution of organic functionalities in the framework. Differences in cross-peak intensities are observed in the HETCOR spectra for the jointly pre-hydrolyzed solids and for the reference -CH_2-CH_2-/-CH=CH-PMO (Table 5.5). For the jointly pre-hydrolyzed PMOs (Figure 5.22 top) an increase in cross-peak intensity between the silicon -CH_2CH_2- $T^{2,3}$ sites and the proton -CH=CH- site is observed. This suggests that the such frameworks are more homogeneous compared to the reference material as indicated by ^{1}H-^{29}Si VCT CP/MAS data (Figure 5.20, Table 5.4). The cross-peak for the ^{1}H resonance at *ca.* 4.2 ppm to all four silicon sites confirms its assignment as H-bonded water molecules close enough in space to the silicon sites to act as CP 'donors'. An H_2O peak is observed at *ca.* 4.2 ppm in the ^{1}H MAS NMR spectra although its intensity is reduced in the HETCOR experiments.

The ^{1}H-^{29}Si HETCOR spectra of the S-PMO-30 and S-PMO-60 show a decreased intensity of the peak of the surface hydroxyl group at 0.8 ppm upon increased pre-hydrolysis time. A reduction in cross-peak intensities for the silicon -CH_2-CH_2- $T^{2,3}$ and -CH=CH- proton resonances along with a similar reduction for correlations between the silicon -CH=CH- $T^{2,3}$ sites and -CH_2-CH_2- proton sites are observed for S-PMOs in comparison to J-PMOs and the reference material (table 5.5). This can only be observed if the two different organic bridges are within the same mesoporous framework proving phase purity of S-PMOs. It is clear that a structure with domains consisting preferentially of -CH_2-CH_2- and -CH=CH- functional groups in the same mesoporous framework is formed proving the

efficiency of pre-hydrolysis procedure relying on the co-condensation of mono organo-functionalised SBUs (scheme 1).

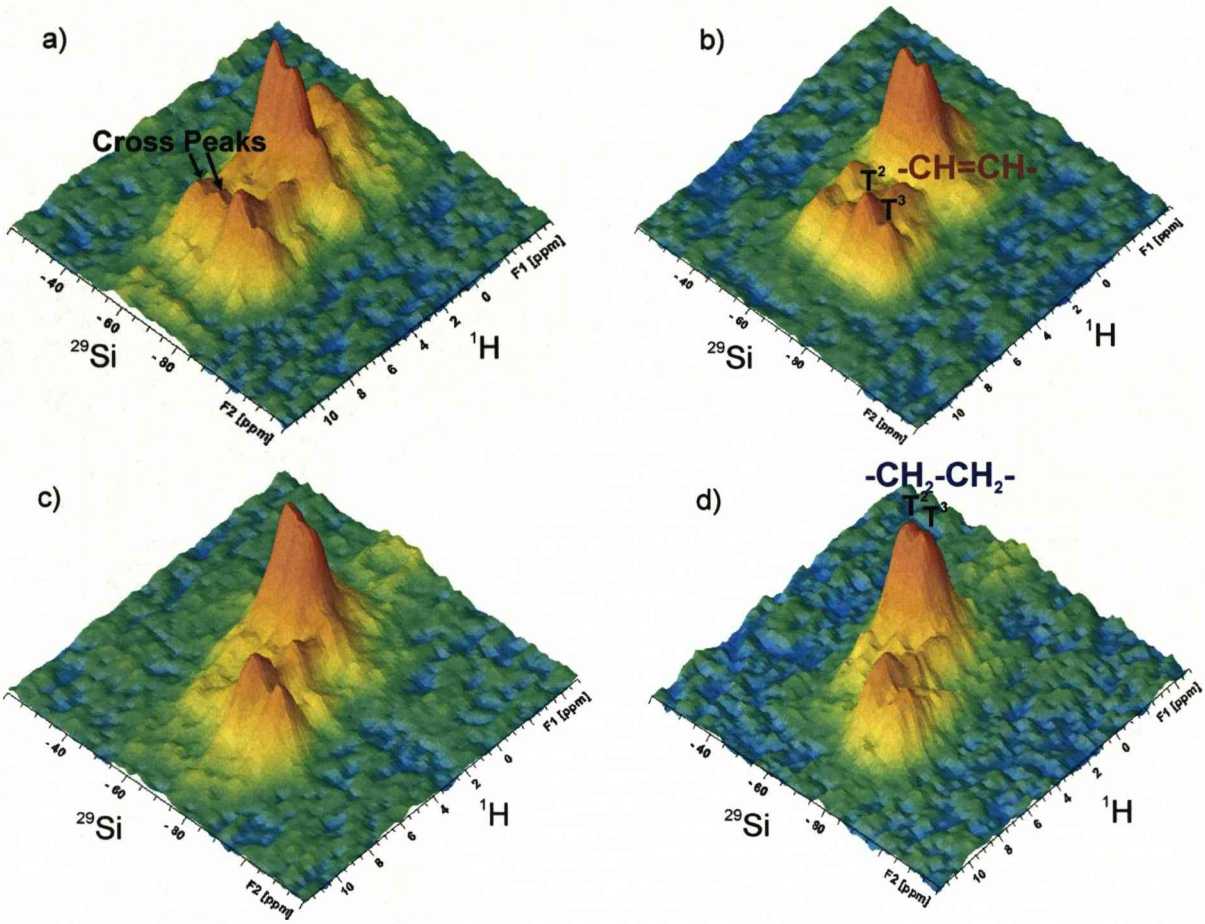

Figure 5.22. ^{1}H-^{29}Si HETCOR NMR spectra of the template extracted PMOs. a) J-PMO-30 b) J-PMO-60 c) S-PMO-30 d) S-PMO-60.

The HETCOR and ^{1}H-^{29}Si VCT CP/MAS NMR results are complementary and suggest that when joint pre-hydrolysis is used, the products are similar to the reference material and feature an increasingly homogeneous framework as hydrolysis time increases. For separately pre-hydrolyzed solids the organic functionalities become more segregated as pre-hydrolysis time increases. The homogeneity of the products depends on the pre-hydrolysis conditions, with respect to the predominant co-condensation (homo *vs.* hetero condensation of the organosilica precursors), in the formation of organosilane SBUs.

Table 5.5. Intensities of cross-peaks in the ^{1}H-^{29}Si HETCOR NMR spectra. Values are normalized to those of the $-CH_2CH_2-$ T^3 resonance.

^{29}Si Resonance / ^{1}H Resonance	$-CH_2CH_2-$		-CH=CH-	
	T^2	T^3	T^2	T^3
$-CH_2CH_2-$/-CH=CH-PMO				
$-CH_2CH_2-$	0.952	1.00	0.591	0.288
-CH=CH-	0.326	0.414	0.573	0.429
(Auto peak $T^2 + T^3$)/ (Cross peak $T^2 + T^3$)	2.64		1.14	
J-PMO-30				
$-CH_2CH_2-$	1.11	1.00	0.592	0.298
-CH=CH-	0.473	0.512	0.665	0.514
(Auto peak $T^2 + T^3$)/ (Cross peak $T^2 + T^3$)	2.14		1.32	
J-PMO-60				
$-CH_2CH_2-$	1.04	1.00	0.460	0.252
-CH=CH-	0.367	0.433	0.692	0.521
(Auto peak $T^2 + T^3$)/ (Cross peak $T^2 + T^3$)	2.55		1.70	
S-PMO-30				
$-CH_2CH_2-$	1.07	1.00	0.458	0.186
-CH=CH-	0.202	0.234	0.680	0.584
(Auto peak $T^2 + T^3$)/ (Cross peak $T^2 + T^3$)	4.75		1.96	
S-PMO-60				
$-CH_2CH_2-$	0.984	1.00	0.400	0.107
-CH=CH-	0.081	0.124	0.647	0.524
(Auto peak $T^2 + T^3$)/ (Cross peak $T^2 + T^3$)	9.68		2.31	

5.5 ^{1}H Spin diffusion NMR

The presence of structural changes as a function of pre-hydrolysis can be further confirmed using 2D ^{1}H-^{1}H spin diffusion NMR. The 2D spin diffusion experiment is essentially the same as 2D NOESY which has been used in the study of proteins and membranes to determine inter-nuclear distances *via* cross relaxation rates in solution NMR.[220-222] However, in solids the presence of ^{1}H spin diffusion means that cross peak intensities indicate the magnitude of ^{1}H spin diffusion between the two different proton environments. As spin diffusion is dependent on homonuclear dipolar couplings, which in turn are a function of ^{1}H-^{1}H distance, the intensity of the cross-peaks increases as the proton environments are closer together.

^{1}H spin diffusion MAS NMR spectra of the template extracted J-PMO-60 and S-PMO-60 (Fig. 5.23) show than under joint pre-hydrolysis conditions the cross-peak intensities are increased. This confirms the ^{1}H-^{29}Si HETCOR results in that the organic bridges are closer in space under joint than separate pre-hydrolysed PMOs.

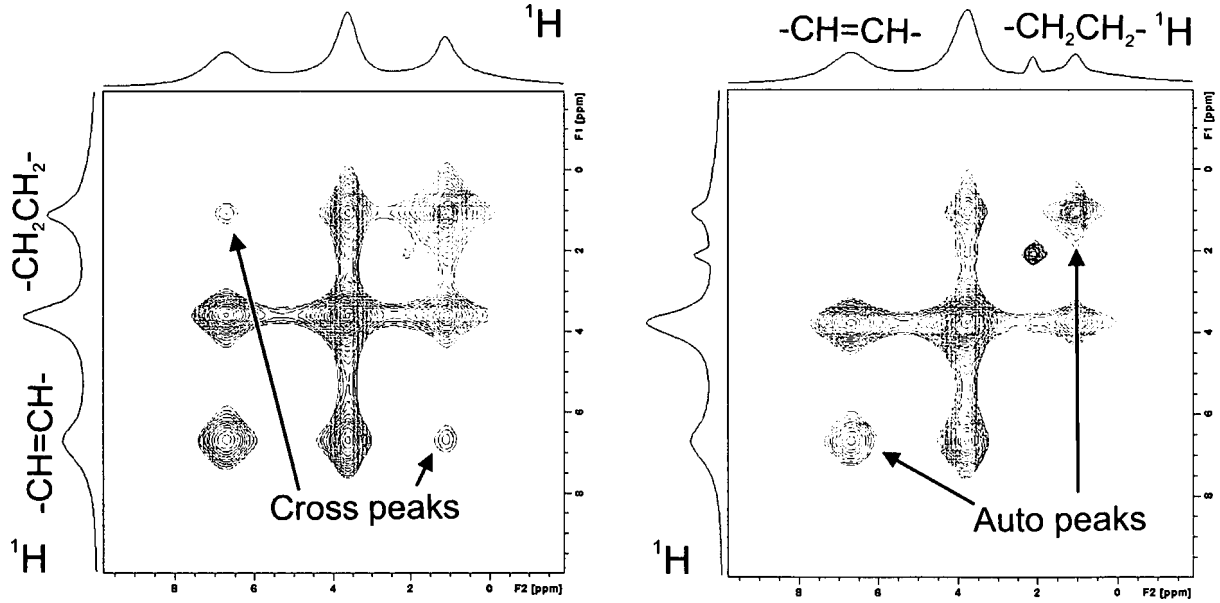

Figure 5.23. ^{1}H MAS spin diffusion NMR of the template extracted J-PMO-60 (left) and S-PMO-60 (right).

The much faster experimental time of 2D ^{1}H-^{1}H spin diffusion compared to the ^{1}H-^{29}Si HETCOR experiments has enabled us to monitor the build up of cross peak intensities as

a function of mixing time (Fig. 5.24). The Build up of cross peak intensities can be fitted using a spin pair model[223] (Eq. 5.1) to yield cross relaxation rates (σ_{ij}):

$$A_{ij}(t_m) = (A_{jj}(0)/2)(1 - \exp(-2\sigma_{ij}t_m))\exp(-t_m/T_{ij}) \qquad \textbf{Eq. 5.1}$$

Where $A_{ij}(t_m)$ is the cross peak volume at mixing time t_m and $A_{jj}(0)$ the diagonal peak volume at $t_m = 0$. The rate of magnetisation leakage towards the lattice is defined by $1/T_{ij}$.

The cross-peaks for J-PMO-60 are of a higher intensity irrespective of mixing time further confirming the organic bridges are in closer proximity. The curves reach a maximum after 60 - 80 ms. This indicates "leakage" of cross-peak magnetisation back to the lattice *via* T_1 relaxation.[223]

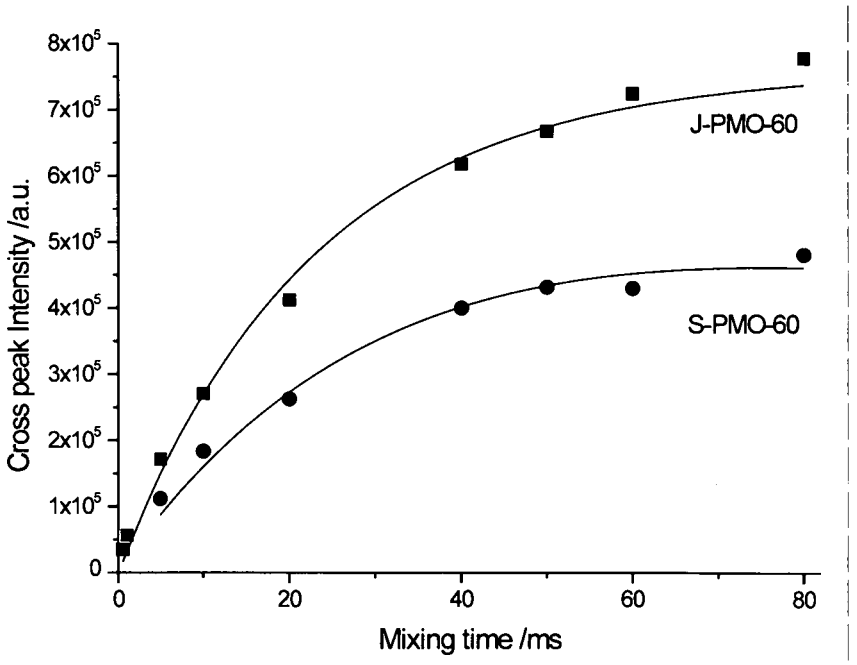

Figure 5.24. ^{1}H 2D spin diffusion cross peak intensities *versus* mixing time for the template extracted J-PMO-60 and S-PMO-60.

The use of equation 5.1 is limited in the case of solid-state NMR as the spin diffusion process resulting in cross peak build-up is different to that of the polarisation transfer Nuclear Overhauser Effect (NOE) observed in solution state NMR. That is NOE occurs *via* incoherent cross relaxation induced by the irreversible stochastic modulation of local fields by molecular motion.[160] Therefore, the process of cross peak build up in the solid-state

NMR can only yield relative distances between ^{1}H environments. This is especially true for non-crystalline solids due to the lack of long range ordering and consequent fluctuation of ^{1}H distances. More recently the application of ^{1}H CRAMPS spin diffusion NMR has been applied to the crystalline molecule thymol found in the oil of thyme.[224] The results of the spin diffusion NMR coupled with the knowledge of unit cell coordinates and space group could be used to propose structural models and determine ^{1}H distances via molecular modelling.[224]

5.6 Conclusions

Mesoporous bifunctional -CH_2-CH_2-/-CH=CH-PMOs with both organic functionalities incorporated in the same mesoporous framework have been prepared in the presence of a non-ionic block co-polymer surfactant, using a modified synthetic procedure to control the properties of the products. The distribution of organic groups in PMOs can be controlled using pre-hydrolysis of organosilica precursors. In joint pre-hydrolysis conditions a homogenous distribution of the two organic groups was observed. However, when separate pre-hydrolysis conditions were used a domain type structure containing segregated regions of -CH_2CH_2- and -CH=CH- bridges within the same mesostructural framework was obtained (Scheme 5.2). The distribution of organic functional groups was confirmed by ^{1}H-^{29}Si HETCOR, CP kinetics and ^{1}H 2D NOESY NMR.

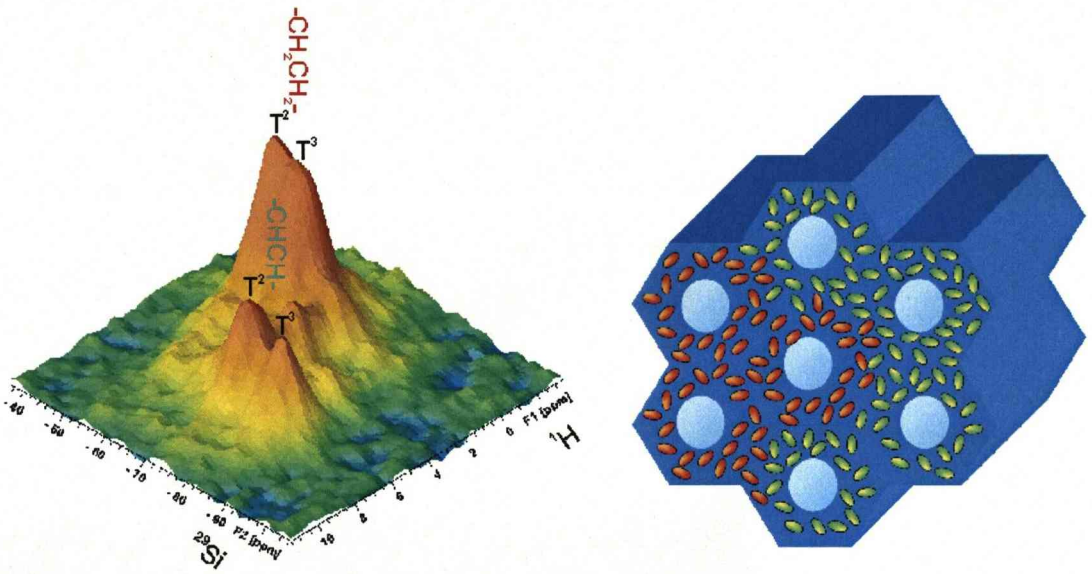

Scheme 5.2. ^{1}H-^{29}Si HETCOR spectrum of S-PMO-30 (left) and the proposed picture representation of the organic bridge distribution.

The determination of domain sizes within the separately pre-hydrolysed PMOs may be possible if the process of ^{1}H spin diffusion can be quantified. As spin diffusion is dependent on internuclear distance, a measurement of the rate of spin diffusion could yield information on average ^{1}H-^{1}H distances. Methods proposed by Wu *et al.* by using depolarisation of the rare spins in CP/MAS could be used here however, the applicability of this technique to amorphous frameworks is untested as only glycine was used.[225] Further experiments for determination of domain sizes in polymers used the 2D ^{13}C CP/MAS correlation driven by ^{1}H spin diffusion, which can characterise domain sizes in the region of

1 to 200 nm.[226,227] This approach appears to be more suited to PMOs as the experiments have been tested on semi-crystalline solids. The drawback of the 2D ^{13}C correlation experiments are the need for partial enrichment or long experimental times to provide useful information.

PMOs prepared using both joint and separate pre-hydrolysis showed high surface areas and large pore volumes with narrow pore size distributions. These properties would make these materials ideal for the use in molecular recognition/separation of medium or large organic molecules. The ability of controlling the distribution of organic functionalities and characterizing the resulting complex porous structure with limited long range ordering can be considered as a step forward in both the synthesis of complex hierarchical materials.

Bifunctional -CH_2CH_2-/-C_6H_4-PMOs: Comparison of S^+I^- and $S^0H^+X^-I^+$ Templating Pathways

Chapter 6

6.1 Introduction

Under acidic conditions the application of pre-hydrolysis protocols to bi-functional -CH_2CH_2-/-CH=CH-PMOs resulted in the formation of domain type structures. In this chapter we describe systems where the -CH=CH- functionality was substituted with aromatic -C_6H_4- groups to test the compatibility of the pre-hydrolysis protocols to different organic bridges. This is essential if the pre-hydrolysis protocols are to be used in the future design of porous hybrids incorporating more complex bridges and/or tethers. Secondly, the synthesis was also carried out in basic medium using quaternary ammonium cationic surfactants *via* S^+I^- templating pathway.

The use of aromatic precursors in basic conditions results in molecular level ordering within the pore walls as first reported by Inagaki *et al.*[57] Such ordering is due to the stacking of the delocalised electron clouds of the aromatic rings. The π-π stacking then leads to the formation of repeating aromatic layers within the pore walls of the hexagonal mesostructure detected by higher order reflections in powder x-ray diffraction (PXRD) patterns. The presence of such molecular level ordering in PMOs is unique to functionalities which can form π-π stacking conformations. In general, only PMOs synthesised in basic conditions have shown high levels of molecular level ordering. However, Sayari *et al.* indicated the presence of molecular level ordering in bi-phenyl-PMOs synthesised under acidic conditions using block-copolymer templates. Though the degree of mesoscopic ordering determined from PXRD was reduced significantly compared to bi-phenyl-PMOs prepared under basic conditions.[90] Molecular level ordering of C_6H_4-PMOs has also been achieved by using post synthetic treatments of the as-synthesised PMO in alkaline solutions of NH_3, NaOH and TPAOH yet these treatments resulted in the degradation of the mesostructure as seen by PXRD.[228]

The synthesis of molecularly ordered bi-functional PMOs was demonstrated for phenyl/bi-phenyl PMOs under basic conditions.[90] The authors concluded that their PMOs were either forming segregated domains or phase separation was occurring. This conclusion is derived from PXRD reflections, attributed to both functionalities when equimolar mixtures where used, although no detailed NMR analysis was conducted.[90] The synthesis of molecularly ordered bi-functional PMOs containing aliphatic organic functionalities, to the best of our knowledge, is yet to be demonstrated. Therefore, the preparation of a –CH_2CH_2-/C_6H_4-PMO under basic conditions would be interesting in terms of how the aliphatic

component influences molecular scale periodicity. Furthermore, the application of pre-hydrolysis may also produce bi-functional PMOs where there are segregated domains of molecularly ordered aromatic functionalities and amorphous aliphatic bridges. Finally, how the use of two different, S^+I^- and $S^0H^+X^-I^+$ synthetic pathways, affects the $-CH_2CH_2-$/$-C_6H_4-$ PMOs in terms of meso- and molecular level organisation, textural properties and composition; in addition to, the influence of the pre-hydrolysis protocols will be investigated.

6.2 Results and Discussion

The synthesis conditions of the PMOs presented in this chapter are described in detail in chapter 3. Briefly, the S^+I^- templated PMOs are synthesised using the quaternary ammonium surfactant (ODTABr) in aqueous/NaOH solutions. Whereas the $S^0H^+X^-I^+$ templated PMOs are prepared using a block co-polymer template (P123) under aqueous/acidic conditions. The organosilicas precursors undergo hydrolysis/condensation reactions and subsequently co-condensates around the template micelles to yield the as-synthesised organosilicas.

All the standard mono- and bi-functional PMOs are labelled according to the organic functionalities incorporated. The bi-functional pre-hydrolysed PMOs are all labelled according to the pre-hydrolysis conditions, X-PMO-Y-Z where X = J or S indicate joint or separate pre-hydrolysis, Y = 2.6 or 14 is the Si/NaOH ratio in the pre-hydrolysis mixtures and Z = 30 or 60 indicate the duration of pre-hydrolysis time (minutes) before addition to the template solution.

6.2.1 Powder X-ray Diffraction

6.2.1.1 S^+I^- templated PMOs

Powder X-ray diffraction patterns were measured for all as-synthesised (not shown) and template extracted products at both low and high 2θ ranges.

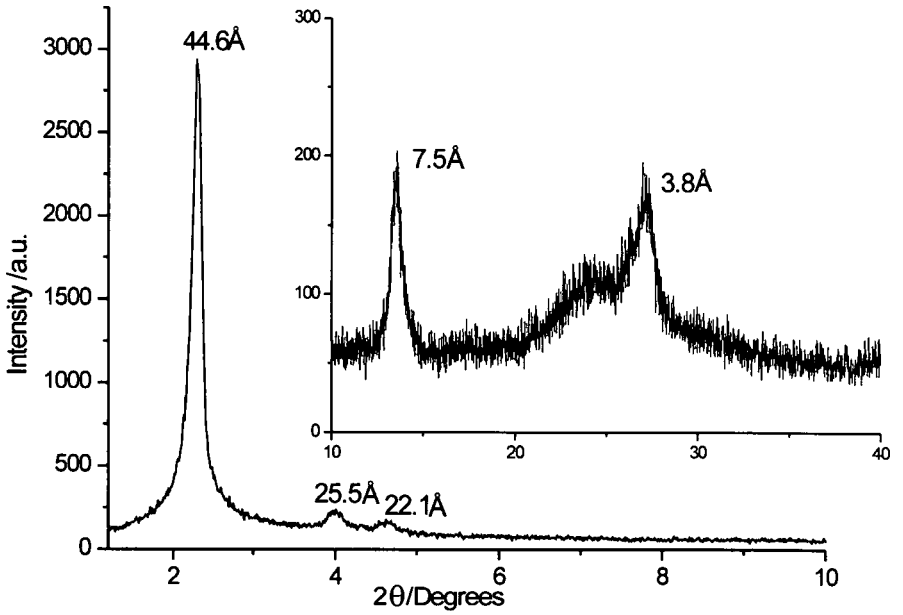

Figure 6.1. PXRD pattern of template extracted -CH_2CH_2-/-C_6H_4-PMO prepared *via* S^+I^- synthetic pathway with no pre-hydrolysis.

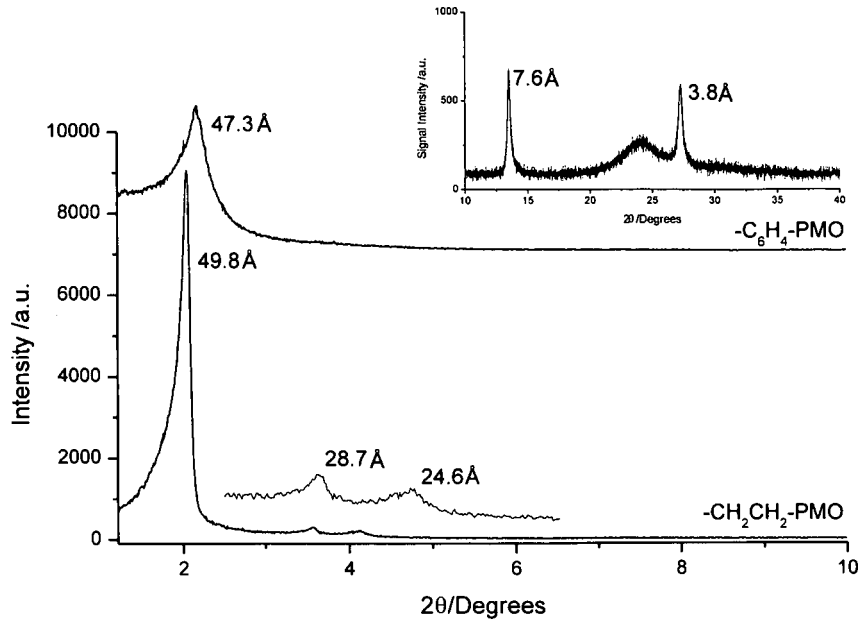

Figure 6.2. PXRD patterns of the mono-functional PMO standards prepared *via* S^+I^- synthetic pathway.

PXRD patterns of the standard PMOs prepared without pre-hydrolysis (Fig. 6.1 and 6.2) show high levels of mesoscopic ordering with an intense (100) and minor (110), (200) reflections with d_{100}-spacings 44 - 50 Å consistent with formation of a hexagonal mesophase. The reflections at 7.5 and 3.8 Å, indexed as the (001) and (002) directions of a lamellar structure, observed for the aromatically functionalised PMOs are a direct result of π-π stacking of the aromatic rings. The reflection at 7.5 Å corresponds to the length of the Si-C_6H_4-Si- moiety whilst the broad hump at *ca.* 4.3 Å is due to the fluctuation in atomic positions of the silicon and oxygen atoms within the pore walls.[228] The reduction of peak intensity of higher angle reflections and the increase in relative intensity of the broad hump at 4.3 Å between the pure -C_6H_4-PMO and the bi-functional -CH_2CH_2-/-C_6H_4-PMO is to be expected as the layered organisation of the pore walls is disrupted by the incorporation of the aliphatic component.

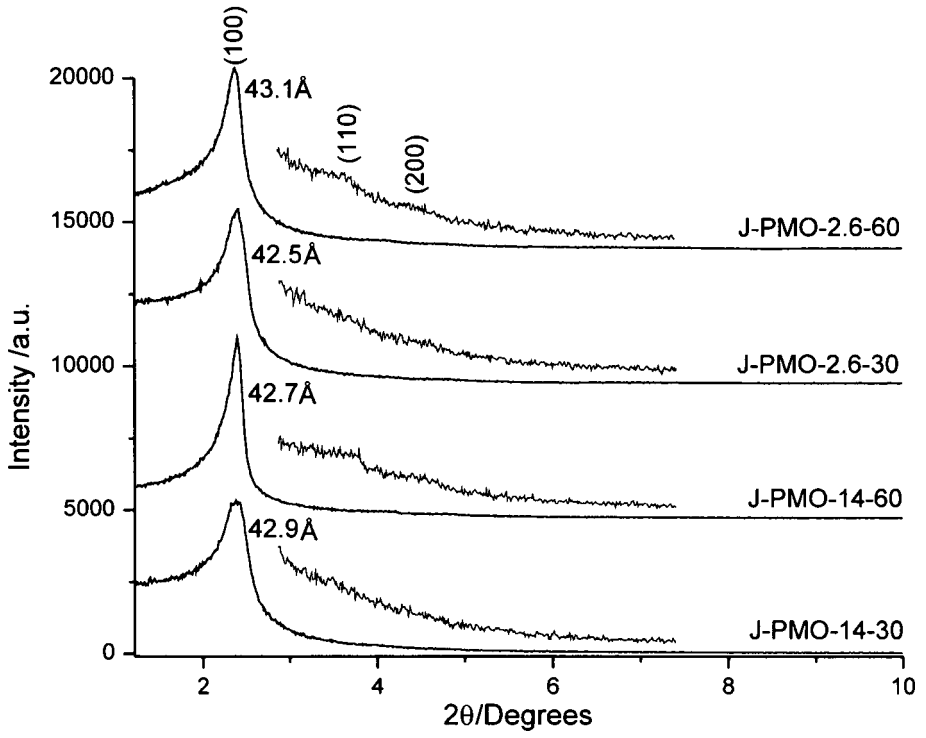

Figure 6.3. Low-angle PXRD patterns of the template extracted bi-functional PMOs prepared *via* cationic templating using joint pre-hydrolysis protocols.

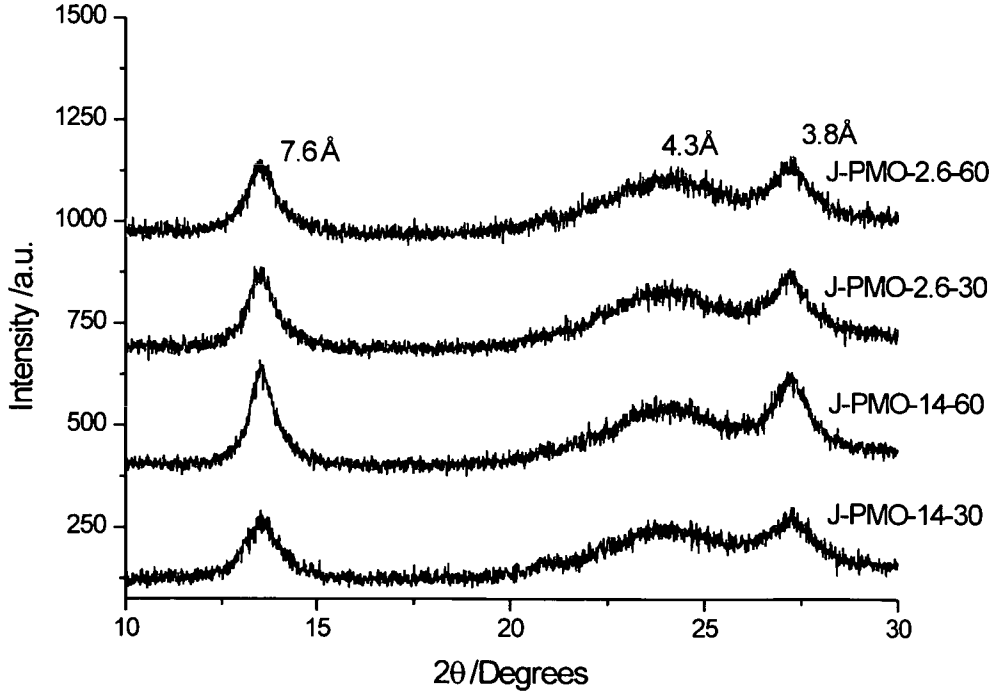

Figure 6.4. High angle PXRD patterns of the template extracted bi-functional PMOs prepared *via* cationic templating using joint pre-hydrolysis protocols.

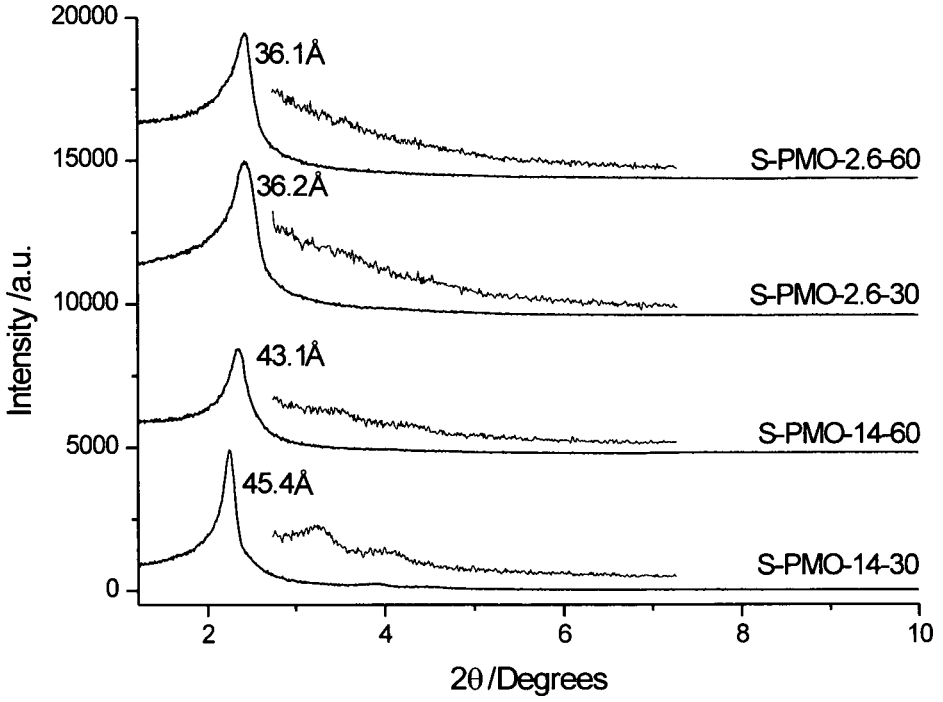

Figure 6.5. Low angle PXRD patterns of the template extracted bi-functional PMOs prepared *via* cationic templating using Separate pre-hydrolysis protocols.

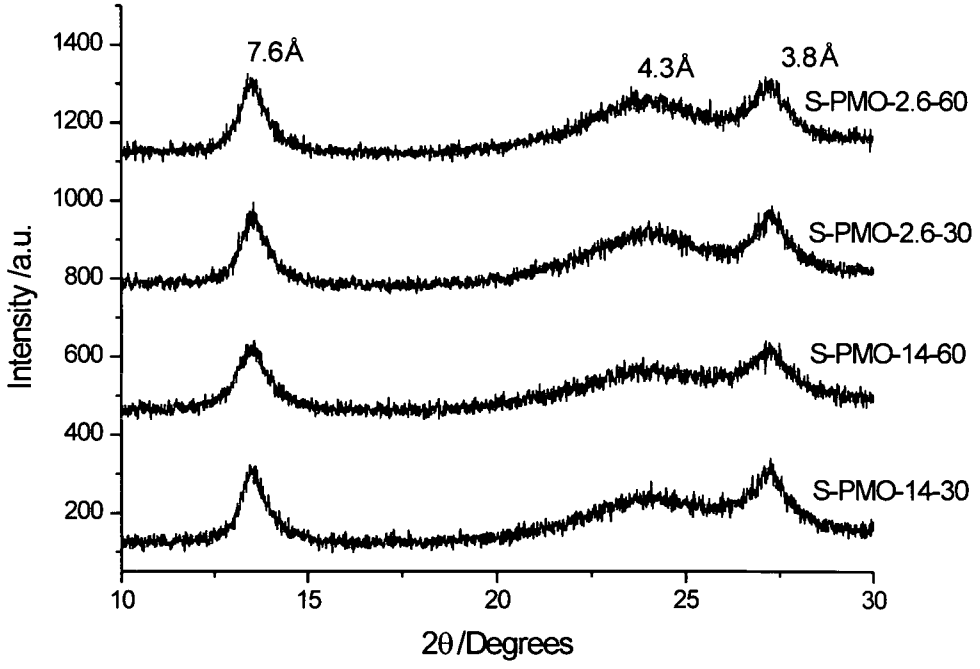

Figure 6.6. High angle PXRD patterns of the template extracted bi-functional PMOs prepared *via* cationic templating using Separate pre-hydrolysis protocols.

In general, the use of joint and separate pre-hydrolysis protocols has resulted in a decrease in mesoscopic ordering in comparison to the standard bi-functional PMO (fig. 6.1). Similar diffraction patterns at low angles with intense (100) reflections at d_{100} spacings of up

to *ca.* 45 Å have been observed. The S-PMO-2.6-30/-60 show a decrease in d_{100} spacings to *ca.* 36 Å. Mesoscopic ordering is affected in different ways depending on the pre-hydrolysis protocols used. For J-PMOs (fig. 6.3) the intensity of (110) and (200) reflections is increased with pre-hydrolysis time. In contrast, for the S-PMOs (fig. 6.5) only the S-PMO-14 shows evidence of these reflections. These reflections are more intense for S-PMO-14-30 than S-PMO-14-60. Therefore, long range ordering decreases with increasing pre-hydrolysis time.

The diffraction patterns of the pre-hydrolysed PMOs at higher angles (fig. 6.4 and 6.6) show evidence of molecular organisation, although, compared to the pure -C_6H_4-PMO, the peak intensity is decreased and full-width-half-maximum (FWHM) is increased (Table 6.1). No change in molecular level ordering as a function of joint or separate pre-hydrolysis protocols *c.f.* to the standard bi-functional PMO implies that the aromatic precursor would preferentially undergo homo condensation to form mono-functional Secondary Building Units (SBUs). The formation of mono-functional -C_6H_4- SBUs is related to the energetically favourable π-π stacking layered conformation and is irrespective of pre-hydrolysis protocol used. Similar observations have been reported for phenyl-polysilsesquioxanes ($POSS_{ph}$).[229] Whereby the $POSS_{ph}$ used to terminate polymer chains of an epoxy-amine network are clustered due to π-π stacking interactions of the POSS phenyl functionalities. The size of such $POSS_{ph}$ crystallites was found to be *ca.* 30 nm, determined using small angle x-ray scattering (SAXS).[229,230] From computer models and DFT calculations two main types of π-π stacking of aromatics exist. That is, a parallel displaced π-π stacking conformation due to the electrostatic repulsion of the π electron clouds and an eclipsed π-π stacking conformation induced by the substitution of fluorine for hydrogen atoms (Scheme 6.1).[231,232]

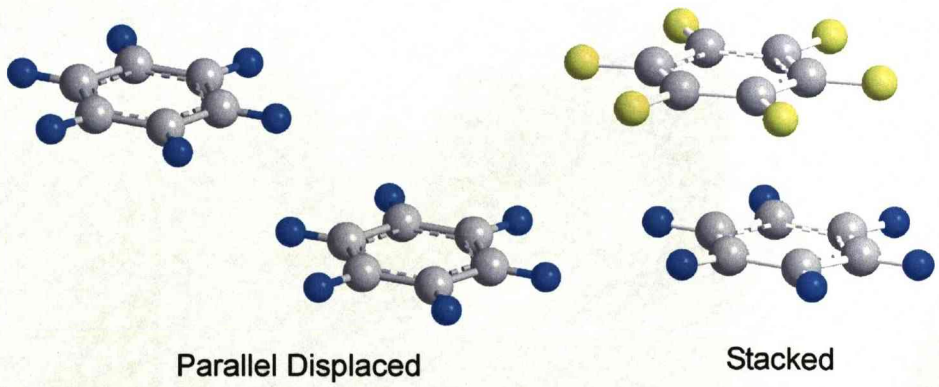

Scheme 6.1. Atomic representation of parallel displaced conformation found in benzene and the stacked conformation found in flourobenzene π- π stacking.[232]

In phenyl functionalised PMOs it is unlikely that only one π-π stacking conformation exists due to steric/electronic effects of the silicon tetrahedra bound as 1,4-substituents. Although simulations of the structure of -C_6H_4-PMOs based on TEM images have been reported in the literature, no discussion on the form (staggered or eclipsed) of the π-π stacking is presented (chapter 1).[57]

The formation pathways for molecularly ordered PMOs, *i.e.* synthesis of a biphenyl-PMO *via* basic/cationic templating, were studied by *in-situ* small angle X-ray scattering/X-ray diffraction (SAXS/XRD).[233] The presence of a hexagonal mesophase was evident after 60 minutes and coincided with the observation of reflections corresponding to ordering within the pore walls. Therefore, the authors concluded that the formation of the mesophase served to induce the local ordering within the pore walls and both processes occurred simultaneously. Hence, the molecular level periodicity was a result of a fully cooperative process.[233] Further work by Inagaki *et al.* on sol-gel chemistry of 1,3-, 1,4-phenyl and 4,4-biphenyl bridged organosilanes in basic solutions and in the absence of template showed the formation of lamellar phases due to π-π stacking interactions.[228] Such materials are essentially sheets composed of alternating organic/ silica layers. Evidently, the findings of Inagaki *et al.* are in disagreement with the results of Morell *et al.*[233] However, both reports do show the formation of molecular level ordering and from the data obtained in these reports both conclusions are valid as the main difference between the two reports is that Morrell *et al.* monitors the process in the presence of template.

We have isolated a series of -C_6H_4-PMOs at set times during synthesis to monitor the formation of the mesophase and molecular ordering in the walls.

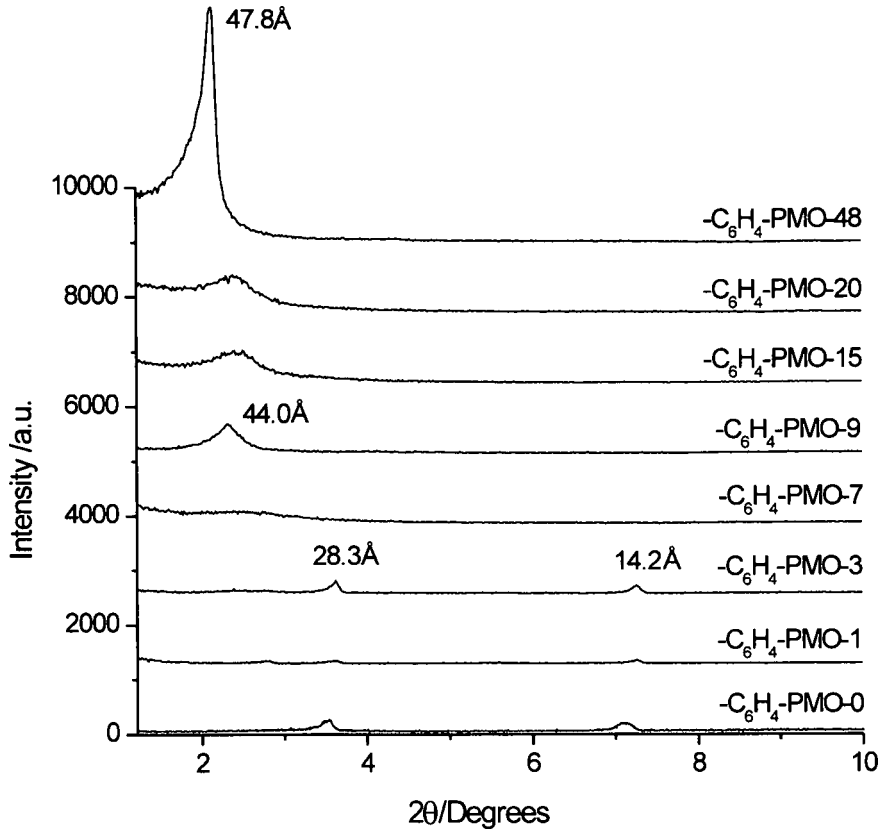

Figure 6.7. Low angle PXRD patterns of the as-synthesised -C_6H_4-PMO-X where X denotes the time in minutes at which the PMO is isolated from the reaction mixtures.

The powder XRD patterns of the as-synthesised -C_6H_4-PMO-48 and -C_6H_4-PMO (Fig. 6.2) are similar. The -C_6H_4-PMO-3 and -7 exhibit the high-angle reflections with increasing intensity corresponding to the π-π stacking (fig 6.8). These reflections appear before the hexagonal mesophase is formed suggesting that in this system mesoscopic organisation follows the molecular level periodicity of phenyl-silica moieties. Therefore, confirming the aromatic precursor forms stable π-π stacked SBUs prior to co-assembly with the template micelles. This is also consistent with the observations made for the pre-hydrolysed PMOs. The products isolated before 3 hours of heating all displayed lamellar structures indicated by (100) and (200) low angle reflections at 28.3 and 14.2 Å and additional reflections at higher angles. The latter reflections correspond to the un-reacted template in an all-trans layered conformation. The appearance of a broad reflection at *ca.* 45 Å in -C_6H_4-PMO-7, which becomes more defined at 44.0 Å in -C_6H_4-PMO-9 (Fig. 6.7), coincides with the disappearance of reflections corresponding to the template phase. Therefore, the PXRD data confirm the formation of the hexagonal mesophase occurs in the region of 3 to 7 hours.

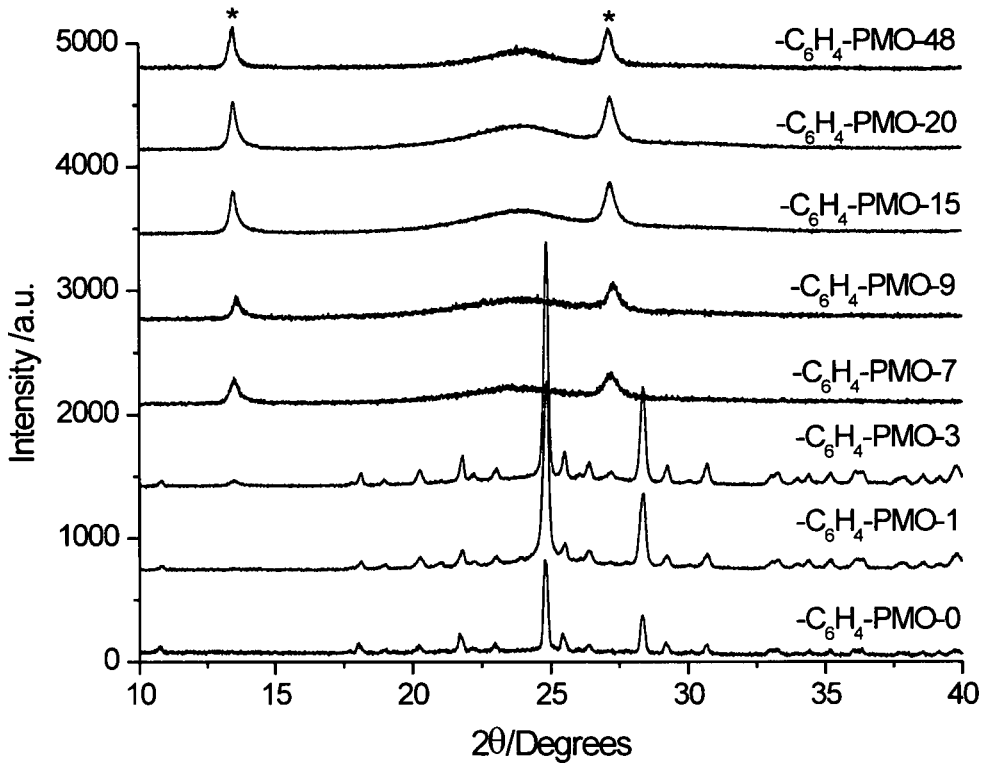

Figure 6.8. High angle PXRD patterns of the as-synthesised -C_6H_4-PMO-X isolated from the reaction mixtures at intervals indicated in the figure. Asterisks correspond to reflections due to π-π stacking.

Table 6.1. Powder XRD line-width analysis of patterns of -CH_2CH_2-/-C_6H_4-PMOs prepared *via* joint and separate pre-hydrolysis protocols.

Sample	2θ /Degrees	d-spacing /Å	FWHM /Degrees	Abs. Intensity counts /a.u.
C_6H_4-PMO	13.5	7.6	0.326	525
	27.2	3.8	0.402	423
-CH_2CH_2-/-	13.5	7.5	0.653	195
C_6H_4-PMO	27.3	3.8	0.705	180
J-PMO-14.1-30	13.6	7.6	0.863	137
	27.3	3.8	0.994	85
J-PMO-14.1-60	13.5	7.6	0.762	223
	27.2	3.8	0.827	149
J-PMO-2.6-30	13.5	7.6	0.775	177
	27.2	3.8	0.805	109
J-PMO-2.6-60	13.5	7.6	0.837	154
	27.2	3.8	0.858	101
S-PMO-14.1-30	13.5	7.6	0.769	173
	27.2	3.8	0.901	120
S-PMO-14.1-60	13.5	7.6	0.835	150
	27.2	3.8	0.963	89
S-PMO-2.6-30	13.5	7.6	0.759	171
	27.2	3.8	0.794	114
S-PMO-2.6-60	13.5	7.6	0.761	174
	27.2	3.8	0.855	112

6.2.1.2 $S^0H^+X^-I^+$ templated PMOs

Powder XRD of the standard mono-functional -CH_2CH_2- and -C_6H_4-PMOs (Fig. 6.9) showed three reflections at low angles attributed to (100), (110) and (200) reflections corresponding to a 2D hexagonal structure with d_{100}-spacings of 99.1 and 97.8 Å respectively. The high angle powder XRD pattern of -C_6H_4-PMO shows evidence of molecular level periodicity with (001) and (002) reflections at 7.6 and 3.6 Å. These lines are considerably broader than those observed for the analogous S^+I^- templated PMO confirming the degree of periodicity is significantly lower.

The molecular periodicity in aromatic PMOs prepared under acidic conditions has been reported for benzene PMOs[62] yet the high angle reflections are significantly broadened (Fig. 6.10) *c.f.* to the -C_6H_4-PMO presented here. Higher levels of periodicity have been observed for biphenyl PMOs where a series of (001), (002) and (003) reflections at 11.5, 5.7 and 3.9 Å of higher intensity relative to the phenyl-PMO presented here were observed. However, the mesoscopic ordering was significantly reduced as only a single broad low angle peak was observed compared to the three reflections observed here.[234] The -CH_2CH_2-/-C_6H_4-PMO reference material shows a low angle diffraction pattern similar to the mono-functional PMOs yet with a reduced d_{100} spacing of 90.1 Å. The absence of any reflections at higher angles confirms that the aliphatic component disrupts molecular level ordering.

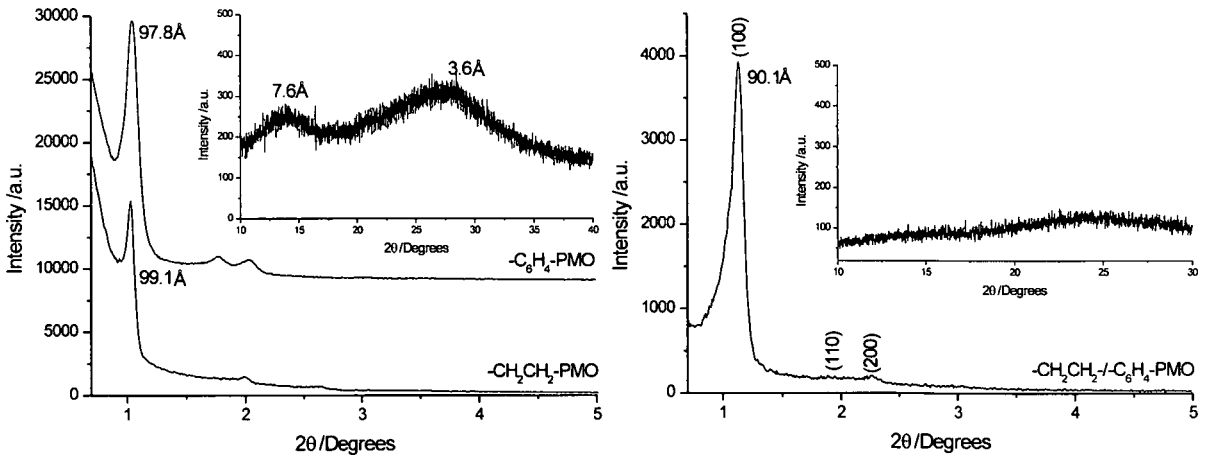

Figure 6.9. PXRD patterns of template extracted mono- (left) and bi-functional (right) standard PMOs prepared *via* non-ionic templating.

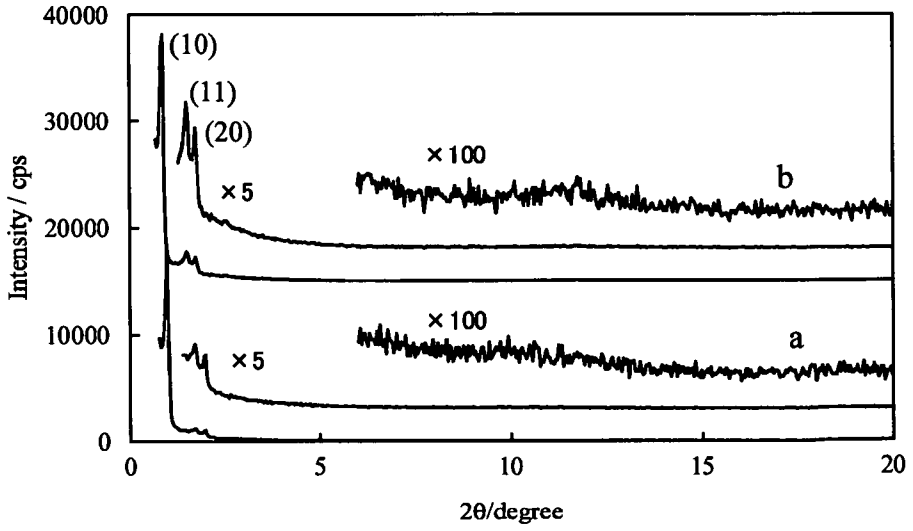

Figure 6.10. PXRD patterns of template extracted a) -C_6H_4-PMO and b) after post-synthesis treatment by placing as made -C_6H_4-silca in H_2O at 100 °C for 72 hrs reported by Inagaki *et al.*[62]

The PXRD patterns of the template extracted PMOs prepared using the pre-hydrolysis protocols (Fig. 6.11) all show a reduction in mesoscopic ordering compared to the standard -CH_2CH_2-/-C_6H_4-PMO. This is due to the formation of more condensed SBUs with reduced reactivity as the number of Si-OH groups is decreased prior to their addition to the template solution therefore, are less reactive towards co-assembly with the template micelles (see chapter 5). We also note a reduction in the $d_{(100)}$ spacings for all pre-hydrolysed PMOs compared to the standard –CH_2CH_2-/-C_6H_4-PMO. Such a change was not observed for the template extracted –CH_2CH_2-/-CH=CH-PMOs.

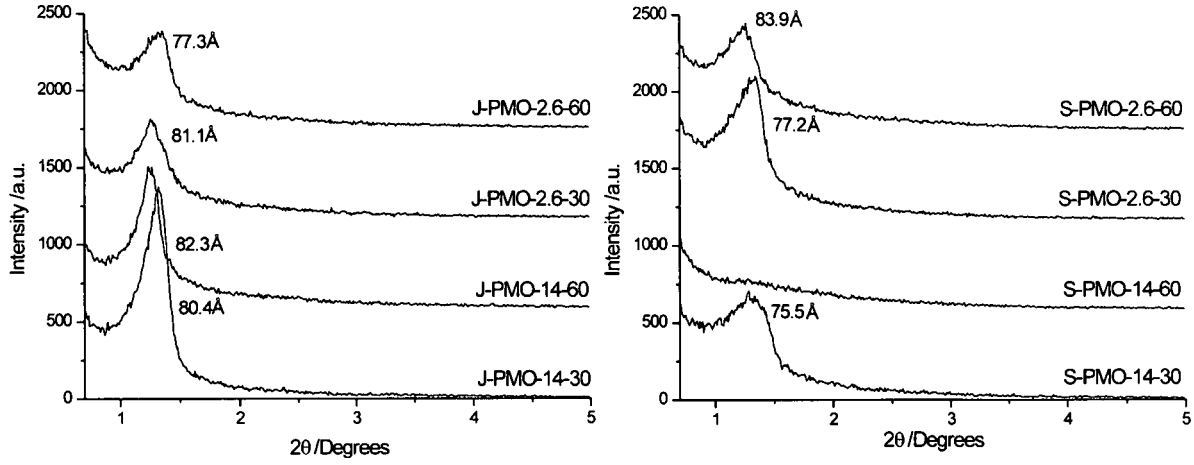

Figure 6.11. PXRD patterns of the template extracted PMOs prepared using joint (left) and separate (right) pre-hydrolysis protocols *via* non-ionic templating pathway.

In general, the mesoscopic ordering is reduced in the separately pre-hydrolysed solids compared to the J-PMOs, without affecting the d_{100}-spacing. This is in contrast to the -CH_2CH_2-/-CH=CH-PMOs. This was not the only difference observed when the -CH=CH- was replaced with the -C_6H_4- bridge. Thus, when the same Si/EtOH = 0.18 was used no mesostructured ordering was observed for any pre-hydrolysed –CH_2-CH_2-/-C_6H_4-PMOs and an increase in ethanol content to Si/EtOH = 0.12 was required to give ordered products. Increasing ethanol content during pre-hydrolysis enhances molecular separation effects and enables the rate of hydrolysis/condensation to be reduced so that mesoporous materials form preferentially to an amorphous organosilica phase.

When Si/HCl = 14, the level of ordering is reduced dramatically as pre-hydrolysis time is increased from 30 to 60 minutes (no mesoscopic ordering is observed S-PMO-14-60). Interestingly, the pre-hydrolysed –CH_2CH_2-/-CH=CH- containing S-PMO-14-60 was also amorphous (chapter 5). This is in contrast with the S^+I^- templated PMOs, where the pre-hydrolysis conditions had only a minor effect on mesoscopic ordering.

The hydrolysis and condensation reactions would be expected to occur simultaneously in both acidic and basic media as the silicon precursors and water are miscible in the solvent ethanol.[213] However, hydrolysis of alkyl silicon esters, R'-$Si(OR)_3$ in acidic conditions is rapid due to the stabilisation of the reactive R'$(OR)_2Si^+$ complex by the inductive effect of the alkyl radicals.[235,236] The same effect in basic solutions reduces the rate of hydrolysis. Therefore, the initial nucleophilic attack of the base becomes more difficult. The mechanisms of hydrolysis of alkyl silicon esters in pure H_2O, H_2O/HCl and H_2O/NaOH systems are described in scheme 6.2. The steps in the Scheme below are as follows: 1) nucleophilic attack of the H_2O molecule; 2) proton transfer from H_2O ligand to the leaving alkoxy group to produce ≡Si-OH and ROH. 3) The H^+ is picked up by the lone electron pair on oxygen causing an increase in positive charge at the silicon centre as the Si-O bond becomes highly polarized allowing efficient nucleophilic attack by H_2O. 4) After the leaving of ROH the acid is regenerated by the leaving of H^+ to form the ≡Si-OH functionality. 5) The base catalyst acts as a nucleophile attacking the silicon centre; 6) the alkoxy leaving group takes up a proton to regenerate the base to give ≡Si-OH and ROH.

The rapid hydrolysis/condensation of the aromatic silicon precursor under acidic conditions occurs, most probably, under kinetic control. Therefore, the partially condensed SBU's are "locked" in a specific conformation and are unable to re-arrange into a more thermodynamically favourable structure. However, in basic conditions the hydrolysis/

condensation is slow and under thermodynamic control, henceforth reversible and the energetically favourable π-π stacking conformation is obtained.

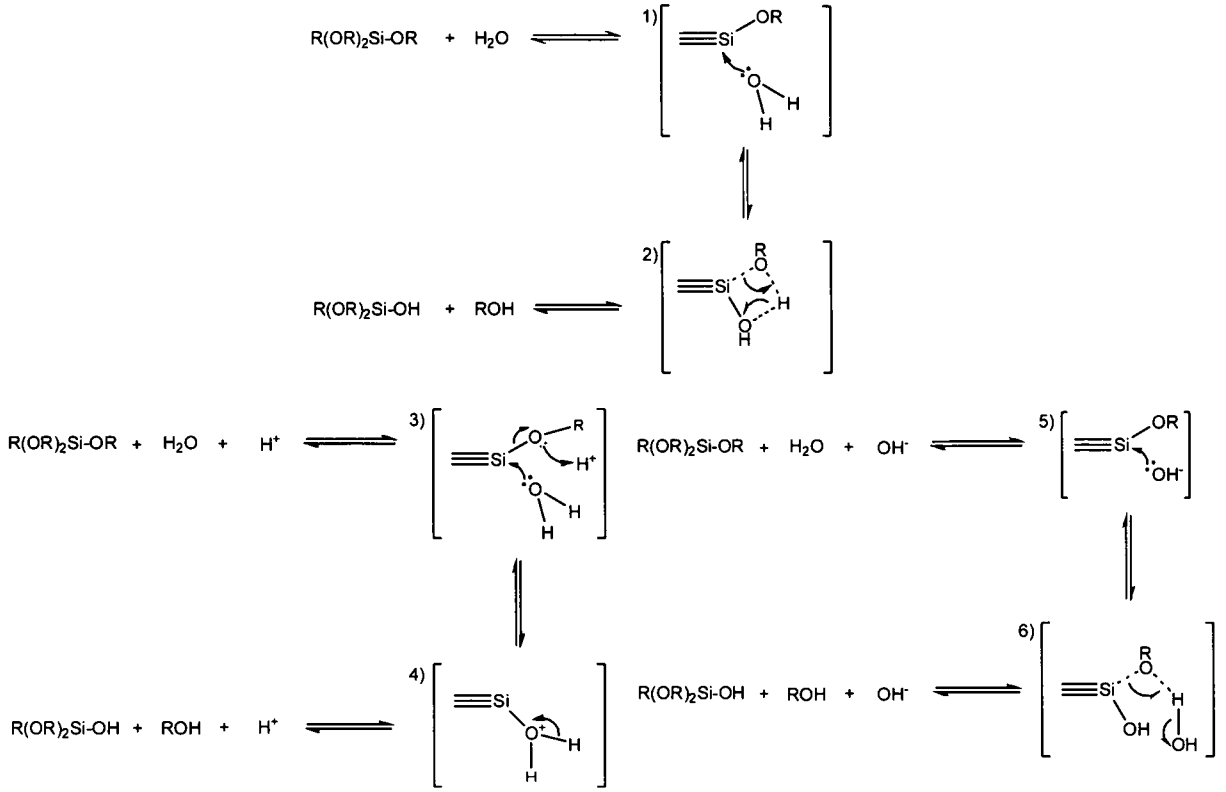

Scheme 6.2. Hydrolysis mechanisms of alkyl silicon esters using pure H_2O (top), H_2O/ acid (bottom left) and H_2O/ base (bottom right).

The afore mentioned hydrolysis mechanisms of the silicon alkoxides under both acidic and basic conditions are consistent with the changes in ordering for the pre-hydrolysed PMOs (Figs. 6.3 to 6.6 and 6.11). That is under acidic conditions a large effect on the resulting PMO is observed between the different pre-hydrolysis conditions and under basic conditions little change is seen.

6.3 N_2 Adsorption-desorption isotherms

6.3.1 Textural Properties of S^+I^- templated PMOs

The N_2 adsorption/desorption measurements for the standard PMOs (fig. 6.12, table 6.2) showed type IV isotherms according to IUPAC definition with a capillary condensation step in the region of p/p_0 = 0.3-0.4. The capillary condensation step is more pronounced for the mono-functional standards with $-CH_2CH_2$-PMO having the sharpest step, highest pore volume and narrowest pore size distribution. The absence of a hysteresis in the region of the capillary condensation step indicates the pore openings are of the same diameter as the pore channels and that no partial pore blocking has occurred.

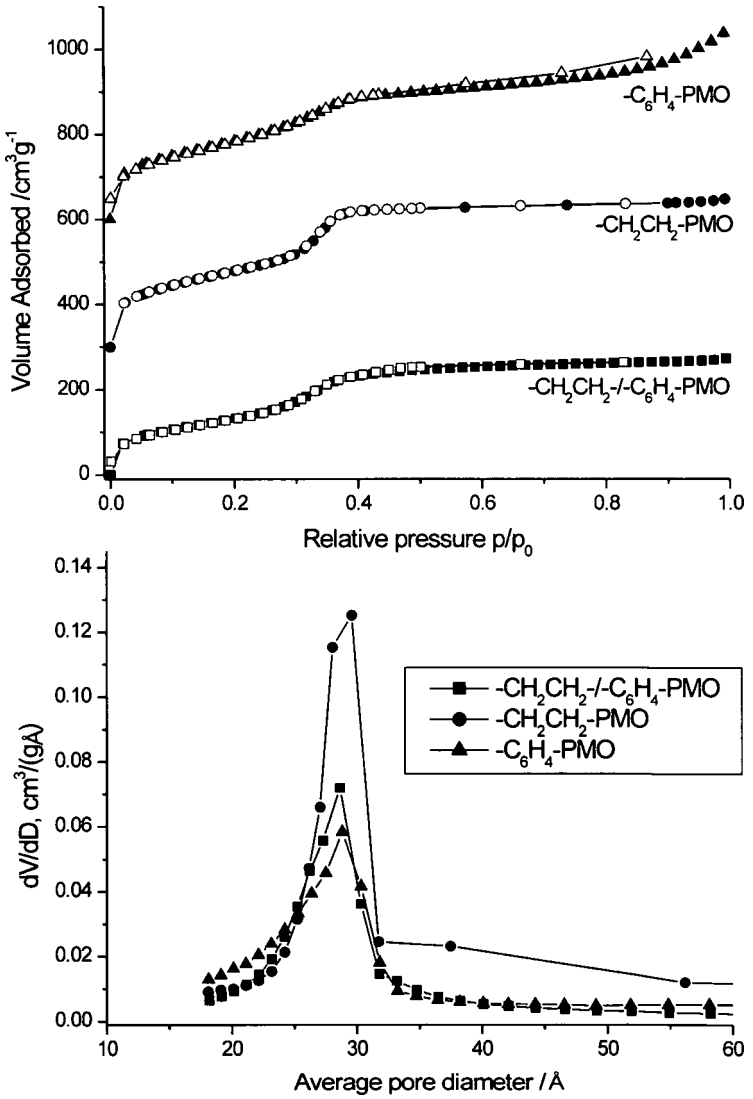

Figure 6.12. N_2 adsorption/desorption isotherms and pore size distribution curves of the template extracted standard PMOs prepared *via* the I^-S^+ pathway

The N_2 adsorption/desorption isotherms of the template extracted jointly pre-hydrolysed PMOs (Fig. 6.13) indicated a decrease in mesoscopic ordering compared to the bi-functional standard as a broadening of the capillary condensation step at $p/p_0 = 0.3 - 0.4$ is observed. The sample S-PMO-14-30 is an exception as its isotherm was similar to that of the bi-functional standard. This indicates a well ordered porous network, consistent with powder XRD. In general, the jointly and separately pre-hydrolysed PMOs showed higher surface areas and pore volumes than the standard mono-/ bi-functional PMOs. The increased S_{BET} and V_{ads} (Table 6.2) are related to the formation of large SBUs during pre-hydrolysis. That is a more open porous structure is formed due to the decrease in template framework interactions during synthesis. On the other hand, the unit cell parameter *a* and wall thickness remain unchanged between the bi-functional and pre-hydrolysed PMOs with the exception of S-PMO-2.6-30 /-60. The decrease in wall thickness to ~16.7 Å is not accompanied by a decrease in degree of pore wall condensation (see ^{1}H-^{29}Si CP/MAS NMR section).

A hysteresis at $p/p_0 > 0.5$ is observed for the jointly pre-hydrolysed PMOs. The size of the hysteresis increases with pre-hydrolysis time and base content. The PSD plot of the desorption branch of the N_2 isotherms for J-PMOs (Fig. 6.14) confirm the presence of expanded pore openings with two pore windows of 27.0 Å (the same size as the pore channels) and 35.9 Å. The population of pore openings with diameter of 35.9 Å increases relative to the openings at *ca.* 27.0 Å as pre-hydrolysis time and base content is increased with the exception of J-PMO-14-60. One possible explanation for this is that prolonged exposure of the materials to base may cause degradation at the pore openings (the most accessible region of the framework) resulting in a 'funnel' shaped opening. In order to confirm this high resolution microscopy such as AFM or HR-TEM would be required.

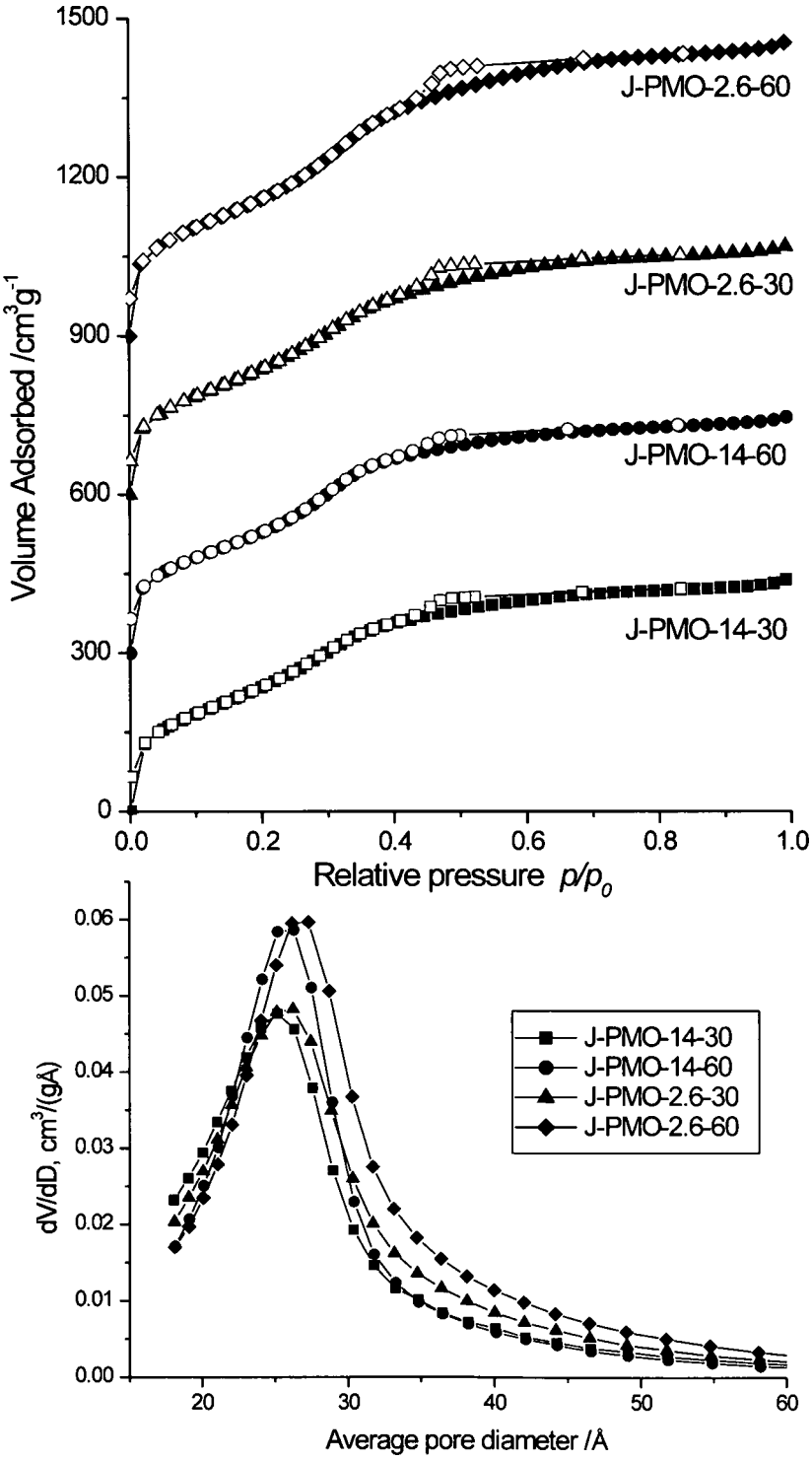

Figure 6.13. N_2 adsorption/desorption isotherms (top) and PSD curves (bottom) of the jointly pre-hydrolysed template extracted PMOs prepared *via* the I^-S^+ pathway.

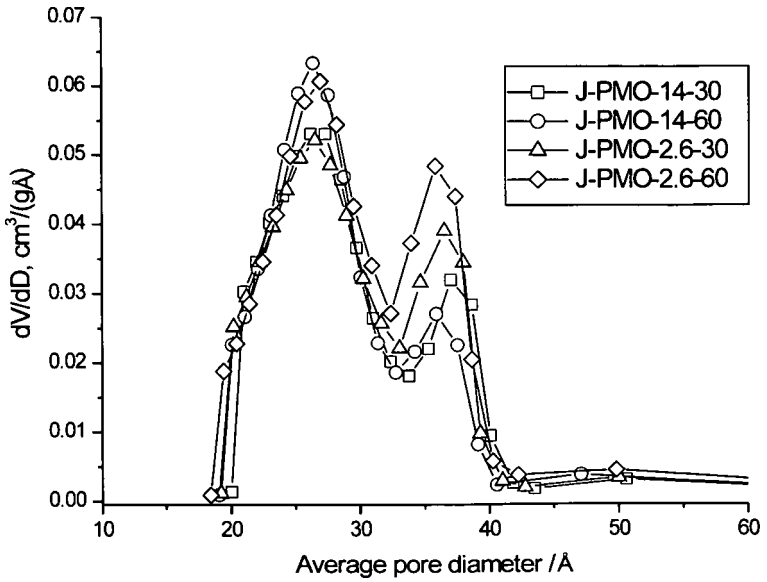

Figure 6.14. Pore size distribution plots obtained from the desorption branch of N_2 isotherm for template extracted J-PMOs prepared *via* S^+I^- synthetic pathway.

Table 6.4. Textural properties of template extracted bi-functional PMOs prepared *via* the I^-S^+ pathway

Sample	S_{BET} /m^2g^{-1}	V_{ads} /cm^3g^{-1}	D_{AV}^{ads} /Å	d_{100} /Å	$a^{\dagger}$ /Å	W /Å
CH_2CH_2/C_6H_4-PMO	731	0.54	28.7	44.6	51.5	22.8
CH_2CH_2-PMO	686	0.53	29.9	49.8	57.5	27.6
C_6H_4-PMO	717	0.64	28.8	47.3	54.6	25.8
J-PMO-14-30	975	0.67	25.1	42.9	49.5	24.4
J-PMO-14-60	962	0.68	26.2	42.7	49.3	23.1
J-PMO-2.6-30	1000	0.71	26.2	42.5	49.1	22.9
J-PMO-2.6-60	1077	0.85	27.3	43.1	49.8	22.5
S-PMO-14-30	950	0.73	27.4	45.4	52.4	25.0
S-PMO-14-60	910	0.51	25.1	43.1	49.8	24.7
S-PMO-2.6-30	1015	0.70	25.1	36.2	41.8	16.7
S-PMO-2.6-60	843	0.61	25.2	36.1	41.7	16.5

Pore volumes determined at $P/P_0 = 0.9$.
† Unit cell parameter $\bar{a}$ determined from d_{100} values using $\bar{a} = 2d_{100}/\sqrt{3}$.
W is wall thickness determined from $\bar{a} - D_{av}$.

6.3.2 Textural Properties of $S^0H^+X^-I^+$ templated PMOs

The N_2 adsorption/ desorption isotherms of the acid catalysed standard PMOs (fig. 6.15) show type IV isotherms with a sharp capillary condensation step on the adsorption branch at of $p/p_o \approx 0.55$ - 0.75. In contrast to the base catalysed analogues, the desorption branch indicates a type HI hysteresis suggesting the presence of cylindrical pores of a uniform size and shape.

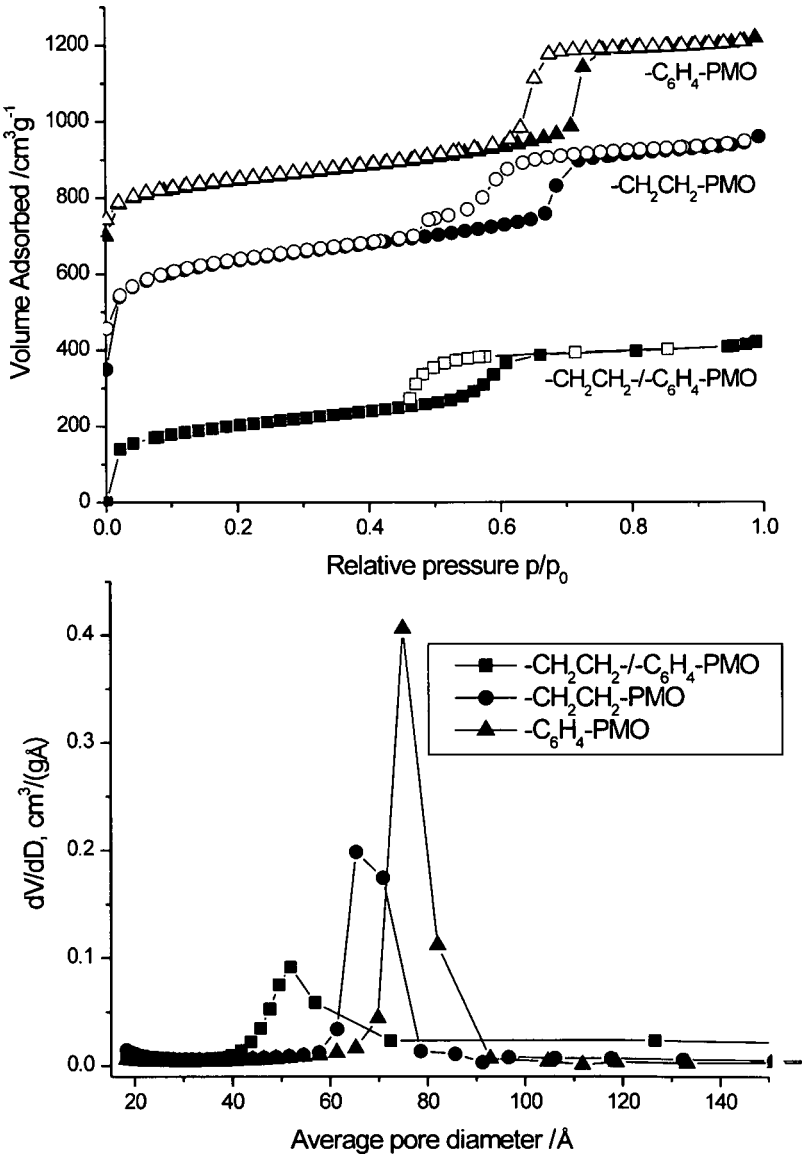

Figure 6.15. N_2 adsorption/desorption isotherms (top) and PSD curves (bottom) of the template extracted standard PMOs prepared *via* the $S^0H^+X^-I^+$ pathway.

A higher degree of mesoscopic ordering for mono-functional-PMOs is confirmed by a narrower PSD and sharper capillary condensation step compared to $-CH_2CH_2-/C_6H_4$-PMO. This is consistent with the PXRD results (fig. 6.9). Interestingly, the pore diameter decreases

in the order of -C_6H_4-PMO > CH_2CH_2-PMO > -CH_2CH_2-/-C_6H_4-PMO yet the trend is reversed for the wall thickness. The increased wall thickness of CH_2CH_2-PMO compared to -C_6H_4-PMO coincides with an increased degree of pore wall condensation in the aliphatic PMO (Section 6.4.2.1). The bifunctional PMO does not comply with this conclusion as its framework is less condensed than the CH_2CH_2-PMO yet has a larger wall thickness. The N_2 isotherm of -CH_2CH_2-PMO shows a second desorption step at p/p_0 = 0.47. Similarly to some of the -CH_2CH_2-/-CH=CH-PMOs, this may result from partial pore blocking or two different sizes of pore openings (as discussed in chapter 5).

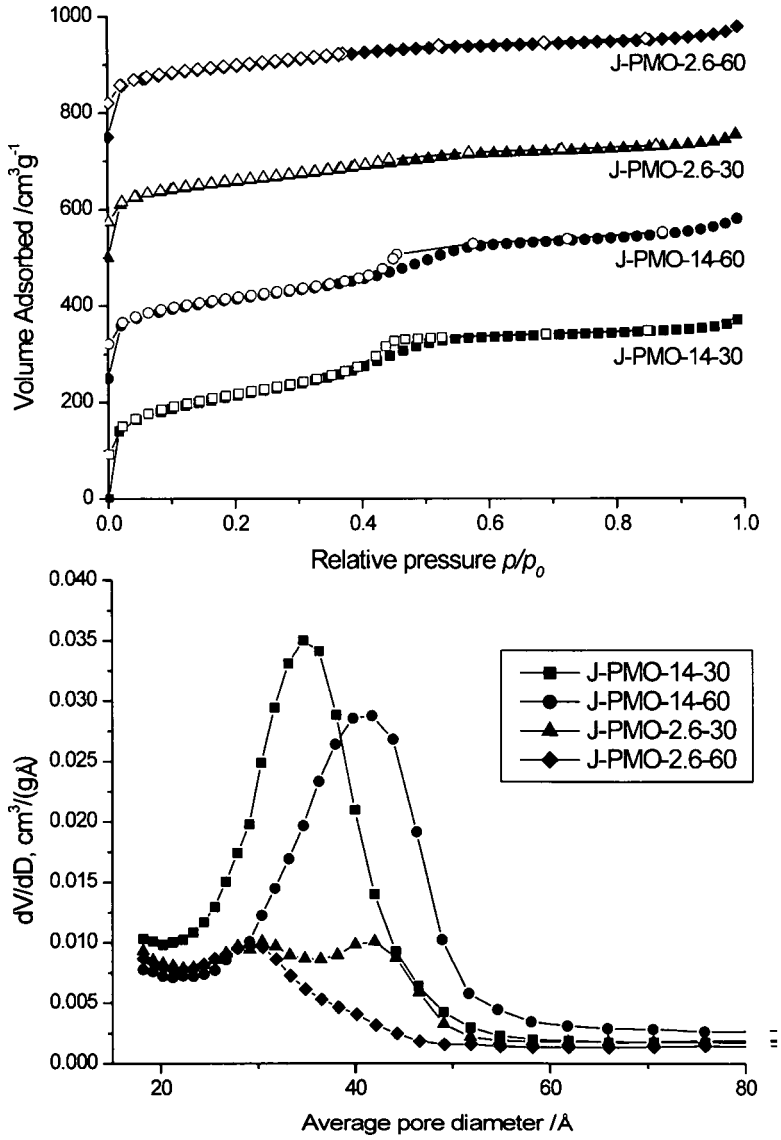

Figure 6.16. N_2 adsorption/desorption isotherms (top) and PSD curves (bottom) of the jointly pre-hydrolysed template extracted PMOs prepared *via* the $S^0H^+X^-I^+$ pathway.

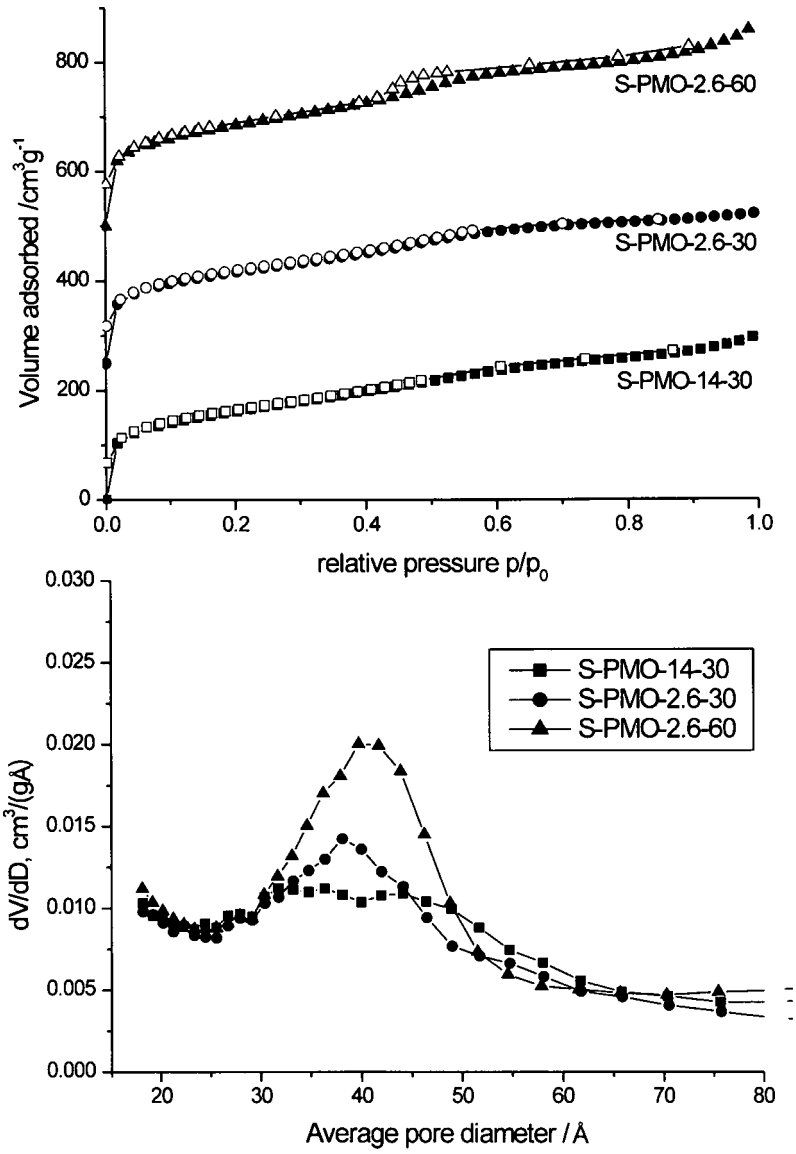

Figure 6.17. N_2 adsorption/desorption isotherms (top) and PSD curves (bottom) of the separately pre-hydrolysed template extracted PMOs prepared *via* the $S^0H^+X^-I^+$ pathway.

The N_2 adsorption/ desorption isotherms for the jointly and separately pre-hydrolysed PMOs (fig. 6.16 and 6.17 respectively) indicate a significant decrease in mesoscopic ordering, S_{BET} (with the exception of J-PMO-14-30), and pore volume (Table 6.5). J-PMO-14-30/60 show the narrowest pore size distribution (PSD) of all the pre-hydrolysed solids which suggests that under the mildest conditions moderately ordered networks still form. When the acid content was increased to Si/HCl = 2.6 for J-PMOs the PSD became broader and for J-PMO-2.6-60 a bimodal PSD was observed with maxima at 30 and 41 Å. The bimodal PSD was also seen for S-PMO-14-30 however not as pronounced as for J-PMO-2.6-

60. The broadening of the PSD curves is a result of poorly defined pore architecture due to reduced mesoscopic ordering.

Table 6.5. Textural properties of template extracted bi-functional PMOs prepared *via* the $S^0H^+X^-I^+$ pathway

Sample	S_{BET} /m^2g^{-1}	V_{ads} /cm^3g^{-1}	D_{AV}^{ads} /Å	d_{100} /Å	$a^{\dagger}$ /Å	W /Å
CH_2CH_2/C_6H_4-PMO	677	0.64	51.8	90.1	104	52.2
-CH_2CH_2-PMO	946	0.92	65.3	99.1	114	48.7
-C_6H_4-PMO	519	0.78	75.0	97.8	113	38.0
J-PMO-14-30	729	0.56	34.7	80.4	92.8	58.1
J-PMO-14-60	563	0.49	41.7	82.3	95.0	53.3
J-PMO-2.6-30	523	0.38	29.1	81.1	93.6	64.5
J-PMO-2.6-60[a]	489	0.33		77.3	89.3	
S-PMO-14-30[a]	553	0.45		75.5	87.2	
S-PMO-2.6-30	559	0.42	38.1	77.2	89.1	51.0
S-PMO-2.6-60	630	0.54	40.7	83.9	96.9	56.2

Pore volumes determined at $P/P_0 = 0.9$.
† Unit cell parameter $\bar{a}$ determined from d_{100} values using $\bar{a} = 2d_{100}/\sqrt{3}$.
W is wall thickness determined from $\bar{a} - D_{av}$.
[a] D_{av} and W undetermined for J-PMO-2.6-60 and S-PMO-14-30 due to bimodal porous distribution.

Results of PXRD and N_2 adsorption/ desorption suggest the pre-hydrolysis protocols to have a much greater effect on the mesostructure and textural properties of acid catalysed PMOs. This may be related to different mechanisms of hydrolysis/ condensation in different media (discussed in details in section 6.2.2). It may also be possible that after pre-hydrolysis under basic conditions any organo-silsesquioxanes formed may re-disperse upon addition to the template solution (see chapter 7).

6.4 Solid-state NMR

6.4.1 Composition of base catalysed PMOs

6.4.1.1 Reference PMOs

^{1}H-^{13}C CP/MAS NMR provided information on the nature of the organic functionalities incorporated into the hybrid walls of the PMOs. The ^{1}H-^{13}C CP/MAS spectra of the template extracted standard PMOs (Fig. 6.18) confirmed the presence of the -C_6H_4- and -CH_2CH_2- functionalities (resonances at *ca.* 134.2 and 5.6 ppm respectively) and the efficient removal of the organic template with only minor resonances in the region of 20 to 30 ppm being observed. A -C_6H_4-/-CH_2CH_2- ratio of 0.96 was obtained using a Gaussian deconvolution function indicating a 1:1 level of incorporation, although it is important to note that CP is only semi-quantitative.

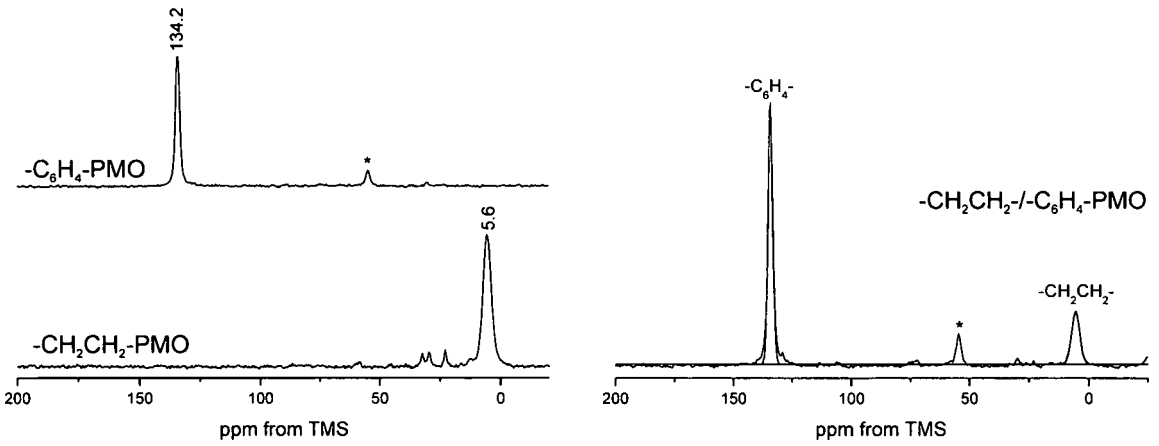

Figure 6.18. ^{1}H-^{13}C CP/MAS NMR spectra of the template extracted standards prepared *via* cationic templating.

^{1}H-^{29}Si CP/MAS NMR provides information on the nature of silicon environments and the degree of silicon condensation in the hybrid walls of the PMOs. The ^{1}H-^{29}Si CP/MAS NMR spectra of bi-functional -CH_2CH_2-/-C_6H_4-PMO (Figure 6.19) show five resonances which can be assigned as follows: the resonance at -49.1 ppm corresponds to -CH_2CH_2-**Si**$(OH)_2(OSi)$ T^1 environment. The resonances at -56.6 and -69.1 ppm correspond to R-**Si**$(OH)(OSi)_2$ T^2 environments and the peaks at -80.6 ppm represent fully condensed R-**Si**$(OSi)_3$ T^3 sites bound to -CH_2CH_2- and -C_6H_4- bridges respectively. The ratio of [-C_6H_4-/-CH_2CH_2-]-Si T sites for the bifunctional PMO standard is 0.96. This is in good agreement with the initial synthesis composition and the ratio

determined from ^{13}C CP/MAS NMR spectra (Fig. 6.18). Both the mono-functional PMOs have more condensed frameworks than the -CH_2CH_2-/-C_6H_4-PMO (fig. 6.19).

The co-condensation process around the template is influenced by the different size of the organic bridges.[203] When two organic bridges of different lengths ($^-$OSi-CH_2CH_2-SiO$^-$ (5.7 Å) and $^-$OSi-C_6H_4-SiO$^-$ (7.6 Å)) are used a disruption in the charge balancing distribution between Si-O$^-$ and $^+$N(CH_3)- species may occur.[32,237] There is also the differing hydrophobic properties of the organic bridges as increasing the hydrophobic nature of the framework may reduce the efficiency of co-assembly.

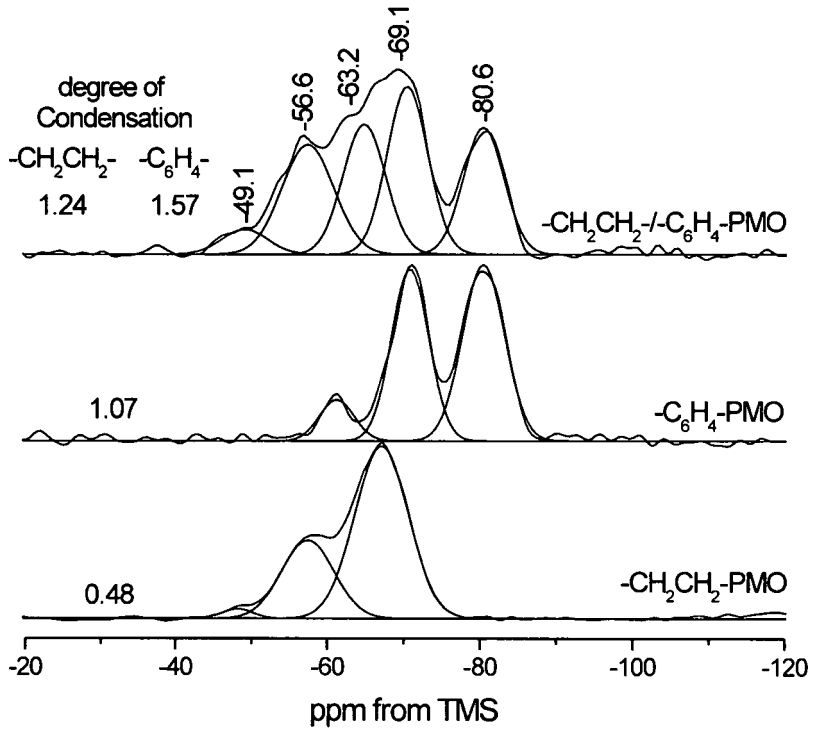

Figure 6.19. ^1H-^{29}Si CP/MAS NMR spectra of the template extracted standard PMOs prepared *via* S^+I^- templating pathway.

^1H MAS NMR spectra of the bifunctional -CH_2CH_2-/-C_6H_4-PMO (Fig. 6.20) show three broad resonances. The peak at 1.2 ppm is attributed to the -CH_2CH_2- functionality. The peak at 3.6 ppm is assigned to H-bonded water molecules in exchange with surface silanols, ≡Si-OH···OH_2 (1.5 + 5.5)/2 = 3.5 ppm (Fig. 6.21d and e), consistent with previous studies on water environments of MCM-41.[198] The resonance at 6.9 ppm is assigned to the -C_6H_4- functionality.

The ^1H MAS NMR spectrum of the -CH_2CH_2-PMO shows evidence of residual template with sharp resonances at 0.8 and 1.2 ppm due to the aliphatic chain. The -CH_2CH_2-

bridge gives a much broader line superimposed with the template peaks. The broad resonance at *ca.* 5 ppm is possibly due to free $(H_2O)_n$ clusters (Fig. 6.21b) within the pore channels.[198,238,239]

The ^{1}H MAS NMR spectrum of the -C_6H_4-PMO shows a broad minor resonance at *ca.* 1.0 ppm attributable to surface Si-OH groups,[158,159] similar to those observed for zeolite surface defects, as the resonance is too broad to be residual template species. The other two resonances at 3.6 and 6.9 ppm are the same as those for the bifunctional PMO standard.

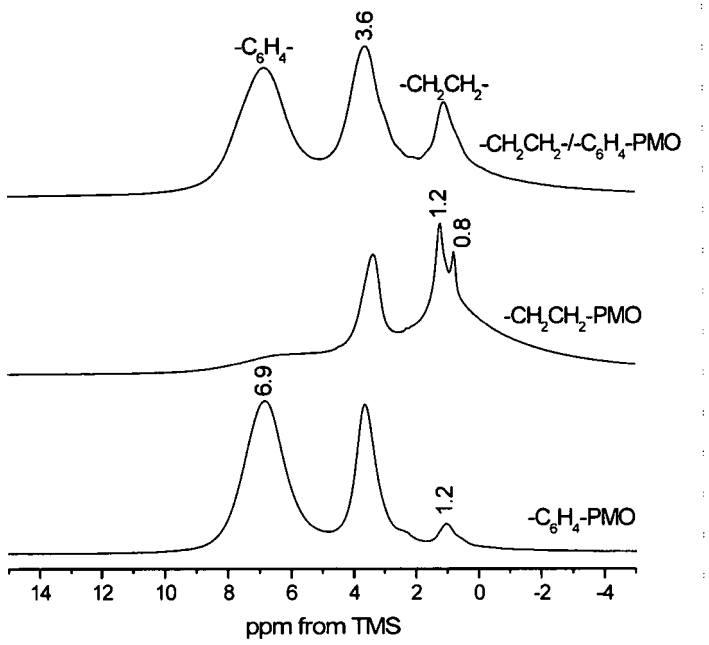

Figure 6.20. ^{1}H MAS NMR spectra of the template extracted standard PMOs prepared *via* the I^-S^+ synthetic pathway.

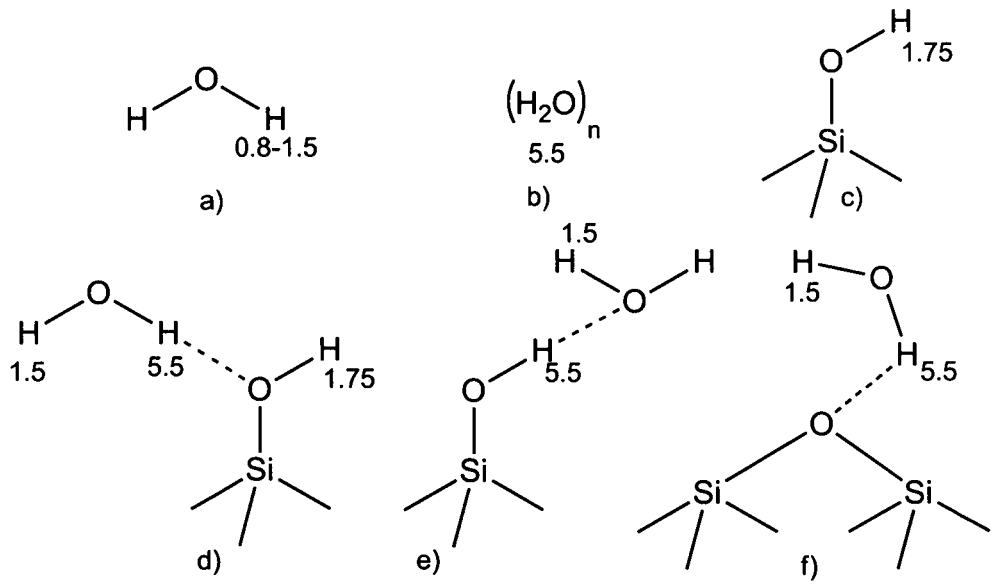

Figure 6.21. Proposed ^{1}H environments present in the template extracted PMOs, a) water, b) water cluster, c) surface silanol and d-f) various H-bonding possibilities.[198]

6.4.1.2. Pre-hydrolysed PMOs

^{1}H-^{13}C CP/MAS NMR spectra of the pre-hydrolysed products (Fig. 6.22) show the same two resonances as those for the standard bi-functional PMO (Fig. 6.18). However, the FWHM for -CH_2CH_2- resonance is increased from 387 Hz for the -CH_2CH_2-/-CH=CH-PMO to *can* average of *ca.* 415 Hz suggesting a decrease in local ordering of this environment as a function of pre-hydrolysis. The ratios of incorporated -C_6H_4-/-CH_2CH_2- functionalities as a function of pre-hydrolysis conditions are indicated in the figure.

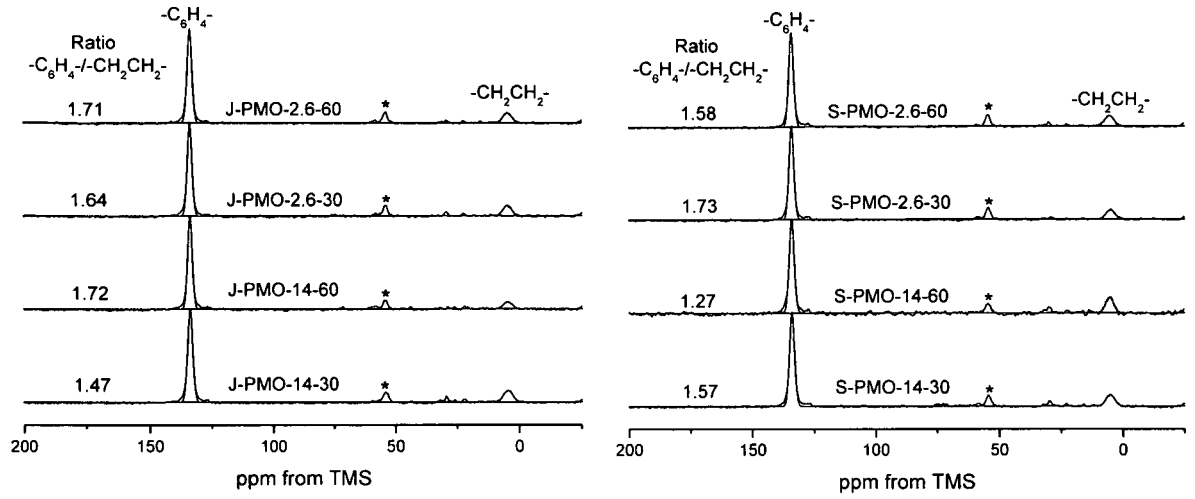

Figure 6.22. ^{1}H-^{13}C CP/MAS NMR spectra of the template extracted PMOs prepared *via* cationic templating using joint (left) and separate (right) pre-hydrolysis protocols.

The ^{1}H-^{29}Si CP/MAS NMR spectra of the template extracted pre-hydrolysed PMOs (Fig. 6.23) all show the same five resonances observed for the standard bi-functional PMO (the ratios of -C_6H_4-/-CH_2CH_2- silicon T sites are indicated within the figure). Both the ^{13}C and ^{29}Si CP/MAS data confirm a reduced -CH_2CH_2- content in pre-hydrolysed products compared with the standard -CH_2CH_2-/-C_6H_4-PMO. However, within the pre-hydrolysed PMOs the ^{13}C CP/MAS data indicates a higher –CH_2CH_2- content compared to the ^{29}Si CP/MAS data, with the exception of J-PMO-2.6-60 (Table 6.6).

The level of incorporation of –CH_2-CH_2- bridges is reduced with pre-hydrolysis time under joint pre-hydrolysis (with the exception of the ^{29}Si CP/MAS data for J-PMO-2.6-60). This trend is reversed when using separate pre-hydrolysis conditions. The two J-PMOs with the lowest amount of the -CH_2CH_2- bridges display the highest degree of mesoscopic ordering (Fig. 6.3). However, under separate pre-hydrolysis conditions only PMOs prepared with a Si/NaOH = 14 display (110) and (200) reflections yet these have a similar or higher -CH_2CH_2- content than S-PMO-2.6-30/-60. The incorporation of the –CH_2CH_2- functionality

is hampered as Si/NaOH ratio decreases from 14 to 2.6 under both joint and separate pre-hydrolysis protocols, with the exception of the ^{29}Si CP/MAS data for J-PMO-14(to 2.6)-60. This is consistent with the rate of hydrolysis of the $-CH_2CH_2-$ component to decreases upon increasing base content.[235]

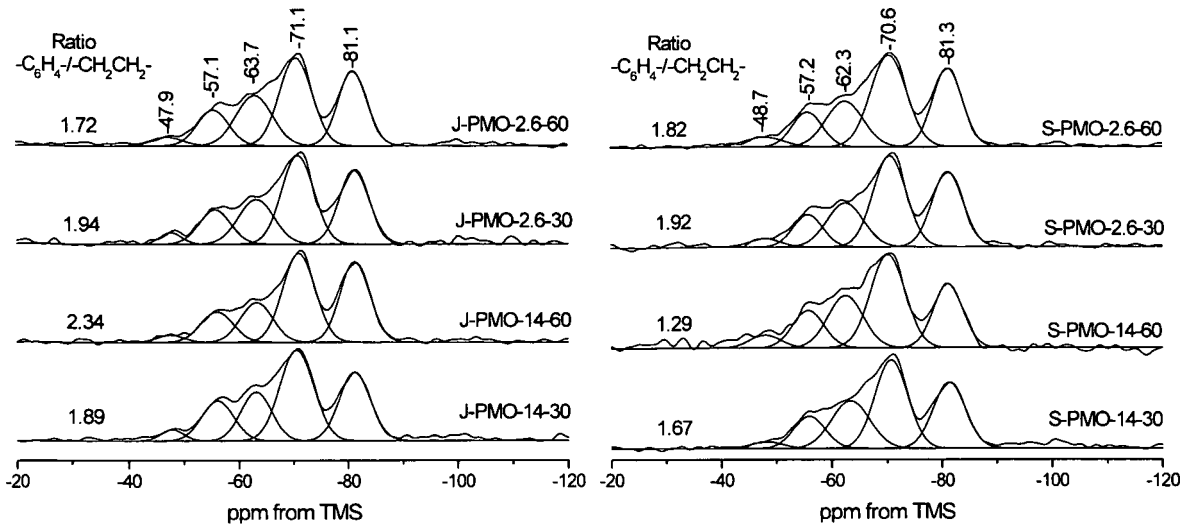

Figure 6.23. ^{1}H-^{29}Si CP/MAS NMR spectra of the template extracted PMOs prepared *via* cationic templating using joint (left) and separate (right) pre-hydrolysis protocols.

The difference in hydrolysis/condensation rates of the two silica precursors influences the composition of the resulting PMOs. The Silicon nuclei are more electropositive in the aromatic than in the aliphatic precursors, confirmed by the deshielding observed in ^{29}Si high-resolution NMR ($((EtO)_3Si)_2[CH_2CH_2]$, δ = -46.0 ppm $((EtO_3)Si)_2[C_6H_4]$, δ = -58.9 ppm). This suggests the Si centre of the aromatic precursor to be more susceptible to nucleophilic attack. Therefore it would hydrolyse faster than the $-CH_2CH_2-$ precursor. For joint pre-hydrolysis systems the $-C_6H_4-$ precursor uses the nucleophile ($H_2O/^-OH$) first to undergo hydrolysis and form the reactive ≡Si-OH intermediates before the ≡Si-CH_2CH_2-Si≡ precursor. However, the aliphatic component is able to undergo some degree of hydrolysis due to the 2 and 10 times excess of H_2O in the pre-hydrolysis solutions when Si/NaOH = 14 and 2.6 respectively. Subsequently, when the joint pre-hydrolysis mixtures are added to the template/base solution the aromatic SBUs co-assembles before the $-CH_2CH_2-$ component thus resulting in its reduced incorporation as a function of pre-hydrolysis time. In the separately pre-hydrolysing systems the nucleophilie, $H_2O/^-OH$ is equally available to both components. Therefore an increased incorporation of the $-CH_2CH_2-$ with increasing separate pre-hydrolysis time is observed due to the possibility of the aliphatic SBUs to have a sufficient reactivity to undergo co-assembly with the

template. In addition, the reduced incorporation of the aliphatic component may be related to its increased solubility in increasingly more basic solutions. Indeed, a study by Kaiser *et al.* showed that increasing the base content in aqueous/TEOS solutions ehanced the rate of hydrolysis and condensation. However, increasing the base content in aqueous/alkyl substituted alkoxysilanes ($R\text{-}Si(OEt)_3$) resulted in a reduction of hydrolysis and condensation rates.[235] A similar effect was observed during the optimisation of the synthesis for $-CH_2CH_2$-PMO where an increased base content resulted in only a clear solution being obtained after 3 days of hydrothermal treatment.

Table 6.6. Comparison of $-C_6H_4-/-CH_2CH_2-$ ratios determined from ^{13}C and ^{29}Si CP/MAS NMR spectra.

Sample	$-C_6H_4-/-CH_2CH_2-$ ratio		^{13}C CP/MAS - ^{29}Si CP/MAS
	^{13}C CP/MAS[a]	^{29}Si CP/MAS	
$-CH_2CH_2/-C_6H_4$-PMO	0.96	0.96	0.00
J-PMO-14-30	1.47	1.73	-0.26
J-PMO-14-60	1.72	2.16	-0.44
J-PMO-2.6-30	1.64	1.78	-0.14
J-PMO-2.6-60	1.71	1.57	0.14
S-PMO-14-30	1.57	1.67	-0.10
S-PMO-14-60	1.27	1.29	-0.02
S-PMO-2.6-30	1.73	1.92	-0.19
S-PMO-2.6-60	1.58	1.82	-0.24

[a] Values scaled by dividing peak area ratio by 3 (see text for details).

In general, the PMOs prepared using either joint or separate pre-hydrolysis showed the $-CH_2CH_2-$ environment to be more condensed compared to the standard mono- and bi-functional $-CH_2CH_2-/-C_6H_4$-PMO (Table 6.7). The $O_3Si\text{-}C_6H_4\text{-}SiO_3$ sites show slight increases or similar levels of condensation compared to $-CH_2CH_2-/-C_6H_4$-PMO with the exception of S-PMO-14-60. The enhanced degree of condensation of the silicon environments is to be expected as the introduction of pre-hydrolysis allows additional time for the simultaneous hydrolysis/ condensation process to occur (see section 6.2.1.2 (PXRD)). The degree of condensation of the $-CH_2CH_2$-Si environments increases for J-PMOs and decreases for S-PMOs with pre-hydrolysis time. Under joint pre-hydrolysis the degree of

condensation for the silicon –CH_2CH_2- sites increases with NaOH content. However, the trend is reversed under separate conditions after 30 minutes of pre-hydrolysis with no significant change after 60 minutes. Therefore (Tables 6.6 and 6.7) an increased degree of condensation of the Si–CH_2CH_2- $T^{2/3}$ sites comes at the expense of incorporation into the PMO under both pre-hydrolysis protocols.

Table 6.7. Degree of pore wall condensation derived from ^1H-^{29}Si CP/MAS NMR spectra

Sample	Peak Area					-CH_2CH_2- $(T^1 + T^2)/ T^3$	-C_6H_4- T^2/ T^3
	-CH_2CH_2-			-C_6H_4-			
	T^1	T^2	T^3	T^2	T^3		
-CH_2CH_2-PMO	0.27	3.80	8.54	//	//	0.48	//
-C_6H_4-PMO	1.31[a]	//	//	5.92	6.77	//	1.07
-CH_2CH_2/-C_6H_4-PMO	1.07	5.30	5.13	6.32	4.71	1.24	1.34
J-PMO-14-30	0.65	3.26	3.81	7.86	5.49	1.03	1.43
J-PMO-14-60	0.50	2.51	3.26	7.35	6.17	0.92	1.19
J-PMO-2.6-30	0.61	2.70	3.99	7.25	5.72	0.83	1.27
J-PMO-2.6-60	0.70	2.85	4.63	7.29	5.56	0.77	1.31
S-PMO-14-30	0.52	2.48	4.46	7.16	5.29	0.67	1.35
S-PMO-14-60	0.76	3.62	4.80	7.05	4.76	0.91	1.48
S-PMO-2.6-30	0.63	2.33	3.92	7.44	5.78	0.76	1.28
S-PMO-2.6-60	0.92	2.56	4.18	8.17	5.80	0.83	1.41

[a] T^1 silicon environment of the -C_6H_4- bridging group.

In line with the observations from high angle PXRD, the changes in the degree of condensation observed for the –CH_2CH_2- functionality suggest that after pre-hydrolysis the aliphatic component is disrupting the aromatic π-π stacking layers. The standard -CH_2CH_2-/-C_6H_4-PMO shows a higher degree of molecular level ordering, higher aliphatic content and lower pore wall condensation which suggests in this case the aliphatic component does not interfere with the aromatic π-π stacking to the same degree as for the pre-hydrolysed systems. However, the increased aliphatic content is at the expense of degree of condensation.

The ^{1}H MAS NMR spectra of the template extracted pre-hydrolysed PMOs (Fig. 6.24) gave similar spectra to those of -CH_2CH_2-/-C_6H_4-PMO (Fig 6.20). The changes in chemical shift of the water in J-PMO-2.6-60 and S-PMO-14-30 could be explained by the increase in water content relative to the organic functionalities. The resonance at *ca.* 3.9 ppm can be assigned as the same ≡Si-OH···OH_2 as for the standard PMOs (Fig. 6.20). The other pre-hydrolysed PMOs show a resonance in the region of *ca.* 3.0 - 3.2 ppm due to the lower water content where an asymmetric exchange process between three different proton spin environments ((1.5 + 1.75 + 5.5)/3 = 2.9 ppm and (1.5 + 1.5 + 5.5)/3 = 2.8 ppm, Fig. 6.21d and e). There is also the possibility for this resonance to arise from the presence of 'surface-hopping' of water molecules accompanied by the breaking of covalent -OH bonds and O···H hydrogen bonds.[198,238]

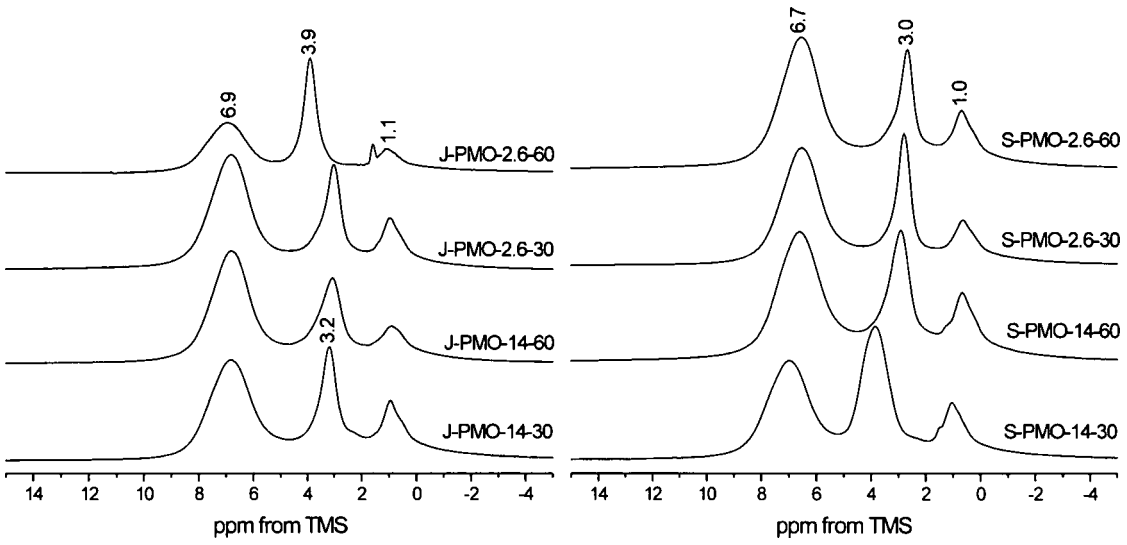

Figure 6.24. ^{1}H MAS NMR spectra of the template extracted Jointly (left) and Separately (right) pre-hydrolysed PMOs prepared *via* the I^-S^+ synthetic pathway.

6.4.2 Composition of acid catalysed PMOs

6.4.2.1 Reference PMOs

^{1}H-^{13}C CP/MAS NMR spectra of the template extracted standard PMOs (Fig. 6.25) show two resonances attributed to the organic functionalities. An additional resonance at *ca.* 70 ppm results from PEO blocks of the residual template whilst the peaks at 16 and 58 ppm correspond to silica surface ethoxy groups. The ratio of -C_6H_4-/-CH_2CH_2- bridges in the bi-functional standard is 0.50. This is in contrast to the base catalysed PMOs. The increased aliphatic content may be related to the lack of molecular level organisation observed in the pore walls. This is consistent with the acid catalysed systems being under kinetic control in that the –CH_2CH_2- and –C_6H_4- are "locked" into the structure. Therefore, in contrast to basis systems, the aromatic precursor no longer forms an energetically stable π-π stacking conformation.

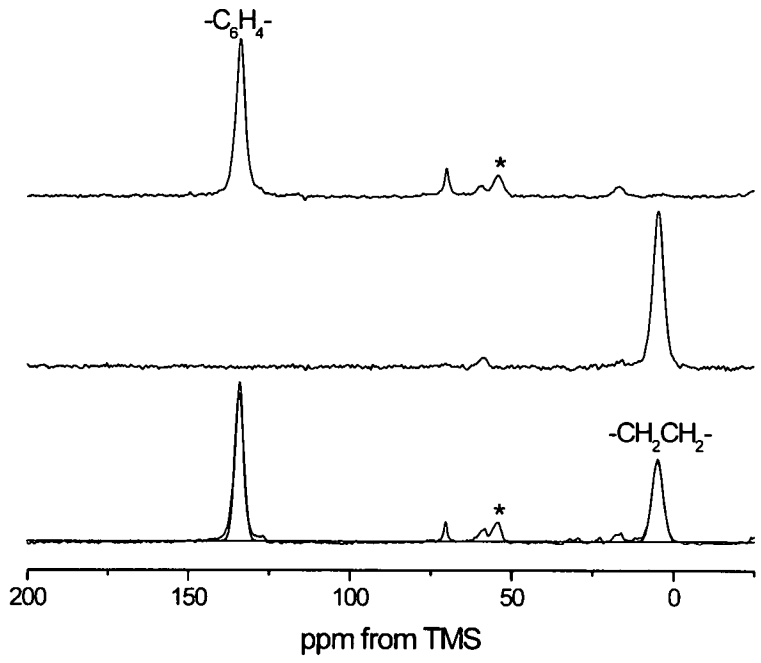

Figure 6.25. ^{1}H-^{13}C CP/MAS NMR spectra of the template extracted -C_6H_4-/-CH_2CH_2-PMO (bottom), -CH_2CH_2-PMO (middle) and -C_6H_4-PMO (top) prepared *via* non-ionic templating.

^{1}H-^{29}Si CP/MAS NMR spectra of the template extracted standard mono- and bi-functional PMOs with assignment of the resonances are shown in the fig. 6.26. The ratio T^n(-C_6H_4-)/T^n(-CH_2CH_2-) = 0.60 is consistent with the ^{1}H-^{13}C CP/MAS data (fig. 6.25). The mono-functional PMOs both showed a lower degree of pore wall condensation ((T^1 + T^2) /T^3) compared to the analogous I^-S^+-templated PMOs. The absence of any Q^n resonances in

the region from -90 to -120 ppm indicates that there was no Si-C bond cleavage during synthesis or template extraction.

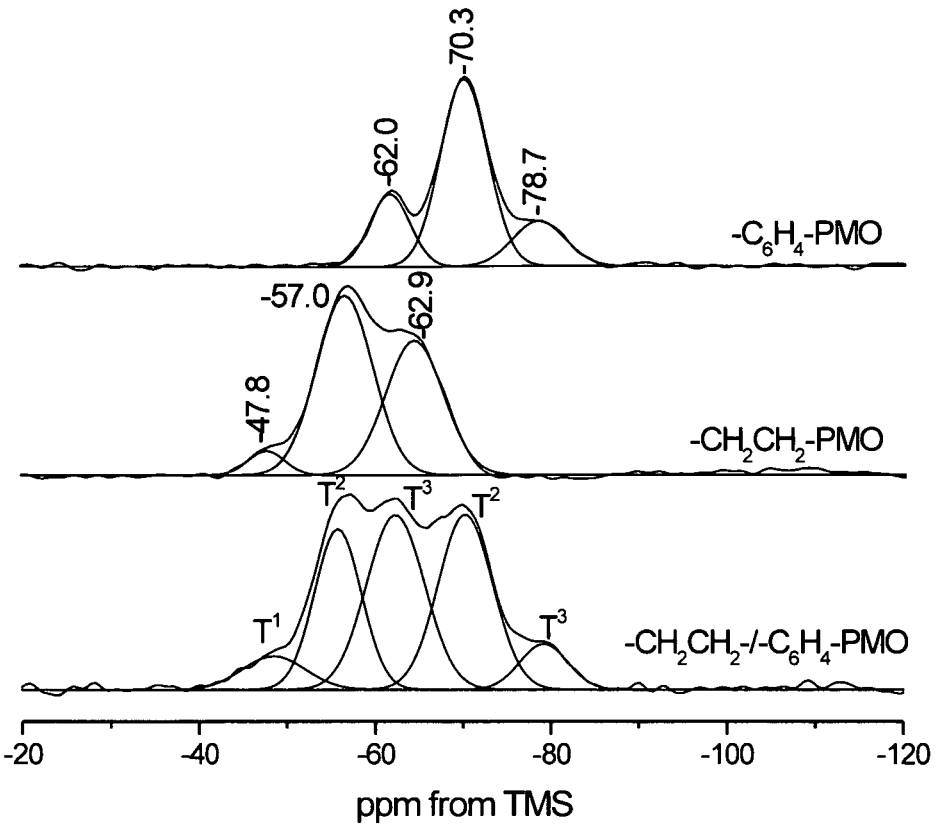

Figure 6.26. ^{1}H-^{29}Si CP/MAS spectra of the template extracted standard PMOs prepared *via* non-ionic templating.

^{1}H MAS NMR spectra (fig. 6.27) of the template extracted standard bi-functional -CH_2CH_2-/-C_6H_4-PMO show four resonances. The peak at *ca.* 1.0 ppm corresponds to the aliphatic bridge and the resonance at *ca.* 7.5 ppm is attributed to the aromatic functionality. The peak at 4.2 ppm is between predicted values for water clusters at 5.5 ppm and exchange with surface silanols at 3.6 ppm. This suggests the presence of a unimodal distribution of water layers on the pore surface in a similar fashion to that observed for SBA-15 upon increasing water content.[198] The mono-functional -C_6H_4-PMO indicates the presence of low intensity resonances at 3.4 and 1.0 ppm which can be assigned to residual PEO components of the template, surface Si-OH functionalities and/ or some residual template PPO -CH_3 protons remaining in pores respectively (fig. 6.27, insert).

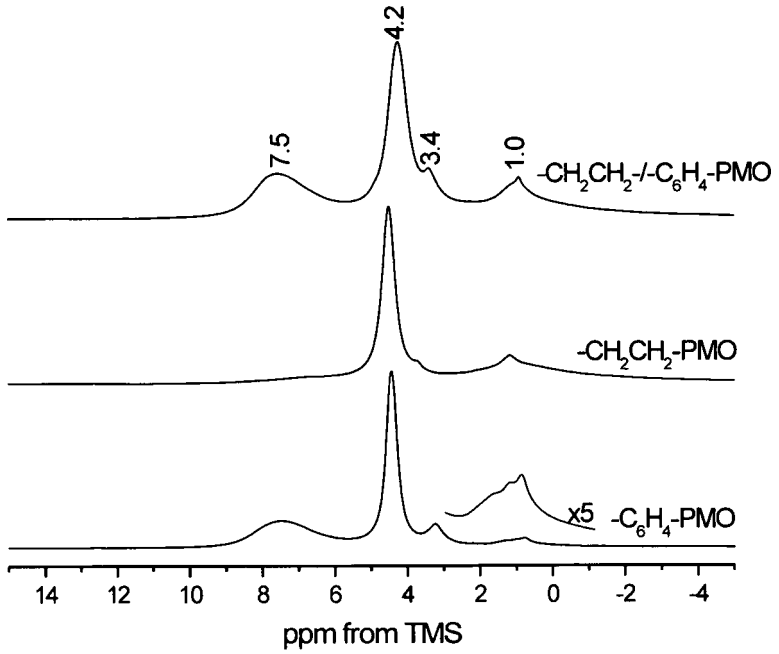

Figure 6.27. ^{1}H MAS NMR spectra of the template extracted standard PMOs prepared *via* the $S^{0}H^{+}X^{-}I^{+}$ synthetic pathway.

6.4.2.2. Pre-hydrolysed PMOs

The ^{1}H-^{13}C CP/MAS NMR spectra of the pre-hydrolysed PMOs (Fig. 6.28) show the same two major resonances due to the organic bridges as well as minor peaks attributed to residual template and surface ≡Si-OC_2H_5 groups. The -C_6H_4-/-CH_2CH_2- ratios in the pre-hydrolysed PMOs determined using ^{1}H-^{13}C CP/MAS NMR are similar to that of the standard –CH_2CH_2-/-C_6H_4-PMO.

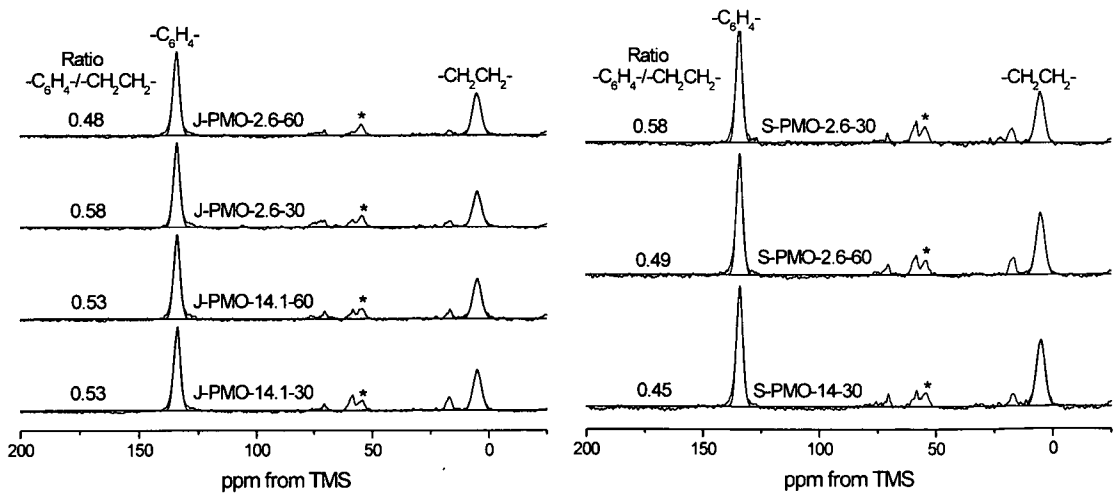

Figure 6.28. ^{1}H-^{13}C CP/MAS NMR spectra of the template extracted joint (left) and separate (right) pre-hydrolysed bi-functional PMOs prepared *via* non-ionic templating.

The ^{1}H-^{29}Si CP/MAS NMR spectra of the pre-hydrolysed PMOs (Fig. 6.29) also indicate similar $-C_6H_4$-/-CH_2CH_2- ratios to those of the $-CH_2CH_2$-/-C_6H_4-PMO. For the pre-hydrolysed solids the degree of condensation of the O_3Si-CH_2CH_2-SiO_3 units is similar in to that for bi-functional reference PMO.

The degree of condensation of the -C_6H_4- bridges increased in the pre-hydrolysed PMOs compared to the mono- and bi- functional PMO standards (table 6.8). In contrast to expected trend, the degree of condensation decreases slightly with increasing pre-hydrolysis time for both J/S-PMOs (the one exception is the aromatic bridging silicon environments become more condensed with pre-hydrolysis time for J-PMO-2.6-30 to -60). This effect could be related to the inability of larger, bulkier SBU to condense around the template micelles as efficiently as smaller SBUs. The anomaly observed for the -C_6H_4- bridges for J-PMO-2.6-30 to -60 could indicate an equilibrium point with an optimum size of SBUs and efficient co-assembly around the template. The effect of the Si/HCl ratio in the pre-hydrolysis mixtures on the degree of pore wall condensation was less systematic and no clear trends were observed in the resulting PMOs.

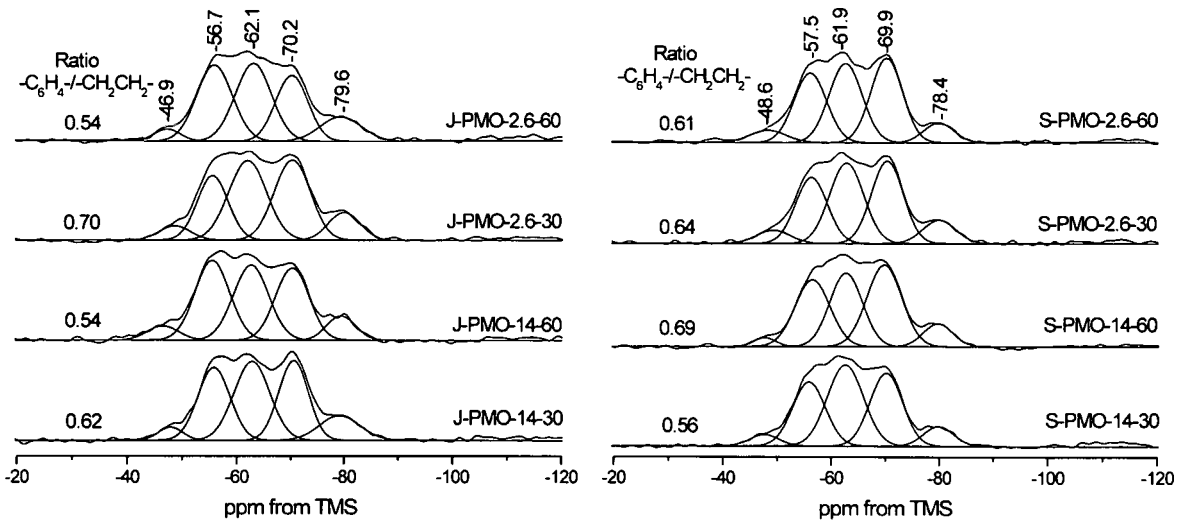

Figure 6.29. ^{1}H-^{29}Si CP/MAS NMR spectra of the template extracted jointly (left) and separately (right) pre-hydrolysed bi-functional PMOs prepared *via* non-ionic templating.

Table 6.8. ^{1}H-^{29}Si CP/MAS NMR deconvoluted peak areas of silicon T^n sites and degree of pore wall condensation.

Sample	Peak Area					$-CH_2CH_2-$	$-C_6H_4-$
	$-CH_2CH_2-$			$-C_6H_4-$			
	T^1	T^2	T^3	T^2	T^3	$(T^1 + T^2)/ T^3$	$(T^1 + T^2)/ T^3$
$-CH_2CH_2$-PMO	0.66	7.59	5.87	//	//	1.41	//
$-C_6H_4$-PMO	2.18[a]	//	//	6.65	1.78	//	4.96
$-CH_2CH_2/-C_6H_4$-PMO	1.57	5.63	7.63	7.21	1.64	0.94	5.35
J-PMO-14-30	0.81	5.91	7.21	6.01	2.57	0.93	2.65
J-PMO-14-60	1.12	6.96	6.73	6.18	1.78	1.20	4.10
J-PMO-2.6-30	1.12	4.99	7.63	7.34	2.25	0.80	3.76
J-PMO-2.6-60	0.77	6.78	7.06	5.33	2.56	1.07	2.38
S-PMO-14-30	0.81	5.29	7.38	5.99	1.50	0.83	4.53
S-PMO-14-60	0.48	5.83	6.00	7.16	1.69	1.05	4.52
S-PMO-2.6-30	1.11	5.22	6.84	6.25	1.93	0.93	3.81
S-PMO-2.6-60	1.11	5.68	6.55	6.70	1.49	1.04	5.24

[a] T^1 silicon environment of the $-C_6H_4-$ bridging group.

The ^{1}H MAS NMR spectra of the template extracted J- and S-PMOs (Fig. 6.30) show the same four resonances as the bi-functional standard PMO. Interestingly, the water resonance at *ca.* 4.2 ppm is shifted slightly to higher ppm in all J-PMOs with the exception of J-PMO-14-30. This is most likely due to an increase in number of the water layers within the pore structure resulting in a chemical shift increase as $(H_2O)_n$ clusters become more predominant compared to the standard $-CH_2CH_2-/-C_6H_4$-PMO.

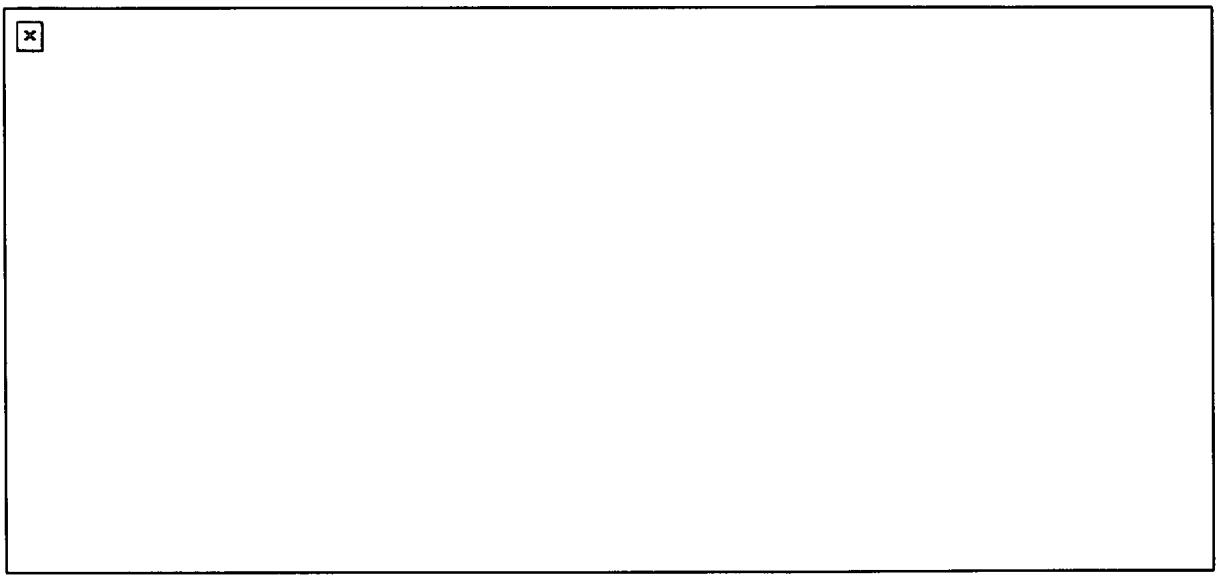

Figure 6.30. ^{1}H MAS NMR spectra of the template extracted J- (left) and S-PMOs (right) PMOs prepared *via* the $S^{0}H^{+}X^{-}I^{+}$ synthetic pathway.

6.4.3 ^{1}H-^{29}Si CP/MAS kinetics of the $S^{+}I^{-}$ templated PMOs

^{1}H-^{29}Si CP/MAS kinetics has proven invaluable in probing the silicon environments of pore walls at a molecular level. The ^{1}H-^{29}Si CP/MAS kinetics curves and fitting parameters of the standard PMOs (Fig. 6.31 and Table 6.8 respectively) indicate changes in the frameworks between mono- and bi-functional PMOs.

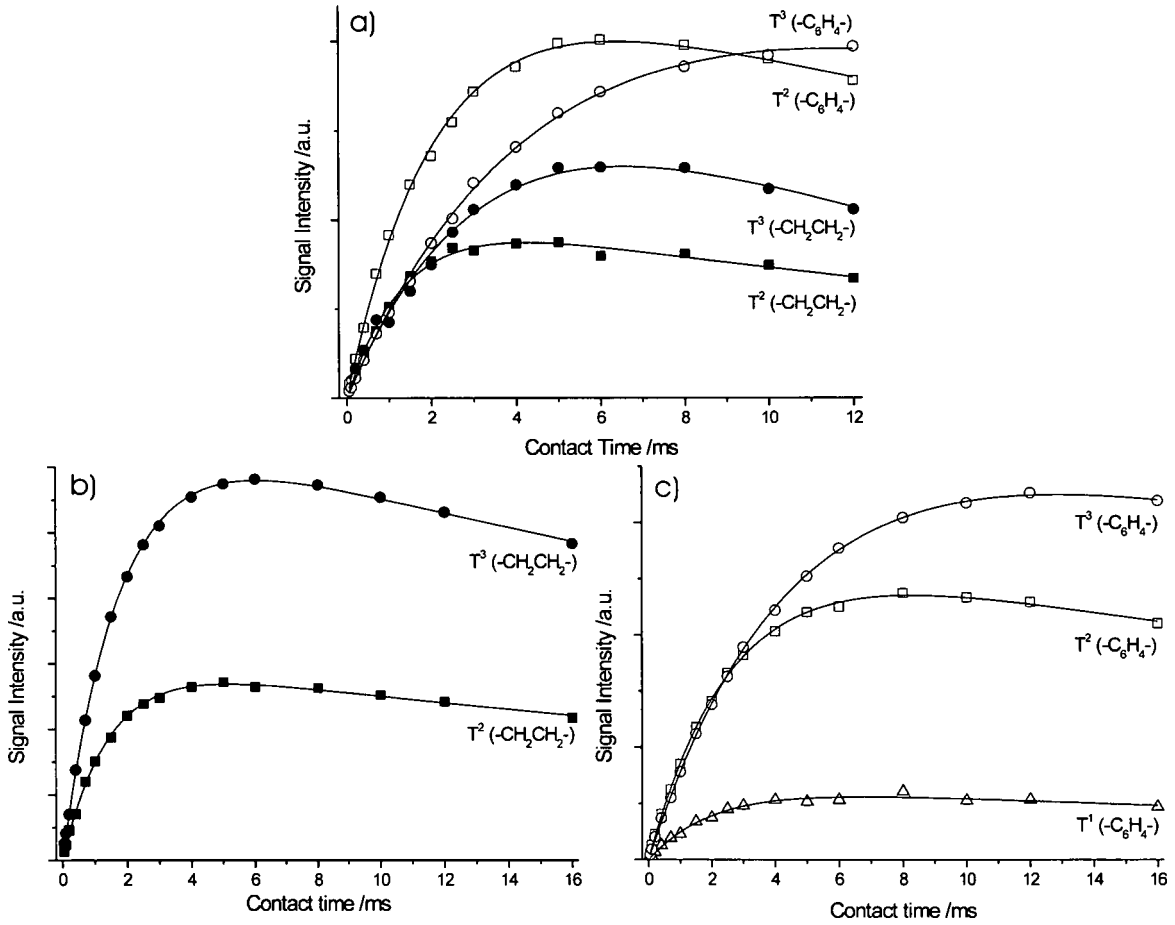

Figure 6.31. ^{1}H-^{29}Si CP/MAS kinetics curves of the template extracted standards a) -CH_2CH_2-/-C_6H_4-PMO, b) -CH_2CH_2-PMO and c) -C_6H_4-PMO prepared via $S^{+}I^{-}$ synthetic pathway.

The T_{CP} times for the -CH_2CH_2- $T^{2/3}$ silicon environments are shorter than for the -C_6H_4- $T^{2/3}$ sites in -CH_2CH_2-/-C_6H_4-PMO. This is expected as the average internuclear distance between the Silicon centre and the ^{1}H CP source is increased. The T_{CP} time is longer for the -C_6H_4- T^2 silicon environments in -C_6H_4-PMO compared to the corresponding silicon environment in the -CH_2CH_2-/-C_6H_4-PMO. This suggests the -C_6H_4- silicon T^2 sites have more 'CP donors' in close proximity in the bi-functional standard. The protons from the aliphatic bridges may now provide CP to the $T^2(C_6H_4)$ sites, confirmed by ^{1}H-^{29}Si

HETCOR spectrum (fig. 6.35a). No significant changes in the T_{CP} values of the aromatic silicon T^3 environments have been observed between the two PMOs. Taking into account effects seen for the aromatic silicon T^2 sites, one can suggest the presence of a core of aromatic environments within the bulk of the pore walls, thus retaining the layered π-π stacking formation as seen by PXRD (Fig. 6.1). That is, around the π-π stacked layers peripheral layers of aliphatic bridges which co-condense with the partially condensed aromatic T^2 sites resulting in 'onion type' layers of organic functionality are formed (Scheme 1).

With the exception of the aromatic T^3 site, the $T_{1\rho}{}^H$ times are decreased for all the silicon environments in the bi-functional PMO standard compared to their mono-functional PMO counterparts. This indicates a decrease in mobility and/ or increase in density of the proton environments providing CP which is consistent with the conclusions derived from the changes in T_{CP}.

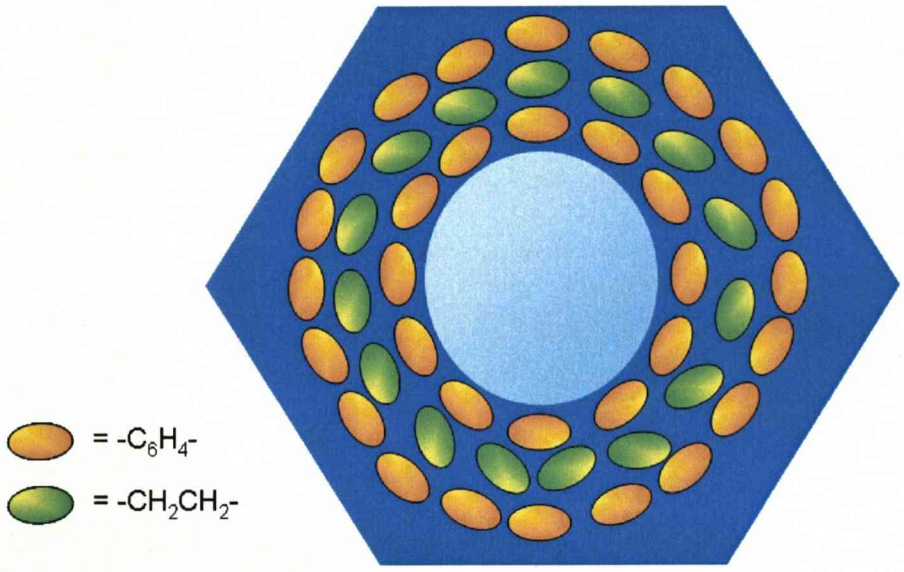

Scheme 6.3. Representation of the 'onion type' molecular level organisation present within the bifunctional PMOs prepared *via* S^+I^- synthetic pathway.

Table 6.9. ^{1}H-^{29}Si CP/MAS kinetics parameters for the standard PMOs prepared *via* $S^{+}I^{-}$ synthetic pathway.

Resonance /ppm	^{29}Si Site	Signal Intensity /10^7	T_{IS} /ms	$T_{1\rho}^{H}$ /ms	R^2
-CH_2CH_2-/-C_6H_4-PMO					
-56.8	-CH_2CH_2- T^2	1.04 ±0.03	1.38 ±0.09	24.8 ±3.32	0.995
-62.2	-CH_2CH_2- T^3	1.70 ±0.04	2.81 ± 0.17	23.3 ± 3.30	0.991
-69.6	-C_6H_4- T^2	2.41 ±0.07	2.16 ±0.09	33.6 ±4.57	0.999
-80.9	-C_6H_4- T^3	2.55 ±0.22	4.62 ±0.48	> 50.0	0.999
-CH_2CH_2-PMO					
-58.1	-CH_2CH_2- T^2	3.00 ±0.02	1.42 ±0.02	47.6 ±2.30	0.999
-66.9	-CH_2CH_2- T^3	6.60 ±0.05	1.78 ±0.03	46.5 ±2.07	0.999
-C_6H_4-PMO					
-60.9	-C_6H_4- T^1	0.64 ±0.01	2.06 ±0.10	47.8 ±7.29	0.990
-70.8	-C_6H_4- T^2	2.77 ±0.05	3.19 ±0.20	49.9 ±4.69	0.999
-80.1	-C_6H_4- T^3	4.00 ±0.02	4.58 ±0.04	>50.0	0.999

The ^{1}H-^{29}Si VCT CP/MAS kinetics of the J/S-PMOs (Fig. 6.32 and Table 6.10 respectively) highlight differences in their frameworks to that of the standard -CH_2CH_2-/-C_6H_4-PMO. The T_{CP} times for the Si-CH_2CH_2- T^2 and Si-C_6H_4- $T^{2/3}$ sites remain unaltered by pre-hydrolysis. Whereas the T_{CP} times for -CH_2CH_2-T^3 sites decrease slightly for all pre-hydrolysed PMO compared to -CH_2CH_2-/-C_6H_4-PMO. This could indicate an increase in number of 'CP donors' in close proximity to the –CH_2CH_2-T^3 sites.

The introduction of pre-hydrolysis has a more pronounced effect on the $T_{1\rho}^{H}$ times of the silicon environments bound to both organic bridges (with the exception of the -C_6H_4-Si≡ T^3 environment which displays very long $T_{1\rho}^{H}$ times of > 40 ms). The -CH_2CH_2-Si≡ $T^{2/3}$ sites in both the J- and S- PMOs display longer $T_{1\rho}^{H}$ times compared to the reference -CH_2CH_2-/-C_6H_4-PMO. This observation along with the decreasing T_{CP} times of the aliphatic silicon T^3 site (from 2.81 (standard PMO) to *ca.* 1.83 ms (pre-hydrolysed PMOs)), suggests more protons from surrounding functionalities are acting as 'CP donors' and are increasingly mobile compared to the reference PMO.[154] The CP kinetics of the –CH_2CH_2-/-C_6H_4-PMO (Fig. 6.31) indicate the aliphatic T^3 environments are close in space to the T^2(C_6H_4) sites

within the framework which appears to be the same for all pre-hydrolysed PMOs. This confirms the pre-hydrolysed PMOs under basic conditions to have of a similar pore wall structure to that outlined for the $-CH_2CH_2$-/-C_6H_4-PMO (scheme 1). Differences between the ^1H-^{29}Si CP/MAS kinetics as a function of joint and separate pre-hydrolysis are less pronounced.

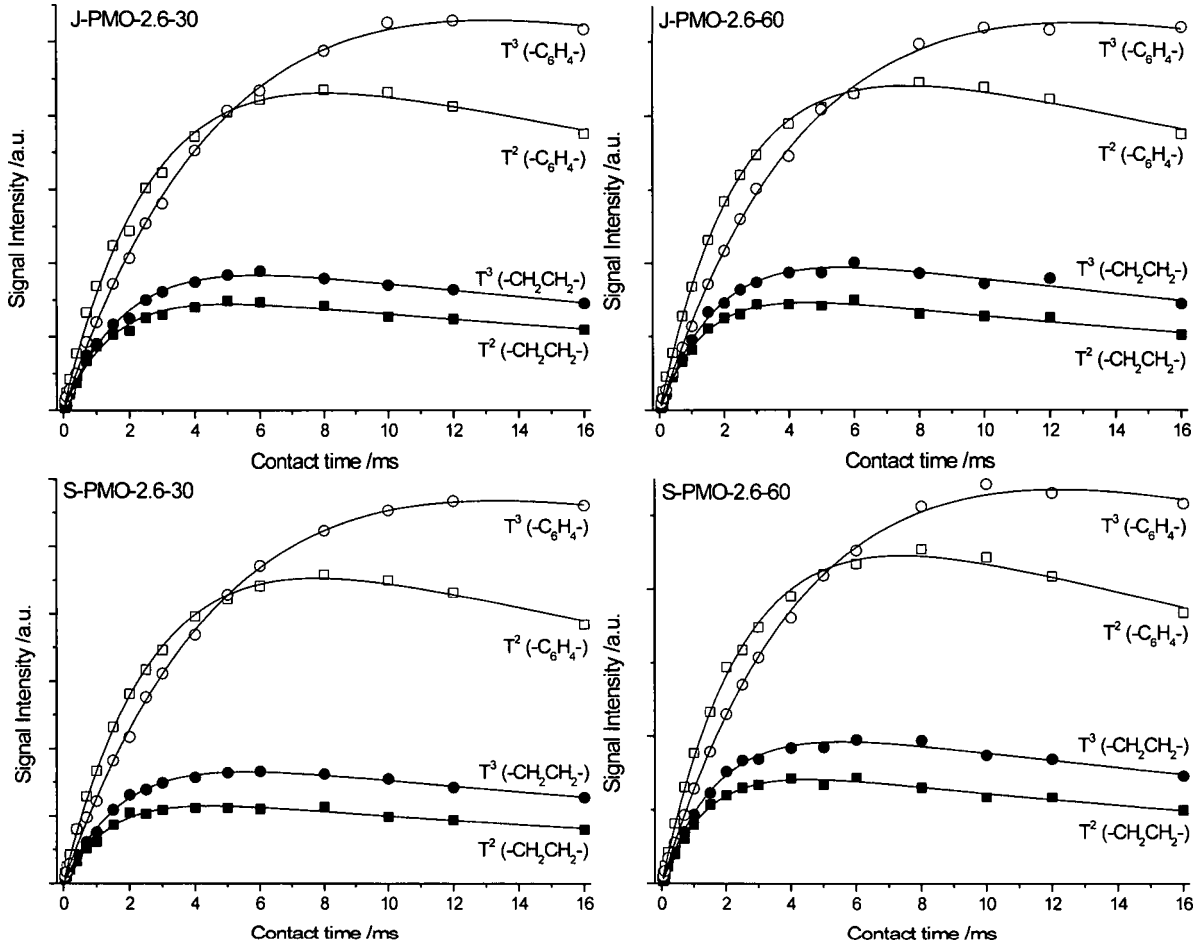

Figure 6.32. ^1H-^{29}Si CP/MAS kinetics curves of the template extracted jointly (top) and separately (bottom) PMOs prepared via S^+I^- synthetic pathway.

Table 6.10. ^{1}H-^{29}Si CP/MAS kinetics parameters for the pre-hydrolysed PMOs prepared *via* $S^{+}I^{-}$ synthetic pathway.

Resonance /ppm	^{29}Si Site	Signal Intensity /10^7	T_{IS} /ms	$T_{1\rho}^{H}$ /ms	R^2
J-PMO-2.6-30					
-56.5	$-CH_2CH_2-$ T^2	1.66 ±0.028	1.52 ±0.067	35.6 ±3.48	0.992
-62.3	$-CH_2CH_2-$ T^3	2.16 ±0.029	1.91 ±0.063	35.9 ±2.80	0.995
-70.6	$-C_6H_4-$ T^2	5.18 ±0.064	2.72 ±0.077	43.4 ±3.67	0.997
-81.2	$-C_6H_4-$ T^3	6.95 ±0.058	5.28 ±0.099	48.1 ±3.04	0.999
J-PMO-2.6-60					
-56.4	$-CH_2CH_2-$ T^2	1.68 ±0.044	1.37 ±0.077	30.8 ±3.33	0.995
-62.5	$-CH_2CH_2-$ T^3	2.28 ±0.032	1.81 ±0.063	32.9 ±2.51	0.995
-71.1	$-C_6H_4-$ T^2	5.27 ±0.114	2.56 ±0.090	41.5 ±4.18	0.999
-81.3	$-C_6H_4-$ T^3	6.83 ±0.058	5.13 ±0.096	48.9 ±3.16	0.999
S-PMO-2.6-30					
-56.2	$-CH_2CH_2-$ T^2	1.33 ±0.041	1.39 ±0.090	29.6 ±3.63	0.993
-61.6	$-CH_2CH_2-$ T^3	1.95 ±0.049	1.79 ±0.086	33.6 ±3.56	0.997
-70.7	$-C_6H_4-$ T^2	5.58 ±0.121	2.77 ±0.094	36.9 ±3.29	0.999
-81.0	$-C_6H_4-$ T^3	7.37 ±0.631	5.26 ±0.564	50.9 ±4.55	0.998
S-PMO-2.6-60					
-56.4	$-CH_2CH_2-$ T^2	1.65 ±0.040	1.43 ±0.072	28.5 ±2.66	0.996
-61.7	$-CH_2CH_2-$ T^3	2.27 ±0.029	1.80 ±0.059	33.3 ±2.38	0.995
-70.6	$-C_6H_4-$ T^2	5.49 ±0.050	2.64 ±0.055	35.1 ±1.83	0.998
-80.8	$-C_6H_4-$ T^3	7.03 ±0.058	4.94 ±0.091	44.5 ±2.60	0.999

6.4.4. ^1H-^{29}Si CP/MAS kinetics of $S^0H^+X^-I^+$ templated PMOs

^1H-^{29}Si CP/MAS kinetics (Fig. 6.33 and table 6.11 respectively) highlight differences in the pore wall dynamics between the mono and bi-functional PMOs and with the base catalysed counterparts (fig. 6.30). As seen for the base catalysed PMOs, the T_{CP} times of the silicon $-CH_2CH_2-$ $T^{2/3}$ sites are shorter than for their corresponding $-C_6H_4-$ environments. In comparison to the standard PMOs synthesized *via* the S^+I^- pathway, all acid catalysed PMOs show much faster ^1H relaxation times in the rotating frame. This indicates PMOs prepared *via* the $S^0H^+X^-I^+$ pathway have an increased proton density, hence stronger ^1H-^1H dipolar coupling. This can be related to their approximately doubled wall thickness (Table 6.5). The $-C_6H_4$-PMO T^n sites show shorter $T_{1\rho}{}^H$ times compared to the bi-functional standard which is in contrast to the mono-/ bifunctional PMOs prepared *via* the S^+I^- pathway.

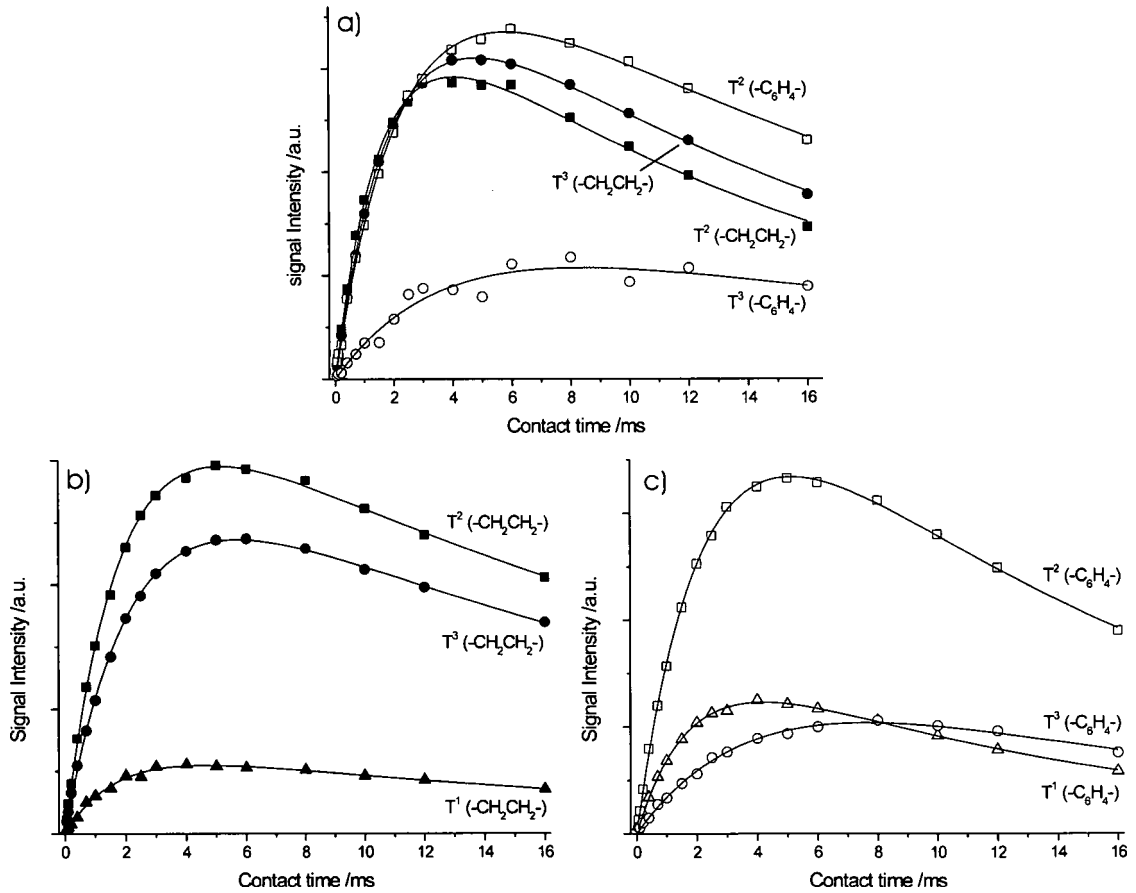

Figure 6.33. ^1H-^{29}Si CP/MAS kinetics curves of the template extracted standards a) -CH_2CH_2-/-C_6H_4-PMO, b) -CH_2CH_2-PMO and c) -C_6H_4-PMO prepared *via* the $S^0H^+X^-I^+$ synthetic pathway.

The T_{CP} times vary only slightly between the mono- and bi-functional PMOs synthesised in acidic systems, thus the majority of the 'CP donors' to the silicon T sites

comes from their covalently bound organic bridges. On the other hand, the $T_{1\rho}^{H}$ times are different between the mono- and bi-functional PMOs. The difference in $T_{1\rho}^{H}$ times between the $-CH_2CH_2-$ and $-C_6H_4-$ organic bridges silicon $T^{2/3}$ sites in the bi-functional standard is an average of 6.5 ms (calculated by $((-C_6H_4-\ T^2 + T^3)/2)-((-CH_2CH_2\ T^2 + T^3)/2)$, whereas, the difference between the two mono-functional PMOs is an average of 9.2 ms. Therefore one can conclude the bi-functional standard has a homogeneous distribution of organic functionalities. This is confirmed by ^{1}H-^{29}Si HETCOR experiments (Fig. 6.36).

Table 6.11. ^{1}H-^{29}Si VCT CP/MAS kinetics curve fitting parameters for the standard PMOs prepared *via* the $S^0H^+X^-I^+$ synthetic pathway.

Resonance /ppm	^{29}Si Site	Signal Intensity /10^7	T_{IS} /ms	$T_{1\rho}^{H}$ /ms	R^2
$-CH_2CH_2-/-C_6H_4-$PMO					
-56.6	$-CH_2CH_2-\ T^2$	1.88 ±0.034	1.58 ±0.055	15.7 ±0.708	0.998
-61.4	$-CH_2CH_2-\ T^3$	2.05 ±0.022	1.96 ±0.036	17.0 ±0.444	0.999
-69.8	$-C_6H_4-\ T^2$	2.19 ±0.050	2.32 ±0.088	21.6 ±1.39	0.999
-78.5	$-C_6H_4-\ T^3$	0.755 ±0.037	3.78 ±0.421	24.1 ±5.30	0.956
$-CH_2CH_2-$PMO					
-48.0	$-CH_2CH_2-\ T^1$	0.672 ±0.023	1.65 ±0.111	22.6 ±2.46	0.993
-56.7	$-CH_2CH_2-\ T^2$	3.61 ±0.049	1.81 ±0.046	25.3 ±1.15	0.999
-62.5	$-CH_2CH_2-\ T^3$	2.99 ±0.053	2.15 ±0.066	24.3 ±1.35	0.999
$-C_6H_4-$PMO					
-61.7	$-C_6H_4-\ T^1$	1.68 ±0.033	1.79 ±0.061	13.5 ±0.564	0.998
-70.1	$-C_6H_4-\ T^2$	4.67 ±0.065	2.30 ±0.051	15.3 ±0.464	0.999
-78.7	$-C_6H_4-\ T^3$	1.68 ±0.024	4.26 ±0.124	15.8 ±0.686	0.996

The ^{1}H-^{29}Si CP/MAS kinetics curves and fitting parameters (Fig. 6.34 and Table 6.12 respectively) of the joint and separately pre-hydrolysed PMOs prepared via $S^{0}H^{+}X^{-}I^{+}$ pathway indicate slight changes in the CP dynamics compared to the standard -CH_2CH_2-/-C_6H_4-PMO. The $T_{1\rho}^{H}$ times for the -CH_2CH_2- silicon $T^{2/3}$ sites and -C_6H_4- T^{2} environments in all the pre-hydrolysed PMOs are decreased *c.f.* to -CH_2CH_2-/-C_6H_4-PMO. Whilst the $T_{1\rho}^{H}$ times for the -C_6H_4- silicon T^{3} site in the J-PMOs are *ca.* 20 ms, in the S-PMOs the values are increased to ca. 25 - 30 ms with the bi-functional standard being in between the two pre-hydrolysis protocols. The aromatic T^{3} site shows long $T_{1\rho}^{H}$ and T_{CP} times *c.f.* to the aliphatic T^{3} environment suggesting there are fewer 'CP donors' in close proximity. The reduction in the $T_{1\rho}^{H}$ times for the aliphatic silicon sites may result from the formation of SBUs during pre-hydrolysis which could decrease the proton mobility within the pore walls. The decrease in the $T_{1\rho}^{H}$ times for aromatic T^{2} environments and their similar values to the aliphatic sites in both J and S-PMOs cannot be explained easily as from the ^{1}H-^{29}Si HETCOR experiments (see section 6.4.6) both joint and separate pre-hydrolysis resulted in a more heterogeneous distribution of organic functionalities *c.f.* to the standard bi-functional PMO.

Differences in the CP kinetics as a function of pre-hydrolysis protocols are much less pronounced than those observed for the -CH_2CH_2-/-CH=CH-PMO systems described in chapter 5. This is due to the similarity in distribution of the organic moieties in the -CH_2CH_2-/-C_6H_4- J/S-PMOs as seen by ^{1}H-^{29}Si HETCOR (Fig. 6.36). However, it is possible to conclude that the -C_6H_4- T^{3} sites in the S-PMOs have slightly more efficient CP build up, indicating an increase in magnitude of the ^{1}H-^{29}Si heteronuclear dipolar interactions, and longer $T_{1\rho}^{H}$ times.

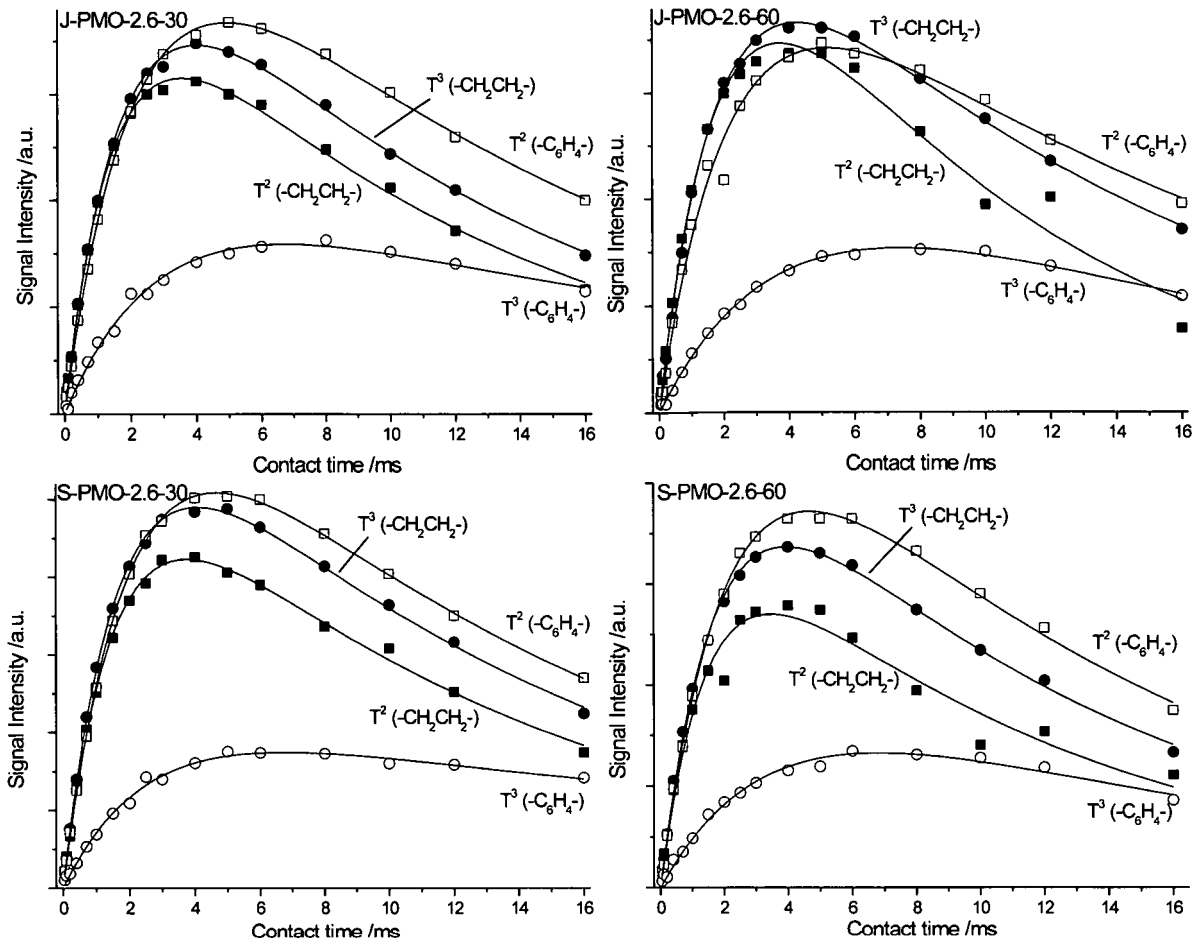

Figure 6.34. ^{1}H-^{29}Si CP/MAS kinetics curves of the template extracted jointly (top) and separately (bottom) pre-hydrolysed PMOs prepared *via* $S^{0}H^{+}X^{-}I^{+}$ synthetic pathway.

Table 6.12. ^{1}H-^{29}Si CP/MAS kinetics parameters for the pre-hydrolysed PMOs prepared *via* $S^{+}I^{-}$ synthetic pathway.

Resonance /ppm	^{29}Si Site	Signal Intensity /10^7	T_{IS} /ms	$T_{1\rho}^{H}$ /ms	R^2
J-PMO-2.6-30					
-57.0	$-CH_2CH_2-$ T^2	2.14 ±0.040	1.52 ±0.052	11.5 ±0.431	0.998
-62.1	$-CH_2CH_2-$ T^3	2.40 ±0.040	1.78 ±0.052	12.2 ±0.410	0.999
-70.1	$-C_6H_4-$ T^2	2.59 ±0.035	2.23 ±0.049	14.4 ±0.418	0.999
-78.3	$-C_6H_4-$ T^3	1.09 ±0.020	2.91 ±0.117	21.4 ±1.51	0.992
J-PMO-2.6-60					
-57.0	$-CH_2CH_2-$ T^2	2.54 ±0.057.	1.76 ±0.088	9.26 ±0.480	0.986
-61.6	$-CH_2CH_2-$ T^3	2.54 ±0.045	1.88 ±0.057	13.1 ±0.480	0.999
-70.0	$-C_6H_4-$ T^2	2.39 ±0.042	2.31 ±0.104	15.6 ±0.972	0.989
-78.7	$-C_6H_4-$ T^3	1.11 ±0.013.	3.50 ±0.097	19.3 ±0.911	0.997
S-PMO-2.6-30					
-57.5	$-CH_2CH_2-$ T^2	2.85 ±0.059	1.58 ±0.060	12.6 ±0.554	0.998
-61.9	$-CH_2CH_2-$ T^3	3.31 ±0.044	1.72 ±0.040	13.5 ±0.386	0.999
-70.0	$-C_6H_4-$ T^2	3.52 ±0.042	2.05 ±0.041	14.4 ±0.369	0.999
-78.3	$-C_6H_4-$ T^3	1.08 ±0.017	2.44 ±0.090	30.7 ±2.51	0.994
S-PMO-2.6-60					
-57.4	$-CH_2CH_2-$ T^2	1.86 ±0.137	1.51 ±0.201	10.9 ±1.57	0.969
-62.2	$-CH_2CH_2-$ T^3	2.36 ±0.054	1.78 ±0.071	11.6 ±0.523	0.998
-70.2	$-C_6H_4-$ T^2	2.69 ±0.069	2.22 ±0.089	12.5 ±0.621	0.998
-79.5	$-C_6H_4-$ T^3	0.830 ±0.021	2.67 ±0.148	26.4 ±2.94	0.988

6.4.5. ^{1}H-^{29}Si HETCOR NMR of the $S^{+}I^{-}$ templated PMOs

As shown above, ^{1}H-^{29}Si Heteronuclear correlation experiments have proven essential in determining the spatial proximity between two organic functionalities within the same mesoporous framework.

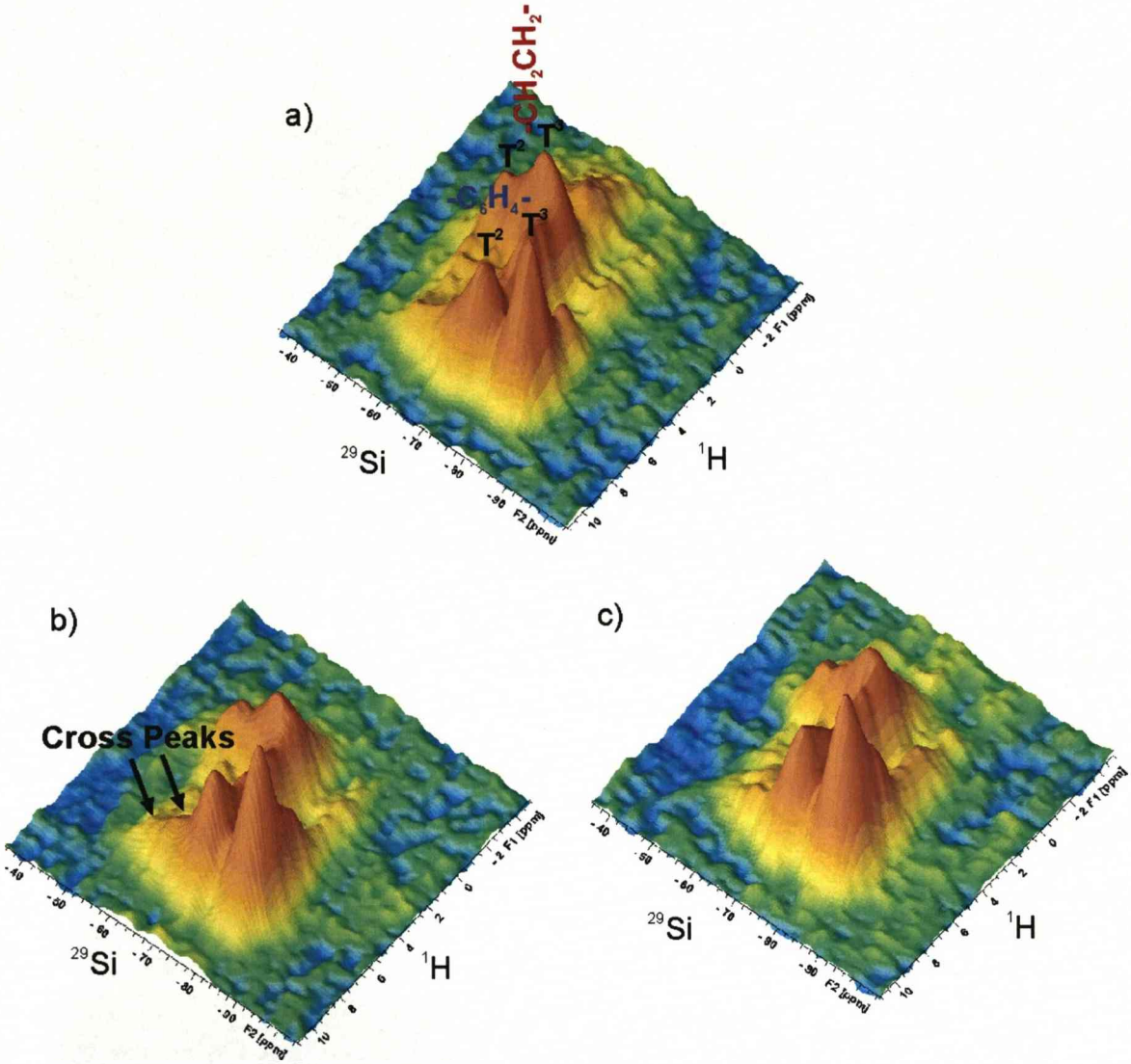

Figure 6.35. ^{1}H-^{29}Si HETCOR NMR spectra of the template extracted PMOs. a) $-CH_2CH_2-$/-C_6H_4-PMO, b) J-PMO-2.6-60 and c) S-PMO-2.6-60.

The ^{1}H-^{29}Si HETCOR spectrum for the standard $-CH_2CH_2-$/-C_6H_4-PMO (fig. 6.35a) shows four resonances in the ^{1}H indirect t_1 dimension. The first one at 0.6 ppm corresponds to surface Si-OH functionalities. The resonance at 1.3 ppm is due to $-CH_2CH_2-$ protons which show strong correlations to the $T^{2/3}(CH_2\text{-}CH_2)$ resonances at -58.0 and -67.2 ppm respectively. There are also strong correlations between the ^{1}H resonance at *ca.* 7.0 ppm and the $T^{2/3}(C_6H_4)$ sites at -71.5 and -81.4 ppm in the direct dimension t_2. These auto-peaks are

to be expected as the protons are covalently bound to the silicon nuclei *via* carbon atoms and confirm their assignment in the 1D ^{1}H MAS and ^{29}Si CP/MAS spectra. In addition, cross-peaks correlating the ^{1}H's of the -C_6H_4- bridges with resonance of the -CH_2CH_2-Si≡ $T^{2/3}$ sites and *vice-versa* are seen, although they are of a much reduced intensity compared to the auto-peaks. Therefore, the HETCOR spectra suggest formation of a bi-functional framework with domain functionality, further supporting the conclusions made from the ^{1}H-^{29}Si VCT CP/MAS NMR. A correlation of a minor ^{1}H resonance at *ca.* 4.2 ppm with all $T^{2/3}$ environments, confirms this peak to be a result of H-bonded water species close enough in space to the silicon T sites to provide magnetization for CP transfer. The same resonance was observed in the ^{1}H MAS NMR spectra yet its intensity is reduced in the ^{1}H-^{29}Si HETCOR spectra.

The HETCOR spectra of J-PMO-2.6-60 and S-PMO-2.6-60 along with the auto and cross peak intensities (Fig. 6.35b, c and table 12 respectively) show similar auto-peak correlations to those observed for the standard -CH_2CH_2-/-C_6H_4-PMO. The minor changes in the cross-peak intensities between the jointly and separately pre-hydrolyzed PMOs indicate the S-PMO-2.6-60 to be more homogeneous compared to both the jointly pre-hydrolyzed and standard PMO (Table 6.13). This observation is consistent with the ^{1}H-^{29}Si CP/MAS NMR kinetics. The changes in cross-peak intensities between J-PMO-2.6-60 and the standard material are very small and would suggest these two frameworks are similar in structure. Thus, joint pre-hydrolysis is ineffective in improving homogeneity under these conditions.

Table 6.13. Intensities of cross-peaks in the ^{1}H-^{29}Si HETCOR NMR spectra. Values are normalized to those of the $-CH_2CH_2-$ T^3 resonance.

^{29}Si Resonance / ^{1}H Resonance	$-CH_2CH_2-$		$-C_6H_4-$	
	T^2	T^3	T^2	T^3
$-CH_2CH_2-/-C_6H_4-$PMO				
$-CH_2CH_2-$	0.60	1.00	0.59	0.22
$-C_6H_4-$	0.24	0.60	0.87	1.26
(Auto peak $T^2 + T^3$)/ (Cross peak $T^2 + T^3$)	1.90		2.63	
J-PMO-2.6-60				
$-CH_2CH_2-$	0.63	1.00	0.80	0.28
$-C_6H_4-$	0.28	0.56	1.22	1.77
(Auto peak $T^2 + T^3$)/ (Cross peak $T^2 + T^3$)	1.94		2.77	
S-PMO-2.6-60				
$-CH_2CH_2-$	0.57	1.00	0.82	0.37
$-C_6H_4-$	0.18	0.88	1.11	1.66
(Auto peak $T^2 + T^3$)/ (Cross peak $T^2 + T^3$)	1.48		2.33	

6.4.6. ^{1}H-^{29}Si HETCOR NMR of the $S^{0}H^{+}X^{-}T^{+}$ templated PMOs

^{1}H-^{29}Si HETCOR NMR spectra (Fig. 6.36) of J-PMO-2.6-60 and S-PMO-2.6-60 show the same four resonances as the $S^{+}I^{-}$ synthesised PMOs. The auto correlation peaks between the silicon $T^{2/3}$ sites and their respective organic bridges ^{1}H environments are observed for all PMOs. The evidence of moderately intense cross-peaks between the $-C_6H_4-$ aromatic protons and the $-CH_2CH_2-$ silicon $T^{2/3}$ sites confirms, in accordance with the ^{1}H-^{29}Si VCT CP/MAS kinetics, a homogeneous distribution of organic functionalities in the framework of the standard $-CH_2CH_2-/-C_6H_4-$PMO (Fig. 6.36a). The acid catalysed standard bi-functional PMO is likely to be more homogeneous than the base catalysed analogue based on the CP kinetics and HETCOR data.

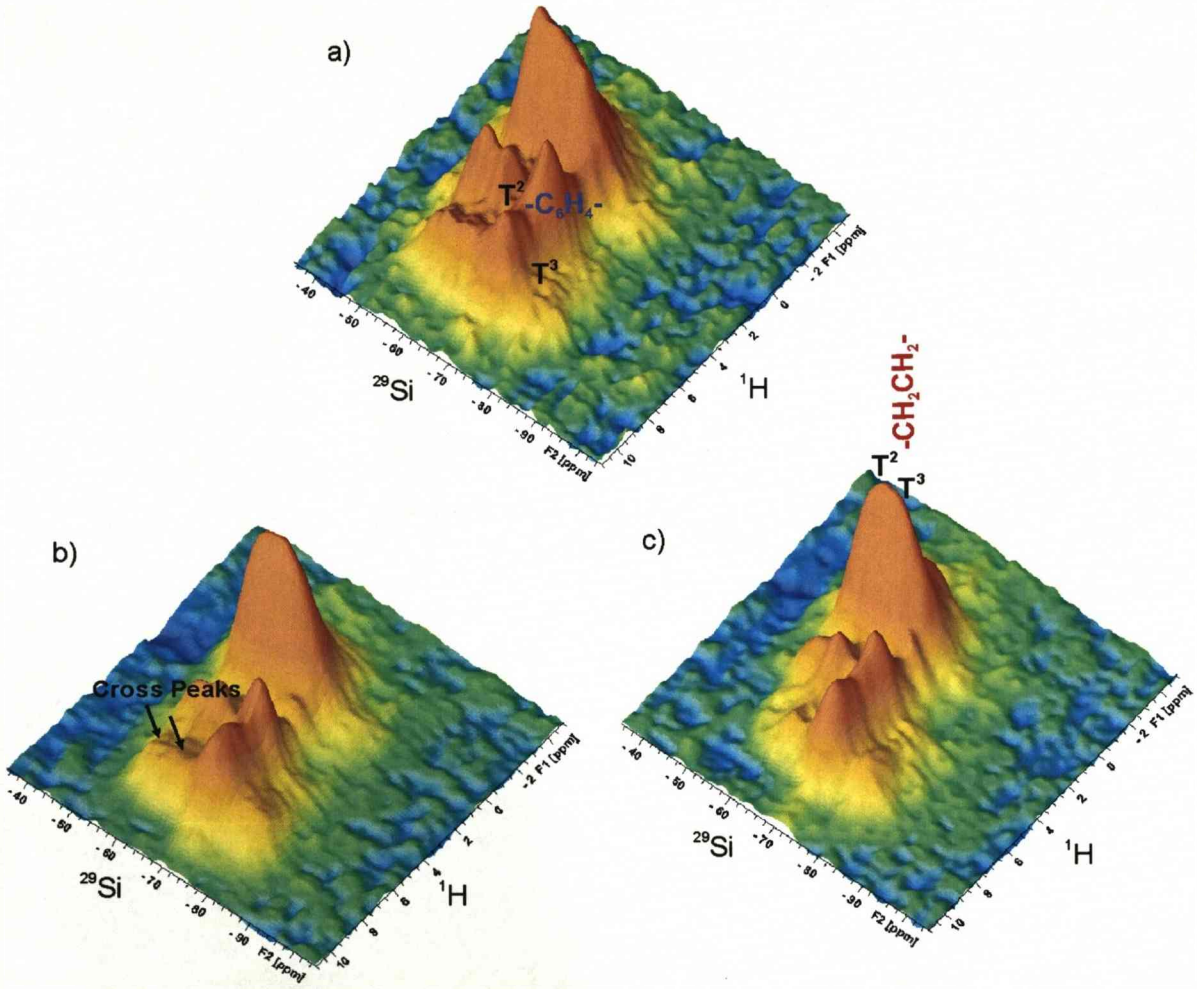

Figure 6.36. ^{1}H-^{29}Si HETCOR NMR spectra of the template extracted PMOs. a) $-CH_2CH_2-/-C_6H_4-$PMO, b) J-PMO-2.6-60 and c) S-PMO-2.6-60 prepared *via* $S^{0}H^{+}X^{-}T^{+}$ synthetic pathway.

The jointly and separately pre-hydrolysed PMO's have reduced cross-peak intensities (Fig. 6.36b/c and Table 6.14) compared to the standard PMO. This corroborates the evidence from CP kinetics suggesting both J and S-PMOs to be more heterogeneous, consisting of domains composed of different organic functionalities. The heterogeneous nature of J-PMO-2.6-60 is in contrast to the $-CH_2CH_2-$/-CH=CH-PMOs (chapter 5) and results from the introduction of the pre-hydrolysis step. A possible explanation is that, during pre-hydrolysis, the increased hydrophobic nature of the aromatic precursor in the aqueous/acidic/ethanol solution disturbs co-condensation with the aliphatic precursor. The aromatic functionality also hydrolyses faster than the aliphatic component in the pre-hydrolysis solutions; however; in the synthesis of the standard PMO this difference could be decreased.

Table 6.14. Intensities of cross-peaks in the ^1H-^{29}Si HETCOR NMR spectra. Values are normalized to those of the $-CH_2CH_2-$ T^3 resonance.

^{29}Si Resonance / ^1H Resonance	$-CH_2CH_2-$		$-C_6H_4-$	
	T^2	T^3	T^2	T^3
$-CH_2CH_2-$/$-C_6H_4-$PMO				
$-CH_2CH_2-$	1.04	1.00	0.55	0.18
$-C_6H_4-$	0.35	0.39	0.60	0.21
(Auto peak $T^2 + T^3$)/ (Cross peak $T^2 + T^3$)	2.76		1.11	
J-PMO-2.6-60				
$-CH_2CH_2-$	0.99	1.00	0.51	0.14
$-C_6H_4-$	0.22	0.27	0.56	0.24
(Auto peak $T^2 + T^3$)/ (Cross peak $T^2 + T^3$)	4.06		1.23	
S-PMO-2.6-60				
$-CH_2CH_2-$	0.99	1.00	0.44	0.10
$-C_6H_4-$	0.11	0.25	0.58	0.25
(Auto peak $T^2 + T^3$)/ (Cross peak $T^2 + T^3$)	5.53		1.54	

6.5 Discussion and conclusion

The two synthetic pathways, S^+I^- and $S^0H^+X^-I^+$ described in this chapter have a substantial effect on both the mesoscopic ordering and molecular scale organisation. The S^+I^- templated PMOs, containing aromatic functionalities, all displayed molecular level organisation irrespective of pre-hydrolysis conditions. In contrast, PMOs prepared *via* $S^0H^+X^-I^+$ templating showed no molecular level organisation with the exception of $-C_6H_4-$ PMO after post synthetic hydrothermal treatment, yet to a much lesser extent. The PXRD, ^1H-^{29}Si CP kinetics and HETCOR data obtained for the bi-functional PMOs prepared *via* the S^+I^- synthetic pathway all suggested that the pore walls consisted of layered aromatic domains disrupted by disordered $-CH_2CH_2-$ groups within the pore walls (Scheme 6.4). The inhomogeneous distribution of organic functionalities under basic conditions when using joint pre-hydrolysis is a result of preferential homo condensation of the aromatic precursor as discussed in section 6.2.1. Despite the possible layering of the organic components within the pore walls, the ^1H-^{29}Si HETCOR experiments confirm the materials are phase pure and there are regions where the two different functionalities are close in space.

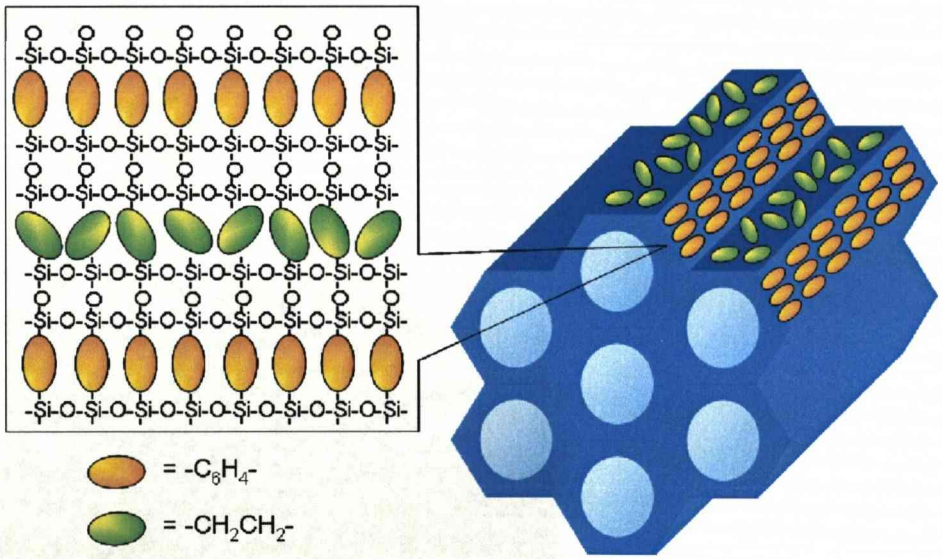

Scheme 6.4. Representation of organic functionalities distribution in the pore walls of the S^+I^- templated bi-functional PMOs mesoporous framework.

The standard bi-functional PMO synthesised *via* the $S^0H^+X^-I^+$ pathway formed a more homogenous network than the S^+I^- analogue as shown by the high intensities of the cross peaks in the ^1H-^{29}Si HETCOR (Fig. 6.33a). This confirms the standard bi-functional PMO synthesised under acidic conditions forms a homogeneous porous composite. The

homogenous distribution of functional groups seen when using $-CH_2CH_2-$ and -CH=CH- or $-C_6H_4-$ components confirms the method of synthesis is reproducible for differing organic functionalities in the absence of pre-hydrolysis.

The application of pre-hydrolysis to $-CH_2CH_2-/-C_6H_4-$ functionalised PMO gave inconsistent results compared to those seen for the $-CH_2CH_2-/-$CH=CH-PMOs discussed in chapter 5. The aromatic functionalised J/S-PMO both resulted in a heterogeneous structure with domains of differing functionality. Whereas one would expect joint pre-hydrolysis of $-CH_2CH_2-/-C_6H_4-$PMOs to give a random distribution of functionalities similar to the standard material as seen for $-CH_2CH_2-/-$CH=CH-PMOs.

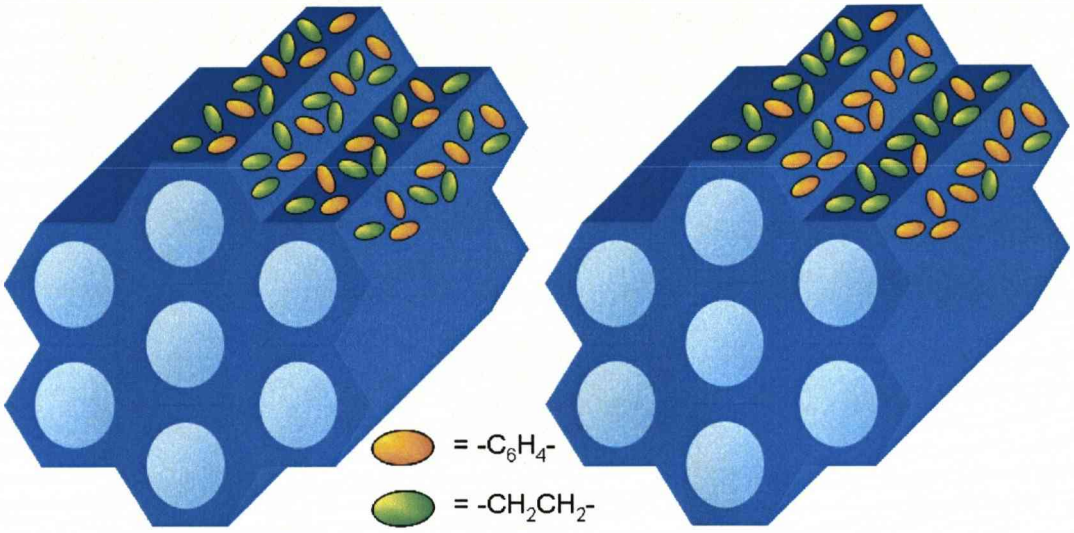

Scheme 6.5. Distribution of the organic functionalities within the bi-functional PMOs synthesised via $S^0H^+X^-I^+$ pathway, homogeneous distribution *i.e.* standard material (left) and heterogeneous domain structure *i.e.* J/S-PMOs.

Incorporation of Aluminium into Bi-functional PMOs

Chapter 7

7.1. Introduction

The previous chapters focused on the synthesis of PMOs where two different organic functionalities were the origin of the bi-functionality. The possibility of introducing an additional organic functionality was considered, however, the characterisation and conformation of bridge ratios by ^{1}H-^{29}Si CP/MAS and HETCOR experiments would not be possible due to poor spectral resolution. In chapter 6 it was shown that the process of joint and separate pre-hydrolysis under basic conditions was complex in -CH_2CH_2-/-C_6H_4-PMOs. Therefore, in order to investigate the effects of pre-hydrolysis in basic conditions further probe heteroatoms were added to the synthesis and incorporated into a -CH_2CH_2-/-CH=CH-PMO *via* isomorphous substitution.

Heteroatoms such as, Aluminium, Titanium and Vanadium have been introduced previously into purely siliceous mesoporous molecular sieves and mono-functional PMOs. Such heteroatoms widened the catalytic properties of PMO composites as discussed in chapter 1.[217,240,241,242-246] The incorporation of Titanium and Vanadium was considered initially. However, the difficulty of NMR detection for Ti and introducing V precursors into the PMO synthesis ruled these metals out. Aluminium was chosen due to its high NMR sensitivity and ease of introducing to PMO synthesis. The incorporation of aluminium into organosilica frameworks yielded bridging hydroxyls (≡Si-OH-Al≡) which was confirmed using pyridine adsorption and subsequent FTIR measurments.[129] These materials are promising as acid catalysts with the opportunity for greater control of hydrophilic/hydrophobic properties. They may also subsequently replace Al-MCM-41 to be employed as an acid catalyst for the alkylation of hydrocarbons.[247,248] The synthesis of tri-functional PMOs also provides the possibility for expanding the use of precursor pre-hydrolysis leading to structural heterogeneities in the framework of bifunctional PMOs. The application of separate pre-hydrolysis whereby aluminium is added to only one organosilica precursor may enable the selective alumination of one type of organic domain. The ability to design such complex solids could have particular use in chromatographic or controlled molecule release applications.

The introduction of aluminium into the pre-hydrolysis solution results in the formation of organo-aluminosilicate sol-gels analogous to aluminosilicates gels, precursors to zeolite frameworks, which have been studied extensively.[241,249-253] The formation of reactive intermediates/SBUs of clear aluminosilicate gels has been monitored successfully using multinuclear NMR by McCormick *et al.*[250] The authors detect the formation of Q^1 and

Q^2 silicate species in TEOS/H_2O/EtOH/HCl prior to the addition of the aluminium precursors. The ^{17}O NMR was applied to monitor the formation of Si-OH, Si-O-Si and Si-O-Al as a function of Al addition to the silicate solution. Harris *et al.* applied ^{27}Al NMR to confirm the presence of Al q^0, q^1, q^2, q^3 and q^4 environments, whereby the superscript represents the number of oxygen bridges to silicon, in aluminosilicate solutions containing HMBTP hydroxide (2,3,4,5,6,7,8,9-octahydro-2,2,5,5,8,8-hexamethyl-1H-benzo[1,2-c:3,4-c':5,6-c"]tripyrrolium). The use of ^{27}Al 2D exchange spectroscopy (EXSY) also shows the presence of q^0, q^1, q^2 exchange, of which, the rate increases with temperature.[252] Obviously, NMR spectroscopy is not the only technique which can monitor the formation of zeolites from aluminosilicate gels. Other methods *i.e.* small and wide angle X-ray scattering (SAXS/WAXS) and dynamic light scattering (DLS) have been used to probe particle size in solutions.[241,254-256] Sankar and Okubo *et al.* applied combined *in situ* SAXS/WAXS to monitor the nucleation and particle growth of nanosized LTA in the presence of tetramethyl ammonium cations (TMA^+). The authors determined the presence of species of homogeneous precursors of 10 nm in size as well as final LTA crystallites (80 - 160 nm) and concluded that the initial precursor size is independent of temperature, however, the size of final LTA crystallites increases as a function of temperature.[241] A recent study into the compositions of clear solutions for silicalite-1 zeolite synthesis combined ^{29}Si NMR, SAXS and DLS measurements to confirm the presence of oligomeric double six-ring (D6R), double five-ring (D5R) and cubic octamer (D4R) silicate polyanions.[254]

In this chapter the synthesis of bi-functional -CH_2CH_2-/-CH=CH- and tri-functional Al-/-CH_2CH_2/-CH=CH-PMOs under basic conditions *via* the S^+I^- synthetic pathway is described. We have monitored the effects of pre-hydrolysis on the resulting PMO. We also studied the influence of aluminium on the properties of the pre-hydrolysed PMOs in comparison to those without aluminium. The use of acidic conditions *via* the $S^0H^+X^-I^+$ pathway (as in chapter 5) was dismissed due to the difficulty in incorporating aluminium into the structure.

7.2 Results and Discussion

The materials in this section are split into aluminium free and aluminium containing -CH_2CH_2-/-CH=CH-PMOs. The two reference –CH_2CH_2-/-CH=CH-PMO and Al-/-CH_2CH_2-/-CH=CH-PMO were synthesised without any pre-hydrolysis. The pre-hydrolysis of the Al-free PMOs was analogous to that described in the previous chapter, whereby for J-PMOs both organosilicas precursors are pre-hydrolysed together. For the S-PMOs the precursors are pre-hydrolysed separately and added to the template solution simultaneously after a set period of time. The separately pre-hydrolysed Al-PMOs were obtained using a slightly modified procedure: the aluminium source was combined with only one organosilica precursor during pre-hydrolysis prior to their addition to the template solution. The Si/NaOH ratio in the pre-hydrolysis mixtures was 14 as a higher base content resulted in disordered PMOs (Fig. 7.4).

The PMOs have been labelled according to their pre-hydrolysis conditions and Si/Al ratio. Therefore, the Al-free PMOs are labelled X-PMO-X-Z where X = J or S corresponding to joint or separate pre-hydrolysis, X = 0 or 5 indicating the Al content and Z = 30 or 60 corresponding to the pre-hydrolysis time. The aluminium containing J-PMOs are labelled using the same notation. For the separately pre-hydrolysed Al-PMOs (-CH_2CH_2- + Al) or (-CH=CH- +Al) are added to indicate which silicon precursor the aluminium source was combined with during pre-hydrolysis. For example, S-PMO-5-30 (-CH_2CH_2- + Al) indicates separate pre-hydrolysis was used for 30 minutes with a Si/Al = 5 and the aluminium source was combined with the –CH_2CH_2- precursor during pre-hydrolysis.

7.2.1 Powder XRD

The powder XRD patterns of the template extracted reference PMOs (Fig. 7.1) confirm the presence of a 2D hexagonal mesostructure with d_{100} spacings of 49.0 Å for -CH_2CH_2-/-CH=CH-PMO and 42.7 Å for –Al/-CH_2CH_2-/-CH=CH-PMO. The reduction of the unit cell upon incorporation of aluminium is coupled with improved mesostructural ordering indicated by more intense (110) and (200) reflections compared to the Al free PMO. A possible rationale for this observation lies in the generation of negatively charged framework by isomorphous substitution of Si^{4+} for Al^{3+}, balanced by either an acidic proton or counter cation (Na^+, K^+ *etc.*). As these PMOs are synthesised *via* the S^+I^- pathway (S^+ represents the cationic surfactant head group and I^- the negatively charged silicate species),

the self-assembly relies on the electrostatic interaction between S^+ and I^-. The generation of negative framework sites for aluminium-containing PMOs would, therefore, induce a greater electrostatic interaction. A steady increase in mesoscopic ordering as Al content was increased in a series Si/Al = 20, 10 and 5 corroborates this hypothesis and is in agreement with reported Al-/-CH_2CH_2-PMOs.[129]

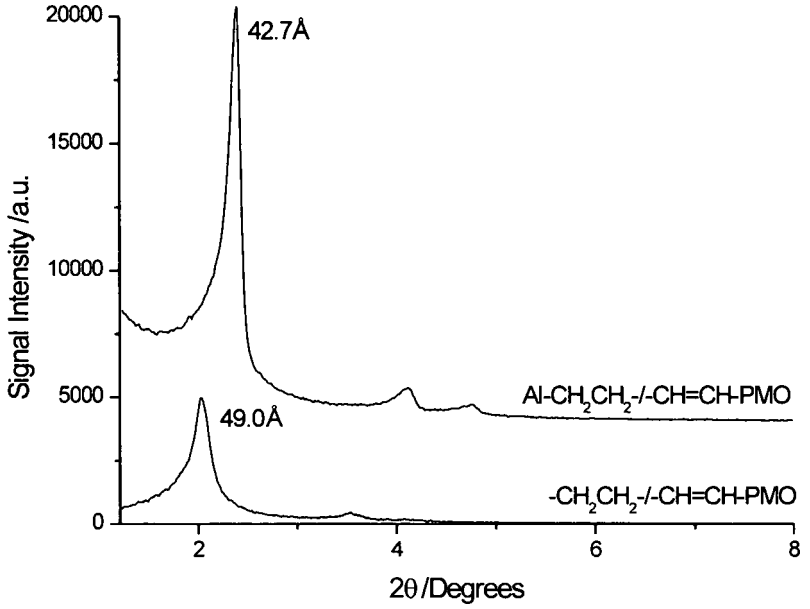

Figure 7.1. PXRD patterns of the template extracted reference PMOs.

The application of the pre-hydrolysis protocols to the aluminium free systems resulted in an improvement of mesoscopic ordering compared to -CH_2CH_2-/-CH=CH-PMO (Fig. 7.2). For -CH_2CH_2-/-CH=CH- system a Si/NaOH = 14.1 gave the highest degree of mesoscopic ordering. The d_{100} spacings decreased in the J-PMOs to *ca.* 42 Å compared to the standard and S-PMOs (*ca.* 49 Å). Increasing pre-hydrolysis time favours an increase in mesoscopic ordering for both J-PMO-0-60 and S-PMO-0-60. This is unexpected as in all previous systems studied mesoscopic ordering was reduced with pre-hydrolysis time. Interestingly these solids, to the best of our knowledge, display the highest degree of mesoscopic ordering for bifunctional PMOs prepared *via* S^+I^- templating to date. Therefore, pre-hydrolysis may also be seen as a method of improving mesoscopic ordering.

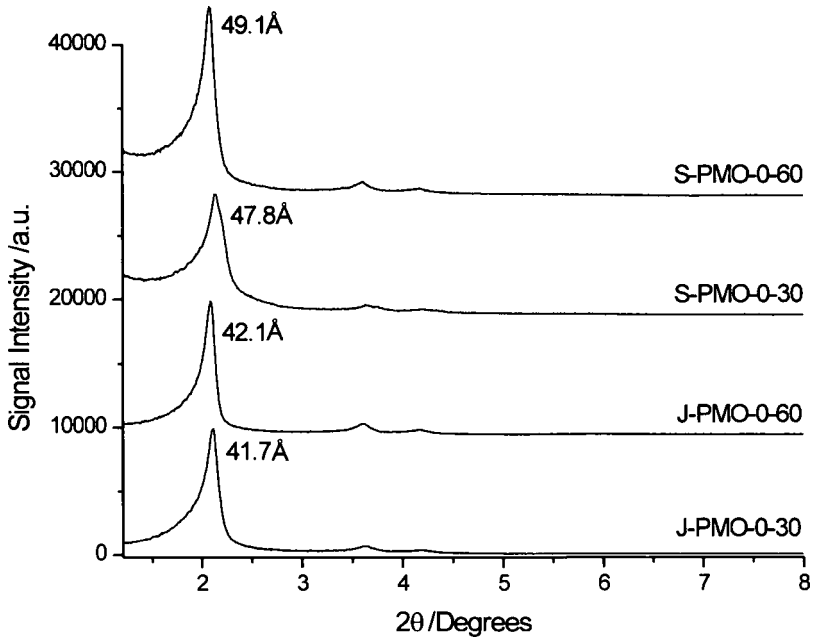

Figure 7.2. Powder XRD patterns of the template-extracted pre-hydrolysed bi-functional PMOs.

The powder XRD patterns of the template-extracted tri-functional PMOs (Fig. 7.3) all display d_{100} spacings of *ca.* 44 Å, similar to the standard Al-CH_2CH_2-/-CH=CH-PMO. The degree of mesoscopic ordering is reduced in all the pre-hydrolysed samples (with the exception of J-PMO-5-30 and S-PMO-5-30 (-CH=CH- + Al) which show patterns similar to the standard Al/-CH_2CH_2-/-CH=CH-PMO). The hydrolysis of Al($^iOC_3H_7$)$_3$ and alkyl silicon alkoxides in H_2O/OH^- media would lead to negatively charged clusters. Such clusters would also be bulky and possibly cause electrostatic repulsion between one another and thus when added to the template solution, reduce the efficiency of co-assembly with the template micelles. This in turn leads to a reduction in mesoscopic ordering, confirmed by PXRD. However, the high degree of mesoscopic ordering seen for J-PMO-5-30 and S-PMO-5-30 (-CH=CH- + Al) suggests that pre-hydrolysis and the formation of SBUs before addition to the template is not the only factor to consider. Other parameters such as, the efficiency of aluminium incorporation and –CH_2CH_2-/-CH=CH- ratio do not show any coherent correlation between mesoscopic ordering and Al content or increasing –CH_2CH_2-/-CH=CH- ratios.

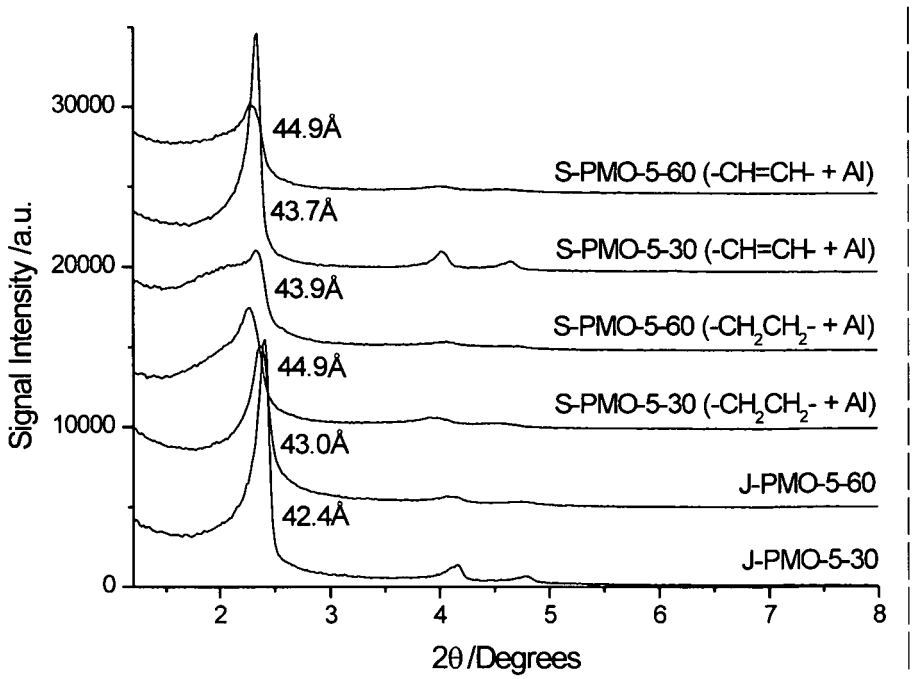

Figure 7.3. Powder XRD patterns of the template extracted pre-hydrolysed tri-functional PMOs.

Under alkaline conditions, the hydrolysis of metal alkoxides produces strong nucleophiles *via* the deprotonation of hydroxo groups. Rapid co-condensation occurs forming T-O-T-O-T (T = Si/Al) SBUs. The formation of ordered composites relies on the ability for these SBUs to assemble around template aggregates; smaller, more reactive SBUs are more likely to undergo a more efficient assembly with template compared to larger units. In pre-hydrolysis systems, a low base content (Si/NaOH = 14.1) favours the formation of highly ordered PMOs compared to solids obtained using a high base content (Si/NaOH = 2.6) which gave disordered products. However, this appears to be unique for the Al-/-CH_2CH_2-/-CH=CH-PMOs as both –CH_2CH_2-/-CH=CH-(not shown) and -CH_2CH_2-/-C_6H_4-PMOs (Chapter 6) still formed ordered arrays under these conditions. Therefore, this effect is a direct consequence of aluminium incorporation.

7.3 N_2 Adsorption-Desorption Isotherms

N_2 adsorption-desorption isotherms were used to monitor the effects of incorporation of aluminium and pre-hydrolysis on the textural properties of the resulting PMOs. Both PMOs display type IV isotherms confirming their mesoporous structure. An additional broad capillary condensation step is observed in the region of $p/p_0 = 0.4$ to 0.6. Such change in hysteresis from a Type H1 to H3 along with a second maximum on the PSD plot at *ca.* 128 Å suggest the presence of inter-particle porosity.

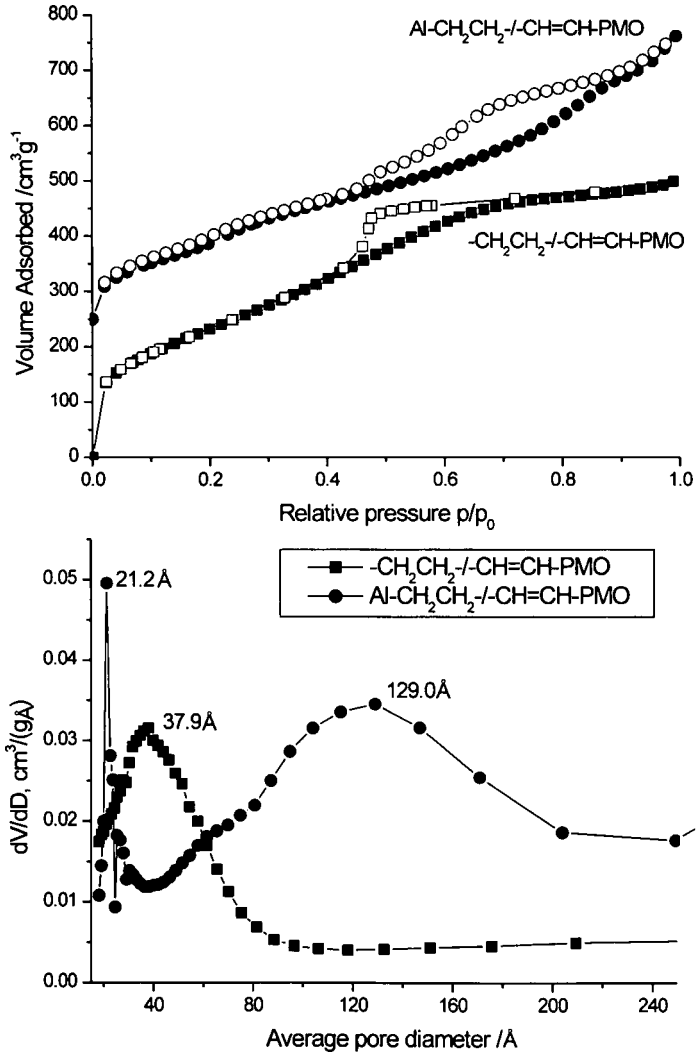

Figure 7.4. N_2 adsorption-desorption isotherms and PSD plots of the two reference PMOs.

The introduction of pre-hydrolysis for the $-CH_2CH_2-/-CH=CH-$ PMOs resulted in an improvement in ordering consistent with results of powder XRD and indicated by a much sharper capillary condensation step in the region of $p/p_0 = 0.4$ (Fig. 7.5). The PSD curves

showed a narrow pore size distribution in the region of 32 Å (with the exception of J-PMO-0-60 were this was increased to 38 Å). In general, the values of S_{BET} are similar to the standard PMO, however the pre-hydrolysed solids tend to have larger pore volumes.

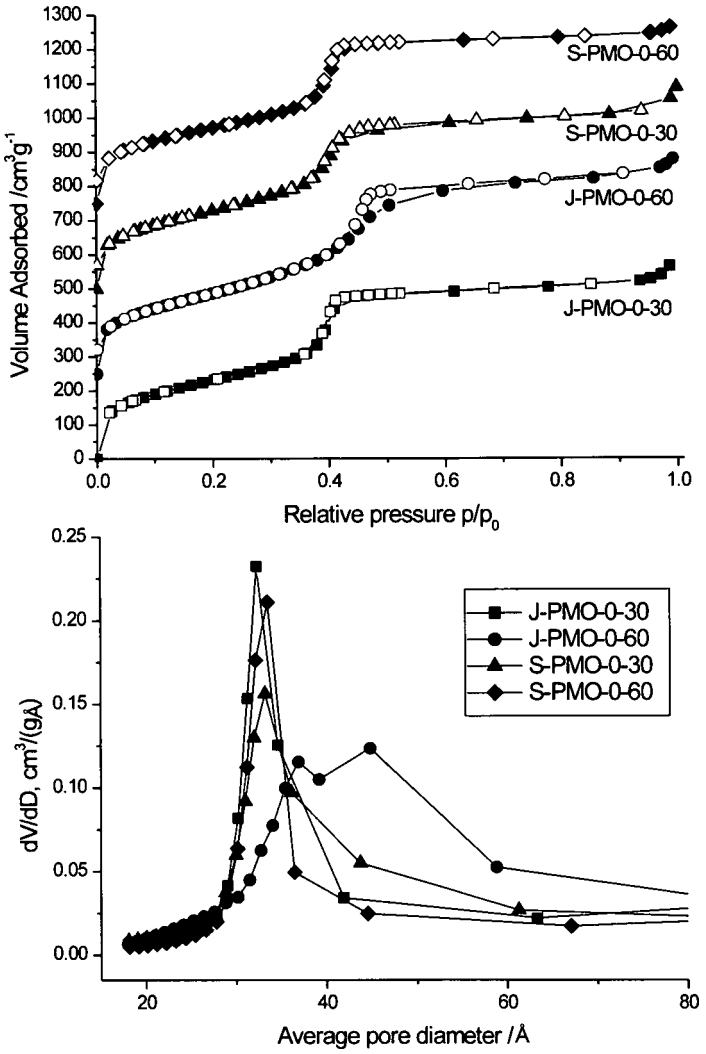

Figure 7.5. N_2 adsorption-desorption isotherms and PSD plots of the bi-functional pre-hydrolysed PMOs.

The adsorption-desorption isotherms for aluminium containing J/S-PMOs N_2 (Figs. 7.6 and 7.7) again show type IV isotherms but the capillary condensation step is less well defined indicating a less uniform porous structure. The isotherm of S-PMO-5-60 (-CH=CH-Al) resembles a type II isotherm confirmed by the absence of a capillary condensation step in the region of $p/p_0 = 0.2–0.6$. The decrease in surface area and mesoscopic ordering with increasing pre-hydrolysis time suggest that formation of Al-PMOs is hampered once pre-hydrolysis time exceeds 60 minutes. The PSD plots also confirm this observation.

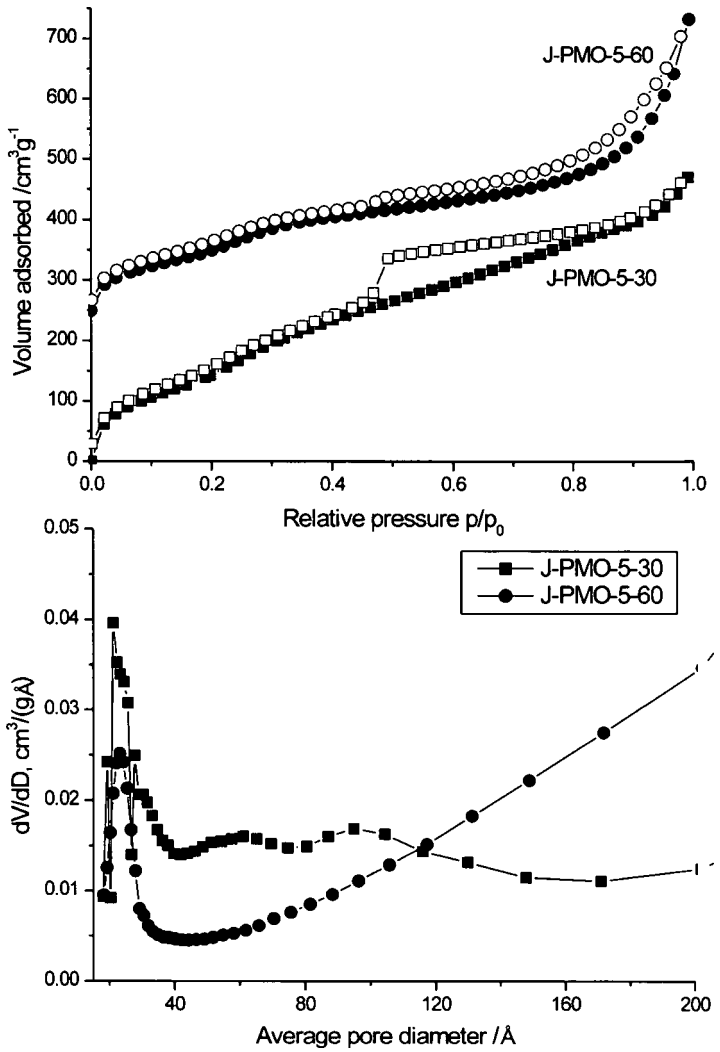

Figure 7.6. N_2 adsorption-desorption isotherms (top) and PSD plots (bottom) of the aluminium containing jointly pre-hydrolysed PMOs.

The incorporation of aluminium into $-CH_2CH_2-$/-CH=CH-PMOs causes a reduction in S_{BET}, pore diameter and pore volume and an increase in wall thickness (Table 7.1). These reductions are at their greatest after 60 minutes of pre-hydrolysis under separate conditions (for example, for S-PMO-5-60 (-CH=CH- + Al) S_{BET} = 181 m^2g^{-1}). The increased amounts of residual template in the extracted Al-PMOs (confirmed by ^1H-^{13}C CP/MAS NMR, Fig. 7.8) than the in bi-functional products would cause such reductions in porosity. The reduced pore diameters may also be accounted for by the incorporation of more template into the as-synthesised Al-PMOs (confirmed by ^1H-^{13}C CP/MAS kinetics, fig. 7.9). This is related to the presence of a negative charge on the framework (as discussed above).

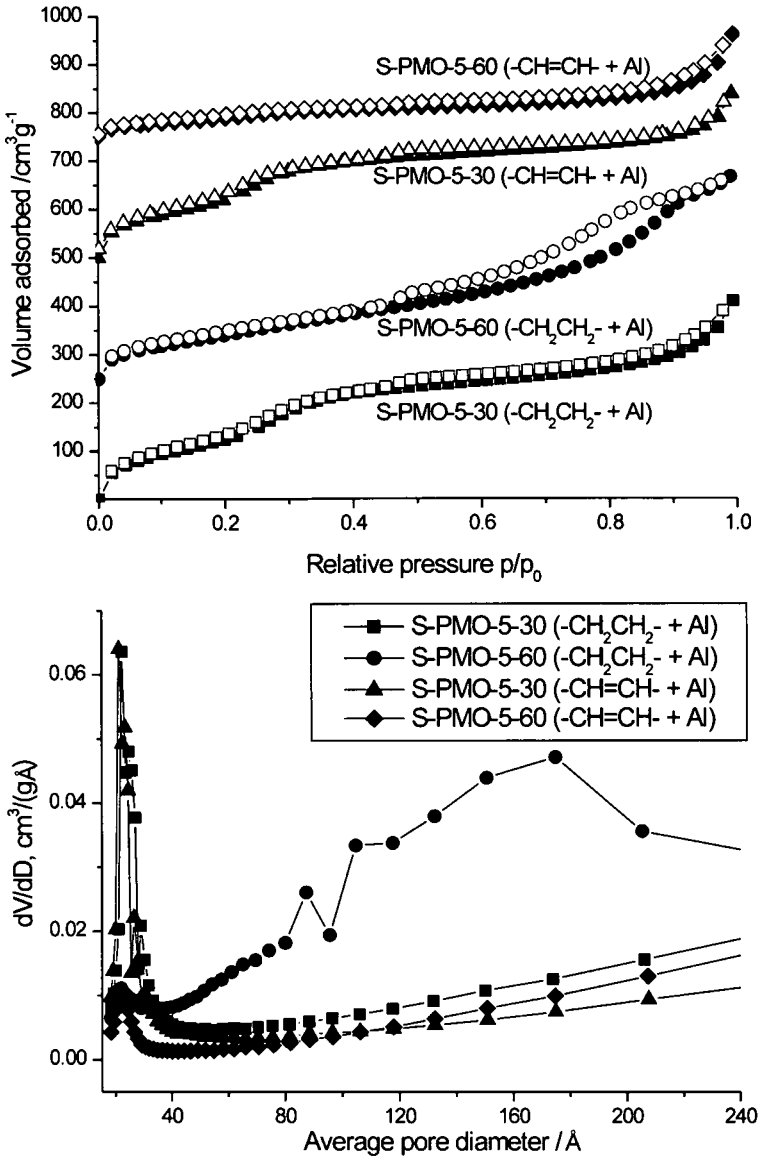

Figure 7.7. N_2 adsorption-desorption isotherms isotherms (top) and PSD plots (bottom) of the aluminium containing separately pre-hydrolysed PMOs.

Table 7.1. Textural properties of template extracted bi- and tri-functional PMOs

Sample	S_{BET} /$m^2\ g^{-1}$	V_{ads} /$cm^3\ g^{-1}$	D_{AV}^{ads} /Å	d_{100} /Å	$a^{\dagger}$ /Å	W /Å
-CH_2CH_2-/-CH=CH-PMO	876	0.76	37.9	49.0	56.6	18.7
Al-CH_2CH_2-/-CH=CH-PMO	627	0.75	21.2	42.7	49.3	28.1
J-PMO-0-30	863	0.83	32.3	41.7	48.2	15.9
J-PMO-0-60	905	0.94	40.0	42.1	48.6	8.6
S-PMO-0-30	866	0.96	33.0	47.8	55.2	22.2
S-PMO-0-60	815	0.78	33.5	49.1	56.7	23.2
J-PMO-5-30	673	0.68	21.1	42.4	49.0	27.9
J-PMO-5-60	465	0.61	23.1	43.0	49.7	26.6
S-PMO-5-30 (-CH_2CH_2- + Al)	631	0.55	22.3	44.9	51.8	29.5
S-PMO-5-60 (-CH_2CH_2- + Al)	380	0.62	~ 21	43.9	50.7	29.7
S-PMO-5-30 (-CH=CH- + Al)	646	0.45	21.2	43.7	50.5	29.3
S-PMO-5-60 (-CH=CH- + Al)	181	0.24	~ 22	44.9	51.8	29.8

Pore volumes determined at $P/P_0 = 0.9$.
† Unit cell parameter $\bar{a}$ determined from d_{100} values using $\bar{a} = 2d_{100}/\sqrt{3}$.
W is wall thickness determined from $\bar{a} - D_{av}$.

7.4 Local structure of the mesoporous composites

7.4.1 Composition of standard PMOs

A typical ^{1}H-^{13}C CP/MAS NMR spectrum for as-synthesised PMO (Fig. 7.8, top) shows several resonances between 23.5 to 67.3 ppm attributed to the template (a full assignment is given in the figure). The aliphatic chain end methyl group is rarely observed in CP spectra recorded using short contact times due to its high mobility. However, this site can be seen *via* ^{1}H-^{13}C MAS-J-INEPT and $^{13}C\{^{1}H\}$ MAS NMR at *ca.* 15 ppm (fig. 7.8 top). The broad peaks at *ca.* 5 and 146 ppm correspond to $-CH_2$-CH_2- and -CH=CH- functionalities respectively and confirm their incorporation into both mesostructures. The spectrum of the Al-CH_2CH_2-/-CH=CH-PMO shows evidence of template species even after three extractions, although the corresponding relative intensities are reduced. Despite this the material is still mesoporous and further extraction procedures would lead to complete dealumination and collapse of the framework.

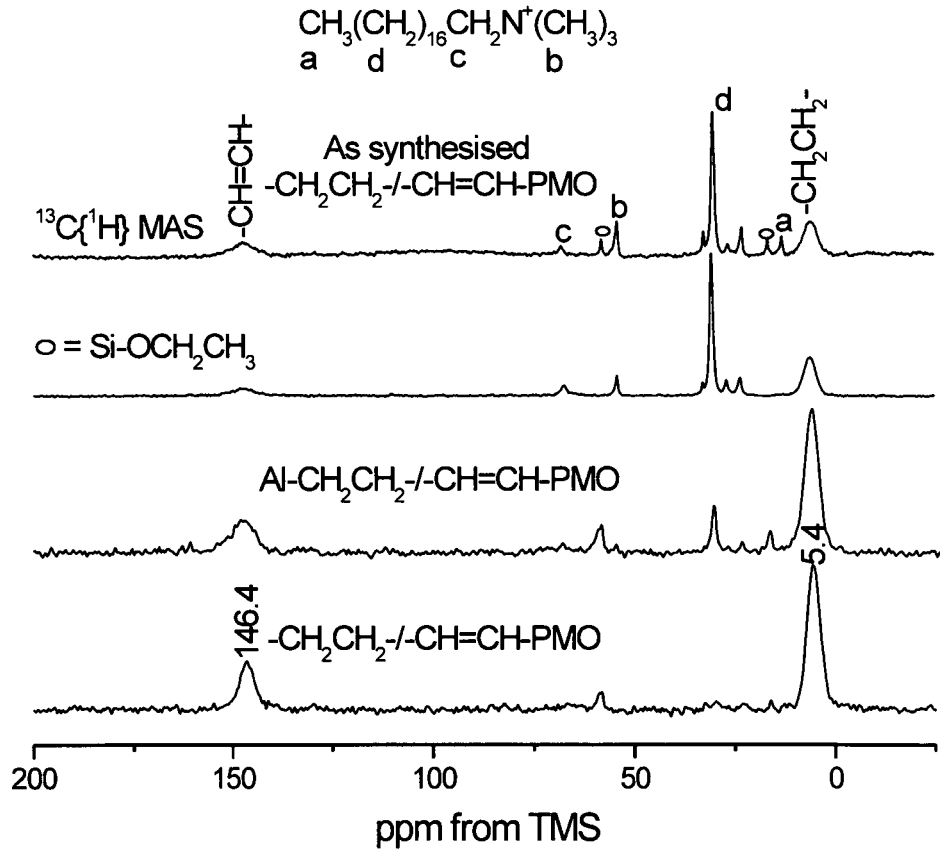

Figure 7.8. ^{1}H-^{13}C CP/MAS NMR spectra of the as synthesised (Top) and template extracted standard $-CH_2CH_2$-/-CH=CH-PMO (bottom) with the template extracted Al-PMO (middle).

The application of ^{1}H-^{13}C CP/MAS (Fig. 7.9) kinetics to the as-synthesised standard PMOs confirmed a higher template content for the aluminium containing analogue. Integration of the spectra recorded at 2 ms revealed the template content to be 3 times higher for the Al-/-CH_2CH_2-/-CH=CH-PMO compared to the -CH_2CH_2-/-CH=CH-PMO. Integration of the ^{13}C CP/MAS spectra of the Al-/-CH_2CH_2-/-CH=CH-PMO after three acid extractions showed a template content of 8.6 %. No evidence of template was seen in the Al-free PMO standard.

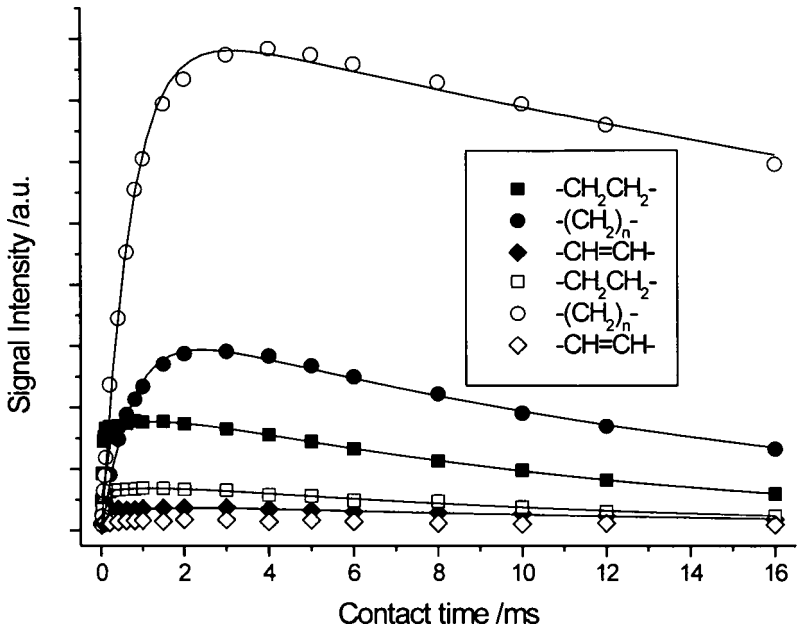

Figure 7.9. ^{1}H-^{13}C CP/MAS kinetics curves of the as-synthesised -CH_2CH_2-/-CH=CH-PMO (filled symbols) and Al-/-CH_2CH_2-/-CH=CH-PMO (hollow symbols). Only the organic bridges and template -$(CH_2)_n$- resonance at *ca.* 31 ppm are shown for clarity.

^{1}H-^{29}Si CP/MAS NMR spectrum of the –CH_2CH_2-/-CH=CH-PMO (Fig. 7.10, bottom) shows three intense resonances at *ca.* –56, -64 and –81 ppm corresponding to silicon –CH_2-CH_2- $T^{2}/^{3}$ sites (CH_2-CH_2-Si$(OSi)_2(OH)$ and CH_2-CH_2-Si$(OSi)_3$) respectively, whilst the peak at -81 ppm corresponds to a fully condensed silicon –CH=CH- T^3 site (-CH=CH-Si$(OSi)_3$). A partially condensed silicon –CH=CH- T^2 environment is also present as a shoulder at *ca.* -71 ppm off the silicon –CH_2-CH_2- T^3 site resonance. The low-intensity peak at *ca.* –49 ppm corresponds to a poorly condensed silicon –CH_2-CH_2- T^1 site (CH_2-CH_2-Si$(OSi)(OH)_2$). The absence of any resonances in the region of -90 to –120 ppm

corresponding to silicon Q^n sites indicates no Si-C bond cleavage has occurred during synthesis or template extraction.

The introduction of Al into the framework has resulted in a shift of both $-CH_2CH_2-$ and -CH=CH- silicon T^3 environments to higher ppm (Fig. 7.10, top). This confirms the shielding effect of the aluminium on the chemical shift of ^{29}Si nuclei similar to that observed in Zeolites.[158,159] The increase in peak area of both silicon T^2 environments is a result of spectral overlap of T^2 silicon Al free and T^3 R-Si(OSi)$_2$(OAl) Al containing sites. However, to confirm this, the ^{27}Al-^{29}Si HETCOR experiments are required to probe the location of the aluminium with respect to silicon T sites.

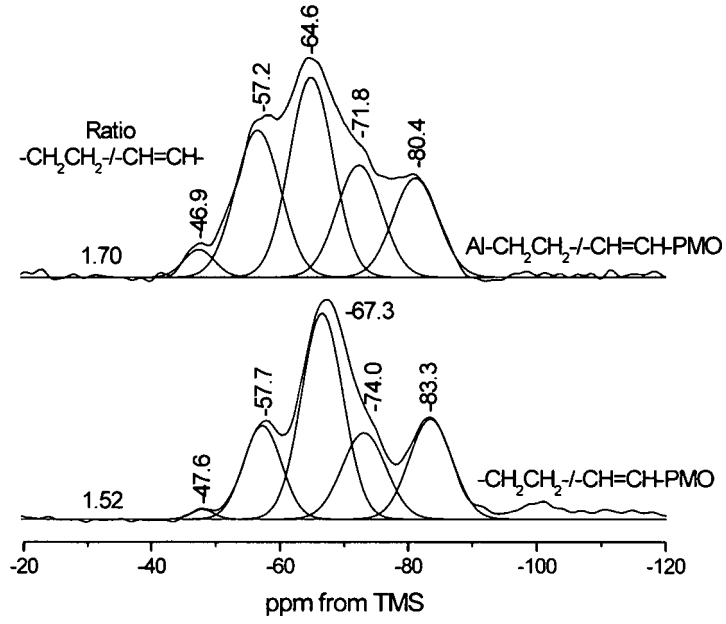

Figure 7.10. ^1H-^{29}Si CP/MAS NMR spectra of the template extracted reference PMOs.

7.4.2 Composition of the pre-hydrolysed Al free PMOs

^{1}H-^{13}C CP/MAS NMR spectra of the template extracted J/S-PMOs (Fig. 7.11) confirm the presence and stability of the organic bridges during synthesis and template extraction. The absence of intense peaks in the region of 15 - 60 ppm confirm the removal of the template.

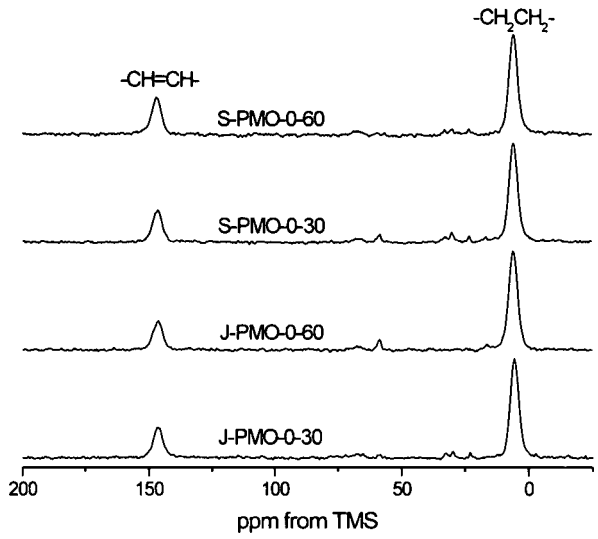

Figure 7.11. ^{1}H-^{13}C CP/MAS NMR spectra of the template extracted pre-hydrolysed Al free PMOs.

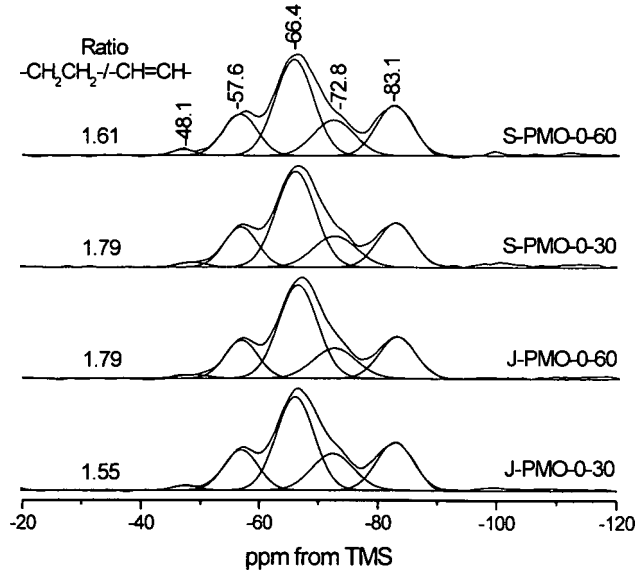

Figure 7.12. ^{1}H-^{29}Si CP/MAS NMR spectra of the template extracted pre-hydrolysed PMOs.

^{1}H-^{29}Si CP/MAS NMR spectra of the J/S pre-hydrolysed PMOs (Fig. 7.12) showed spectra similar to those for the standard Al-free PMO (Fig. 7.10). The incorporation of the -CH=CH- component is slightly reduced as a consequence of pre-hydrolysis.

Similar levels of pore wall condensation have been observed for both organosilica units in the pre-hydrolysed and $-CH_2CH_2-$/-CH=CH-PMO (Table 7.2). A lower than expected (from the composition of the initial synthesis mixtures) degree of incorporation of -CH=CH- functionality has been observed. The application of pre-hydrolysis increases the $-CH_2CH_2-$/-CH=CH- ratio further. The reduced levels of incorporation of the silicon precursor that hydrolyses at a faster rate in the $-CH_2CH_2-$/-CH=CH-PMOs is in contrast to the $-CH_2CH_2-$/-C_6H_4-PMOs (chapter 6).

Table 7.2. ^1H-^{29}Si CP/MAS NMR deconvoluted peak areas of silicon T^n sites and degree of pore wall condensation.

Sample	Peak Area					$-CH_2CH_2-$	-CH=CH-
	$-CH_2CH_2-$			-CH=CH-			
	T^1	T^2	T^3	T^2	T^3	$(T^1 + T^2)/ T^3$	T^2/ T^3
$-CH_2CH_2$/-CH=CH-PMO	0.19	3.12	7.58	3.37	3.80	0.44	0.89
J-PMO-0-30	0.23	2.85	7.33	3.12	3.61	0.42	0.86
J-PMO-0-60	0.22	2.61	7.62	2.71	3.14	0.37	0.86
S-PMO-0-30	0.26	2.79	7.85	2.80	3.29	0.39	0.85
S-PMO-0-60	0.29	2.97	7.68	3.02	3.77	0.42	0.80

7.4.3 Composition of the pre-hydrolysed Al-PMOs

^1H-^{13}C CP/MAS NMR spectra of the jointly pre-hydrolysed Al-PMOs show the presence of both $-CH_2CH_2-$ and -CH=CH- bridges at *ca.* 5 and 146 ppm respectively. The repeated extraction removed a large amount of the organic template although residual amounts remain as seen by the resonance at *ca.* 30 ppm as seen with the standard Al-PMO. This is related to the increased content of template (as shown by ^1H-^{13}C CP/MAS kinetics (fig. 7.9)) due to a negatively charged framework upon Al incorporation, thus the template is more difficult to extract than for the Si-PMOs.

The use of alternative extraction protocols, *i.e.* 50/50 v/v Acetic acid/ ethanol mixtures did remove the entire organic template in Al-CH_2CH_2-PMO without Al leaching. However, when this procedure was applied for the Al/-CH_2CH_2-/-CH=CH-PMOs the template remained in the pores, suggesting the -CH=CH- bridge induces an increase in template framework interactions from an Al-CH_2CH_2-PMO. ^1H-^{13}C CP/MAS spectra of the

separately pre-hydrolysed Al-PMOs after three extractions (Fig. 7.13) show a reduction in template content compared to the J-PMOs.

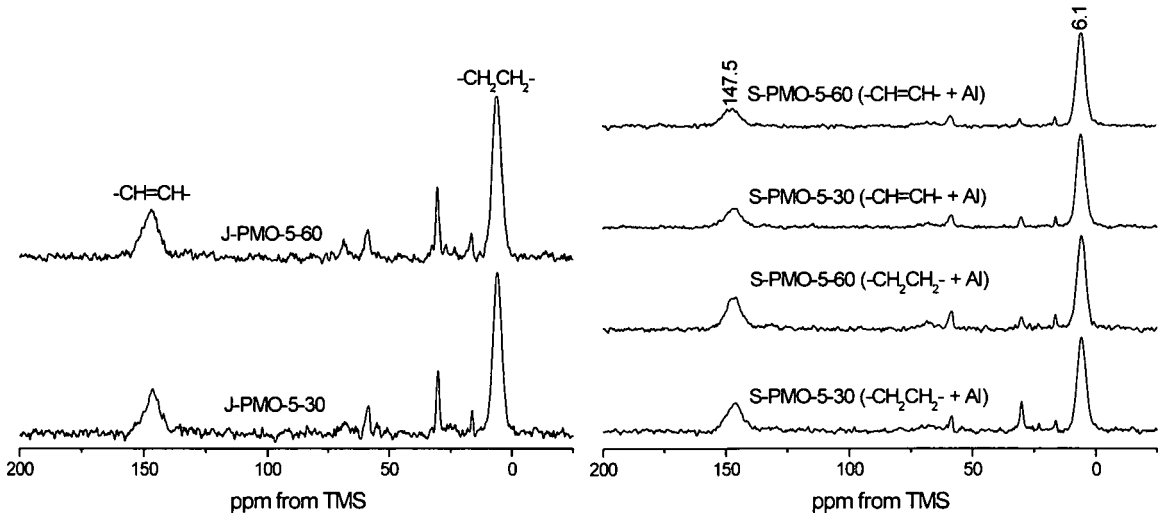

Figure 7.13. ^{1}H-^{13}C CP/MAS NMR spectra of the template extracted J/S pre-hydrolysed aluminium containing PMOs.

^{1}H-^{29}Si CP/MAS NMR spectra of the jointly pre-hydrolysed Al-PMOs display an increased population of -CH=CH-T sites at -71.8 ppm relative to the T^3 environments (Fig 7.10). As in the standard Al-PMO this could be explained by incorporation of aluminium in the pore walls as $\equiv Si(OSi)_2(OAl)$ or $\equiv Si(OSi)(OAl)_2$ T^3 sites. The calculation of the degree of condensation of pore walls for the aluminium containing PMOs has been omitted due to the variation in chemical shifts of the $T^{2/3}$ sites.

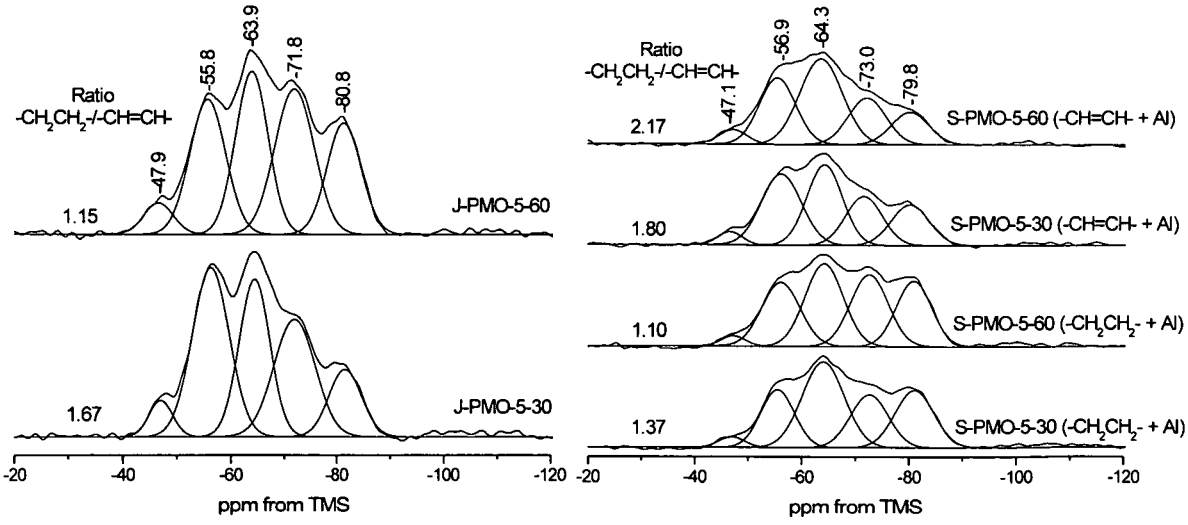

Figure 7.14. ^{1}H-^{29}Si CP/MAS NMR spectra of the template extracted jointly (left) and separately (right) pre-hydrolysed Al-PMOs.

^{1}H-^{27}Al CP/MAS NMR spectra of all the Al-PMOs (Fig. 7.15) confirm the presence of aluminium after three template extractions. The resonance at *ca.* 54 ppm confirms the aluminium is tetrahedrally bound into the mesoporous framework. The tetrahedral bound Al sites are also indicative of acidic properties of the PMOs. Octahedrally bound extra-framework $[Al(H_2O)_6]^{3+}$ sites at *ca.* 0 ppm result from leaching of small amounts of aluminium from the framework during the extraction procedure. Such leaching is not problematic as the majority of aluminium is still present within the porous framework as seen in the ^{27}Al MAS NMR (fig. 7.16).

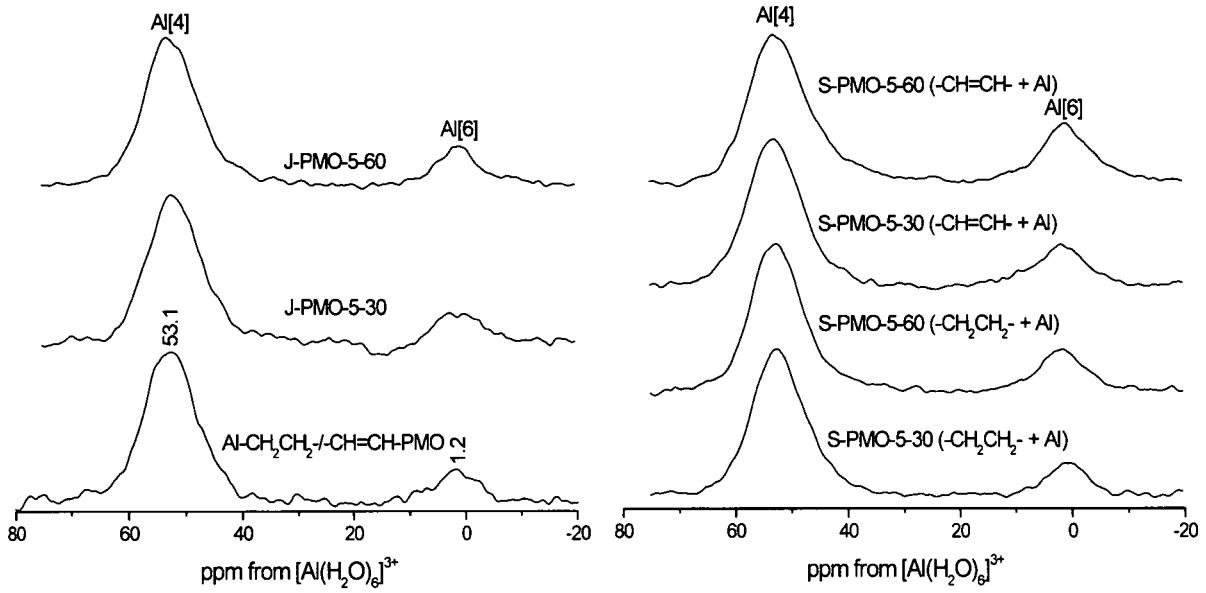

Figure 7.15. ^{1}H-^{27}Al CP/MAS NMR spectra of the template extracted tri-functional PMOs.

^{27}Al MAS NMR (Fig. 7.15) provided quantitative information on the aluminium content in the PMOs. The ability to obtain quantitative information on relative Al content between samples was ensured by conducting the ^{27}Al MAS measurements using exactly the same sample volume and experimental conditions (number of scans, offset, recycle delay *etc.*). The ^{27}Al MAS NMR spectra show the same tetrahedral peak observed in the CP spectra (Fig. 7.14) yet the intensity of the resonance at *ca.* 0 ppm in ^{27}Al MAS NMR is reduced. The aluminium content of the PMOs is increased with pre-hydrolysis time for both J- and S-PMOs (determined from a Gaussian deconvolution of the Al[4] resonance).

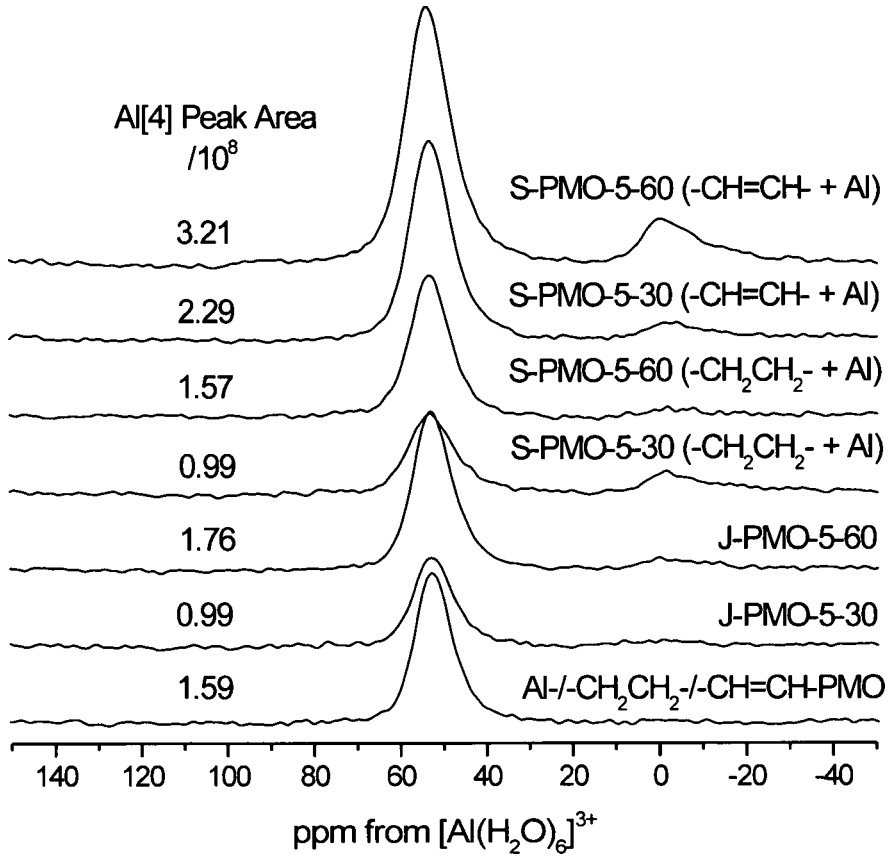

Figure 7.16. ^{27}Al MAS NMR spectra of the template extracted Al-/-CH_2CH_2-/-CH=CH-PMOs. Measurements were conducted using exactly the same sample volume and experimental conditions (number of scans, offset, recycle delay *etc.*).

The ^{13}C, ^{27}Al and ^{29}Si NMR spectra all show changes in the –CH_2CH_2-/-CH=CH- ratios as well as levels of Aluminium incorporation as a function of pre-hydrolysis conditions (Table 7.3). The –CH_2CH_2-/-CH=CH- ratio determined from ^{1}H-^{13}C CP/MAS is higher than that from ^{1}H-^{29}Si CP/MAS NMR spectra. This is expected due to the decrease in directly attached protons in the –CH=CH- functionality. In general the changes in -CH_2CH_2-/-CH=CH- ratio between the different pre-hydrolysis protocols determined from ^{13}C and ^{29}Si data are also different. However, some significant changes are observed as summarised below:

a) J-PMO-0-30/60 show a decrease in –CH=CH- content with increasing pre-hydrolysis time while the opposite is observed for S-PMO-0-30/60.

b) J-PMO-5-30/60 and S-PMO-5-30/60 (-CH_2CH_2- + Al) have a higher content of both –CH=CH- and Al[4] with increasing pre-hydrolysis time,

with the 60 minute analogues having the highest –CH=CH- content of all Al-PMOs.

c) S-PMO-5-30/60 (-CH=CH- + Al) have increased Al[4] and decreased –CH=CH- content with increasing pre-hydrolysis time.

d) The S-PMO-5-30/60 (-CH=CH- + Al) show the highest Al[4] and lowest -CH=CH- content of all Al-PMOs.

Clearly, one can see that when the aluminium precursor was pre-hydrolysed with only the $-CH_2CH_2-$ functionality these SBUs promoted co-assembly of the –CH=CH- SBUs with the template micelles. However, (–CH=CH- + Al) SBUs promoted a higher degree of Al incorporation at the expense of the –CH=CH- functionalities. For such changes to be observed the aluminium -organosilica SBUs must re-disperse to some extent in the reaction mixtures after addition to the templates. The re-dispersion of aluminium and its subsequent homogenous distribution about the framework was confirmed by ^{1}H-^{27}Al HETCOR experiments.

Several hypotheses on zeolite formation have been drawn based on computer simulations and experimental results yet, systematic studies of the mechanisms explaining the formation of multifunctional PMOs are limited. The hypothesis proposed by Lowe *et al.* uses a thermodynamics-based equilibrium model for zeolite synthesis.[257,258] In this model an amorphous solid is in equilibrium with solution species. The initial equilibrium is then maintained while the crystals grow from the supersaturated solution. The formation of the crystalline zeolites is driven by the ratio of precursor and product solubility as this is directly related to solution supersaturation and thus the driving force for crystallisation.[259] However, this model is too simplistic when explaining formation of PMOs as factors such as, hydrophobicity of the organic bridges and the lack of a crystalline product are not relevant for the zeolite model. Despite this some correlations can be made. For instance, small oligomers and SBUs formed during pre-hydrolysis re-disperse in the template solutions (confirmed by ^{1}H-^{27}Al HETCOR, section 7.7). That is an equilibrium between the hydrolysis/ condensation of the organosilicate SBUs and the final PMO product must be established.

The afore mentioned hypothesis does not explain why there is an increase Al[4] content in S-PMO-5-30/60 (-CH=CH- + Al) compared to the other Al-PMOs. This may be a result of the $Al(^{i}OC_3H_7)_3$ having a higher affinity towards the -CH=CH- than the $-CH_2CH_2-$ precursor.

Table 7.3. Summary of $-CH_2CH_2-/-CH=CH-$ ratio and aluminium incorporation into the template extracted PMOs

Sample	-CH_2CH_2-/-CH=CH-		^{27}Al[4] Peak area /10^8
	^{13}C	^{29}Si	
-CH_2CH_2-/-CH=CH-PMO	2.71	1.52	//
Al/-CH_2CH_2-/-CH=CH-PMO	2.30	1.70	1.59
J-PMO-0-30	2.36	1.55	//
J-PMO-0-60	3.21	1.79	//
S-PMO-0-30	2.79	1.79	//
S-PMO-0-60	2.38	1.61	//
J-PMO-5-30	2.39	1.67	0.99
J-PMO-5-60	2.10	1.15	1.76
S-PMO-5-30 (-CH_2CH_2- + Al)	1.99	1.37	0.99
S-PMO-5-60 (-CH_2CH_2- + Al)	1.75	1.10	1.52
S-PMO-5-30 (-CH=CH- + Al)	2.88	1.80	2.29
S-PMO-5-60 (-CH=CH- + Al)	2.94	2.17	3.21

7.5 ^{1}H-^{29}Si CP/MAS kinetics

7.5.1 Standard PMOs

^{1}H-^{29}Si CP/MAS kinetics (fig. 7.17 and table 7.3 respectively) indicate changes is $T_{1\rho}{}^{H}$ times as a consequence of incorporation of aluminium. For both organic bridges, the silicon T^2 sites always show faster CP build up than their respective T^3 environments for reasons explained in previous chapters. As expected, the incorporation of aluminium has no effect on the T_{IS} times because aluminium does not influence the ^{1}H-^{29}Si heteronuclear dipolar coupling.

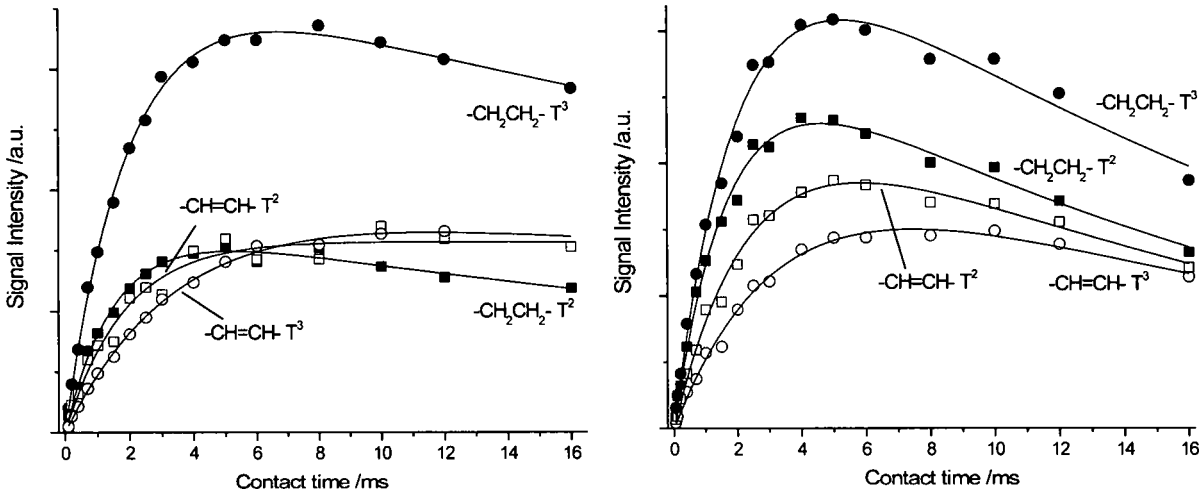

Figure 7.17. ^{1}H-^{29}Si CP/MAS kinetics curves of -CH_2CH_2-/-CH=CH-PMO (left) and Al-CH_2CH_2-/-CH=CH-PMO (right).

The incorporation of aluminium has resulted in an increase in relative intensity of both -CH_2CH_2- and -CH=CH-T^2 sites at *ca.* 57.2 and 71.8 ppm compared to the resonances at *ca.* 64.6 and 80.4 ppm respectively. This observation is further confirmation that Al containing silicon T^3 sites resonate at the same frequency as the Al free silicon T^2 environments. The presence of aluminium led to a decrease in the $T_{1\rho}{}^{H}$ times for all silicon $T^{2/3}$ sites providing further confirmation that aluminium is embedded in the pore walls. The influence of residual template on $T_{1\rho}{}^{H}$ times can be ignored as relaxation times for the T^3 sites (located away from the template in bulk pore wall) are also reduced. This change is a result of a $^{1}H/^{27}Al/^{29}Si$ dipolar coupled system where relaxation in the rotating frame is facilitated by the quadrupolar (I = 5/2) aluminium nucleus.[137]

Table 7.3. ^{1}H-^{29}Si CP/MAS kinetics parameters for extracted standard PMOs.

Resonance /ppm	^{29}Si site	Signal Intensity /10^7	T_{IS}/ms	$T_{1\rho}{}^{H}$/ms	R^2
-CH_2CH_2-/-CH=CH-PMO					
-57.2	-CH_2CH_2- T^2	1.71 ±0.04	1.53 ± 0.09	39.8 ± 5.78	0.995
-66.8	-CH_2CH_2- T^3	3.75 ±0.09	1.98 ± 0.08	>50	0.998
-73.3	-CHCH- T^2	1.70 ±0.14	2.05 ± 0.34	>50	0.965
-82.4	-CHCH- T^3	1.87 ±0.15	3.41 ± 0.36	>50	0.998
Al-CH_2CH_2-/-CH=CH-PMO					
-57.6	-CH_2CH_2- T^2	15.2 ±2.00	1.77 ± 0.13	18.3 ± 1.92	0.992
-66.4	-CH_2CH_2- T^3	18.5 ±2.82	2.10 ± 0.16	19.5 ± 2.41	0.992
-73.0	-CHCH- T^2	9.57 ±0.18	2.48 ± 0.24	18.9 ± 2.95	0.991
-82.9	-CHCH- T^3	6.35 ±0.20	3.47 ± 0.53	20.5 ± 5.56	0.989

7.5.2 ^{1}H-^{29}Si CP/MAS kinetics of the Pre-hydrolysed Al-free PMOs

The CP kinetics of the J/S pre-hydrolysed PMOs (Fig. 7.18 and Table 7.4) indicate motional differences of both the organic functionalities as a function of pre-hydrolysis conditions. There are no substantial changes in relaxation times between the $-CH_2-CH_2-$ $T^{2,3}$ and $-CH=CH-$ $T^{2,3}$ sites within all the individual PMOs. Therefore, the silicon sites obtain CP from a homogeneous 'proton pool' suggesting a homogeneous distribution of the organic functionalities in the mesoporous framework. All the T sites in J/S-PMO-0-30 show faster $T_{1\rho}{}^{H}$ times compared to the standard $-CH_2CH_2-$/-CH=CH-PMO whereas, the J/S-PMO-0-60 show $T_{1\rho}{}^{H}$ times similar to the standard PMO.

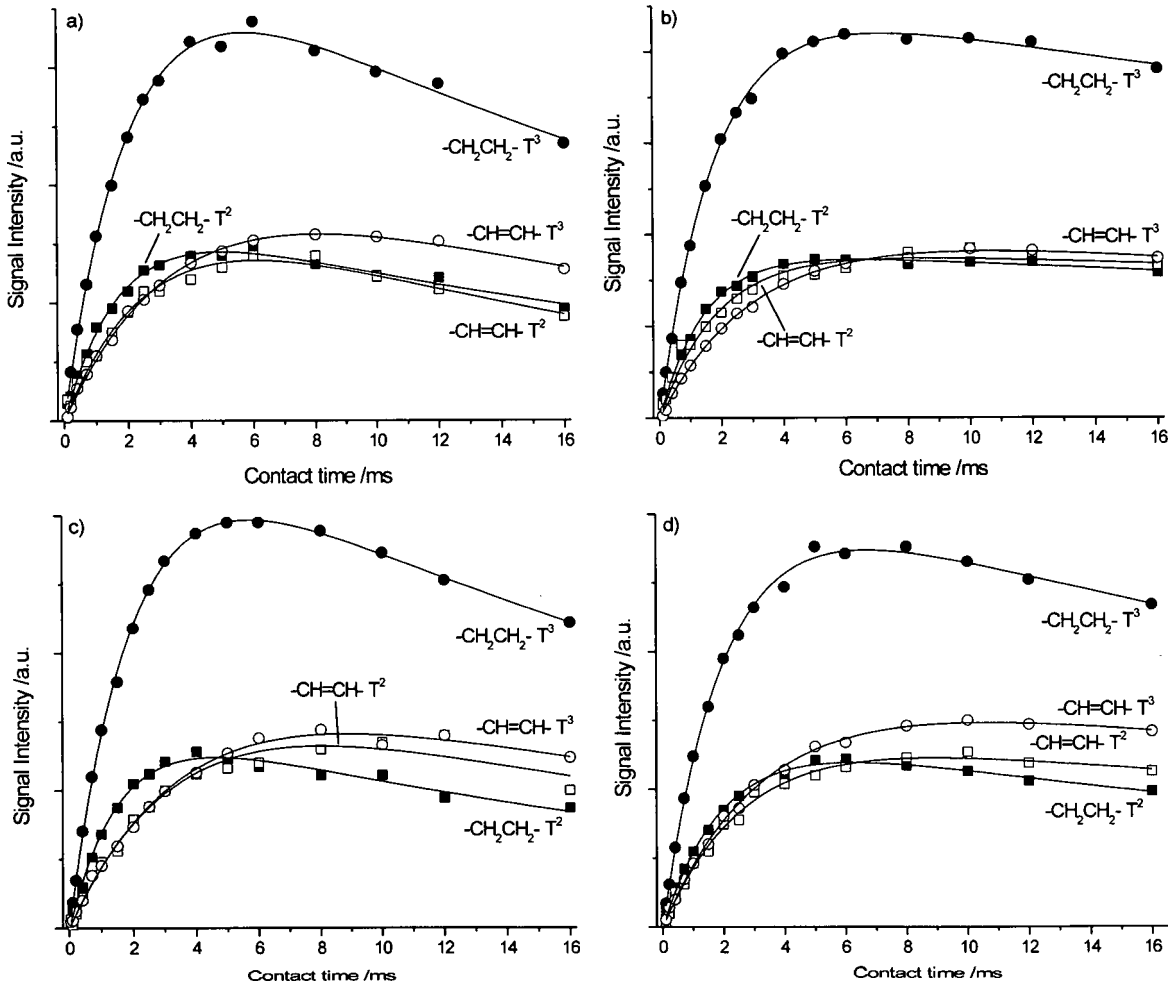

Figure 7.18. ^{1}H-^{29}Si CP/MAS kinetics curves of the template extracted pre-hydrolysed PMOs a) J-PMO-0-30, b) J-PMO-0-60, c) S-PMO-0-30 and d) S-PMO-0-60.

Table 7.4. ^{1}H-^{29}Si CP/MAS kinetic parameters for extracted J- and S- Al free PMOs

Resonance/ ppm	^{29}Si site	Signal Intensity /10^7	T_{IS}/ms	$T_{1\rho}{}^{H}$/ms	R^2
J-PMO-0-30					
-57.5	-CH_2CH_2- T^2	1.75 ±0.05	1.73 ±0.10	24.5 ±2.60	0.993
-66.8	-CH_2CH_2- T^3	4.13 ±013	2.10 ±0.12	23.1 ±2.62	0.996
-73.1	-CHCH- T^2	1.78 ±0.04	2.45 ±0.14	20.7 ±1.99	0.981
-82.9	-CHCH- T^3	2.24±0.12	3.67 ±0.26	25.1 ±3.22	0.998
J-PMO-0-60					
-57.2	-CH_2CH_2- T^2	1.33±0.03	1.52 ±0.05	>50	0.997
-67.0	-CH_2CH_2- T^3	1.75 ±0.02	1.96 ±0.05	>50	0.998
-73.6	-CHCH- T^2	1.83±0.01	3.24 ±0.25	>50	0.976
-83.1	-CHCH- T^3	2.04 ±0.07	3.52 ±0.16	>50	0.998
S-PMO-0-30					
-57.6	-CH_2CH_2- T^2	1.49 ±0.04	1.55 ±0.09	25.4 ± 2.66	0.994
-66.8	-CH_2CH_2- T^3	3.62 ±0.05	1.99 ±0.05	28.5 ± 1.54	0.999
-72.8	-CHCH- T^2	1.80 ± 0.06	3.46 ±0.25	26.0 ± 3.84	0.980
-83.4	-CHCH- T^3	1.88 ±0.03	3.66 ±0.12	30.8 ± 2.36	0.996
S-PMO-0-60					
-57.6	-CH_2CH_2- T^2	1.40 ±0.04	2.01 ±0.10	38.2 ± 5.02	0.996
-66.4	-CH_2CH_2- T^3	3.15 ±0.07	2.04 ±0.08	47.0 ± 5.62	0.998
-72.8	-CHCH- T^2	1.41 ±0.08	2.72 ±0.26	>50	0.994
-83.1	-CHCH- T^3	1.71 ±0.07	3.26 ±0.21	>50	0.998

7.5.3 ^{1}H-^{29}Si CP/MAS kinetics of the Pre-hydrolysed Al-PMOs

Similarly to the standard PMOs, the incorporation of aluminium into the jointly pre-hydrolysed PMOs resulted in an overall decrease in $T_{1\rho}^{H}$ times for reasons explained in section 7.5.1. The relative intensity of the -CH=CH-Si $T^{2/3}$ sites is increased compared to the $-CH_2CH_2-$ environments with increasing pre-hydrolysis time (Fig. 7.19 and Table 7.5).

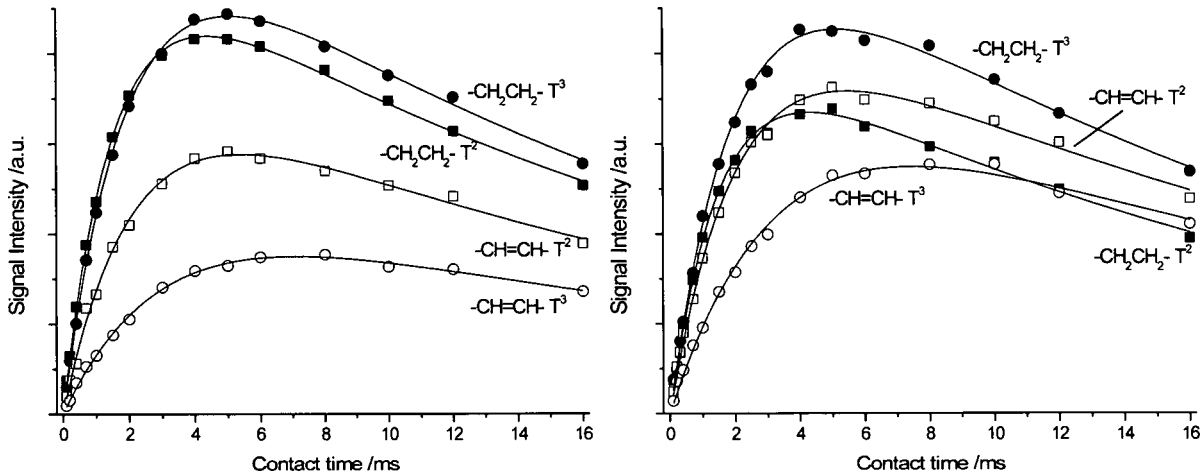

Figure 7.19. ^{1}H-^{29}Si CP/MAS kinetics curves of the template extracted J-PMO-5-30 (left) and J-PMO-5-60 (right).

Table 7.5. ^{1}H-^{29}Si CP/MAS kinetic parameters for extracted J-Al-PMOs

Resonance /ppm	^{29}Si site	Signal Intensity /10^7	T_{1S}/ms	$T_{1\rho}^{H}$/ms	R^2
J-PMO-5-30					
-56.6	$-CH_2CH_2-$ T^2	2.59 ±0.03	1.55 ±0.03	20.8 ±0.61	0.999
-64.3	$-CH_2CH_2-$ T^3	2.85 ±0.04	1.97 ± 0.05	19.9 ±0.74	0.999
-72.4	-CHCH- T^2	1.86 ±0.06	2.09 ±0.12	21.4 ±2.07	0.996
-81.4	-CHCH- T^3	1.17 ±0.05	2.96 ±0.19	24.2 ±2.89	0.998
J-PMO-5-60					
-55.8	$-CH_2CH_2-$ T^2	2.08 ±0.04	1.53 ±0.06	19.9 ±1.13	0.997
-63.9	$-CH_2CH_2-$ T^3	2.76 ±0.06	2.01 ±0.08	19.6 ±1.21	0.998
-71.8	-CHCH- T^2	2.27 ±0.06	2.05 ±0.10	22.8 ±1.94	0.997
-80.8	-CHCH- T^3	1.93 ± 0.03	3.37 ±0.12	21.7 ±1.40	0.994

^{1}H-^{29}Si CP/MAS kinetics of the separately pre-hydrolysed PMOs (Fig. 7.20 and Table 7.6) highlight changes in the $T_{1\rho}{}^{H}$ times depending on the silicon precursor/ $Al(O^{i}C_3H_7)_3$ combination during the pre-hydrolysis step. The T_{1S} times of the various T sites followed the same trends as seen for the standard PMOs.

The [-CH_2CH_2- + Al] products indicate a very homogeneous structure as $T_{1\rho}{}^{H}$ times for all T sites are similar irrespective of pre-hydrolysis time. The intensity of the peaks of -CH=CH- T sites is increasingly similar to those of -CH_2CH_2- T sites with increasing pre-hydrolysis time. This is consistent with the analysis of the ^{29}Si CP/MAS NMR data which suggested a higher -CH=CH- content in comparison to the S-PMO-5-30/60 [-CH=CH- + Al].

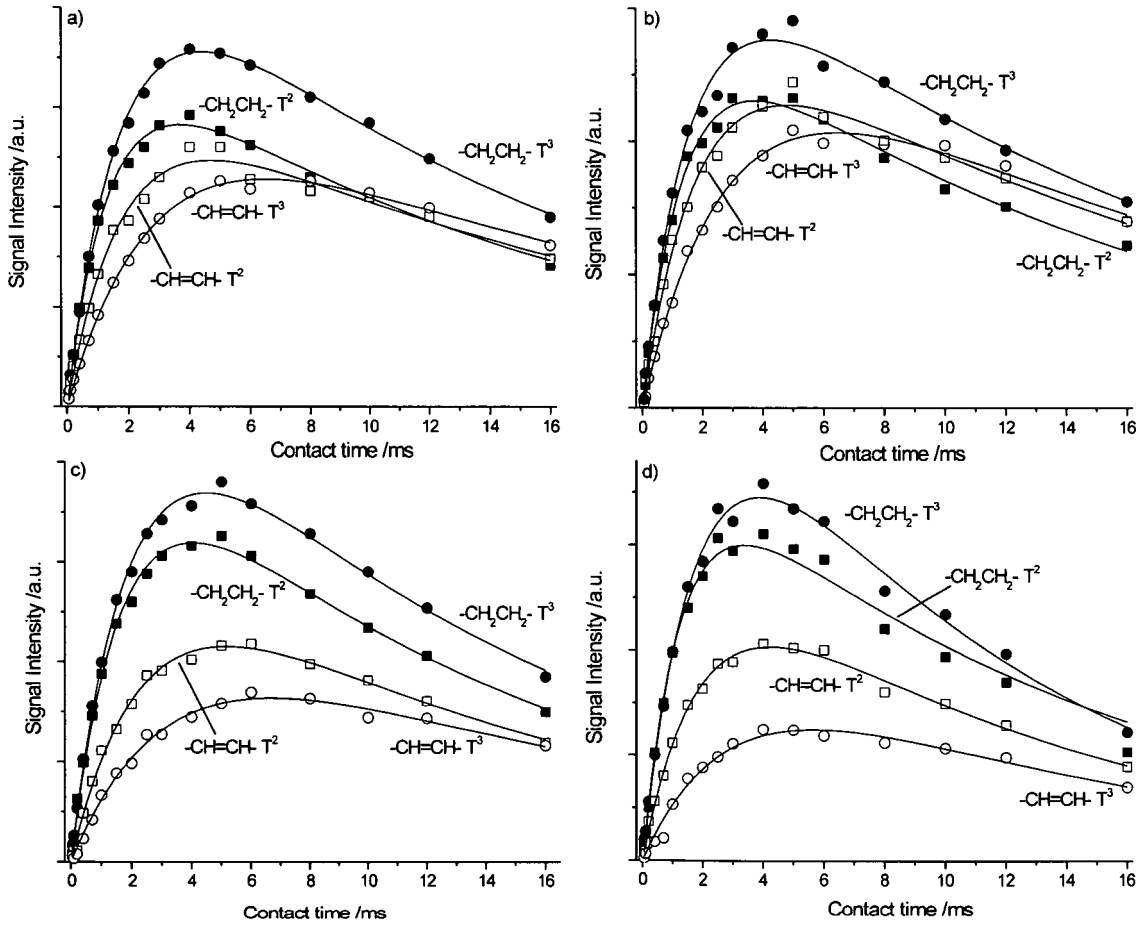

Figure 7.20. ^{1}H-^{29}Si CP/MAS kinetics curves for the template extracted separately pre-hydrolysed Al-PMOs a) S-PMO-5-30 (-CH_2CH_2- + Al), b) S-PMO-5-60 (-CH_2CH_2- + Al), c) S-PMO-5-30 (-CH=CH- + Al) and d) S-PMO-5-60 (-CH=CH- + Al).

The [-CH=CH- + Al] PMOs displayed faster $T_{1\rho}{}^{H}$ times than the [-CH_2CH_2- + Al] PMOs. This indicates an increased Al content, confirmed by ^{27}Al MAS NMR, is influencing the $T_{1\rho}{}^{H}$ times of the framework. $T_{1\rho}{}^{H}$ times are also decreased as pre-hydrolysis time

increases for both S-PMO-5-30/60 (-CH_2CH_2- + Al) and S-PMO-5-30/60 (-CH=CH- + Al) which is again consistent with increasing Al content (Fig. 7.16). The faster $T_{1\rho}^{H}$ times with increasing Al content is further proof to the presence of a three spin coupled system of $^{1}H/^{27}Al/^{29}Si$ whereby Al facilitates relaxation.

Table 7.6. ^{1}H-^{29}Si CP/MAS kinetic parameters for template extracted separately pre-hydrolysed PMOs.

Resonance /ppm	^{29}Si site	Signal Intensity /10^7	T_{IS}/ms	$T_{1\rho}^{H}$/ms	R^2
S-PMO-5-30 (-CH_2CH_2- + Al)					
-57.6	-CH_2CH_2- T^2	1.76 ±0.04	1.34 ±0.06	16.5 ±0.99	0.996
-66.4	-CH_2CH_2- T^3	2.34 ± 0.04	1.76 ±0.06	15.9 ±0.70	0.998
-73.0	-CHCH- T^2	1.58 ± 0.08	1.80 ±0.16	19.1 ±2.49	0.988
-82.9	-CHCH- T^3	1.58 ±0.06	2.87 ±0.16	19.9 ±1.96	0.997
S-PMO-5-60 (-CH_2CH_2- + Al)					
-57.4	-CH_2CH_2- T^2	16.7 ±1.48	1.39 ±0.07	16.0 ±1.08	0.994
-66.4	-CH_2CH_2- T^3	18.9 ±2.32	1.62 ±0.11	17.4 ±1.67	0.992
-72.9	-CHCH- T^2	14.5 ±2.00	1.87 ±0.14	18.6 ±2.06	0.992
-83.0	-CHCH- T^3	9.12 ±1.31	2.95 ±0.22	18.4 ±2.28	0.996
S-PMO-5-30 (-CH=CH- + Al)					
-56.9	-CH_2CH_2- T^2	2.31 ±0.06	1.68±0.09	13.9 ±0.92	0.986
-66.4	-CH_2CH_2- T^3	2.51 ±0.07	1.92 ±0.09	14.4 ±0.74	0.993
-72.9	-CHCH- T^2	1.52 ±0.07	2.37 ±0.18	14.6 ±1.50	0.994
-82.3	-CHCH- T^3	1.20 ±0.10	3.26 ±0.39	17.1 ±2.92	0.982
S-PMO-5-60 (-CH=CH- + Al)					
-56.9	-CH_2CH_2- T^2	1.92 ± 3.33e5	1.29 ±0.06	13.7 ±0.59	0.986
-66.4	-CH_2CH_2- T^3	2.53 ± 1.05e6	1.88 ±0.13	10.0 ±0.74	0.993
-72.9	-CHCH- T^2	1.44 ± 5.90e5	1.95 ±0.13	11.9 ±0.95	0.994
-82.3	-CHCH- T^3	0.97 ± 1.25e6	2.99 ±0.54	12.6 ±2.92	0.982

7.6 ^{1}H-^{29}Si HETCOR experiments

2D ^{1}H-^{29}Si HETCOR experiments probed the spatial proximity of the organic functionalities in the framework. The same $T^{2/3}$ sites as those in the 1D ^{1}H-^{29}Si CP/MAS (Figs. 7.10 and 7.11) in the direct dimension are correlated to the FSLG decoupled ^{1}H MAS spectrum in the indirect dimension.

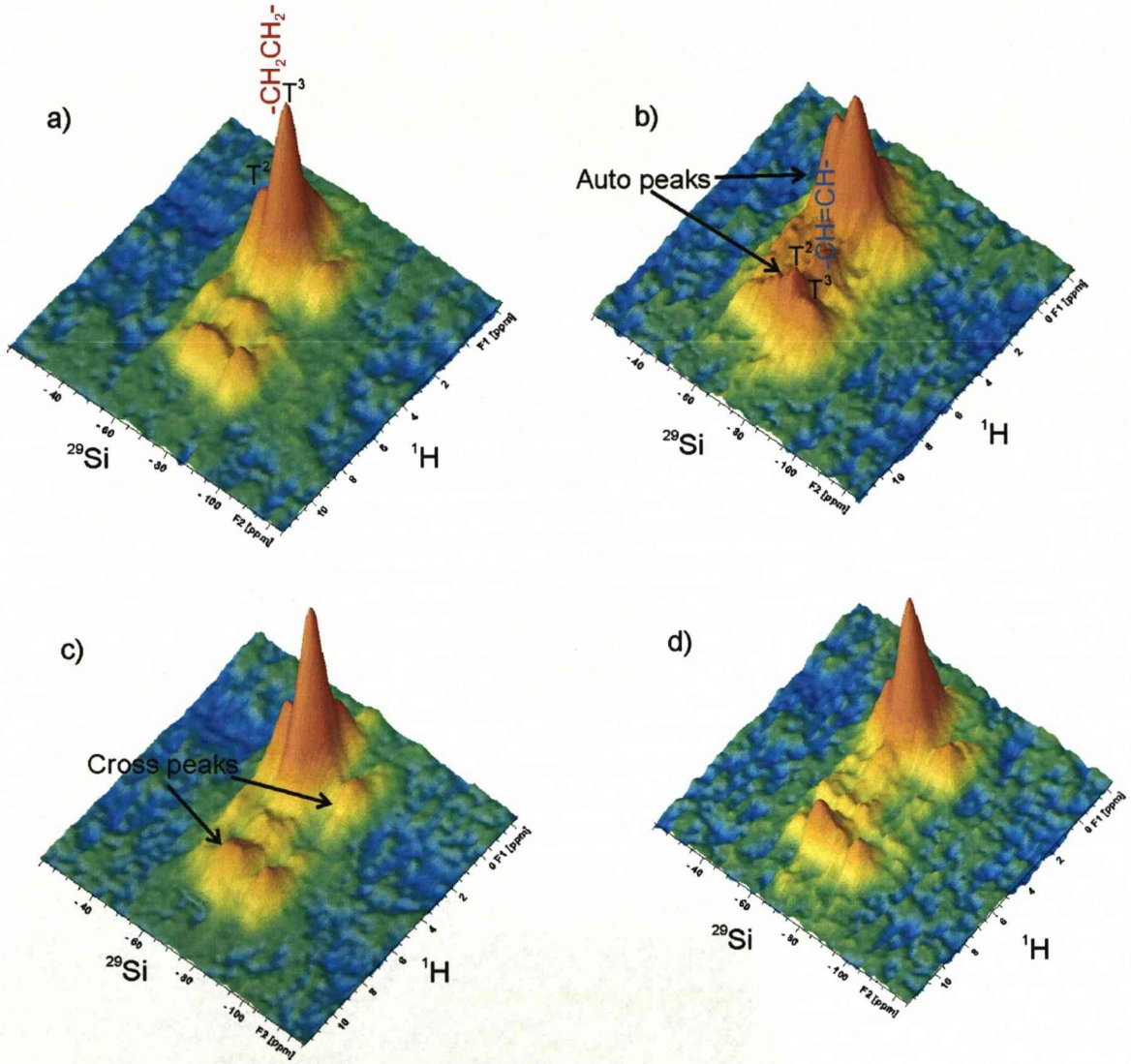

Figure 7.21. ^{1}H-^{29}Si HETCOR NMR spectra of the template extracted a) $-CH_2CH_2-$/-CH=CH-PMO b) Al/$-CH_2CH_2-$/-CH=CH-PMO c) J-PMO-0-60 and d) S-PMO-0-60.

The ^{1}H-^{29}Si HETCOR spectra of the standard Al-free PMO and those for J-PMO-0-60 and S-PMO-0-60 (Fig. 7.21) are similar. The ^{1}H dimension exhibits four/five resonances. The resonances at 0.8 and 4.2 ppm are assigned to surface hydroxyls (silanol groups) and H-

bonded water located within the pore walls, close to the silicon $T^{2,3}$ sites. The peak at 1.8 ppm is attributed to the $-CH_2-CH_2-$ protons with auto-peaks observed in the ^{29}Si direct dimension at –56.6 and –63.9 ppm correlating to $\equiv Si-CH_2-CH_2-Si\equiv$ $T^{2,3}$ environments. The peak at 6.8 ppm is assigned to the –CH=CH- protons with auto-peaks observed in the ^{29}Si dimension at –72.0 and –82.2 ppm indicative of $\equiv Si-CH-CH-Si\equiv$ $T^{2,3}$ sites. In addition, cross-peaks correlating the $-CH_2-CH_2-$ bridge ^1H resonance to the –CH=CH- silicon $T^{2,3}$ sites and *vice versa* are observed. The $^1H-^{29}Si$ HETCOR spectrum of the standard Al-PMO (Fig. 7.21b) shows an increase in the -CH=CH- auto-peak intensity relative to the $-CH_2CH_2-$ sites compared to the $-CH_2CH_2-/-CH=CH-$PMO.

The degree of heterogeneity can be estimated using intensities of $-CH_2-CH_2-$ and –CH=CH- $^1H-^{29}Si$ correlations from the 2-dimensional data set. High auto peak/cross peak ratios indicate a heterogeneous domain type distribution whereas lower values suggest a more homogenous framework (Table 7.7). J-PMO-0-60 exhibits an increased ratio for the $-CH_2-CH_2-$ sites compared to $-CH_2CH_2-/-CH=CH-$PMO however, the ratio for the -CH=CH- environments is reversed (Table 7.7). S-PMO-0-60 has a decreased $-CH_2CH_2-$ $T^{2/3}$ ratio and an increased -CH=CH- ratio compared to J-PMO-0-60. The analogous acid catalysed $-CH_2CH_2-/-CH=CH-$PMOs (chapter 5) showed a distinct difference in $^1H-^{29}Si$ correlation intensities as a function of pre-hydrolysis protocols whereby, J-PMOs displayed homogeneous structures and S-PMOs displayed heterogeneous structures. In the S^+I^- systems the distribution of organic functionalities is less homogenous than in the acid catalysed J-PMOs, however, more homogeneous than in the acid catalysed S-PMOs (Chapter 5). Therefore the S^+I^- $-CH_2CH_2-/-CH=CH-$PMOs have an intermediate structure were domains exist but are smaller and/or less segregated. The homogeneity of Al/$-CH_2CH_2-/-CH=CH-$PMO is increased compared to the Al free analogue with an increase in cross-peak intensities of both organic functionalities. This confirms aluminium to affect the co-assembly and formation of the mesostructure during synthesis as was observed using powder XRD (Fig. 7.1).

Table 7.7. Intensities of cross-peaks in the ^{1}H-^{29}Si HETCOR NMR spectra. Values are normalized to those of the $-CH_2CH_2-$ T^3 resonance.

^{29}Si Resonance / ^{1}H Resonance	-CH_2CH_2-		-CH=CH-	
	T^2	T^3	T^2	T^3
-CH_2CH_2-/-CH=CH- PMO				
-CH_2CH_2-	0.44	1.00	0.32	0.19
-CH=CH-	0.09	0.22	0.21	0.23
(Auto peak $T^2 + T^3$)/ (Cross peak $T^2 + T^3$)	4.51		0.87	
Al/-CH_2CH_2-/-CH=CH- PMO				
-CH_2CH_2-	0.78	1.00	0.37	0.28
-CH=CH-	0.21	0.36	0.48	0.39
(Auto peak $T^2 + T^3$)/ (Cross peak $T^2 + T^3$)	3.12		1.34	
J-PMO-0-60				
-CH_2CH_2-	0.38	1.00	0.53	0.17
-CH=CH-	0.01	0.19	0.21	0.21
(Auto peak $T^2 + T^3$)/ (Cross peak $T^2 + T^3$)	6.90		0.60	
S-PMO-0-60				
-CH_2CH_2-	0.37	1.00	0.46	0.58
-CH=CH-	0.01	0.30	0.20	0.24
(Auto peak $T^2 + T^3$)/ (Cross peak $T^2 + T^3$)	4.41		0.42	

7.7 ^{1}H-^{27}Al HETCOR experiments

^{1}H-^{27}Al HETCOR experiments were used to study the distribution of aluminium in the mesoporous framework. The application of ^{1}H-^{27}Al HETCOR experiments has been limited to the study of zeolites, Al doped mesoporous silicas and clays.[260,261] This is in part due to the poor resolution in both ^{1}H and ^{27}Al dimensions resulting from homonuclear dipolar coupling and quadrupolar interactions.

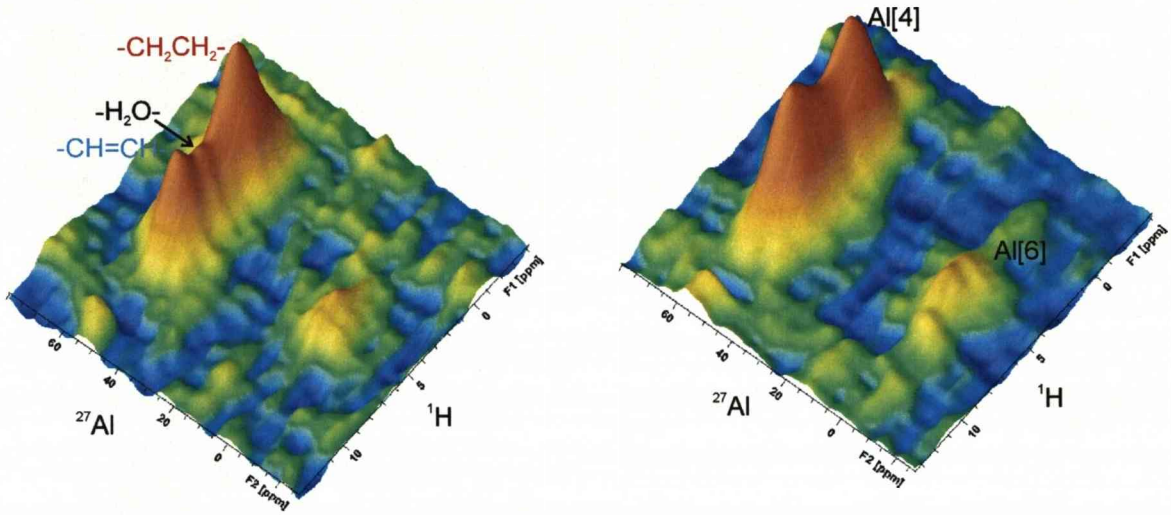

Figure 7.22. ^{1}H-^{27}Al HETCOR NMR spectra of the template extracted Al/-CH_2CH_2-/-CH=CH-PMO (left) and S-PMO-5-30 (-CH_2CH_2- + Al) (right).

The ^{1}H-^{27}Al HETCOR NMR spectra of Al/-CH_2CH_2-/-CH=CH-PMO and S-PMO-5-30 (-CH_2CH_2- + Al) (Fig. 7.22) exhibit Al(4) and Al(6) resonances (Fig. 7.15) in *f2* correlated to the FSLG decoupled ^{1}H MAS NMR spectrum in the *f1* dimension. The ^{1}H dimension exhibits three resonances. The resonance at 4.2 ppm is assigned to acidic protons and adsorbed water with correlation peaks to the ^{27}Al resonances at *ca.* 53 and 0 ppm attributed to framework aluminium ($Al(O)_4$) and octahedrally bound $Al[(H_2O)_6]^{3+}$ species respectively. ^{1}H resonances at 1.8 and 6.8 ppm are due to –CH_2-CH_2- and –CH=CH- protons with correlations observed in the ^{27}Al direct dimension at 52.9 ppm confirming assignment as framework aluminium. No cross-peaks correlating the organic bridges and $Al[(H_2O)_6]^{3+}$ are observed. Therefore, the latter species are located at the surface of the pores. Both the standard Al-PMO and S-PMO-5-30 [-CH_2CH_2- + Al] show near identical cross-peaks with a small increase in –CH=CH-/Al[4] correlation intensity for the latter. This suggests that the aluminium is not located preferentially to a specific organic bridge when using separate pre-

hydrolysis protocols. Therefore the aluminium must re-disperse in the synthesis solution during the low and/or high temperature steps after pre-hydrolysis to be evenly distributed in the framework.

7.8 Discussion and Conclusions

Periodic mesoporous organosilicas containing $-CH_2-CH_2-/-CH=CH-$ and $-Al-/-CH_2-CH_2-/-CH=CH-$ functionalities have been synthesised. Joint and separate pre-hydrolysis protocols were employed in an attempt to control the distribution of the organic and aluminium functionalities into homogeneous and heterogeneous domains.

The introduction of aluminium into the $-CH_2CH_2-/-CH=CH-$PMO resulted in an increase in mesoscopic ordering the origin of which is the negatively charged Al[4] centres within the framework (Scheme 7.1). The presence of negatively charged aluminium sites resulted in an increase in template content in the as-synthesised Al-PMOs compared to the Al free analogues.

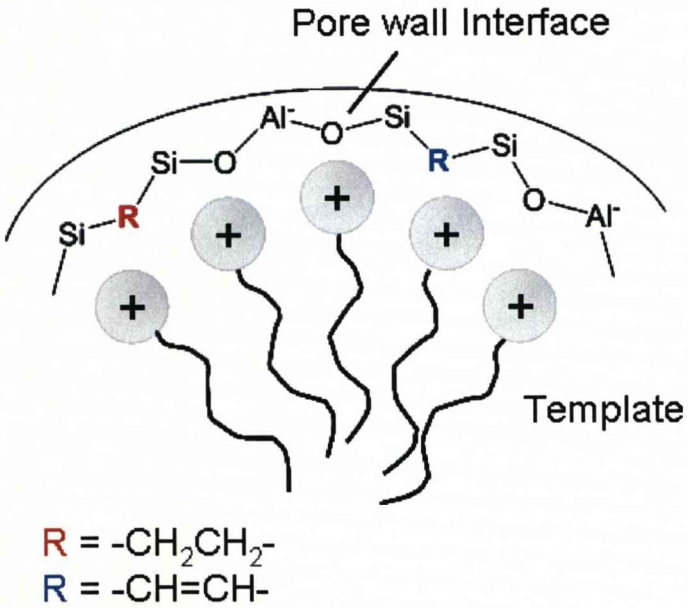

Scheme 7.1. Representation of the template containing negatively charged $Al-/-CH_2CH_2-/-CH=CH-$PMO.

The application of pre-hydrolysis caused a significant increase in mesoscopic ordering compared to the reference $-CH_2CH_2-/-CH=CH-$PMO (confirmed by PXRD and N_2 adsorption isotherms). Reasons for such an observation cannot be explained unambiguously. However, with the application of ^1H-^{13}C CP kinetics one could determine changes in template dynamics as a function pre-hydrolysis. There is also the possibility of using selectively deuterated template polar head groups and applying variable temperature wideline ^2H experiments to probe mobility. The ^1H-^{29}Si CP kinetics and HETCOR experiments suggest the –CH=CH- functionalities to be isolated within regions of the –

CH_2CH_2- groups. This is confirmed by the auto peak/ cross peak ratio being less than 1.00 (Table 7.7) which can only arise if the main CP source is the protons of the $-CH_2CH_2$- bridges. Again this observation is consistent with there being fewer –CH=CH- bridges than $-CH_2CH_2$- bridges in the final PMO product.

The use of Aluminium as a probe enabled further investigation into the influence of Joint and separate Pre-hydrolysis protocols on Al-/-CH_2CH_2-/-CH=CH-PMOs. Aluminium was re-dispersing in the reaction media after the pre-hydrolysis. Re-dispersion may not be isolated to aluminium it is also possible that the $-CH_2CH_2$- and –CH=CH- containing SBUs also partially re-disperse during the synthesis. This hypotheses would be consistent with the conclusions of Lowe *et al.* on zeolite formation (Scheme 7.2).[258,259]

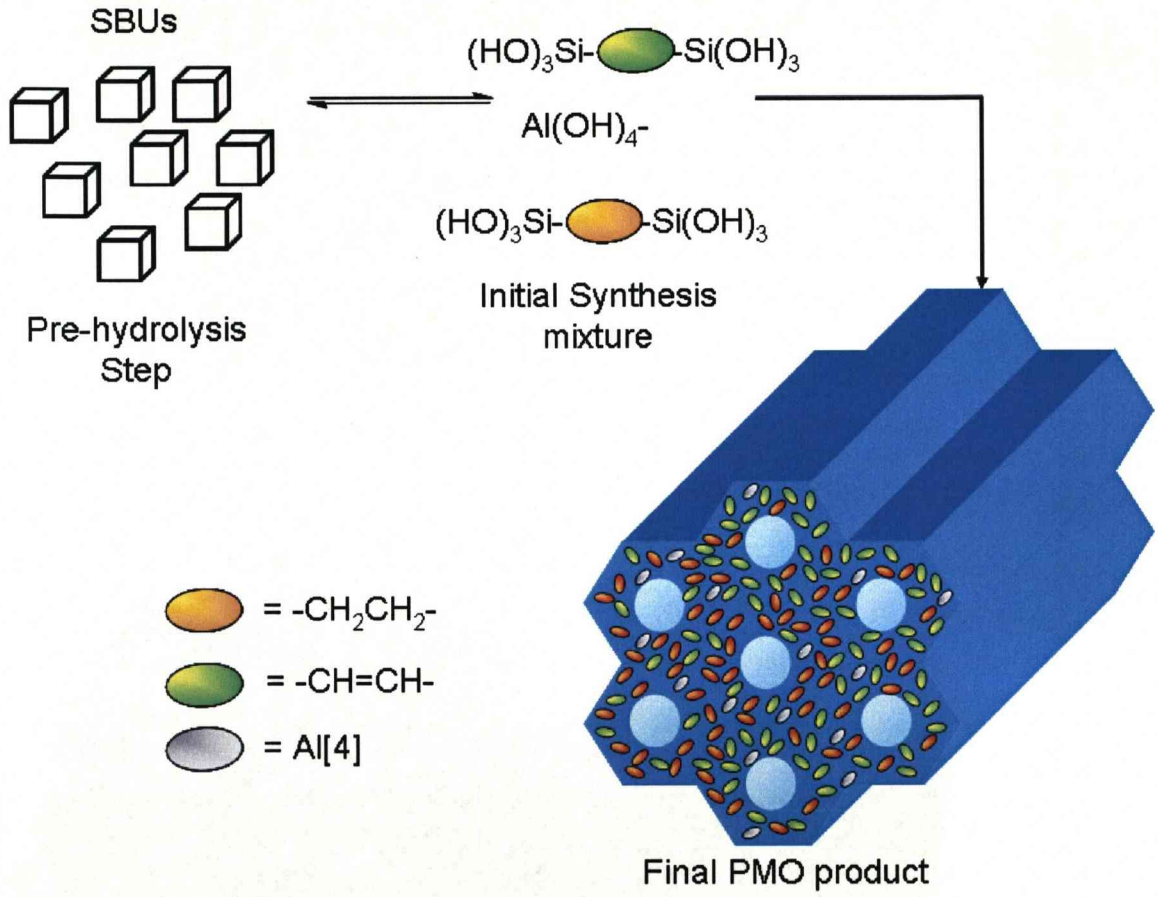

Scheme 7.2. Proposed re-dispersion of SBUs upon addition to the template solution suggested by solid-state NMR experiments.

7.9 Synthesis of Bi-functional PMOs: General summary

Although multi-functional PMO containing a variety of organic bridges have been previously reported, many lack thorough investigation of their molecular level structures. Most of these articles assume a random distribution of organic bridges and do not comment on how the synthesis can affect the relative incorporation of the organic components. In this study the influence of synthetic conditions (*i.e.* acid and base catalysed hydrolysis/ condensation, the application of joint or separate pre-hydrolysis) on the molecular level structure in terms of homogeneity and organic bridge ratio in PMOs has been investigated. We have shown that a multi-functional PMO can consist of domains or exhibit a homogeneous distribution of organic bridges depending on the organic bridges used. Therefore, in terms of materials design, it is important to rationalise how one type of framework structure forms in preference to another and devise a set of synthetic conditions to suit the various types of organic bridges used in PMO synthesis. In this section we aim to show how by considering the type of organic bridges and various synthetic parameters the molecular level structure of multi-functional PMOs could be designed prior to synthesis.

The various synthetic parameters that influence the structure of a multi-functional PMO framework in terms of mesoscopic ordering, homogeneity and incorporation ratio must be considered to select the most appropriate conditions to form the desired product. The key synthetic parameters are discussed below:

Templating pathway - The choice of either block co-polymer ($S^0H^+X^-I^+$) or cationic (S^+I^-) templates is governed initially by the pore dimensions that are required. The differences between solids prepared using either template is well understood. In multi-functional PMO we have seen that the block co-polymer template gave larger pore dimensions and thicker walls irrespective of organic bridges used consistent with mono-functional PMOs.

Acid or base catalysed hydrolysis/condensation – Although the mechanisms of hydrolysis/ condensation are well known, their influence on multi-functional PMOs is less understood. The acid catalysed reactions appear to be under kinetic control whereas the basic systems under thermodynamic control. This was evident form the differences in molecular scale periodicity found in the $-C_6H_4$-PMO and subsequent bi-functional $-CH_2CH_2$-/-C_6H_4-PMO (chapter 6). Further evidence of the basic system being under thermodynamic control was

seen by the re-dispersion of aluminium in template solutions post separate pre-hydrolysis confirmed by ^{1}H-^{27}Al HETCOR experiments (chapter 7).

Silica source pre-hydrolysis – The concept of pre-hydrolysing silica precursors has been used in various syntheses of transition metal containing PMOs in particular titanium as a method of balancing the hydrolysis/ condensation rates in template solutions. In this report pre-hydrolysis was used as a methodology for controlling the homogeneity of PMOs containing multiple organic bridges. Evidently, the three types of organic bridges used here all behaved differently under pre-hydrolysis with both the $-C_6H_4-$ and –CH=CH- functionalities generally reacting faster than $-CH_2CH_2-$ groups.

Other factors influencing the final PMO structure such as, hydrothermal treatment time and temperature are also important yet are more generic to all types of PMOs. Therefore, the three afore mentioned synthetic parameters and their influence on the multi-functional PMO presented here are summarised below.

Mesoporous organosilicas prepared via $S^0H^+X^-I^+$ pathways in the absence of pre-hydrolysis always gave a homogeneous distribution of organic groups. The introduction of pre-hydrolysis under acidic conditions had different effects on the resulting products depending on the organic bridges used. With $-CH_2CH_2-$ and -CH=CH- bridges the distribution was accurately controlled *via* joint and separate pre-hydrolysis to give homogenous and domain structures respectively. However the substitution of -CH=CH- for $-C_6H_4-$ bridges caused the pre-hydrolysis procedures to produce partial domain structures under joint pre-hydrolysis conditions. The influence of pre-hydrolysis on the S^+I^- pathway in terms of framework homogeneity was, as with the acid catalysed PMOs, highly dependent on the organic bridges used in the synthesis. The $-CH_2CH_2-$/$-C_6H_4-$PMOs formed domain structures under basic conditions with or without pre-hydrolysis. Whereas, the analogous $-CH_2CH_2-$/-CH=CH-PMOs formed partial domain structures under all conditions. That is their framework homogeneity was between the jointly and separately pre-hydrolysed $-CH_2CH_2-$/-CH=CH-PMOs under acidic conditions.

The use of pre-hydrolysis was shown to affect the organic bridge ratio in the resulting PMOs. The $-CH_2CH_2-$/-CH=CH- PMO synthesised under acidic conditions showed a near 1:1 incorporation with or without pre-hydrolysis (chapter 5). Whereas, the same combination under basic conditions resulted in increased $-CH_2CH_2-$ content compared to –CH=CH- groups with or without pre-hydrolysis. The $-CH_2CH_2-$/$-C_6H_4-$PMOs prepared

under acidic conditions displayed a higher content of the $-CH_2CH_2-$ functionality under all conditions (chapter 6). The same PMO composition under basic conditions showed that without pre-hydrolysis a 1:1 ratio was obtained, however, under pre-hydrolysis a higher aromatic content was obtained. In contrast to $-CH_2CH_2-/-CH=CH-$PMO where the precursor that hydrolyses the faster (-CH=CH-) has reduced incorporation the $-CH_2CH_2-/-C_6H_4-$PMOs showed the $-C_6H_4-$ precursor incorporated in a higher content than the $-CH_2CH_2-$ bridge. This is a further confirmation the π-π stacking observed in benzene incorporated PMOs to influence the resulting ratio of functionalities in the products.

Pre-hydrolysis also affected mesoscopic ordering especially under the kinetically controlled acidic conditions, where a reduction in ordering was observed irrespective of organic functionality. Thus, if highly ordered PMOs are required, further optimisation of the pre-hydrolysis step should be considered: for example, changing the pre-hydrolysis solvent from ethanol to butanol, which was shown to improve mesoscopic ordering in -CH=CH-PMOs prepared under acidic conditions (chapter 4). The most unusual effect was seen for the $-CH_2CH_2-/-CH=CH-$PMOs, where the introduction of pre-hydrolysis under basic conditions resulted in improved mesoscopic ordering as seen by PXRD and N_2 adsorption isotherms (chapter 7 figs 7.2 and 7.5) *c.f.* the standard $-CH_2CH_2-/-CH=CH-$PMO. This can be viewed as a new method for preparing highly ordered $-CH_2CH_2-/-CH=CH-$PMOs under basic conditions. A representation of the effect of the templating pathway and pre-hydrolysis synthetic parameters influence the mesostructure of the PMO product is shown in scheme 7.3.

The heteroatoms such as bromine and aluminium have both affected the properties of PMOs. Although bromine containing PMOs are limited to the presence of -CH=CH- groups, aluminium containing PMOs can be formed using a wider range of organic bridges. The downside is that only the base catalysed PMOs are considered due to the high solubility of Al^{3+} at very low pH (the optimum range of formation of $S^0H^+X^-I^+$ templated PMO). The post synthetic bromination step has little effect on mesoscopic ordering and textural properties as PXRD and N_2 isotherms remained similar to those of the parent –CH=CH-PMO (chapter 4, fig. 4.1 and 4.2). On the other hand, the incorporation of aluminium *via* co-condensation significantly altered the mesoscopic and textural properties of the PMOs product. The aluminium containing PMO prepared without pre-hydrolysis showed an increase in the mesoscopic ordering, however, the textural properties are significantly altered with a change in pore dimensions (fig. 7.4). Both nuclei also influenced PMO properties on a molecular level confirmed, by ^1H-^{29}Si CP/MAS kinetics as reductions in $T_{1\rho}{}^H$ times are

observed. Therefore, when PMOs containing heteroatoms are required the use of post synthetic modification could be considered if retaining porous architecture is important. If the required PMO is to show high mesoscopic ordering and multi-functionality, then direct addition to a carefully optimised synthetic procedure should be the method of choice.

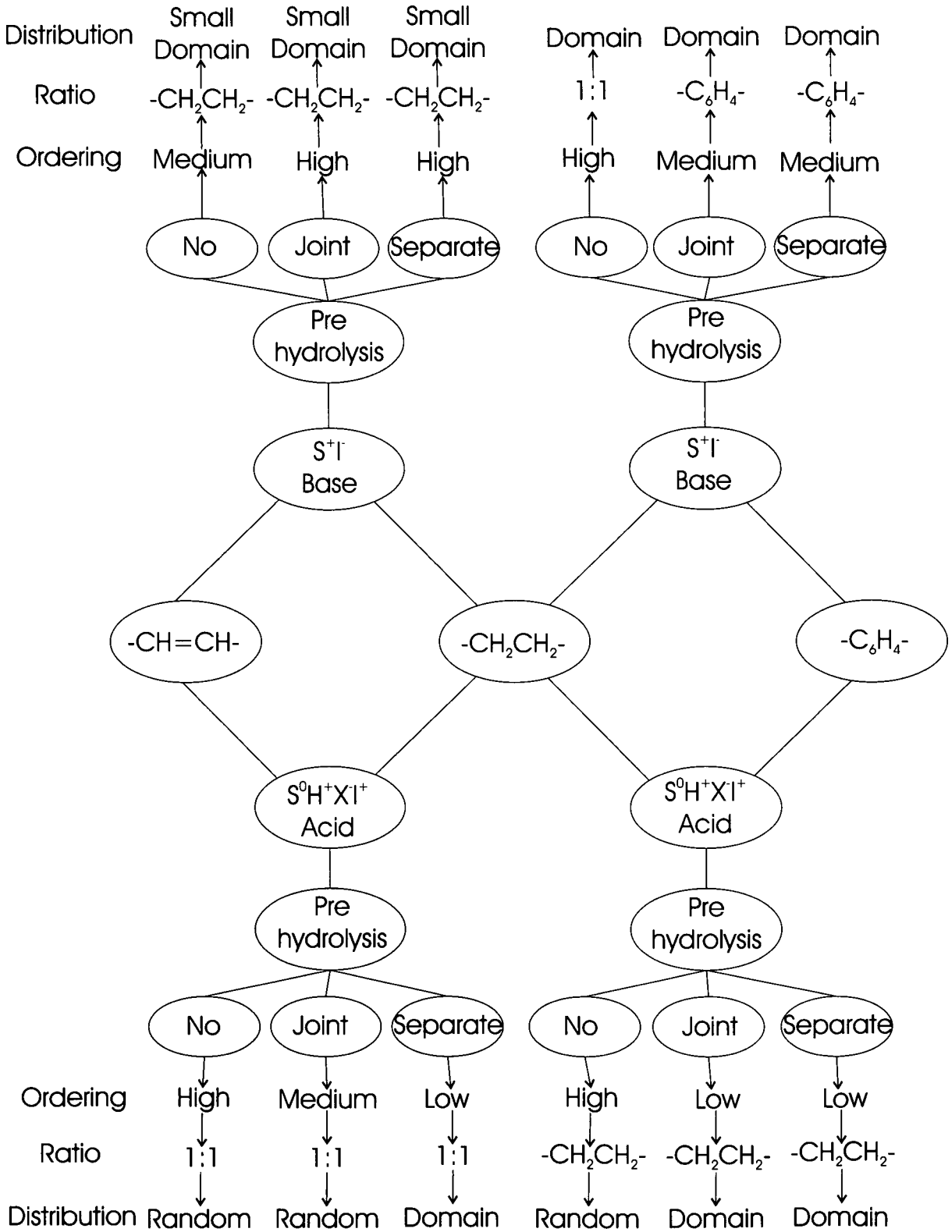

Scheme 7.3. Flow diagram representing the influence of templating pathway and pre-hydrolysis on the final PMO product. The three organic bridges in the middle are combined according to templating pathway then pre-hydrolysis conditions flowing outwards. The influence of the synthetic conditions is measured in terms of high to low ordering (PXRD, N_2 data); the most abundant organic bridge incorporated (^{13}C and ^{29}Si CP/MAS spectra) and organic bridge distribution (^{29}Si HETCOR NMR).

Solid-State NMR Characterisation of Microporous Polymer Networks

Chapter 8

8.1 Introduction

Microporous polymer networks have become increasingly important due to their applications in molecular separation and gas storage, in particular Hydrogen storage.[262,263] The use of microporous polymers offers significant advantages over metal-organic frameworks (MOFs)[16,264] and covalent organic frameworks (COFs)[92,265] as it is possible to achieve control of functionality using various cross coupling reactions. The polymers described in this chapter are based upon poly-(acryleneethynylene)s (PAE) synthesised using Sonogashira-Hagihara cross-coupling.[266] The structures of PAEs are usually linear,[267-270] hyperbanched,[271,272] dendritic[115,273,274] or cross-linked[275] and have incorporated solubilising alkyl or alkoxyl substituents. The conjugated PAEs networks described here display microporosity with high surface areas and are completely insoluble in most organic solvents. The textural properties of such conjugated microporous polymers (CMP) were characterised using gas adsorption techniques. Their structure on a molecular level was modelled using atomistic simulations (conducted by the research group of Prof. A. I. Cooper).

The amorphous nature of conjugated polymers makes their characterisation by X-ray diffraction/ scattering techniques, which are common place in the structural analysis of microporous MOFs and COFs, impossible. The insolubility of the polymers also rules out the use of solution state NMR and Gel permeate chromatography (GPC). Therefore the analytical methodologies available for the structural and molecular level analysis of CMP type networks are limited to solid phase techniques such as, gas sorption for textural properties, scanning electron microscopy (SEM) for morphology and solid-state NMR for molecular level structure. The understanding of molecular level structure in terms of composition and efficiency of cross-linking of CMP type networks is essential for the optimisation of their potential applications such as gas storage *i.e.* maximizing of isosteric heats of H_2 or CH_4 sorption and possible addition of metal centres for their use in catalytic applications.

In this chapter we aim to correlate the differences observed upon changing the composition of such materials indicated by gas adsorption and atomistic simulations with those on a molecular level determined using solid-state NMR. ^{1}H-^{13}C CP/MAS, ^{13}C MAS and CP kinetics experiments were used to probe differences in mobility between the molecular environments present within the various polymer networks. The polymers range from CMP and CPN networks, containing only carbon and hydrogen atoms, to polymers

with heteroatoms such as nitrogen (NCMP) and silicon. In the latter the tetrahedral centres are introduced into the porous polymers. As seen in the tables below, the textural properties of 4 groups of polymers are affected by the variation of the monomers used during synthesis. It is, therefore, important to know how changes in textural properties driven by different monomers influence molecular level structure.

8.2. Experimental Part

8.2.1. Synthesis of CMP networks

The microporous polymer networks were synthesised by the group of Prof. A. I. Cooper. A typical synthesis procedure for CMP-0 was described by Jiang *et al.*[262] 1,3,5-Triethynylbenzene (450.5 mg), 1,3,5-tris(4-iodophenyl)benzene (1368 mg), tetrakis(triphenylphosphine)palladium(0) (100 mg), and copper(I) iodide (30 mg) were dissolved in a mixture of toluene (2.5 mL) and Et_3N (2.5 mL). The reaction mixture was subsequently stirred and heated to 80°C for 72 hours under a nitrogen atmosphere. The products were recovered by filtration, washed and purified *via* Soxhlet extraction with methanol for 48 hours.

Table 8.1 Monomer units of polymer networks with average strut length.

	Ethynyl monomer	Halogen monomer	S_{BET} (m^2/g)[a]	S_{micro} (m^2/g)[b]	V_{total} (cm^3/g)[c]	V_{micro} (cm^3/g)[d]	L_{av} (strut) (nm)[e]	L_{av} (cluster) (nm)[f]
CMP-0	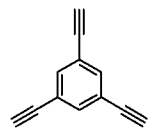	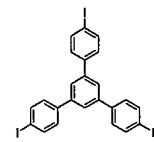	1018 (898)	702	0.56	0.38	0.82	6.3
CMP-1	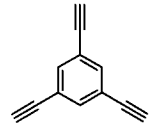	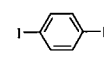	834 (728)	675	0.47	0.33	1.11	6.6
CMP-2	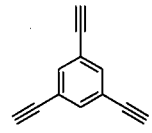	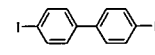	634 (562)	451	0.53	0.25	1.53	7.0
CMP-3	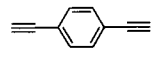	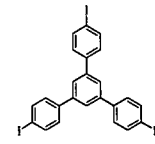	522 (409)	350	0.26	0.18	1.90	7.5
CMP-5	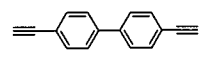	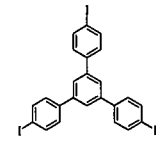	512 (361)	257	0.47	0.16	2.55	7.6

[a]Number in parentheses is the Langmuir surface area calculated from the H_2 adsorption isotherm by application of the Langmuir equation; [b] Micropore surface area calculated from the N_2 adsorption isotherm using t-plot method; [c] Total pore volume at $P/P_0 = 0.99$; [d] The micropore volume derived using the t-plot method based on the Halsey Thickness Equation; [e] Average node-to-node strut length

(measured between connected quaternary carbons) derived from polymer fragment models; [f] Average overall fragment diameter derived from polymer fragments models.

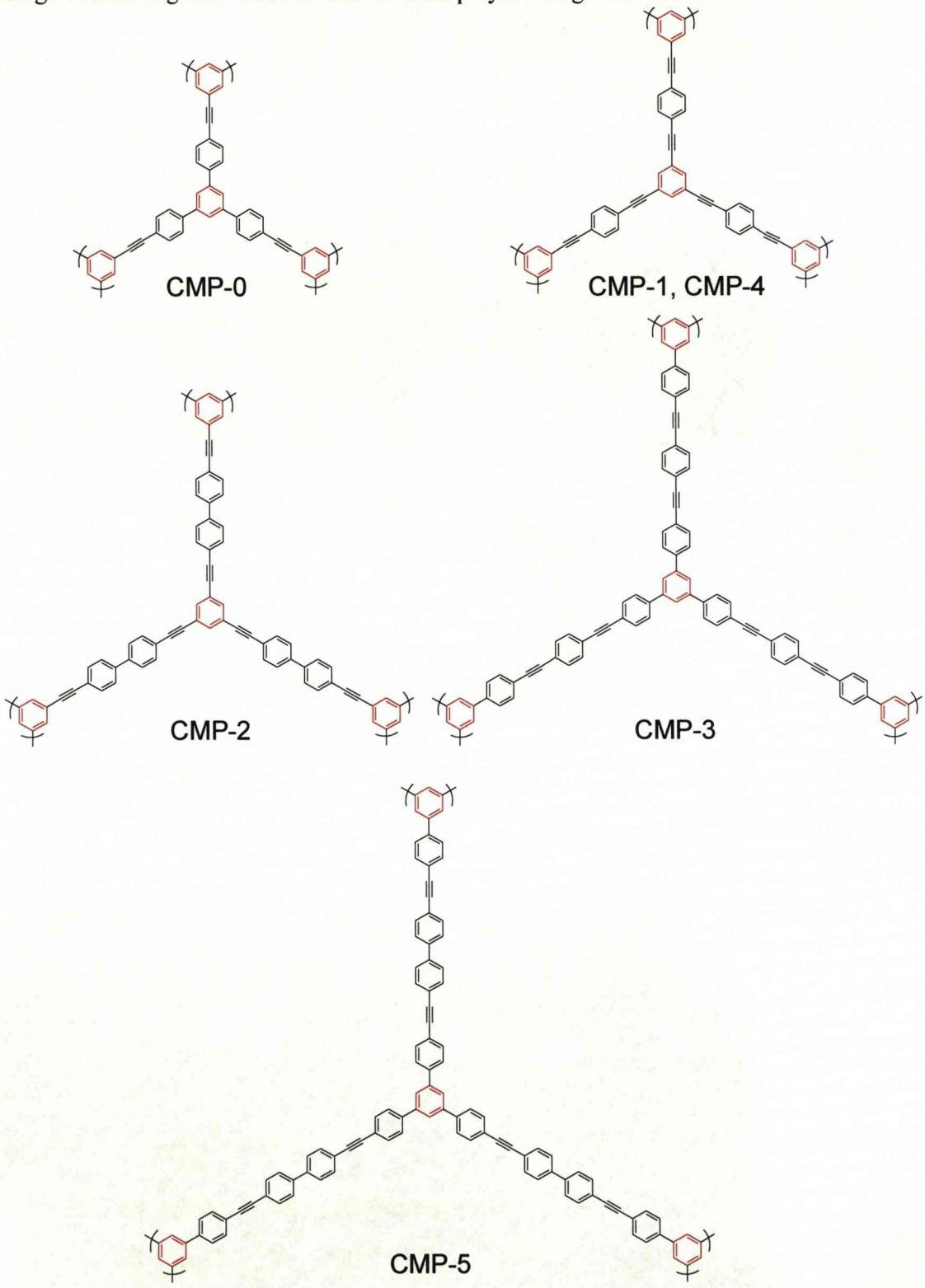

Scheme 8.1. Idealised molecular structures of Conjugated microporous polymer networks CMP-0 to 5. The average strut length is indicated by the distance of the aromatics shown in red.

The ability to control the micropore dimensions and surface area was also tested using copolymerization. While pore properties in MOFs and COFs have been varied systematically by changing the connecting ligands,[17,92,276-278] the structures are "quantized" in terms of the unit of variation – for example, the difference in length between ligands in a series of materials. As such, the gradations between structures in a series may be small but are nevertheless finite, and this strategy requires that each ligand in the series reacts in a similar way to form a stable, crystalline porous structure. Similarly, while MOF "copolymers" have been prepared using more than one connecting ligand,[279-281] the resulting physical properties of the materials are a result of the accessible thermodynamically-stable crystal structures and are not continuously variable as a function of the relative ligand ratio. By contrast, it should be possible to "tune" properties such as micropore size and surface area in amorphous PAE networks in a totally continuous fashion, such that the degree of fine control over these properties is limited only by the degree of inherent variability in the polymerization process itself. Therefore, a series of copolymer of 1,3,5-triethynylbenzene with 1,4-diiodobenzene and/or 4,4′-diiodobiphenyl (CPN-1–6; Table 8.2; Scheme 8.2) were prepared (by the group of Prof. A. I. Cooper). In principle, the average micropore size and surface area would be expected to increase systematically as the percentage of the shorter monomer strut, 1,4-diiodobenzene, is increased.

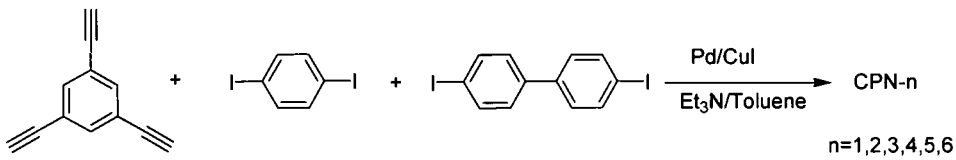

Scheme 8.2. Synthetic route of co-polymerization for CPN-1–6

Table 8.2. Textural properties of Copolymers with different molar ratios of two halogen monomers.

	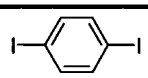	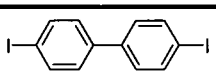	S_{BET} $(m^2/g)^a$	S_{micro} $(m^2/g)^b$	V_{total} $(cm^3/g)^c$	V_{micro} $(cm^3/g)^d$
CPN-1	100	0	856 (726)	665	0.53	0.32
CPN-2	80	20	775 (710)	584	0.42	0.31
CPN-3	60	40	757 (669)	580	0.39	0.30
CPN-4	40	60	749 (638)	576	0.40	0.29
CPN-5	20	80	722 (575)	526	0.39	0.29
CPN-6	0	100	643 (556)	504	0.46	0.25

[a] Surface area calculated from the N_2 adsorption isotherm using the BET method. Number in parentheses is the Langmuir surface area calculated from the H_2 adsorption isotherm by application of the Langmuir equation; [b]Micropore surface area calculated from the N_2 adsorption isotherm using t-plot method; [c]Total pore volume at $P/P_0 = 0.99$; [d]The micropore volume derived using the t-plot method based on the Halsey Thickness Equation.

8.2.2 Synthesis of NCMP networks

NCMP-0: 1,3,5-triethynylbenzene (450.5 mg), tris-(4-iodophenyl)amine (1246 mg), tetrakis-(triphenylphosphine)palladium(0) (35 mg), and copper(I) iodide (7 mg) were dissolved in the mixture of toluene (4 ml) and Et_3N (4 ml). The reaction mixture was heated to 80°C and stirred for 72 h under a nitrogen atmosphere (in order to rigorously exclude oxygen and to prevent any homocoupling of the alkyne monomers). The mixture was cooled to room temperature and the insoluble precipitated network polymer was recovered by filtration. Further purification of the polymer was carried out by Soxhlet extraction with methanol for 48 h. The product was dried in vacuum for 24 h at 70 °C and isolated as a fine light brown powder.[282]

Table 8.3. Monomer units of polymer networks and their textural properties.

polymer	Alkyne monomer	Halogen monomer	S_{BET} (m^2/g)[a]	S_{micro} (m^2/g)[b]	V_{total} (cm^3/g)[c]	V_{micro} (cm^3/g)[d]
NCMP-0	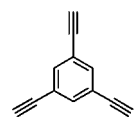	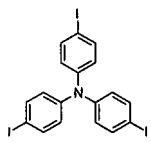	1108	825	0.60	0.51
NCMP-1	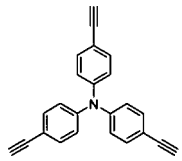	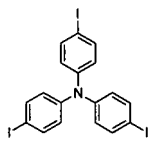	968	648	0.56	0.41
NCMP-2	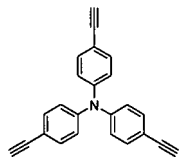	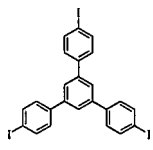	900	586	0.55	0.32
NCMP-3	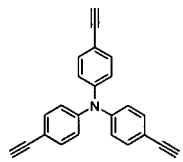	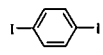	866	559	0.50	0.31
NCMP-4	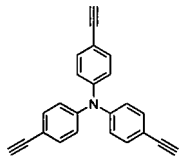	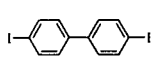	546	327	0.35	0.20

[a]Surface area calculated from the N_2 adsorption isotherm using the BET method. [b]Micropore surface area calculated from the N_2 adsorption isotherm using t-plot method. [c]Total pore volume at $P/P_0 = 0.99$. [d]The micropore volume derived using the t-plot method based on the Halsey Thickness Equation.

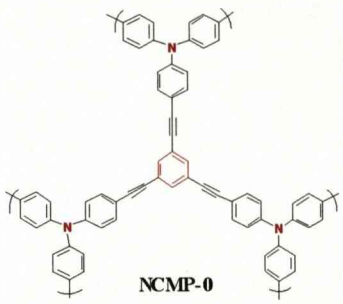

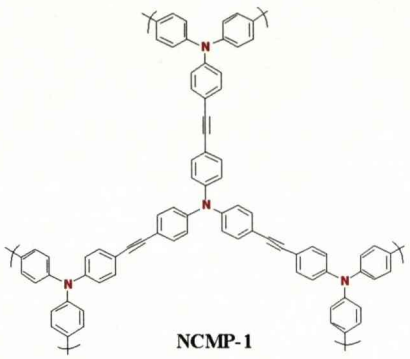

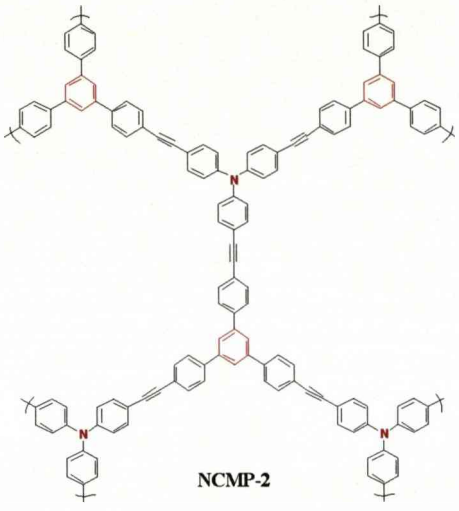

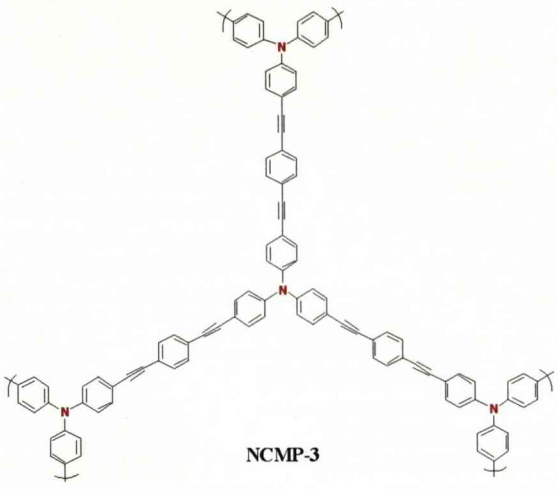

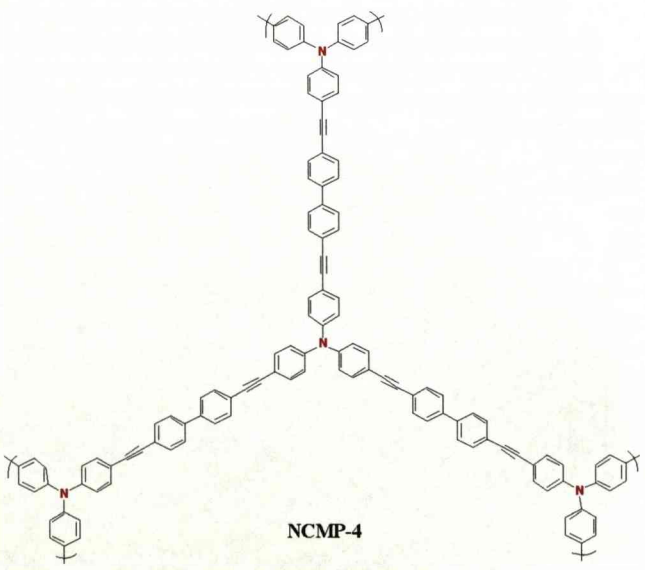

Scheme 8.3. Representative molecular structures for networks NCMP-0–4. The nitrogen and benzene "nodes" in the networks (derived from the trifunctional A_3 or B_3 monomer in each case) are shown in red.

8.2.3. Microporous Poly(aryleneethynylene) Networks using Tetrahedral Carbon- and Silicon-Centred Monomers

Synthesis of E1 and E2: Tetrakis(4-Iodophenyl)methane (1.0 mmol) , 1,4-diethynylbenzene (3.0 mmol) or 1,3,5-triethynylbenzene (2.0mmol), $Pd(PPh_3)_2Cl_2$ (60 mg) and CuI (18 mg) were suspended in a mixture of anhydrous toluene (2.5 mL) and diisopropylamine (2.5 mL). After degassing the mixture was heated to 90 °C under N_2 for 24 h. After cooling to room temperature the polymer was washed excessively with methanol and acetone and soxhlet extracted with methanol overnight. The porous material was dried in a vacuum oven for 24 hours at 60 °C.

Synthesis of E3 and E4: Tetrakis(4-bromophenyl)silane (2.0 mmol), 1,4-diethynylbenzene (6.0 mmol) or 1,3,5-triethynylbenzene (4 mmol), $Pd(PPh_3)_2Cl_2$ (100 mg) and CuI (30 mg) were suspended in a mixture of anhydrous toluene (2.5 ml) and anhydrous triethylamine (2.5 ml). After degassing three times, the mixture was heated to 90 °C under N_2 for 24 h. After cooling to room temperature, the product was washed with THF, water, aqueous hydrochloric acid, water, ethanol and acetone (Again all polymers were provided by the group of prof. A. I. Cooper).[20]

Table 8.3. Textural properties of the tetrahedral networks prepared using Sonogashira-Hagihara coupling.

	Halogen Monomer	Ethynyl Monomer	S_{BET} (m^2/g)	S_{micro} (m^2/g)	V_{micro} (cm^3/g)	V_{total} (cm^3/g)
E1	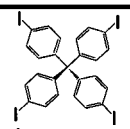	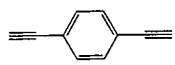	1213 (1618)	834	0.40	0.65
E2	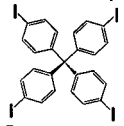	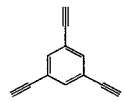	488 (649)	430	0.21	0.22
E3	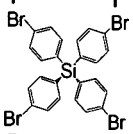	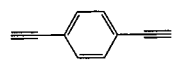	1093 (1486)	311	0.07	1.42
E4	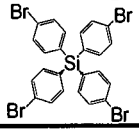	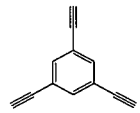	925 (1256)	85	0.18	0.95

8.3. Structural properties

8.3.1 Gas adsorption of the CMP and CPN networks

The CMP networks (Fig. 8.1a) display type I N_2 adsorption-desorption isotherms (according to IUPAC classification) confirming their microporosity.[1] The isotherms of both CMP-3 and CMP-5 show a rise in N_2 uptake at high relative pressure indicative of inter-particle porosity similar to that observed for meso- and macroporous solids. The apparent BET surface area, micropore and total pore volume (Fig 8.1c) are decreased with increasing strut length. On the other hand, the micropore diameter increases with strut length (indicated by the blue arrow in figure 8.1b). The observations confirm the ability to control the microporous properties synthetically by varying strut length.

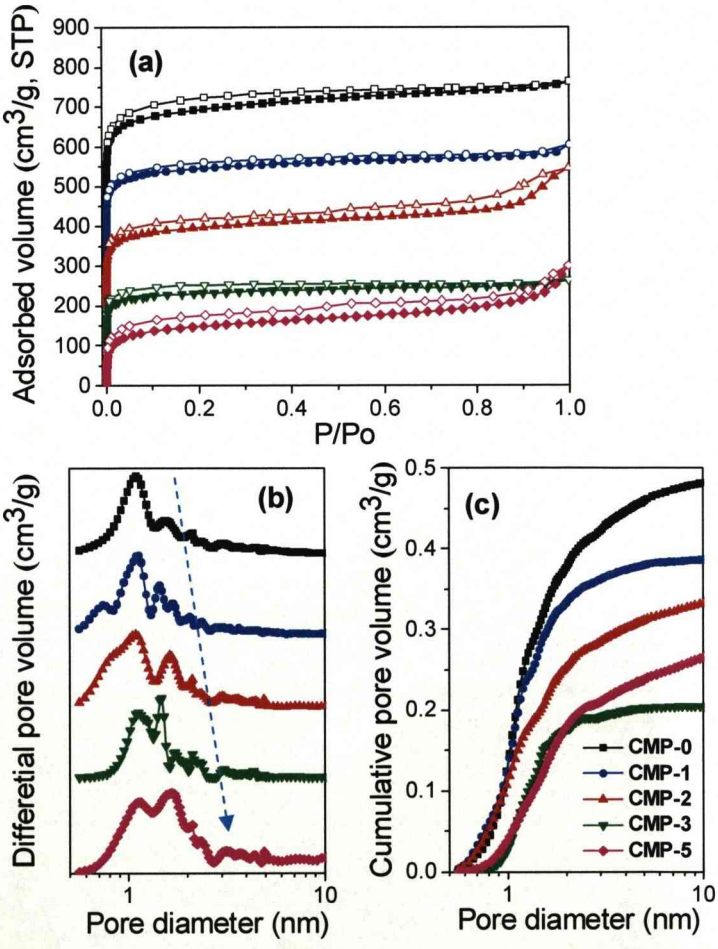

Figure 8.1. (a) N_2 adsorption-desorption isotherms of CMP-0, CMP-1, CMP-2, CMP-3 and CMP-5. (b) NL-DFT pore size distribution curves; the dashed arrow indicates the shift to larger average pore size in this series. (c) Cumulative pore volume curve calculated by application of NL-DFT.

Figure 8.2a shows the N_2 adsorption/desorption isotherms for the CPN networks. All of the copolymers gave rise to Type I isotherms indicating that the materials are microporous and the BET surface areas decrease from 856 m^2/g for CPN-1 to 643 m^2/g for CPN-6. The micropore size distribution is shifted to larger pore diameters for the series of networks from CPN-1 to CPN-6 as the ratio of the longer strut monomer, 4,4′-diiodobiphenyl, increases (Fig. 8.2b). This is also confirmed by the cumulative pore volume plots for these networks (Fig. 8.2c). Even though the changes in the cumulative curves are small (particularly for CPN2 – CPN4), the shift is systematic and all six curves fall in the predicted order. These observations confirm the continuous synthetic variation that can be achieved in terms of micropore size and surface area for conjugated microporous polymers.

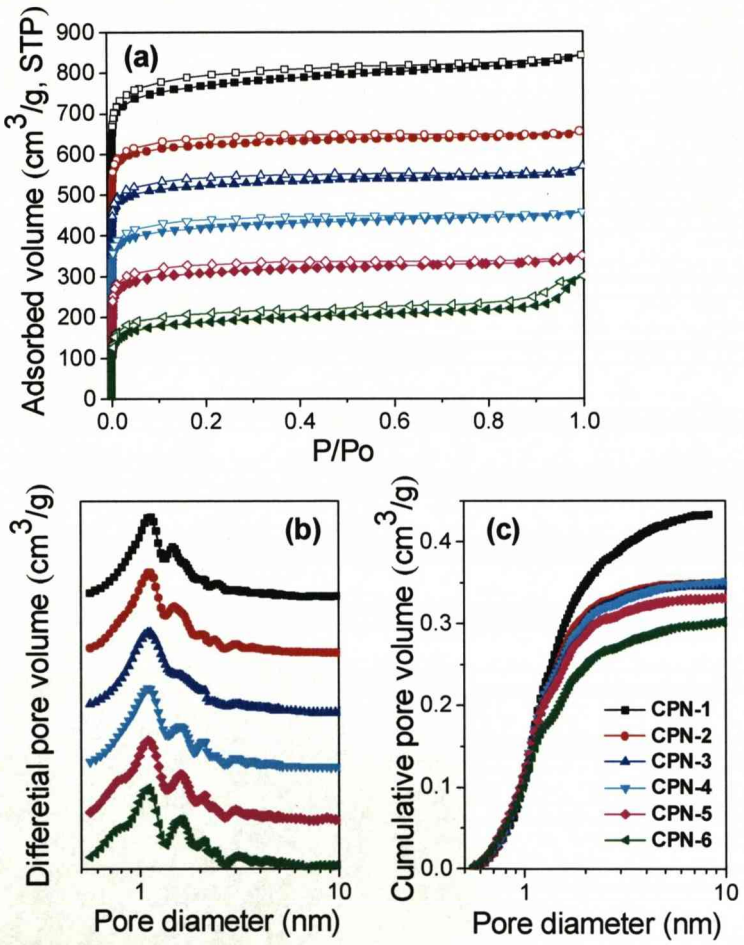

Figure 8.2. (a) N_2 adsorption-desorption isotherms measured at 77.3 K (adsorption branch is labeled with filled symbols and desorption is labelled with empty). For clarity, the isotherms of CPN-1, CPN-2, CPN-3, CPN-4, and CPN-5 are offset along the Y-axis by 100 cm^3/g. (b) Pore size distribution curves. (c) NL-DFT cumulative pore volume curve.

8.3.2 Gas adsorption of the NCMP networks

The N_2 isotherms for the NCMP networks can be classified as Type I isotherms (Fig. 8.3a) indicating that all of the networks are microporous. The surface area for these networks varied between 546 m^2/g (NCMP-4) and 1108 m^2/g (NCMP-0). In general, the micropore size distribution is shifted systematically to larger pore diameters for the series as the monomer strut length is increased whilst the overall micropore volume also falls over this series (Table 8.3). This is also illustrated by NL-DFT cumulative pore volume plots for the five networks (Fig. 8.3c). These observations are consistent with those described for the CMP networks.

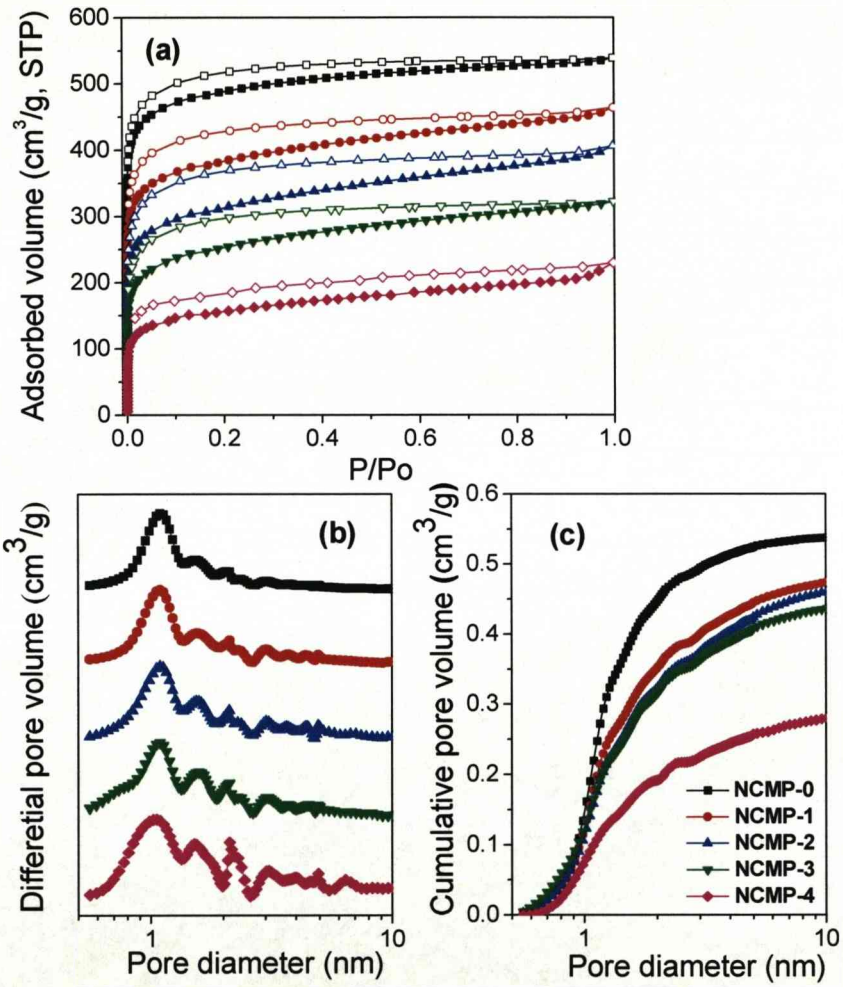

Figure 8.3. (a) N_2 adsorption-desorption isotherms (for clarity, the isotherms of NCMP-0, NCMP-1, and NCMP-2 were shifted vertically by 150, 100 and 50 cm^3/g, respectively). (b) NL-DFT pore size distribution curves. (c) Cumulative pore volume curve calculated by application of NL-DFT.

8.3.3 Gas adsorption of the tetrahedral networks

The N_2 adsorption/desorption isotherms for E1 and E2 are, as with all the polymers thus far, Type I isotherms and show very flat sorption plateaus similar to crystalline COFs (*e.g.*, COF-1),[92,265] and consistent with a microporous material. No hysteresis was observed upon desorption. E1 has a BET surface area of 1212 m^2/g (and a narrow PSD curve peaking at around 1.1 nm) which is larger than any achieved previously using similar Pd coupling chemistry[262,283,284] or organolithiation routes[285,286] and also one of the highest BET surface area reported for a PIM network (1064 m^2/g).[287] The N_2 sorption isotherms for the equivalent Si-containing networks (E3 and E4) showed both Type I and Type IV character and displayed pronounced pore filling (up to approximately 900 cm^3/g for E3) at high relative pressures, as well as some hysteresis upon desorption (Fig. 8.4). For the Si-containing networks (E3 and E4), the N_2 isotherms differed substantially at higher relative pressures (Fig. 8.4). The rise in the N_2 uptake at $P/P_0 > 0.8$ in the adsorption isotherms may arise in part from interparticulate porosity associated with the meso- and macrostructures of the samples. This is consistent with the presence of larger pores (mesopores or small macropores) and indeed micropore volumes were relatively low for both networks despite high S_{BET} values.

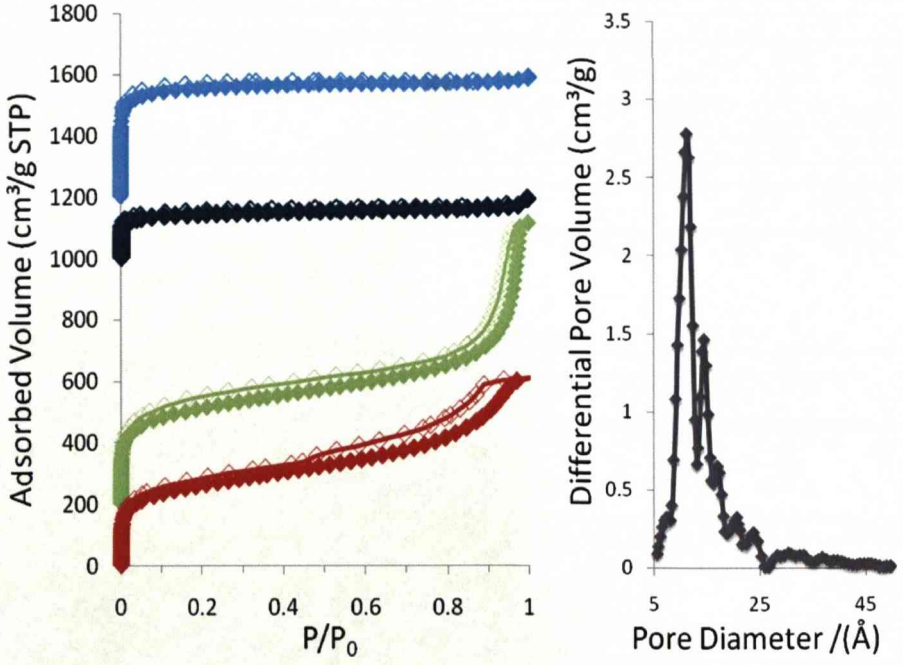

Figure 8.4. (Left) N_2 adsorption-desorption isotherms for E1 (blue), E2 (black), E3 (green) and E4(red). The isotherms for E1, E2 and E3 are shited vertically by 1200, 1000 and 200 cm^3/g, respectively. (Right) NL-DFT pore size distribution curve for E1.

8.3.4 Atomistic simulations of CMP networks

The atomistic simulations were used to build fragment models for each CMP network and assist in explaining the origin of their microporous nature. The simulations of CMP-0, CMP-1 and CMP-5 (Fig. 8.5) indicate the 3-D structures to arise from the bending of the struts out of plane from the benzene nodes (as seen for CMP-1, fig. 8.5a centre) and from bending of the struts themselves (Fig. 8.5a right). The deviation of in-plane and out of plane bond angles from 120° imposed by 1,3,5-substituted node geometry is dependent on the strut length. In general the deviation from 120° is greater with increasing strut length with the exception of CMP-0 where the presence of the 1,3,5 triphenylbenzene node leads to a broader range than that of CMP-1.

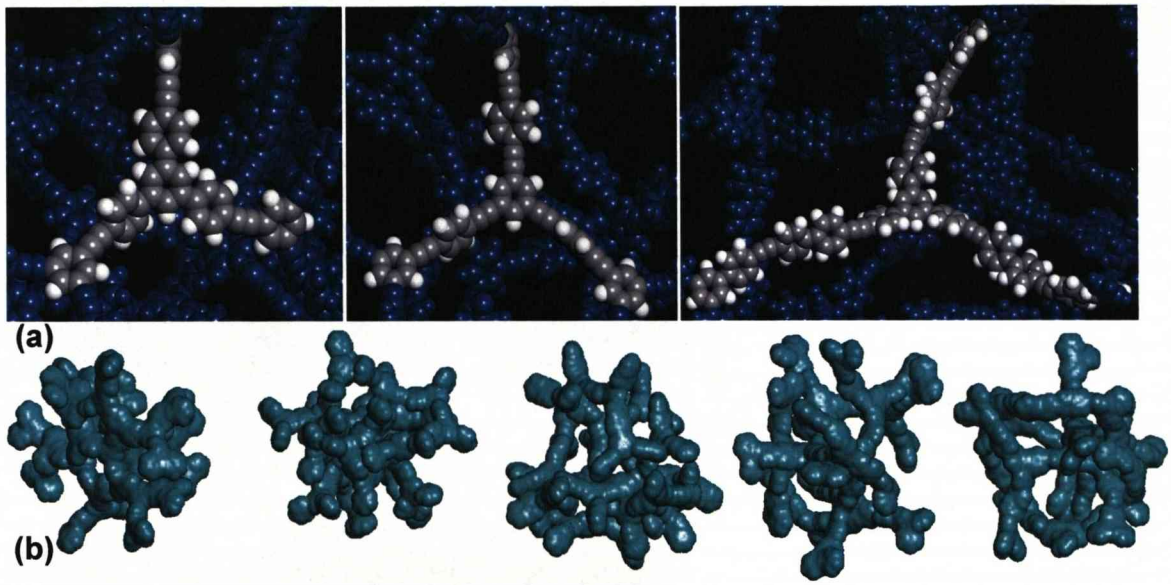

Figure 8.5. Atomistic simulations for PAE networks with different strut lengths. (a) Node-strut topology for simulated network fragments for CMP-0 (left), CMP-1 (centre), and CMP-5 (right). A single 1,3,5-connected benzene node connecting three other nodes via rigid struts is highlighted (in grey/white) in each case. (b) Atomistic simulations of network fragments for CMP-0, CMP-1, CMP-2, CMP-3, and CMP-5 (left to right). Each model was built to have an average number molecular weight in the range 11120−11210 g/mol.

The fragment models of the CMP networks (Fig. 8.5b) also indicate the average cluster size is increased with increasing strut length. With increasing strut length resulting in increased conformational freedom in the models this allows for greater *intramolecular intercalation* and space filling within the fragments. The increased space filling is consistent with a reduction in micropore pore volume (Table 8.1) as strut length is increased.

In summary, from the structural characterisation of both the CMP and NCMP networks it is clear that increasing the strut length increases the pore diameters and conformational freedom. On the other hand, the increased conformational freedom allows greater intramolecular intercalation thus reducing the micropore volumes with increasing strut length. Both of the afore mentioned properties should influence the mobility of the aromatic and acetyl functionalities on a molecular level which can only be assessed using solid-state NMR.

8.4 Solid-state NMR of conjugated porous networks

8.4.1 CMP and CPN networks

^{1}H-^{13}C CP/MAS NMR (Fig. 8.6) provided information on the molecular level environments present in the conjugated polymer networks (the assignment of the resonances is indicated in the figure). The low intensity resonances observed at *ca.* 76 and 82 ppm correspond to -C≡CH end groups (the line at 82 ppm being the quaternary acetylene carbons). The end group content was found to be lower in the polymers produced from 1,4-ethynylbenzene (CMP-3) and 4,4′-diiodobiphenyl (CMP-5), possibly because these longer struts (see table 8.1 and scheme 8.1) give rise to a greater degree of overall conformational freedom and this allows higher levels of conjugation (*i.e.* fewer un-reacted end groups) in the resulting network. CMP-1 also shows low end-group content *c.f.* to CMP-0 and CMP-2. The structure of CMP-1 relies on the smallest halogen monomer (1,4-diiodobenzene) most probably reducing steric hindrance during synthesis.

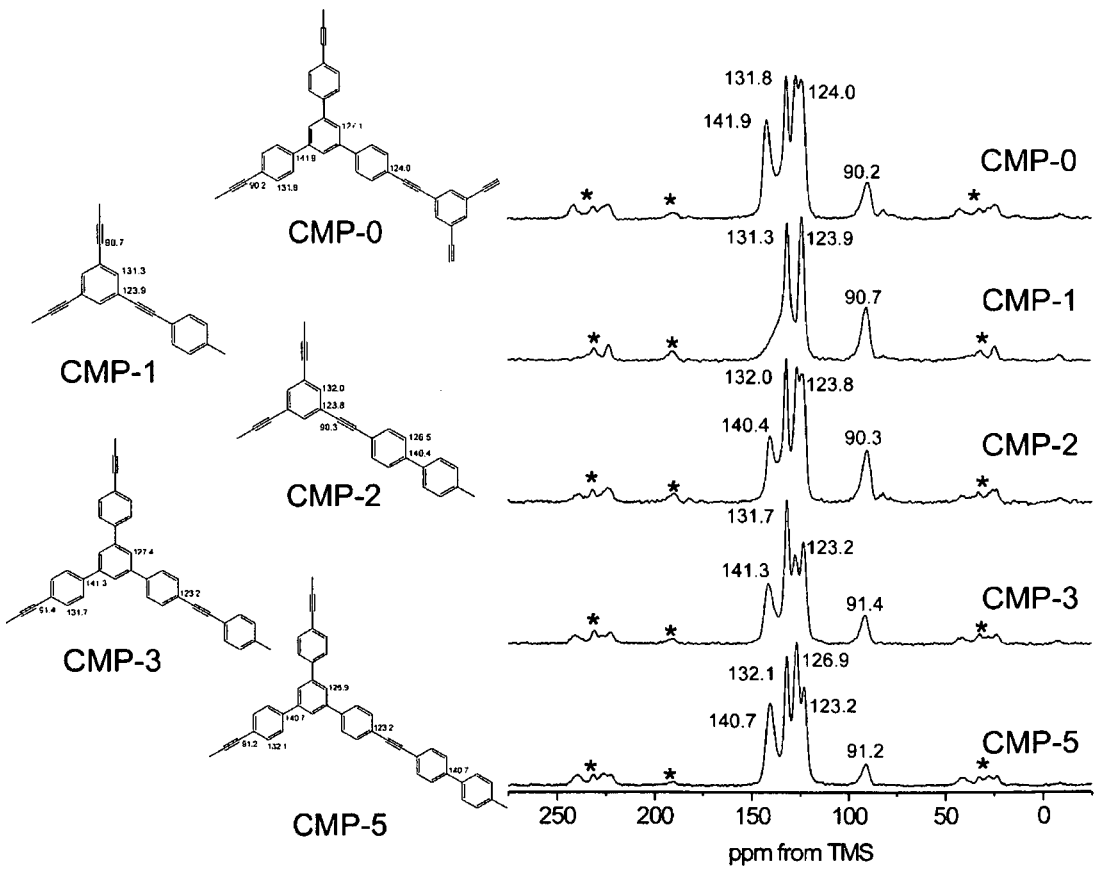

Figure 8.6. ^{1}H-^{13}C CP/MAS NMR spectra of the conjugated microporous PAE networks. Asterisks (*) denote spinning sidebands.

The ratio of peak areas of the acetylenic and aromatic peaks was calculated using Gaussian deconvolution of $^{13}C\{^{1}H\}$ MAS NMR spectra (Fig. 8.7) as follows: CMP-0: 0.16 (expected value 0.18); CMP-1: 0.31 (expected value 0.40); CMP-2: 0.18 (expected value 0.25); CMP-3: 0.15 (expected value 0.18); CMP-5: 0.12 (expected value 0.14). The addition of an extra resonance at *ca.* 135 ppm in the deconvoluted spectra for CMP-0 to CMP-3 was required to take into account un-reacted terminal Iodine aromatic α-CH functionalities. The spectrum of CMP-5 was simulated without an addition of the line at ca. 135 ppm. This is consistent with CMP-5 to show the most efficient linking due to conformational freedom thus containing the fewest amounts of un-reacted end groups.

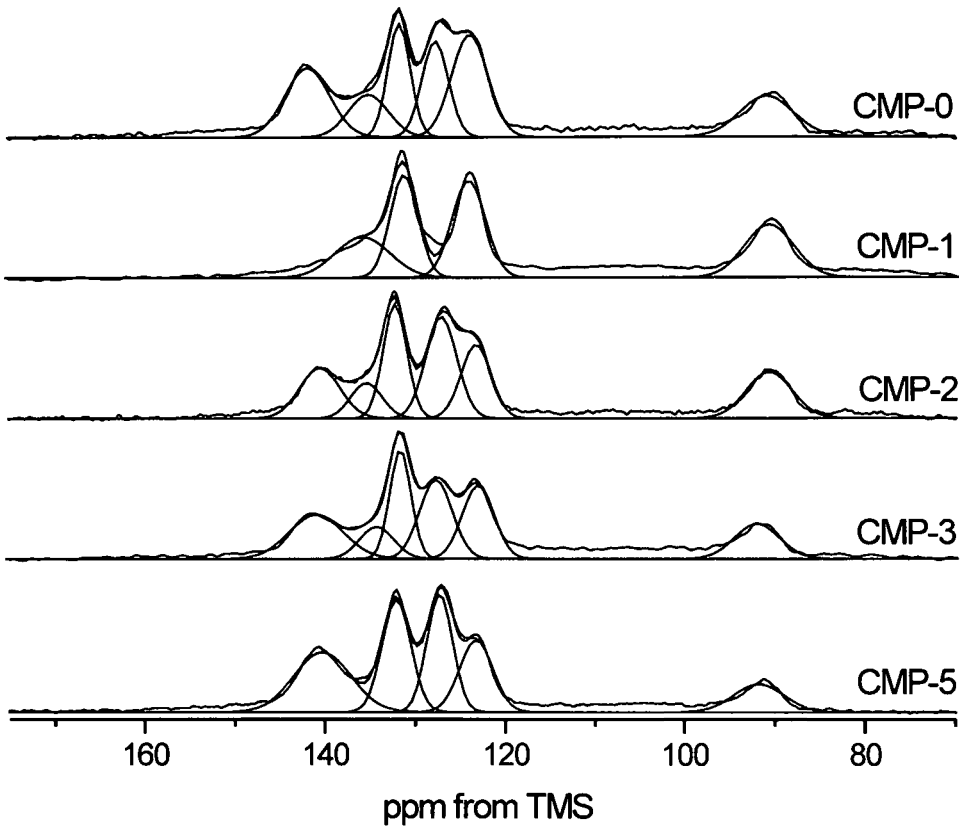

Figure 8.7. $^{13}C\{^{1}H\}$ MAS NMR spectra (deconvoluted using a Gaussian function) of the conjugated microporous PAE networks.

The ^{1}H-^{13}C CP/MAS NMR spectra for the CPN networks (fig. 8.8) confirmed the presence of two different types of building units in the copolymers. The intensity of the peaks at 140.4 and 126.1 ppm, which are characteristic of the 4,4'-diiodobiphenyl monomer, increased systematically with its content in the initial monomer feed. The NMR spectra also confirm the two comonomers had similar reactivates.

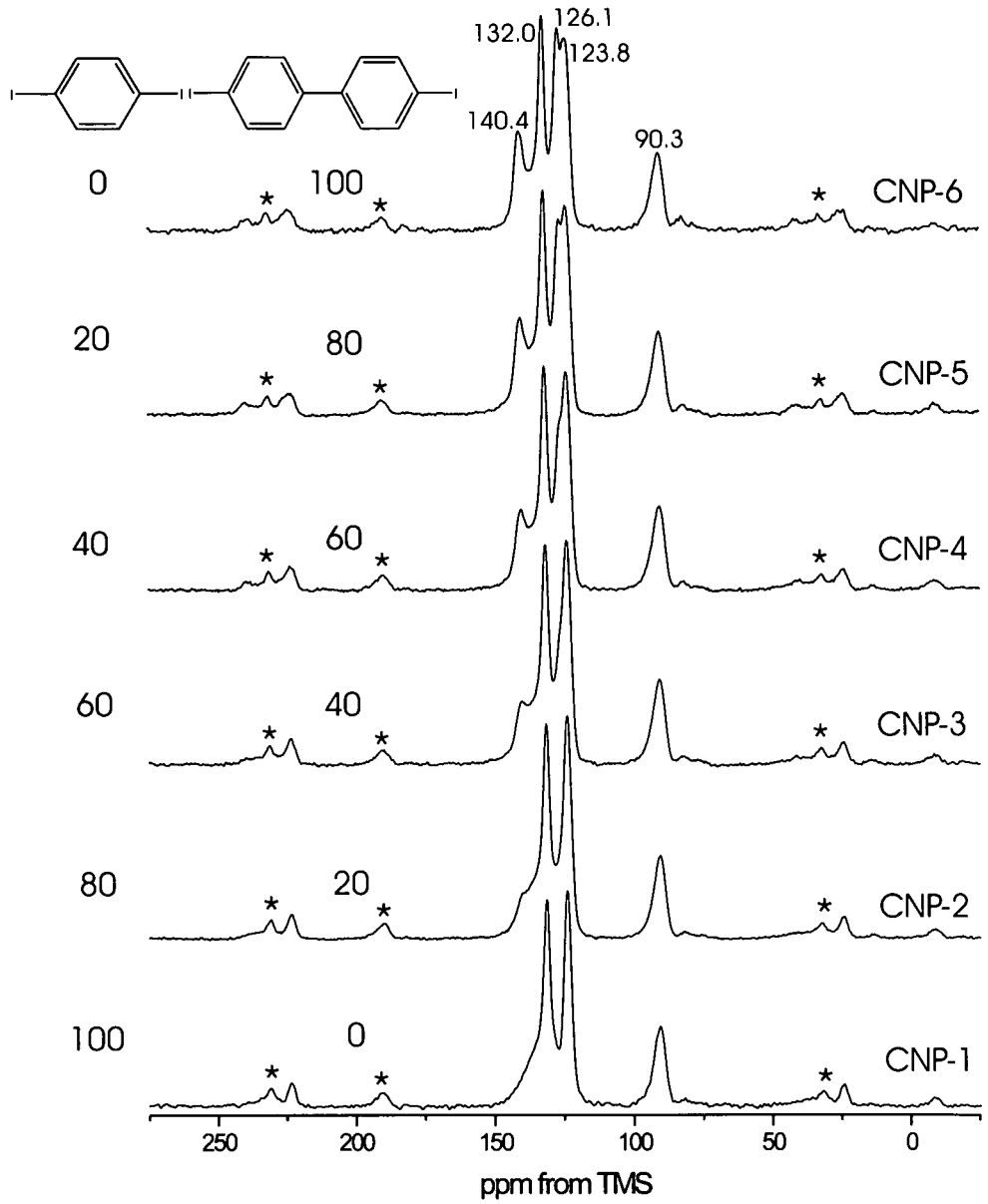

Figure 8.8. ^{1}H-^{13}C CP/MAS NMR spectra of the CPN networks as a function of comonomer concentration. Asterisks (*) denote spinning sidebands.

8.4.2. NCMP networks

Due to the presence of nitrogen in their frameworks, ^{1}H-^{13}C CP/MAS NMR spectra (Fig. 8.9) of the microporous NCMP polymer networks are more complex than the for CMP materials. However, resonances due to *tris*-(phenylethynylene)amine units and aryleneethynylene units which do not bear the nitrogen atoms are easily distinguished.

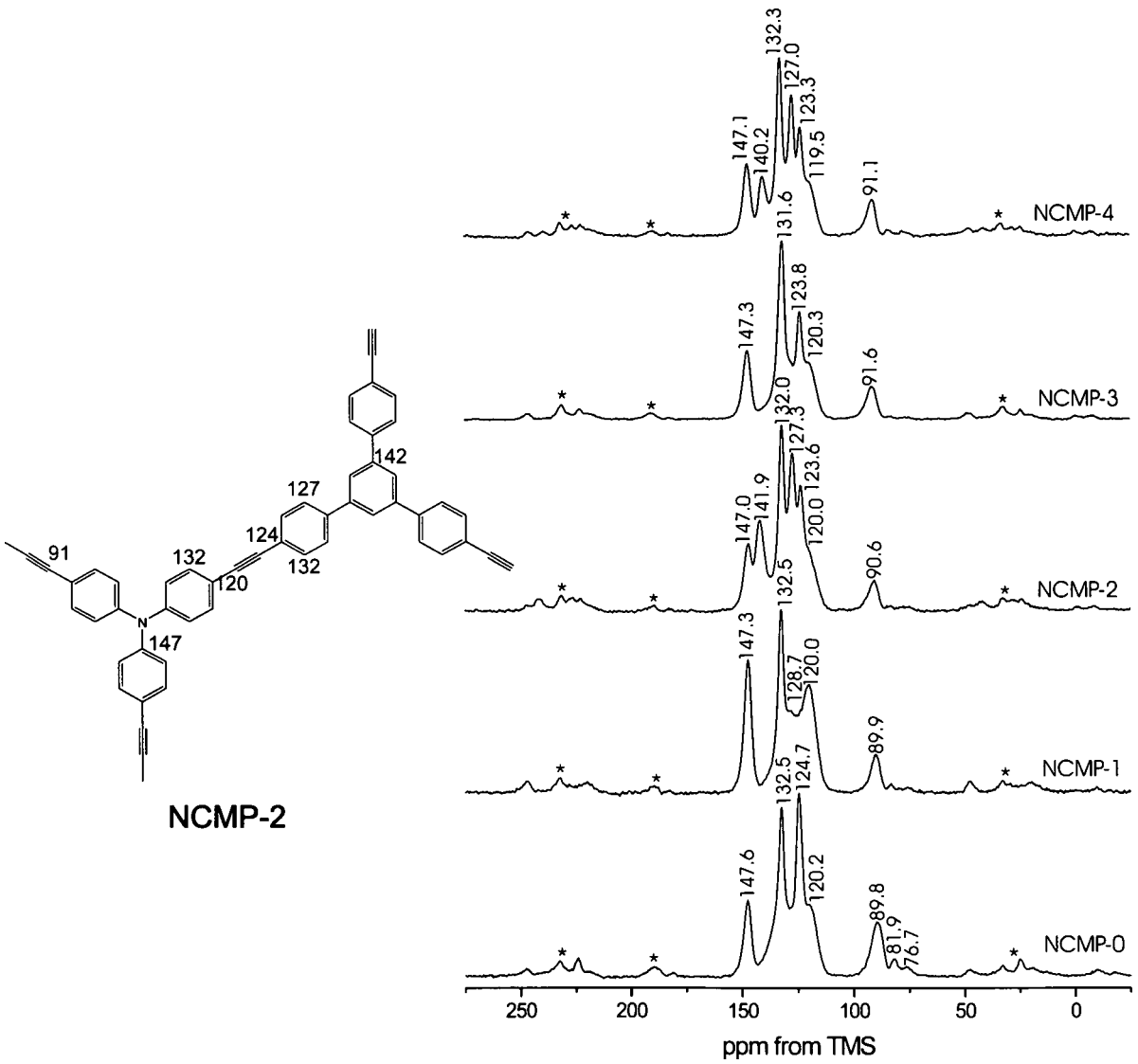

Figure 8.9. ^{1}H-^{13}C CP/MAS NMR spectra of networks NCMP-0–4 with the resonance assignment shown for NCMP-2, which contains all possible carbon environments hence the most complex NMR spectrum. Asterisks denote spinning sidebands.

The assignment of the resonances is consistent with that for the CMP networks and was confirmed by $^{13}C\{^{1}H\}$ MAS NMR spectra and ^{1}H-^{13}C CP/MAS NMR kinetics. Ethynylene C_{ar}–**C≡C**-C_{ar} units are observed at *ca.* 90 ppm and the low intensity resonances at *ca.* 76 and

82 ppm can be ascribed to the -C≡CH end groups as seen in the CMP networks. The content of these end groups was the highest for NCMP-0 network, but does not exceed *ca.* 15 % even for this network. The quaternary N-$\mathbf{C}_{ar}$ sites exhibit a peak at *ca.* 147 ppm. The $\mathbf{C}_{ar}$-C≡C sites for *tris*-(phenylethynylene)amine blocks are observed at *ca.* 120 ppm. These sites are observed for all five of the PTEA networks. The –$\mathbf{C}_{ar}$-$\mathbf{C}_{ar}$- linkages in NCMP-2 and NCMP-4 are observed at *ca.* 141 ppm. The lines at *ca.* 127 ppm in these networks originate from the H-C_{ar}- sites in the aromatic rings *not* connected with nitrogen. The -C≡C-$\mathbf{C}_{ar}$ sites in such benzene rings are observed at *ca.* 124 ppm. The ratios of the intensities of the acetylenic and aromatic peaks were calculated using the $^{13}C\{^1H\}$ MAS NMR spectra are as follows: NCMP-0, 0.23 (expected value 0.25); NCMP-1, 0.11 (expected value 0.17); NCMP-2, 0.12 (expected value 0.14); NCMP-3, 0.18 (expected value 0.22); NCMP-4, 0.12 (expected value 0.17).

8.4.3. Tetrahedral networks

^1H-^{13}C CP/MAS NMR spectra of the tetrahedral polymers are displayed in figure 8.10. Minor resonances at *ca.* 76 and 84 ppm are due to the terminal –C≡CH functionalities. A shoulder resonance at *ca.* 137 ppm can be ascribed to the C-H aromatic carbons arising from unreacted $-C_6H_4I$ moieties (approx. 7 wt. % I in network E1 by EDX). Similar results were obtained for the Si-containing networks, E3 and E4, which also showed the presence of two additional resonances at 12.8 and 26.5 ppm attributable to Si-CH_2CH_3 sites. The ^1H-^{29}Si CP/MAS NMR spectra of E3 and E4 corroborated this; the major peak at –15.2 ppm corresponds to Si(*p*-$C_6H_4)_4$ units which can be compared with the spectrum of the pure Si(p-$C_6H_4Br)_4$ monomer which showed only one resonance at *ca.* –15 ppm. This also agrees with previous NMR measurements for microporous EOFs.[285] We assign the minor resonance at -10.1 ppm to Si(C_2H_5)(*p*-$C_6H_4)_3$ in agreement with the ^1H-^{13}C CP/MAS NMR spectra. This peak was *not* observed when the silane monomer was treated with amine and Pd-catalyst in the absence of alkyne monomer; as such, we ascribe this to some as yet unidentified cross-coupling side reaction involving the base, NEt_3 (the only conceivable ethyl source that is presence in the reaction mixture). No comparable alkyl peaks were observed in the ^1H-^{13}C CP/MAS NMR spectra of the TPM-based networks, E1 and E2.

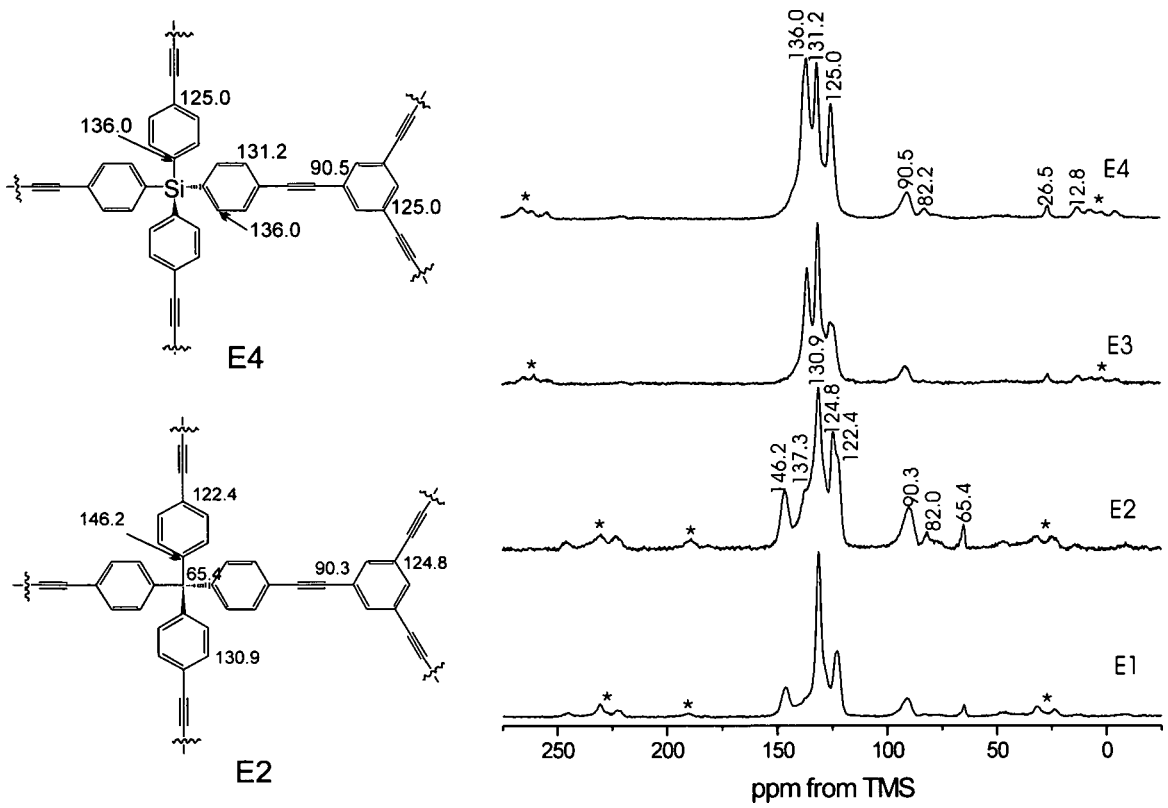

Figure 8.10. ^{1}H-^{13}C CP/MAS NMR spectra of the tetrahedral polymers. The spectra for E1 and E2 were recorded at 10 kHz whilst those for E3 and E4 were recorded at an MAS rate of 13 kHz in order to unmask additional resonances from spinning sidebands indicated by the asterisks (*).

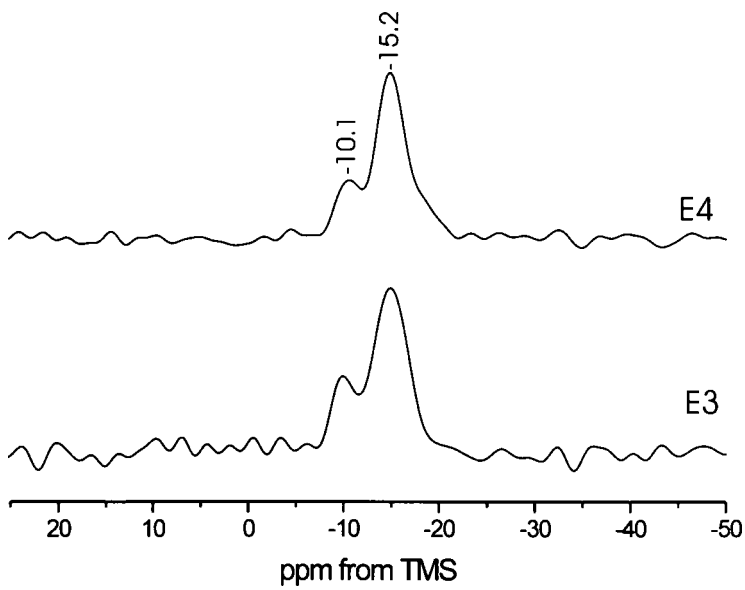

Figure 8.11. ^{1}H-^{29}Si CP/MAS NMR spectra of tetrahedral polymer networks containing silicon centres.

8.5. ^{1}H-^{13}C CP/MAS NMR kinetics

^{1}H-^{13}C CP/MAS kinetics has been used to study the effect of polymer strut length on the mobility of the aromatic proton environments and to confirm the peak assignments proposed for the 1D ^{13}C CP/MAS spectra.

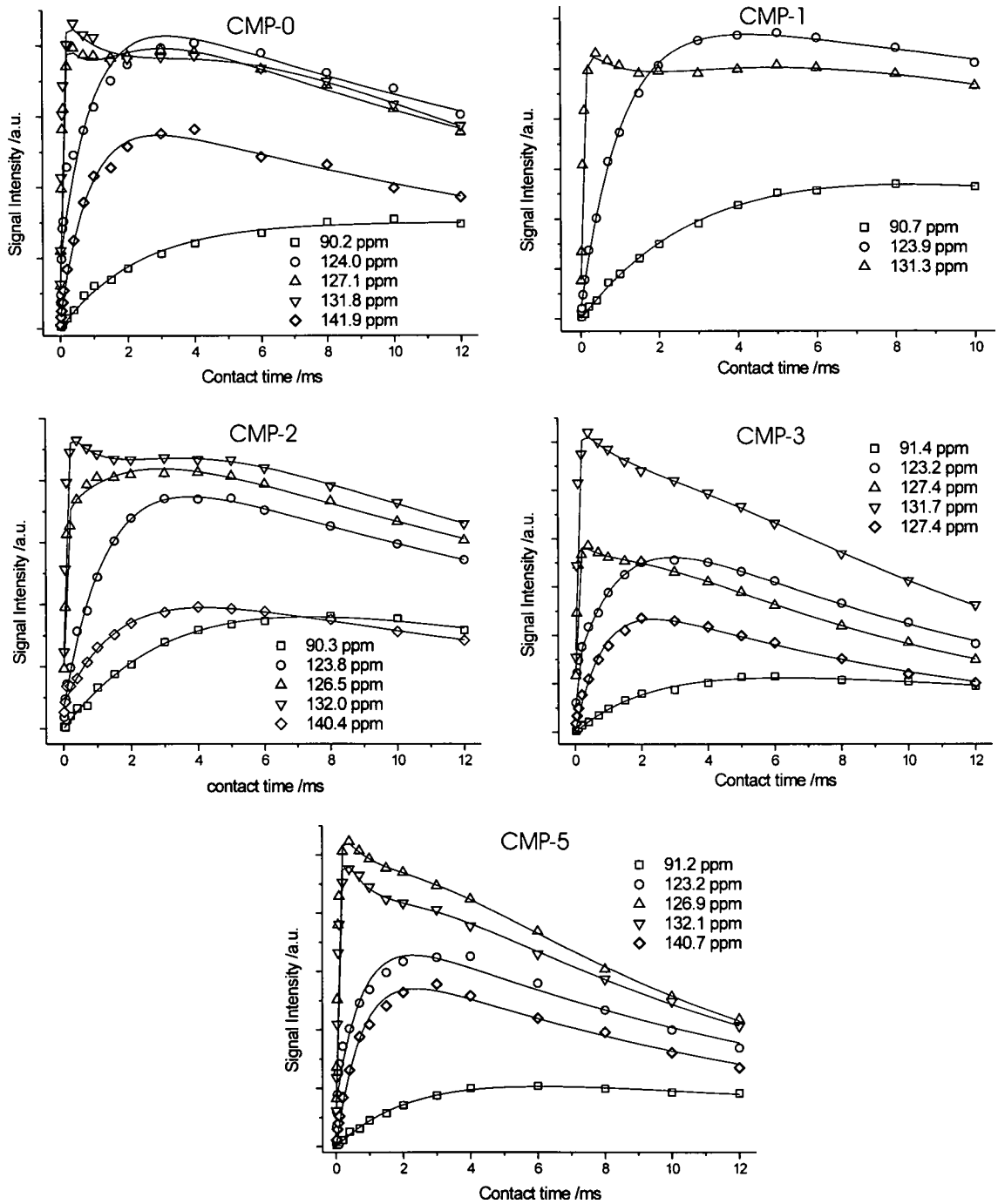

Figure 8.12. ^{1}H-^{13}C CP/MAS kinetics curves of the conjugated microporous PAE networks.

The ^{1}H-^{13}C CP/MAS kinetics curves and fitting parameters (Fig. 8.12 and Table 8.3 respectively) of the CMP networks highlight significant differences between the various aromatic sites. The CP kinetics of the terminal halide and acetyl environments were omitted due to their low population and poor resolution in the CP/MAS spectra. Most notably, both quaternary aromatic carbon environments at *ca.* 124 and 141 ppm in all CMP networks only gave satisfactory results when using a more complex I-I*-S model which accounts for ^{1}H spin diffusion influencing the CP kinetics.[154] All other resonances follow the I-S model. The protonated aromatic carbon sites at *ca.* 126 and 131 ppm show unusual CP kinetics and satisfactory fittings were obtained when two separate T_{IS} and $T_{1\rho}^{H}$ components were considered. The acetylenyl resonance at *ca.* 90 ppm in all CMP networks shows slow T_{IS} times consistent with a carbon environment with no directly attached protons.

The quaternary aromatic carbon environments fitted using the I-I*-S model show high λ values in the region of 0.70 to 0.95. These observation are consistent with previous reports on the CP kinetics of such resonances.[154] The proton spin diffusion times, T_{df}, of both sites remain similar within the same polymer framework, *i.e.* in CMP-5 both resonances at 123.2 and 140.7 ppm show T_{df} times of *ca.* 0.8 ms. This is to be expected as the strength of the ^{1}H homonuclear dipolar coupled network that influences T_{df} will be similar across the entire polymer network whereas slight fluctuations will relate to changes in mobility. The same trend is apparent for the $T_{1\rho}^{H}$ times measured for different aromatic sites in the same microporous network. Changes in T_{df} as a function of conformational freedom for the quaternary aromatic sites bound to the acetylene functionality at *ca.* 124 ppm are also seen. In general, the T_{df} time is increased with conformational freedom about the 1,3,5-substituted node geometry, with the exception of CMP-5. The T_{df} times will be influenced by the strut length, conformational freedom and intramolecular intercalation in that, as strut length increases one would expect T_{df} time to increase due to a mobility induced reduction of ^{1}H-^{1}H homonuclear dipolar couplings. However, the increased intramolecular chalation with increasing strut length would result in a decrease in T_{df} times due to increased rigidity caused by the filling of the pores with polymer and hence higher density of protons. Therefore, the unusual effect observed for CMP-5 is due to the influence of intramolecular intercalation on T_{df} being greater than that of strut length and conformational freedom. The $T_{1\rho}^{H}$ times of the same resonance also follow a similar trend in that they decrease with increasing of conformational freedom with the exception of CMP-5. The quaternary aromatic resonance at *ca.* 141 ppm corresponding to the Ar-Ar linkage shows a similar trend to that of the resonance at *ca.* 124 ppm.

The CP kinetics of the protonated aromatic environments suggest the presence of fast and slow CP 'build up', short and long proton relaxation times present within the same functionality. The CP time constant, T_{IS} of the slow component for all polymers is generally increased from the resonance at *ca.* 126 to 131 ppm again with the anomaly of CMP-5 in which the trend is slightly reversed. The increase in T_{IS} times may be explained as the resonance at *ca.* 131 ppm results from aromatic-CH environments *ortho* to the acetylene aromatic substituent whereas, the resonance at ca. 126 ppm is always *ortho* to another aromatic ring, thus closer to other ^1H 'CP donors'. The T_{IS} of the 'fast' component remains similar for all protonated aromatics with values in the region of 0.5 - 0.7 ms which is to be expected as the C-H aromatic heteronuclear dipolar couplings would remain fairly constant. These observations suggest that the fast CP build up arises from the magnetization transfer from directly attached protons and the slower CP build up is a result of through space dipolar coupling and ^1H spin diffusion throughout the polymer matrix. The fact that CP kinetics of the resonance does not comply with the I-I*-S model would indicate that other factors, such as mobility and orientation may still influence the CP behaviour.

Overall, the CP kinetics of the CMP polymer networks is complex due to the highly conjugated structure and amorphous nature. However, the CP kinetics has enabled the complete assignment of all carbon environments and highlighted differences in mobility which could be correlated with the strut length, conformational freedom, intramolecular chalation and location of functionalities within the molecular structure *i.e.* aromatic groups in the node and strut. In general, with increasing conformational freedom and/or strut length $T_{1\rho}^{H}$ times were decreased suggesting a decrease in proton mobility. This is consistent with the N_2 adsorption data in that the micropore volume decreased due to increased intramolecular interchalation which in turn would decrease proton mobility.

Table 8.3. ^{1}H-^{13}C CP/MAS kinetics parameters derived from the classical I-S or I-I*-S model

^{13}C Site /ppm		T_{IS} / ms	T_{df} / ms	λ	$T_{1\rho}^{H}$ / ms	R^2
CMP-0						
90.2		2.28 ±0.315	//	//	>50	0.994
124.1		//	1.30 ±0.264	0.681 ±0.029	28.0 ±3.27	0.988
126.8	Fast	0.066 ±0.002	//	//	0.780 ±0.019	0.996
	Slow	1.14 ±0.051			22.6 ±1.84	
131.8	Fast	0.064 ±0.003	//	//	1.37 ±0.053	0.995
	Slow	1.98 ±0.147			20.7±3.02	
141.6		//	0.919 ±0.089	0.958 ±0.014	21.6 ±2.71	0.993
CMP-1						
90.7		3.01 ±0.085	//	//	>50	0.999
123.9		//	1.10 ±0.052	0.969 ±0.007	>50	0.999
131.3	Fast	0.065 ±0.003	//	//	1.56 ±0.046	0.997
	Slow	2.15 ±0.151			37.7 ±10.4	
CMP-2						
90.3		2.60 ±0.380	//	//	>50	0.993
123.8		//	1.36 ±0.110	0.934 ±0.011	21.7 ±2.37	0.996
126.5	Fast	0.058 ±0.004	//	//	1.99 ±0.107	0.988
	Slow	1.98 ±0.168			22.5 ±3.99	
132.0	Fast	0.064 ±0.002	//	//	1.35 ±0.034	0.996
	Slow	1.99 ±0.087			20.5 ±1.75	
140.4		//	1.52 ±0.103	0.845 ±0.017	23.3 ±2.38	0.987
CMP-3						
91.4		2.00 ±0.107	//	//	>50	0.992
123.2		//	1.59 ±0.129	0.761 ±0.010	11.6 ±0.628	0.997
127.4	Fast	0.052 ±0.002	//	//	0.992 ±0.032	0.996
	Slow	1.24 ±0.053			10.5 ±0.527	
131.7	Fast	0.064 ±0.003	//	//	1.79 ±0.051	0.996
	Slow	2.37 ±0.200			10.1 ±1.10	

^{13}C Site /ppm		T_{IS} / ms	T_{df} / ms	λ	$T_{1\rho}^{H}$ / ms	R^2
141.3		//	1.17 ±0.076	0.939 ±0.008	9.90 ±0.489	0.997
CMP-5						
91.2		1.93 ±0.084	//	//	>50	0.995
123.2		//	0.845 ±0.188	0.815 ±0.028	14.6 ±2.68	0.954
126.9	Fast	0.063 ±0.002	//	//	1.11 ±0.028	0.998
	Slow	1.43 ±0.056	//	//	10.9 ±0.512	
132.1	Fast	0.075 ±0.002	//	//	0.914 ±0.018	0.997
	Slow	1.25 ±0.066	//	//	12.3 ±0.798	
140.7		//	0.863 ±0.068	0.965 ±0.011	13.8 ±1.01	0.995

8.6. Discussion and Outlook

The characterisation of insoluble microporous polymers using solid-state NMR enabled the confirmation of their proposed molecular structure. The degree of cross-linking determined by NMR correlates well with theoretical values for the CMP networks. CMP-5 exhibits the highest degree of cross-linking confirmed by a reduction in micropore volume. This is further evidenced by modelling data, as CMP-5 shows the highest degree of conformational freedom resulting in increased intramolecular interchalation and largest cluster size.

The CP kinetics studies of the CMP networks confirmed the assignment of the CMP resonances as long CP build up times were observed for the quaternary environments. Interestingly, two component kinetics curves were observed for all C-H aromatic sites which, unlike the previously discussed mesoporous organosilicas, cannot be assigned to surface and bulk functionalities. This could be related to a number of different motional changes such a ring flipping on the aromatics. The adopted explanation of a heterogeneous proton pool, whereby directly attached protons and protons in close proximity provide magnetisation at different rates, is plausible. The presence of domains which results in a heterogeneous proton "pool" could also explain the two component behaviour. However, the I-I*-S model which describes CP kinetics in a heterogeneous proton pool did not give satisfactory fittings. Additional experiments such as low temperature ^{2}H NMR on selectively enriched polymer networks could confirm if this is a motion related effect. Experiments such as LG (Lee-Goldburg) CP/MAS kinetics[227,288] whereby, the process of spin diffusion is eliminated by ^{1}H-^{1}H decoupling during the CP transfer step may also be conducted. Therefore, only direct C-H couplings are observed. The resulting kinetics data of the C-H aromatic sites would be expected to consist of a single component with fast CP build up and relaxation. Such an observation would confirm the presence of two types of proton species providing CP with the one *via* spin diffusion no longer observed under LG CP conditions.

The porous nature of all the polymer networks enables them to be loaded with various organic solvents such as THF. Preliminary work has shown significant changes in the ^{1}H MAS NMR from broad featureless spectra in the dry solids to the emergence of narrow resonances superimposed on broad peaks in the aromatic region for THF loaded polymers. Furthermore, the use of deuterated solvents could also probe which regions of the polymer the guests interact which has previously been investigated in the study of *d*-6

benzene on MOF-5 at low temperatures.[289] There is also the possibility of using hyperpolarized ^{129}Xe NMR which has been used to probe the porous nature of mesoporous silicas MCM-41 and SBA-15. These experiments were sensitive to the presence of micro- and mesoporosity in SBA-15 at the condensation temperature of Xenon.[290] The ability to understand the porous nature of these polymer frameworks on a molecular level would be essential if they were to be used in molecular separations. For example, where one solvent is preferentially adsorbed over another albeit by size exclusion or H-bonding.

9. General Conclusions and Outlook

The synthesis of a variety of multi-functional PMOs has been presented along with their detailed characterisation using a combination of X-ray powder diffraction, N_2 adsorption-desorption isotherms and solid-state NMR. The characterisation of multi-component materials with a lack of long range periodicity on a molecular level has been demonstrated by the application of 2-Dimensional solid-state NMR methodologies.

A -CH=CH-PMO was modified post synthetically *via* bromination or thermal treatment methodologies in order to create a bi-functional framework (chapter 4). The retention of an ordered mesostructure confirmed by PXRD and N_2 sorption measurements upon modification provides a "proof of concept" that additional chemistry is possible in mesoporous organosilicas without destruction of the final framework. The application of ^{29}Si CP/MAS kinetics on Br/-CH=CH-PMO confirmed Bromine has a significant effect across the entire framework and not just at the pore wall interface. This is evident from the decrease in $T_{1\rho}^{H}$ times of all Si T^n sites. Thermally induced metamorphosis *via* proton transfer from silanol groups to ethenylene groups confirmed using ^{13}C and ^{29}Si CP/MAS experiments can be seen as a new approach in the development multi-functional materials. The application of 2D ^{1}H-^{13}C WISE experiments showed evidence of strong template-framework interactions in the as-synthesised –CH=CH-PMO which is consistent with the high mesoscopic ordering. The WISE spectra could act as a reference point for understanding template/framework interactions in more complex multi-functional PMOs.

The preparation of ordered mesoporous bi-functional -CH_2CH_2-/-CH=CH- and -CH_2CH_2-/-C_6H_4- PMOs under both cationic and non-ionic templating using a novel pre-hydrolysis procedure has been presented (chapters 5, 6 and 7). The distribution of the organic functionalities within the framework could be controlled *via* joint or separate pre-hydrolysis conditions yet, was highly dependent on both the templating pathway and organic bridges used. For instance, under acidic conditions joint pre-hydrolysis of the -CH_2CH_2-/-CH=CH- resulted in a homogeneous distribution whilst retaining high mesoscopic ordering, confirmed by ^{1}H-^{29}Si HETCOR and PXRD/ N_2 sorption isotherms respectively (chapter 5). However, the same system prepared under basic conditions using joint pre-hydrolysis showed a domain type structure where the organic functionalities are in isolated regions within the framework (chapter 7). The -CH_2CH_2-/-C_6H_4-PMOs highlighted the difficulties in preparing a pre-hydrolysis system that is consistent and independent of the type of organic

bridges. Indeed, the -CH_2CH_2-/-C_6H_4- PMOs synthesised under basic conditions using pre-hydrolysis always gave a domain type structure, most likely due to the preferential π-π stacking of the aromatic units. Therefore, we conclude that on a molecular level an onion type layering of the organic functionalities is present (chapter 6). On the other hand, the same system under acidic conditions yielded domain structures under pre-hydrolysis yet a homogenous system without, unique to the aromatic containing PMOs.

The introduction of Aluminium into -CH_2CH_2-/-CH=CH-PMOs enabled the confirmation that after pre-hydrolysis under basic conditions the organo-functionalised SBUs re-dispersed as seen from ^{1}H-^{27}Al HETCOR (chapter 7). The most unexpected observations from -CH_2CH_2-/-CH=CH- PMOs prepared *via* the cationic route was the improvement of mesoscopic ordering with the use of joint or separate pre-hydrolysis. This was not seen in any other system studied, and therefore, can be viewed as a new method for preparing highly ordered bi-functional PMOs.

Solid-state NMR provided valuable information on molecular level environments present in the totally amorphous polymer networks. A combination of ^{13}C and ^{29}Si CP/MAS NMR of the tetrahedral Si networks enabled a previously undetected side reaction leading to $SiCH_2CH_3$ sites, previously undetected by other analytical methods. The application of ^{13}C CP/MAS kinetics to show changes in molecular motions as a function of strut length and correlation with atomistic simulations is a first in microporous polymer networks.

The research presented here highlights significant advances in the structural characterisation of complex materials that lack long range periodicity. The project has also lead to the possibility of extending the concepts such as, pre-hydrolysis to other types of organosilicas precursors. The use of $(EtO)_3Si$-R (where R = -$(CH_2)_3NH_2$, -C_6H_5, -$(CH_2)_3SH$ *etc.*) could be added to a bridged precursor to test pre-hydrolysis on tethered R groups. The high throughput (HT) microwave synthesis could be used to optimise the pre-hydrolysis protocol further in the -CH_2CH_2-/-C_6H_4-PMO systems to obtain more homogenous systems. Further to the HT approach, in order to reduce characterisation time, fast acquisition 2D HETCOR experiments similar to those presented by Jäger *et al.*[291] could be applied to rapidly identify the distribution of the organic functionalities. The ^{1}H-^{1}H spin-diffusion experiments provided another approach for rapid screening of homogeneity. However, this requires well resolved ^{1}H spectra of the individual organic components. The determination of the domain sizes in -CH_2CH_2-/-CH=CH-PMOs prepared *via* non ionic templating remains a challenge in terms of NMR development. The low sensitivity of ^{29}Si and ^{13}C spins means a direct correlation experiment could only be performed with isotopic enrichment. A possible

solution could be to use phosphorus containing bridged organosilicas as ^{31}P-^{29}Si or ^{13}C correlation experiments are more feasible.

References

(1) Sing, K. S. W.; Everett, D. H.; Haul, R. A. W.; Moscou, L.; Pierotti, R. A.; Rouquerol, J.; Siemieniewska, T. *Pure and Applied Chemistry* **1985**, *57*, 603-619.

(2) Holland, B. T.; Blanford, C. F.; Stein, A. *Science* **1998**, *281*, 538-540.

(3) Wijnhoven, J.; Vos, W. L. *Science* **1998**, *281*, 802-804.

(4) Beck, J. S.; Vartuli, J. C.; Roth, W. J.; Leonowicz, M. E.; Kresge, C. T.; Schmitt, K. D.; Chu, C. T. W.; Olson, D. H.; Sheppard, E. W.; McCullen, S. B.; Higgins, J. B.; Schlenker, J. L. *Journal of the American Chemical Society* **1992**, *114*, 10834-10843.

(5) Huo, Q. S.; Margolese, D. I.; Ciesla, U.; Feng, P. Y.; Gier, T. E.; Sieger, P.; Leon, R.; Petroff, P. M.; Schuth, F.; Stucky, G. D. *Nature* **1994**, *368*, 317-321.

(6) Zhao, D. Y.; Huo, Q. S.; Feng, J. L.; Chmelka, B. F.; Stucky, G. D. *Journal of the American Chemical Society* **1998**, *120*, 6024-6036.

(7) Zhao, D. Y.; Feng, J. L.; Huo, Q. S.; Melosh, N.; Fredrickson, G. H.; Chmelka, B. F.; Stucky, G. D. *Science* **1998**, *279*, 548-552.

(8) Kresge, C. T.; Leonowicz, M. E.; Roth, W. J.; Vartuli, J. C.; Beck, J. S. *Nature* **1992**, *359*, 710-712.

(9) Bagshaw, S. A.; Pinnavaia, T. J. *Angewandte Chemie-International Edition in English* **1996**, *35*, 1102-1105.

(10) Morris, S. M.; Fulvio, P. F.; Jaroniec, M. *Journal of the American Chemical Society* **2008**, *130*, 15210-15216.

(11) Barrer, R. M. *Nature* **1949**, *164*, 112-113.

(12) Barrer, R. M. *Journal of the Chemical Society* **1950**, 2342-2350.

(13) Zhao, X. B.; Xiao, B.; Fletcher, A. J.; Thomas, K. M.; Bradshaw, D.; Rosseinsky, M. J. *Science* **2004**, *306*, 1012-1015.

(14) Hawxwell, S. M.; Espallargas, G. M.; Bradshaw, D.; Rosseinsky, M. J.; Prior, T. J.; Florence, A. J.; van de Streek, J.; Brammer, L. *Chemical Communications* **2007**, 1532-1534.

(15) Weitkamp, J.; Hunger, M.; Rymsa, U. *Microporous and Mesoporous Materials* **2001**, *48*, 255-270.

(16) Li, H.; Eddaoudi, M.; O'Keeffe, M.; Yaghi, O. M. *Nature* **1999**, *402*, 276-279.

(17) Eddaoudi, M.; Kim, J.; Rosi, N.; Vodak, D.; Wachter, J.; O'Keeffe, M.; Yaghi, O. M. *Science* **2002**, *295*, 469-472.

(18) Park, K. S.; Ni, Z.; Cote, A. P.; Choi, J. Y.; Huang, R. D.; Uribe-Romo, F. J.; Chae, H. K.; O'Keeffe, M.; Yaghi, O. M. *Proceedings of the National Academy of Sciences of the United States of America* **2006**, *103*, 10186-10191.

(19) Masciocchi, N.; Ardizzoia, G. A.; LaMonica, G.; Maspero, A.; Sironi, A. *European Journal of Inorganic Chemistry* **2000**, 2507-2515.

(20) Wood, C. D.; Tan, B.; Trewin, A.; Niu, H. J.; Bradshaw, D.; Rosseinsky, M. J.; Khimyak, Y. Z.; Campbell, N. L.; Kirk, R.; Stockel, E.; Cooper, A. I. *Chemistry of Materials* **2007**, *19*, 2034-2048.

(21) Freyhardt, C. C.; Tsapatsis, M.; Lobo, R. F.; Balkus, K. J.; Davis, M. E. *Nature* **1996**, *381*, 295-298.

(22) Corma, A.; Diaz-Cabanas, M.; Martinez-Triguero, J.; Rey, F.; Rius, J. *Nature* **2002**, *418*, 514-517.

(23) Jones, M. D.; Duer, M. J.; Hermans, S.; Khimyak, Y. Z.; Johnson, B. F. G.; Thomas, J. M. *Angewandte Chemie-International Edition* **2002**, *41*, 4726-4729.

(24) Hartmann, M. *Chemistry of Materials* **2005**, *17*, 4577-4593.

(25) Kokotailo, G. T.; Lawton, S. L.; Olson, D. H.; Olson, D. H.; Meier, W. M. *Nature* **1978**, *272*, 437-438.
(26) Breck, D. W.; Eversole, W. G.; Milton, R. M.; Reed, T. B.; Thomas, T. L. *Journal of the American Chemical Society* **1956**, *78*, 5963-5971.
(27) Reed, T. B.; Breck, D. W. *Journal of the American Chemical Society* **1956**, *78*, 5972-5977.
(28) Vartuli, J. C.; Schmitt, K. D.; Kresge, C. T.; Roth, W. J.; Leonowicz, M. E.; McCullen, S. B.; Hellring, S. D.; Beck, J. S.; Schlenker, J. L.; Olson, D. H.; Sheppard, E. W. *Chemistry of Materials* **1994**, *6*, 2317-2326.
(29) Beck, J. S.; Vartuli, J. C.; Kennedy, G. J.; Kresge, C. T.; Roth, W. J.; Schramm, S. E. *Chemistry of Materials* **1994**, *6*, 1816-1821.
(30) Chen, C. Y., Burkett, S. L., Li, H. X., Davis, M. E. *Microporous materials* **1993**, *2*, 27-34.
(31) Steel, A.; Carr, S. W.; Anderson, M. W. *Journal of the Chemical Society-Chemical Communications* **1994**, 1571-1572.
(32) Monnier, A.; Schuth, F.; Huo, Q.; Kumar, D.; Margolese, D.; Maxwell, R. S.; Stucky, G. D.; Krishnamurty, M.; Petroff, P.; Firouzi, A.; Janicke, M.; Chmelka, B. F. *Science* **1993**, *261*, 1299-1303.
(33) Huo, Q. S.; Margolese, D. I.; Ciesla, U.; Demuth, D. G.; Feng, P. Y.; Gier, T. E.; Sieger, P.; Firouzi, A.; Chmelka, B. F.; Schuth, F.; Stucky, G. D. *Chemistry of Materials* **1994**, *6*, 1176-1191.
(34) Soler-Illia, G.; Crepaldi, E. L.; Grosso, D.; Sanchez, C. *Current Opinion in Colloid & Interface Science* **2003**, *8*, 109-126.
(35) De Paul, S. M.; Zwanziger, J. W.; Ulrich, R.; Wiesner, U.; Spiess, H. W. *Journal of the American Chemical Society* **1999**, *121*, 5727-5736.
(36) Kruk, M.; Jaroniec, M.; Ko, C. H.; Ryoo, R. *Chemistry of Materials* **2000**, *12*, 1961-1968.
(37) Van der Voort, P.; Benjelloun, M.; Vansant, E. F. *Journal of Physical Chemistry B* **2002**, *106*, 9027-9032.
(38) Wang, L. F.; Ma, L.; Wang, A. Q.; Liu, Q.; Mang, T. *Chinese Journal of Catalysis* **2007**, *28*, 805-810.
(39) Hoffmann, F.; Cornelius, M.; Morell, J.; Froba, M. *Angewandte Chemie-International Edition* **2006**, *45*, 3216-3251.
(40) Ritter, H.; Bruhwiler, D. *Journal of Physical Chemistry C* **2009**, *113*, 10667-10674.
(41) Fowler, C. E.; Burkett, S. L.; Mann, S. *Chemical Communications* **1997**, 1769-1770.
(42) Burkett, S. L.; Sims, S. D.; Mann, S. *Chemical Communications* **1996**, 1367-1368.
(43) Richer, R.; Mercier, L. *Chemical Communications* **1998**, 1775-1776.
(44) Melde, B. J.; Holland, B. T.; Blanford, C. F.; Stein, A. *Chemistry of Materials* **1999**, *11*, 3302-3308.
(45) Asefa, T.; MacLachan, M. J.; Coombs, N.; Ozin, G. A. *Nature* **1999**, *402*, 867-871.
(46) Inagaki, S.; Guan, S.; Fukushima, Y.; Ohsuna, T.; Terasaki, O. *Journal of the American Chemical Society* **1999**, *121*, 9611-9614.
(47) Asefa, T.; Yoshina-Ishii, C.; MacLachlan, M. J.; Ozin, G. A. *Journal of Materials Chemistry* **2000**, *10*, 1751-1755.
(48) Sayari, A.; Hamoudi, S.; Yang, Y.; Moudrakovski, I. L.; Ripmeester, J. R. *Chemistry of Materials* **2000**, *12*, 3857-3863.
(49) Guan, S.; Inagaki, S.; Ohsuna, T.; Terasaki, O. *Journal of the American Chemical Society* **2000**, *122*, 5660-5661.
(50) Landskron, K.; Hatton, B. D.; Perovic, D. D.; Ozin, G. A. *Science* **2003**, *302*, 266-269.

(51) Asefa, T.; MacLachlan, M. J.; Grondey, H.; Coombs, N.; Ozin, G. A. *Angewandte Chemie-International Edition* **2000**, *39*, 1808-+.
(52) Zhu, H. G.; Jones, D. J.; Zajac, J.; Roziere, J.; Dutartre, R. *Chemical Communications* **2001**, 2568-2569.
(53) Lee, C. H.; Park, S. S.; Choe, S. J.; Park, D. H. *Microporous and Mesoporous Materials* **2001**, *46*, 257-264.
(54) Burleigh, M. C.; Markowitz, M. A.; Wong, E. M.; Lin, J. S.; Gaber, B. P. *Chemistry of Materials* **2001**, *13*, 4411-+.
(55) Burleigh, M. C.; Markowitz, M. A.; Spector, M. S.; Gaber, B. P. *Chemistry of Materials* **2001**, *13*, 4760-4766.
(56) Temtsin, G.; Asefa, T.; Bittner, S.; Ozin, G. A. *Journal of Materials Chemistry* **2001**, *11*, 3202-3206.
(57) Inagaki, S.; Guan, S.; Ohsuna, T.; Terasaki, O. *Nature* **2002**, *416*, 304-307.
(58) Kapoor, M. P.; Yang, Q. H.; Inagaki, S. *Journal of the American Chemical Society* **2002**, *124*, 15176-15177.
(59) Yang, Q. H.; Kapoor, M. P.; Inagaki, S. *Journal of the American Chemical Society* **2002**, *124*, 9694-9695.
(60) Kuroki, M.; Asefa, T.; Whitnal, W.; Kruk, M.; Yoshina-Ishii, C.; Jaroniec, M.; Ozin, G. A. *Journal of the American Chemical Society* **2002**, *124*, 13886-13895.
(61) Sayari, A.; Yang, Y. *Chemical Communications* **2002**, 2582-2583.
(62) Goto, Y.; Inagaki, S. *Chemical Communications* **2002**, 2410-2411.
(63) Wang, W. H.; Zhou, W. Z.; Sayari, A. *Chemistry of Materials* **2003**, *15*, 4886-4889.
(64) Yokoi, T.; Yoshitake, H.; Tatsumi, T. *Chemistry of Materials* **2003**, *15*, 4536-4538.
(65) Guo, W. P.; Park, J. Y.; Oh, M. O.; Jeong, H. W.; Cho, W. J.; Kim, I.; Ha, C. S. *Chemistry of Materials* **2003**, *15*, 2295-+.
(66) Guo, W. P.; Kim, I.; Ha, C. S. *Chemical Communications* **2003**, 2692-2693.
(67) Burleigh, M. C.; Markowitz, M. A.; Jayasundera, S.; Spector, M. S.; Thomas, C. W.; Gaber, B. P. *Journal of Physical Chemistry B* **2003**, *107*, 12628-12634.
(68) Hunks, W. J.; Ozin, G. A. *Chemistry of Materials* **2004**, *16*, 5465-5472.
(69) Wahab, M. A.; Kim, I.; Ha, C. S. *Journal of Solid State Chemistry* **2004**, *177*, 3439-3447.
(70) Liu, C. Q.; Fu, L.; Economy, J. *Macromolecular Rapid Communications* **2004**, *25*, 804-807.
(71) Wang, W. H.; Xie, S. H.; Zhou, W. Z.; Sayari, A. *Chemistry of Materials* **2004**, *16*, 1756-1762.
(72) Yang, Q. H.; Liu, J.; Yang, J.; Kapoor, M. P.; Inagaki, S.; Li, C. *Journal of Catalysis* **2004**, *228*, 265-272.
(73) Cornelius, M.; Hoffmann, F.; Froba, M. *Chemistry of Materials* **2005**, *17*, 6674-6678.
(74) Zhang, W. H.; Daly, B.; O'Callaghan, J.; Zhang, L.; Shi, J. L.; Li, C.; Morris, M. A.; Holmes, J. D. *Chemistry of Materials* **2005**, *17*, 6407-6415.
(75) Xia, Y. D.; Mokaya, R. *Microporous and Mesoporous Materials* **2005**, *86*, 231-242.
(76) Landskron, K.; Ozin, G. A. *Angewandte Chemie-International Edition* **2005**, *44*, 2107-2109.
(77) Hunks, W. J.; Ozin, G. A. *Advanced Functional Materials* **2005**, *15*, 259-266.
(78) Morell, J.; Wolter, G.; Froba, M. *Chemistry of Materials* **2005**, *17*, 804-808.
(79) Morell, J.; Gungerich, M.; Wolter, G.; Jiao, J.; Hunger, M.; Klar, P. J.; Froba, M. *Journal of Materials Chemistry* **2006**, *16*, 2809-2818.
(80) Grudzien, R. M.; Grabicka, B. E.; Pikus, S.; Jaroniec, M. *Chemistry of Materials* **2006**, *18*, 1722-1725.

(81) Treuherz, B. A.; Khimyak, Y. Z. *Microporous and Mesoporous Materials* **2007**, *106*, 236-245.
(82) Whitnall, W.; Cademartiri, L.; Ozin, G. A. *Journal of the American Chemical Society* **2007**, *129*, 15644-15649.
(83) Cho, E. B.; Kim, D.; Jaroniec, M. *Langmuir* **2007**, *23*, 11844-11849.
(84) Li, C. M.; Liu, J.; Shi, X.; Yang, J.; Yang, Q. H. *Journal of Physical Chemistry C* **2007**, *111*, 10948-10954.
(85) Vercaemst, C.; Ide, M.; Allaert, B.; Ledoux, N.; Verpoort, F.; Van der Voort, P. *Chemical Communications* **2007**, 2261-2263.
(86) Morell, J.; Chatterjee, S.; Klar, P. J.; Mauder, D.; Shenderovich, I.; Hoffmann, F.; Froba, M. *Chemistry-a European Journal* **2008**, *14*, 5935-5940.
(87) Jones, J. T. A.; Wood, C. D.; Dickinson, C.; Khimyak, Y. Z. *Chemistry of Materials* **2008**, *20*, 3385-3397.
(88) Luo, Y.; Yang, P. P.; Lin, J. *Microporous and Mesoporous Materials* **2008**, *111*, 194-199.
(89) Coutinho, D.; Xiong, C. R.; Balkus, K. J. *Microporous and Mesoporous Materials* **2008**, *108*, 86-94.
(90) Yang, Y.; Sayari, A. *Chemistry of Materials* **2008**, *20*, 2980-2984.
(91) Lee, H.; Choi, W. I.; Ihm, J. *Physical Review Letters* **2006**, *97*.
(92) Cote, A. P.; Benin, A. I.; Ockwig, N. W.; O'Keeffe, M.; Matzger, A. J.; Yaghi, O. M. *Science* **2005**, *310*, 1166-1170.
(93) Zhang, L.; Liu, H.; Yang, H.; Yang, Q. H.; Li, C. *Microporous and Mesoporous Materials* **2008**, *109*, 172-183.
(94) Wahab, M. A.; Kim, I.; Ha, C. S. *Journal of Nanoscience and Nanotechnology* **2008**, *8*, 3532-3538.
(95) Dube, D.; Rat, M.; Beland, F.; Kaliaguine, S. *Microporous and Mesoporous Materials* **2008**, *111*, 596-603.
(96) Zhang, W. H.; Zhang, X. N.; Zhang, L. X.; Schroeder, F.; Harish, P.; Hermes, S.; Shi, J. L.; Fischer, R. A. *Journal of Materials Chemistry* **2007**, *17*, 4320-4326.
(97) Rac, B.; Hegyes, P.; Forgo, P.; Molnar, A. *Applied Catalysis a-General* **2006**, *299*, 193-201.
(98) Hamoudi, S.; Kaliaguine, S. *Chemical Communications* **2002**, 2118-2119.
(99) Burleigh, M. C.; Markowitz, M. A.; Spector, M. S.; Gaber, B. P. *Journal of Physical Chemistry B* **2002**, *106*, 9712-9716.
(100) Zhao, L.; Zhu, G. S.; Zhang, D. L.; Di, Y.; Chen, Y.; Terasaki, O.; Qiu, S. L. *Journal of Physical Chemistry B* **2005**, *109*, 764-768.
(101) Yoshina-Ishii, C.; Asefa, T.; Coombs, N.; MacLachlan, M. J.; Ozin, G. A. *Chemical Communications* **1999**, 2539-2540.
(102) Tanev, P. T.; Pinnavaia, T. J. *Science* **1995**, *267*, 865-867.
(103) Wan, Y.; Shi, Y. F.; Zhao, D. Y. *Chemical Communications* **2007**, 897-926.
(104) Chandra, D.; Yokoi, T.; Tatsumi, T.; Bhaumik, A. *Chemistry of Materials* **2007**, *19*, 5347-5354.
(105) Morishita, M.; Shiraishi, Y.; Hirai, T. *Journal of Physical Chemistry B* **2006**, *110*, 17898-17905.
(106) Vinu, A.; Murugesan, V.; Hartmann, M. *Chemistry of Materials* **2003**, *15*, 1385-1393.
(107) Schmidt, R.; Akporiaye, D.; Stocker, M.; Ellestad, O. H. *Journal of the Chemical Society-Chemical Communications* **1994**, 1493-1494.
(108) Mokaya, R.; Jones, W. *Chemical Communications* **1997**, 2185-2186.
(109) Kumaran, G. M.; Garg, S.; Soni, K.; Kumar, M.; Gupta, J. K.; Sharma, L. D.; Rao, K. S. R.; Dhar, G. M. *Microporous and Mesoporous Materials* **2008**, *114*, 103-109.

(110) Chen, H.; Dai, W. L.; Deng, J. F.; Fan, K. N. *Catalysis Letters* **2002**, *81*, 131-136.
(111) Luo, Y.; Lu, G. Z.; Guo, Y. L.; Wang, Y. S. *Catalysis Communications* **2002**, *3*, 129-134.
(112) Melero, J. A.; Iglesias, J.; Arsuaga, J. M.; Sainz-Pardo, J.; de Frutos, P.; Blazquez, S. *Journal of Materials Chemistry* **2007**, *17*, 377-385.
(113) Schulz, P. C.; Morini, M. A.; Palomeque, M.; Puig, J. E. *Colloid and Polymer Science* **2002**, *280*, 322-327.
(114) Sakthivel, A.; Badamali, S. K.; Selvam, P. *Catalysis Letters* **2002**, *80*, 73-76.
(115) Panpranot, J.; Kaewkun, S.; Praserthdam, P.; Goodwin, J. G. *Catalysis Letters* **2003**, *91*, 95-102.
(116) Hu, M. Z. C.; Zielke, J. T.; Byers, C. H.; Lin, J. S.; Harris, M. T. *Journal of Materials Science* **2000**, *35*, 1957-1971.
(117) Eimer, G. A.; Chanquia, C. M.; Sapag, K.; Herrero, E. R. *Microporous and Mesoporous Materials* **2008**, *116*, 670-676.
(118) Li, G.; Zhao, X. S. *Industrial & Engineering Chemistry Research* **2006**, *45*, 3569-3573.
(119) Matsumoto, A.; Chen, H.; Tsutsumi, K.; Grun, M.; Unger, K. *Microporous and Mesoporous Materials* **1999**, *32*, 55-62.
(120) Chen, L. Y.; Ping, Z.; Chuah, G. K.; Jaenicke, S.; Simon, G. *Microporous and Mesoporous Materials* **1999**, *27*, 231-242.
(121) Zeng, S. Q.; Blanchard, J.; Breysse, M.; Shi, Y. H.; Shu, X. T.; Nie, H.; Li, D. D. *Microporous and Mesoporous Materials* **2005**, *85*, 297-304.
(122) Hu, W.; Luo, Q.; Su, Y. C.; Chen, L.; Yue, Y.; Ye, C. H.; Deng, F. *Microporous and Mesoporous Materials* **2006**, *92*, 22-30.
(123) Dragoi, B.; Dumitriu, E.; Guimon, C.; Auroux, A. *Microporous and Mesoporous Materials* **2009**, *121*, 7-17.
(124) Li, W. J.; Huang, S. J.; Liu, S. B.; Coppens, M. O. *Langmuir* **2005**, *21*, 2078-2085.
(125) Kao, H. M.; Ting, C. C.; Chao, S. W. *Journal of Molecular Catalysis a-Chemical* **2005**, *235*, 200-208.
(126) Li, C. L.; Wang, Y. Q.; Guo, Y. L.; Liu, X. H.; Guo, Y.; Zhang, Z. G.; Wang, Y. S.; Lu, G. Z. *Chemistry of Materials* **2007**, *19*, 173-178.
(127) Wang, J. C.; Liu, Q. F.; Liu, Q. *Microporous and Mesoporous Materials* **2007**, *102*, 51-57.
(128) Wang, J. C.; Liu, Q. *Solid State Communications* **2008**, *148*, 529-533.
(129) Hughes, B. J.; Guilbaud, J. B.; Allix, M.; Khimyak, Y. Z. *Journal of Materials Chemistry* **2005**, *15*, 4728-4733.
(130) Cho, W.; Park, J. W.; Ha, C. S. *Materials Letters* **2004**, *58*, 3551-3554.
(131) Xia, Y. D.; Wang, W. X.; Mokaya, R. *Journal of the American Chemical Society* **2005**, *127*, 790-798.
(132) Guo, W. P.; Zhao, X. S. *Microporous and Mesoporous Materials* **2005**, *85*, 32-38.
(133) Shylesh, S.; Singh, A. P. *Microporous and Mesoporous Materials* **2006**, *94*, 127-138.
(134) Shylesh, S.; Srilakshmi, C.; Singh, A. P.; Anderson, B. G. *Microporous and Mesoporous Materials* **2007**, *99*, 334-344.
(135) Levitt, M. H. *Spin Dynamics: Basics of Nuclear Magnetic Resonance*; John Wiley & sons Ltd., 2001.
(136) Laws, D. D.; Bitter, H. M. L.; Jerschow, A. *Angewandte Chemie-International Edition* **2002**, *41*, 3096-3129.
(137) Duer, M. J. *Solid-State NMR Spectroscopy*; 1st ed.; Blackwell Publishing, 2004.
(138) Haeberle.U; Waugh, J. S. *Physical Review* **1968**, *175*, 453-&.

(139) Bielecki, A.; Kolbert, A. C.; Levitt, M. H. *Chemical Physics Letters* **1989**, *155*, 341-346.
(140) Salager, E.; Stein, R. S.; Steuernagel, S.; Lesage, A.; Elena, B.; Emsley, L. *Chemical Physics Letters* **2009**, *469*, 336-341.
(141) Brown, S. P.; Lesage, A.; Elena, B.; Emsley, L. *Journal of the American Chemical Society* **2004**, *126*, 13230-13231.
(142) Lesage, A.; Sakellariou, D.; Hediger, S.; Elena, B.; Charmont, P.; Steuernagel, S.; Emsley, L. *Journal of Magnetic Resonance* **2003**, *163*, 105-113.
(143) Samoson, A.; Lippmaa, E.; Pines, A. *Molecular Physics* **1988**, *65*, 1013-1018.
(144) Chmelka, B. F.; Mueller, K. T.; Pines, A.; Stebbins, J.; Wu, Y.; Zwanziger, J. W. *Nature* **1989**, *339*, 42-43.
(145) Mueller, K. T.; Sun, B. Q.; Chingas, G. C.; Zwanziger, J. W.; Terao, T.; Pines, A. *Journal of Magnetic Resonance* **1990**, *86*, 470-487.
(146) Madhu, P. K.; Goldbourt, A.; Frydman, L.; Vega, S. *Chemical Physics Letters* **1999**, *307*, 41-47.
(147) Medek, A.; Harwood, J. S.; Frydman, L. *Journal of the American Chemical Society* **1995**, *117*, 12779-12787.
(148) Fernandez, C.; Amoureux, J. P. *Chemical Physics Letters* **1995**, *242*, 449-454.
(149) Ashbrook, S. E.; Wimperis, S. *Journal of Magnetic Resonance* **2002**, *156*, 269-281.
(150) Ashbrook, S. E.; Wimperis, S. *Journal of the American Chemical Society* **2002**, *124*, 11602-11603.
(151) Gan, Z. H. *Journal of the American Chemical Society* **2000**, *122*, 3242-3243.
(152) Hatton, B. D.; Landskron, K.; Hunks, W. J.; Bennett, M. R.; Shukaris, D.; Perovic, D. D.; Ozin, G. A. *Materials Today* **2006**, *9*, 22-31.
(153) Detken, A.; Hardy, E. H.; Ernst, M.; Meier, B. H. *Chemical Physics Letters* **2002**, *356*, 298-304.
(154) Kolodziejski, W.; Klinowski, J. *Chem. Rev.* **2002**, *102*, 613-628.
(155) McBrierty, V. J.; Douglass, D. C. *Macromolecular Reviews Part D-Journal of Polymer Science* **1981**, *16*, 295-366.
(156) Slabicki, M. M.; Potrzebowski, M. J.; Bujacz, G.; Olejniczak, S.; Olczak, J. *J. Phys. Chem. B* **2004**, *108*, 4535-4545.
(157) Hunger, M. *Solid State Nuclear Magnetic Resonance* **1996**, *6*, 1-29.
(158) Klinowski, J. *Annual Review Of Materials Science* **1988**, *18*, 189-218.
(159) Klinowski, J. *Chemical Reviews* **1991**, *91*, 1459-1479.
(160) Brown, S. P. *Progress in Nuclear Magnetic Resonance Spectroscopy* **2007**, *50*, 199-251.
(161) Diez-Pena, E.; Quijada-Garrido, I.; Barrales-Rienda, J. M.; Schnell, I.; Spiess, H. W. *Macromolecular Chemistry and Physics* **2004**, *205*, 430-437.
(162) Diez-Pena, E.; Quijada-Garrido, I.; Barrales-Rienda, J. M.; Schnell, I.; Spiess, H. W. *Macromolecular Chemistry and Physics* **2004**, *205*, 438-447.
(163) Schnell, I.; Spiess, H. W. *Journal of Magnetic Resonance* **2001**, *151*, 153-227.
(164) Alam, T. M.; Fan, H. Y. *Macromolecular Chemistry and Physics* **2003**, *204*, 2023-2030.
(165) Fyfe, C. A.; Brouwer, D. H. *Journal of the American Chemical Society* **2006**, *128*, 11860-11871.
(166) Fyfe, C. A.; Brouwer, D. H. *Canadian Journal of Chemistry-Revue Canadienne De Chimie* **2006**, *84*, 345-355.
(167) Pourpoint, F.; Gervais, C.; Bonhomme-Coury, L.; Azais, T.; Coelho, C.; Mauri, F.; Alonso, B.; Babonneau, F.; Bonhomme, C. *Applied Magnetic Resonance* **2007**, *32*, 435-457.

(168) Babonneau, F.; Gualandris, V.; Maquet, J.; Massiot, D.; Janicke, M. T.; Chmelka, B. F. *Journal of Sol-Gel Science and Technology* **2000**, *19*, 113-117.
(169) Baccile, N.; Laurent, G.; Bonhomme, C.; Innocenzi, P.; Babonneau, F. *Chemistry of Materials* **2007**, *19*, 1343-1354.
(170) Dinnebier, R. E., Billinge, S.J.L. *Powder Diffraction Theory and Practice*; 1st ed.; RSC Publishing, 2008.
(171) Pecharsky, V. K., Zavalij, P.Y. *Fundamentals of Powder Diffraction ans Structural Characterization of Materials*; 2nd ed.; Spinger, 2009.
(172) West, A. R. *Basic Solid State Chemistry*; John Wiley & Sons, Ltd., 2000.
(173) Song, Y. N.; Zavalij, P. Y.; Suzuki, M.; Whittingham, M. S. *Inorganic Chemistry* **2002**, *41*, 5778-5786.
(174) Song, Y. N.; Yang, S. F.; Zavalij, P. Y.; Whittingham, M. S. *Materials Research Bulletin* **2002**, *37*, 1249-1257.
(175) Leofanti, G.; Padovan, M.; Tozzola, G.; Venturelli, B. *Catalysis Today* **1998**, *41*, 207-219.
(176) Brunauer, S.; Emmet, P. H. *Journal of the American Chemical Society* **1938**, *60*, 309.
(177) Joyner, L. G.; Barrett, E. P.; Skold, R. *Journal of the American Chemical Society* **1951**, *73*, 3155-3158.
(178) Barrett, E. P.; Joyner, L. G.; Halenda, P. P. *Journal of the American Chemical Society* **1951**, *73*, 373-380.
(179) Pierce, C. *Journal of Physical Chemistry* **1953**, *57*, 149-152.
(180) Cranston, R. W.; Inkley, F. A. *Advances in Catalysis* **1957**, *9*, 143-154.
(181) Broekhof.Jc; Deboer, J. H. *Journal of Catalysis* **1968**, *10*, 153-&.
(182) Broekhof.Jc; Deboer, J. H. *Journal of Catalysis* **1967**, *9*, 15-&.
(183) Xia, Y. D.; Mokaya, R. *Journal of Materials Chemistry* **2006**, *16*, 395-400.
(184) Schmidtrohr, K.; Clauss, J.; Spiess, H. W. *Macromolecules* **1992**, *25*, 3273-3277.
(185) Hediger, S.; Emsley, L.; Fischer, M. *Carbohydrate Research* **1999**, *322*, 102-112.
(186) vanRossum, B. J.; Forster, H.; deGroot, H. J. M. *Journal of Magnetic Resonance* **1997**, *124*, 516-519.
(187) States, D. J.; Haberkorn, R. A.; Ruben, D. J. *Journal of Magnetic Resonance* **1982**, *48*, 286-292.
(188) Keeler, J.; Neuhaus, D. *Journal of Magnetic Resonance* **1985**, *63*, 454-472.
(189) Keeler, J. *Understanding NMR Spectroscopy*; John Wiley & sons Ltd., 2005.
(190) Nakajima, K.; Tomita, I.; Hara, M.; Hayashi, S.; Domen, K.; Kondo, J. N. *Journal of Materials Chemistry* **2005**, *15*, 2362-2368.
(191) Vercaemst, C.; Jones, J. T. A.; Khimyak, Y. Z.; Martins, J. C.; Verpoort, F.; Van der Voort, P. *Physical Chemistry Chemical Physics* **2008**, *10*, 5349-5352.
(192) Khimyak, Y. Z.; Klinowski, J. *Physical Chemistry Chemical Physics* **2001**, *3*, 616-626.
(193) Harris, R. K.; Becker, E. D.; de Menezes, S. M. C.; Goodfellow, R.; Granger, P. *Solid State Nuclear Magnetic Resonance* **2002**, *22*, 458-483.
(194) Nakajima, K.; Lu, D. L.; Kondo, J. N.; Tomita, I.; Inagaki, S.; Hara, M.; Hayashi, S.; Domen, K. *Chemistry Letters* **2003**, *32*, 950-951.
(195) Delevoye, L.; Trebosc, J.; Gan, Z.; Montagne, L.; Amoureux, J. P. *Journal of Magnetic Resonance* **2007**, *186*, 94-99.
(196) Stein, R. S.; Elena, B.; Emsley, L. *Chemical Physics Letters* **2008**, *458*, 391-395.
(197) Orr, R. M.; Duer, M. J. *Solid State Nuclear Magnetic Resonance* **2006**, *30*, 130-134.
(198) Grunberg, B.; Emmler, T.; Gedat, E.; Shenderovich, J.; Findenegg, G. H.; Limbach, H. H.; Buntkowsky, G. *Chemistry-a European Journal* **2004**, *10*, 5689-5696.

(199) Derylo-Marczewska, A.; Marczewski, A. W.; Skrzypek, I.; Pikus, S.; Kozak, M. *Applied Surface Science* **2008**, *255*, 2851-2858.
(200) Calvillo, L.; Celorrio, V.; Moliner, R.; Cabot, P. L.; Esparbe, I.; Lazaro, M. J. *Microporous and Mesoporous Materials* **2008**, *116*, 292-298.
(201) Mohamed, M. M.; Zidan, F. I.; Fodail, M. H. *Journal of Materials Science* **2007**, *42*, 4066-4075.
(202) Sang, S. Y.; Chang, F. X.; Liu, Z. M.; He, C. Q.; He, Y. L.; Xu, L. *Catalysis Today* **2004**, *93-95*, 729-734.
(203) Kapoor, M. P.; Inagaki, S. *Chemistry of Materials* **2002**, *14*, 3509-3514.
(204) Wang, W., Carter, B. O., Bray, C. L., Steiner, A., Bacsa, J., Jones, J. T. A., Cropper, C., Khimyak, Y. Z., Adams, D. J., Cooper, A. I. *Chemistry of Materials* **2009**, *21*, DOI: 10.1021/cm9009628.
(205) Luan, Z. H.; Fournier, J. A.; Wooten, J. B.; Miser, D. E. *Microporous and Mesoporous Materials* **2005**, *83*, 150-158.
(206) Chen, Y. Y.; Huang, Y. L.; Xiu, J. H.; Han, X. W.; Bao, X. H. *Applied Catalysis a-General* **2004**, *273*, 185-191.
(207) Cabrera, S.; El Haskouri, J.; Guillem, C.; Latorre, J.; Beltran-Porter, A.; Beltran-Porter, D.; Marcos, M. D.; Amoros, P. *Solid State Sciences* **2000**, *2*, 405-420.
(208) El Haskouri, J.; Cabrera, S.; Caldes, M.; Guillem, C.; Latorre, J.; Beltran, A.; Beltran, D.; Marcos, M. D.; Amoros, P. *Chemistry of Materials* **2002**, *14*, 2637-2643.
(209) Yoldas, B. E. *Journal of Non-Crystalline Solids* **1986**, *83*, 375-390.
(210) Livage, J.; Henry, M.; Sanchez, C. *Progress in Solid State Chemistry* **1988**, *18*, 259-341.
(211) Barringer, E. A.; Bowen, H. K. *Langmuir* **1985**, *1*, 414-420.
(212) Sanderson, R. T. *Science* **1951**, *114*, 670-672.
(213) Yoldas, B. E. *Journal of Non-Crystalline Solids* **1986**, *82*, 11-23.
(214) Zhu, H.; Jones, D. J.; Zajac, J.; Dutartre, R.; Rhomari, M.; Roziere, J. *Chem. Mater.* **2002**, *14*, 4886-4894.
(215) Fan, J.; Yu, C. Z.; Lei, J.; Zhang, Q.; Li, T. C.; Tu, B.; Zhou, W. Z.; Zhao, D. Y. *Journal of the American Chemical Society* **2005**, *127*, 10794-10795.
(216) Van Der Voort, P.; Ravikovitch, P. I.; De Jong, K. P.; Benjelloun, M.; Van Bavel, E.; Janssen, A. H.; Neimark, A. V.; Weckhuysen, B. M.; Vansant, E. F. *Journal of Physical Chemistry B* **2002**, *106*, 5873-5877.
(217) Van Der Voort, P.; Ravikovitch, P. I.; De Jong, K. P.; Neimark, A. V.; Janssen, A. H.; Benjelloun, M.; Van Bavel, E.; Cool, P.; Weckhuysen, B. M.; Vansant, E. F. *Chemical Communications* **2002**, 1010-1011.
(218) Steinbeck, C. A.; Hedin, N.; Chmelka, B. F. *Langmuir* **2004**, *20*, 10399-10412.
(219) Abelmann, K.; Totsche, K. U.; Knicker, H.; Kogel-Knabner, I. *Solid State Nuclear Magnetic Resonance* **2004**, *25*, 252-266.
(220) Scheidt, H. A.; Huster, D. *Acta Pharmacologica Sinica* **2008**, *29*, 35-49.
(221) Scheidt, H. A.; Pampel, A.; Nissler, L.; Gebhardt, R.; Huster, D. *Biochimica Et Biophysica Acta-Biomembranes* **2004**, *1663*, 97-107.
(222) Gawrisch, K.; Eldho, N. V.; Polozov, I. V. *Chemistry and Physics of Lipids* **2002**, *116*, 135-151.
(223) Macura, S.; Ernst, R. R. *Molecular Physics* **1980**, *41*, 95-117.
(224) Salager, E.; Stein, R. S.; Pickard, C. J.; Elena, B.; Emsley, L. *Physical Chemistry Chemical Physics* **2009**, *11*, 2610-2621.
(225) Wu, X. L.; Xie, X. L.; Wu, X. W. *Chemical Physics Letters* **1989**, *162*, 325-328.
(226) Wilhelm, M.; Feng, H.; Tracht, U.; Spiess, H. W. *Journal of Magnetic Resonance* **1998**, *134*, 255-260.

(227) Aluas, M.; Tripon, C.; Griffin, J. M.; Filip, X.; Ladizhansky, V.; Griffin, R. G.; Brown, S. P.; Filip, C. *Journal of Magnetic Resonance* **2009**, *199*, 173-187.
(228) Goto, Y.; Okamoto, K.; Inagaki, S. *Bulletin of the Chemical Society of Japan* **2005**, *78*, 932-936.
(229) Brus, J.; Urbanova, M.; Strachota, A. *Macromolecules* **2008**, *41*, 372-386.
(230) Romeo, H. E.; Fanovich, M. A.; Williams, R. J. J.; Matejka, L.; Plestil, J.; Jiri, B. *Macromolecules* **2007**, *40*, 1435-1443.
(231) Waller, M. P.; Robertazzi, A.; Platts, J. A.; Hibbs, D. E.; Williams, P. A. *Journal of Computational Chemistry* **2006**, *27*, 491-504.
(232) Inaki, Y.; Yoshida, H.; Kimura, K.; Inagaki, S.; Fukushima, Y.; Hattori, T. *Physical Chemistry Chemical Physics* **2000**, *2*, 5293-5297.
(233) Hoffmann, F.; Cornelius, M.; Morell, J.; Froba, M. *Angew. Chem. Int. Ed.* **2006**, *45*, 3216-3251.
(234) Yang, Y.; Sayari, A. *Chemistry of Materials* **2007**, *19*, 4117-+.
(235) Schmidt, H.; Scholze, H.; Kaiser, A. *Journal of Non-Crystalline Solids* **1984**, *63*, 1-11.
(236) Schmidt, H. *Journal of Non-Crystalline Solids* **1985**, *73*, 681-691.
(237) Ying, J. Y.; Mehnert, C. P.; Wong, M. S. *Angewandte Chemie-International Edition* **1999**, *38*, 56-77.
(238) Shenderovich, I. G.; Mauder, D.; Akcakayiran, D.; Buntkowsky, G.; Limbach, H. H.; Findenegg, G. H. *Journal of Physical Chemistry B* **2007**, *111*, 12088-12096.
(239) Buntkowsky, G.; Breitzke, H.; Adamezyk, A.; Roelofs, F.; Emmler, T.; Gedat, E.; Grunberg, B.; Xu, Y.; Limbach, H. H.; Shenderovich, J.; Vyalikh, A.; Findenegg, G. *Physical Chemistry Chemical Physics* **2007**, *9*, 4843-4853.
(240) Diaz-Morales, U.; Bellussi, G.; Carati, A.; Millini, R.; Parker, W. O.; Rizzo, C. *Microporous and Mesoporous Materials* **2006**, *87*, 185-191.
(241) Fang, Q. R.; Zhu, G. S.; Xue, M.; Sun, J. Y.; Qiu, S. L. *Dalton Transactions* **2006**, 2399-2402.
(242) Wahab, M. A.; Imae, I.; Kawakami, Y.; Ha, C. S. *Chemistry of Materials* **2005**, *17*, 2165-2174.
(243) Shylesh, S.; Singh, A. P. *Micropor. Mesopor. Mater.* **2006**, *94*, 127-138.
(244) Shylesh, S.; Srilakshmi, C.; Singh, A. P.; Anderson, B. G. *Micropor. Mesopor. Mater.* **2007**, *99*, 334-344.
(245) Zhai, S. R.; Park, S. S.; Park, M.; Ullah, M. H.; Ha, C. S. *Eur. J. Inorg. Chem.* **2007**, 5480-5488.
(246) Zhang, X. J.; Ma, T. Y.; Yuan, Z. Y. *J. Mater. Chem.* **2008**, *18*, 2003-2010.
(247) Luan, Z. H.; Cheng, C. F.; Zhou, W. Z.; Klinowski, J. *J. Phys. Chem.* **1995**, *99*, 1018-1024.
(248) Luan, Z. H.; He, H. Y.; Zhou, W. Z.; Cheng, C. F.; Klinowski, J. *Chem. Soc., Faraday Trans.* **1995**, *91*, 2955-2959.
(249) Kinrade, S. D.; Swaddle, T. W. *Inorganic Chemistry* **1989**, *28*, 1952-1954.
(250) Pozarnsky, G. A.; McCormick, A. V. *Journal of Non-Crystalline Solids* **1996**, *201*, 175-175.
(251) May, M.; Asomoza, M.; Lopez, T.; Gomez, R. *Chemistry of Materials* **1997**, *9*, 2395-2399.
(252) Harris, R. K.; SamadiMaybodi, A.; Smith, W. *Zeolites* **1997**, *19*, 147-155.
(253) North, M. R.; Swaddle, T. W. *Inorganic Chemistry* **2000**, *39*, 2661-2665.
(254) Follens, L. R. A.; Aerts, A.; Haouas, M.; Caremans, T. P.; Loppinet, B.; Goderis, B.; Vermant, J.; Taulelle, F.; Martens, J. A.; Kirschhock, C. E. A. *Physical Chemistry Chemical Physics* **2008**, *10*, 5574-5583.

(255) Beale, A. M.; Reilly, L. M.; Sankar, G. *Applied Catalysis a-General* **2007**, *325*, 290-295.
(256) Devriese, L. I.; Cools, L.; Aerts, A.; Martens, J. A.; Baron, G. V.; Denayer, J. F. M. *Advanced Functional Materials* **2007**, *17*, 3911-3917.
(257) Lowe, B. M. *Zeolites* **1983**, *3*, 300-305.
(258) Sen, T.; Tiddy, G. J. T.; Casci, J. L.; Anderson, M. W. *Angewandte Chemie-International Edition* **2003**, *42*, 4649-4653.
(259) Cundy, C. S.; Cox, P. A. *Microporous and Mesoporous Materials* **2005**, *82*, 1-78.
(260) Alba, M. D.; Castro, M. A.; Chain, P.; Naranjo, M.; Perdigon, A. C. *Physics and Chemistry of Minerals* **2005**, *32*, 248-254.
(261) Janicke, M. T.; Landry, C. C.; Christiansen, S. C.; Kumar, D.; Stucky, G. D.; Chmelka, B. F. *Journal of the American Chemical Society* **1998**, *120*, 6940-6951.
(262) Jiang, J. X.; Su, F.; Trewin, A.; Wood, C. D.; Niu, H.; Jones, J. T. A.; Khimyak, Y. Z.; Cooper, A. I. *Journal of the American Chemical Society* **2008**, *130*, 7710-7720.
(263) Dawson, R.; Su, F. B.; Niu, H. J.; Wood, C. D.; Jones, J. T. A.; Khimyak, Y. Z.; Cooper, A. I. *Macromolecules* **2008**, *41*, 1591-1593.
(264) Yaghi, O. M.; Li, H. L.; Davis, C.; Richardson, D.; Groy, T. L. *Accounts of Chemical Research* **1998**, *31*, 474-484.
(265) El-Kaderi, H. M.; Hunt, J. R.; Mendoza-Cortes, J. L.; Cote, A. P.; Taylor, R. E.; O'Keeffe, M.; Yaghi, O. M. *Science* **2007**, *316*, 268-272.
(266) Sonogashira, K.; Tohda, Y.; Hagihara, N. *Tetrahedron Letters* **1975**, 4467-4470.
(267) Moroni, M.; Lemoigne, J.; Luzzati, S. *Macromolecules* **1994**, *27*, 562-571.
(268) Weder, C.; Wrighton, M. S.; Spreiter, R.; Bosshard, C.; Gunter, P. *Journal of Physical Chemistry* **1996**, *100*, 18931-18936.
(269) Weder, C.; Wrighton, M. S. *Macromolecules* **1996**, *29*, 5157-5165.
(270) Babudri, F.; Colangiuli, D.; Di Bari, L.; Farinola, G. M.; Omar, O. H.; Naso, F.; Pescitelli, G. *Macromolecules* **2006**, *39*, 5206-5212.
(271) Kobayashi, N.; Kijima, M. *Journal of Materials Chemistry* **2007**, *17*, 4289-4296.
(272) Mendez, J. D.; Schroeter, M.; Weder, C. *Macromolecular Chemistry and Physics* **2007**, *208*, 1625-1636.
(273) Atas, E.; Peng, Z. H.; Kleiman, V. D. *Journal of Physical Chemistry B* **2005**, *109*, 13553-13560.
(274) Liu, X. Y.; Tian, B. Z.; Yu, C. Z.; Gao, F.; Xie, S. H.; Tu, B.; Che, R. C.; Peng, L. M.; Zhao, D. Y. *Angewandte Chemie-International Edition* **2002**, *41*, 3876-3878.
(275) Trumbo, D. L.; Marvel, C. S. *Journal of Polymer Science Part a-Polymer Chemistry* **1986**, *24*, 2311-2326.
(276) El-Kaderi, H. M.; Hunt, J. R.; Mendoza-Cortes, J. L.; Côté, A. P.; Taylor, R. E.; O'Keeffe, M.; Yaghi, O. M. *Science* **2007**, *316*, 268-272.
(277) Côté, A. P.; El-Kaderi, H. M.; Furukawa, H.; Hunt, J. R.; Yaghi, O. M. *J. Am. Chem. Soc.* **2007**, *129*, 12914-12915.
(278) Côté, A. P.; El-Kaderi, H. M.; Furukawa, H.; Hunt, J. R.; Yaghi, O. M. *Journal of the American Chemical Society* **2007**, *129*, 12914-+.
(279) Wang, C. C.; Kuo, C. T.; Yang, J. C.; Lee, G. H.; Shih, W. J.; Sheu, H. S. *Cryst. Growth Des.* **2007**, *7*, 1476-1482.
(280) Wang, C. C.; Tseng, S. M.; Lin, S. Y.; Liu, F. C.; Dai, S. C.; Lee, G. H.; Shih, W. J.; Sheu, H. S. *Cryst. Growth Des.* **2007**, *7*, 1783-1790.
(281) Yang, E. C.; Zhao, H. K.; Ding, B.; Wang, X. G.; Zhao, X. J. *Cryst. Growth Des.* **2007**, *7*, 2009-2015.
(282) Jiang, J. X.; Trewin, A.; Su, F. B.; Wood, C. D.; Niu, H. J.; Jones, J. T. A.; Khimyak, Y. Z.; Cooper, A. I. *Macromolecules* **2009**, *42*, 2658-2666.

(283) Weber, J.; Thomas, A. *Journal of the American Chemical Society* **2008**, *130*, 6334-+.
(284) Jiang, J. X.; Su, F.; Trewin, A.; Wood, C. D.; Campbell, N. L.; Niu, H.; Dickinson, C.; Ganin, A. Y.; Rosseinsky, M. J.; Khimyak, Y. Z.; Cooper, A. I. *Angewandte Chemie-International Edition* **2007**, *46*, 8574-8578.
(285) Rose, M.; Bohlmann, W.; Sabo, M.; Kaskel, S. *Chemical Communications* **2008**, 2462-2464.
(286) Su, D.; Menger, F. M. *Tetrahedron Letters* **1997**, *38*, 1485-1488.
(287) Ghanem, B. S.; Msayib, K. J.; McKeown, N. B.; Harris, K. D. M.; Pan, Z.; Budd, P. M.; Butler, A.; Selbie, J.; Book, D.; Walton, A. *Chemical Communications* **2007**, 67-69.
(288) Lee, M.; Goldburg, W. I. *Physical Review* **1965**, *140*, 1261-&.
(289) Davidson, A.; Berthault, P.; Desvaux, H. *Journal of Physical Chemistry B* **2003**, *107*, 14388-14393.
(290) Gonzalez, J.; Devi, R. N.; Tunstall, D. P.; Cox, P. A.; Wright, P. A. *Microporous and Mesoporous Materials* **2005**, *84*, 97-104.
(291) Maltsev, S.; Jager, C. *Solid State Nuclear Magnetic Resonance* **2008**, *34*, 175-179.